

Numerical and theoretical study of flapping airfoil aerodynamics using a parallelized
immersed-boundary method

By

Zhenglun (Alan) Wei

Submitted to the graduate degree program in Department of Aerospace Engineering
and the Graduate Faculty of the University of Kansas in partial fulfillment of the
requirements for the degree of Doctor of Philosophy.

Chairperson Dr. Zhongquan Charlie Zheng

Dr. Saeed Farokhi

Dr. Weizhang Huang

Dr. Shawn Keshmiri

Dr. Ray Taghavi

Date Defended: April 11, 2014

The Dissertation Committee for Zhenglun (Alan) Wei
certifies that this is the approved version of the following dissertation:

Numerical and theoretical study of flapping airfoil aerodynamics using a parallelized
immersed-boundary method

Chairperson Dr. Zhongquan Charlie Zheng

Date approved: April 11, 2014

ABSTRACT

Flight has fascinated humans for centuries. Human inventions such as missiles, aircraft, unmanned aerial vehicles (UAV), and micro air vehicle (MAV) are inspired by natural flying expertise. As natural flyers usually operate in a vortex-dominated environment, interactions between their wings and the vortices have significant influences on force generation and flying efficiency. Some interesting phenomena induced from such vortex-body interactions have gotten a lot of attention in the past few decades.

A good example is that birds and insects are credited with extracting energy from ambient vortices. In a simpler form, bio-inspired airfoils with either passive or active flapping motions are found to have the potential to harvest energy from incoming vortices generated from an upstream object, i.e. a cylinder. The current study identified the interaction modes of the leading edge vortex (LEV) and trailing edge vortex (TEV) between the active flapping airfoil and the incoming vortices. The relation between the interaction modes and the energy extraction capacity of an active harvester is investigated guided by a potential theory. The interaction modes induced by a passive energy harvester always benefit the energy extraction efficiency. However, the dynamic response of the passive harvester was found to vary corresponding to the properties of the incoming vortical wake. A profound appreciation of energy extracting mechanisms can provide a solution for the energy consumption issue of MAV and UAV. However, difficulties are encountered in practical applications of energy harvesting on how to detect the locations of generated vortices and what the trajectory of the vortex downstream of the moving body is. Some observations are realized and the fluid dynamics of the phenomena is

beyond the fundamentals described in the textbook. One well-known instance is the asymmetric wake formed downstream of a symmetric sinusoidal heaving airfoil. In this study, factors that influence the formation of the asymmetric wakes on both the near wake and far wake regions are demonstrated. Novel vortex models are developed to explore the vortex dynamic mechanisms of the asymmetric wake and its development from the near wake region to the far wake region.

In order to analyze the flow fields for the bio-inspired problems, Computational Fluid Dynamics (CFD) provides powerful and convenient tools. The shape of bio-inspired wings/airfoils and their maneuvers are usually very complicated. In CFD, the immersed-boundary (IB) method is an advantageous approach to simulate such problems. In this study, an immersed-boundary method is implemented in a parallel fashion in order to speed up the computational rate.. A variety of numerical schemes have been applied to the IB method, including different spatial schemes and temporal schemes; their performances are investigated. In addition, the IB method has been successfully implemented with the fluid-structure interaction models for studying passive mobile objectives, i.e. the energy harvester. The possibility of coupling other fluid dynamic models, i.e. species transport model and turbulence models, is also demonstrated.

Acknowledgement

I would like to thank Dr. Zhongquan Charlie Zheng for his advice not only on exploring the world of science but also for mentoring me to be a better man. His continuous support has enabled my Ph.D study to achieve such an important milestone in my life and, at the same time, to become a promising start to my future career.

I am grateful for the help and input from the rest of the committee members, and thank Dr. Zhijian Wang and Dr. Xuemin Tu for their insightful suggestions on numerical methods.

I also enjoy discussions with all group members of Dr. Zhongquan Zheng and Dr. Zhijian Wang and thank them for sharing their creative ideas on computational fluid dynamics.

Finally, I would like to thank my wife Luyu, my parents, and my friends for their love and full support. It would have been impossible to complete this dissertation without their support.

Table of Contents

1 Introduction	1
1.1 Research Objectives and Background.....	1
1.1.1 Asymmetric Wakes Downstream of Heaving Airfoils	1
1.1.2 Energy Harvesting of Flapping Foils	4
1.2 Numerical Methods.....	7
1.2.1 Immersed Boundary Method.....	7
1.2.2 Parallel Computation.....	12
1.2.3 Fluid-Structure Interactions and Temporal Schemes	13
1.2.4 Turbulence Model	15
1.3 Organization of Thesis	21
2 Numerical Method	23
2.1 Governing Equations Without Turbulence Models.....	23
2.2 Temporal Discretization	25
2.3 Fluid-Structure Interaction Model	32
2.4 Large Eddy Simulation	33
3 Parallel Implementation and Validations	36
3.1 Parallel Implementation	36
3.2 Temporal Schemes and the FSI Model	48
3.2.1 Stationary Cylinder	49
3.2.2 Oscillating Cylinder with Prescribed Motions.....	51
3.2.3 Validation Cases for FSI Model – Vortex-Induced Vibration	54
3.2.4 Other Comments on Temporal Schemes	55
3.3 Large Eddy Simulation	58

4 Rapid Pitching Airfoils.....	63
4.1 Comparisons of Vorticity and Forces	63
4.2 Added-Mass Effect.....	69
4.3 Summary for the Rapid Pitching Airfoil	74
5 Asymmetric Wakes.....	75
5.1 Near Wake Deflections	76
5.2 Discussions of the Factors Influencing Near Wake Deflection.....	82
5.2.1 Effects of the Strouhal Number versus the Individual Effects of the Reduced Frequency and Amplitude	82
5.2.2 Reynolds number effect on the deflection angle.....	89
5.3 Summary of the Near Wake Deflections.....	92
5.4 The Phenomena of Far-Wake Deflection and Switching of Vortex Pattern	93
5.4.1 The Cross-flow Effective Phase Velocity.....	100
5.4.2 The Change of the Self-Induced Dipole Velocity	108
5.4.3 The Effect of the Dipole Angle, α	113
5.5 Summary of the Far Wake Deflection and Vortex Switching	115
6 Energy Harvesting.....	116
6.1 Energy Harvesters with Active Heaving/Pitching Motions	116
6.1.1 Interaction Modes and A Potential-Theory Analysis	120
6.1.2 Purely Heaving Motions	134
6.1.3 Purely Pitching Motions.....	148
6.1.4 Summary of Active Energy Harvesters	161
6.2 Energy Harvesters with Passive Heaving Motions	162

6.2.1 Types of Foil Responses.....	165
6.2.2 Vortex Topology	170
6.2.3 Summary of Passive Energy Harvesters	174
7 Conclusion	175
Reference.....	178
Appendix I.....	189
Appendix II	190
Appendix III.....	191
Appendix IV	192

List of Figures

Figure 1-1 Representation of the points in the vicinity of an immersed boundary used in the sharp interface IB method.	10
Figure 1-2 Decomposition of the energy spectrum of the solution associated with the (a) Reynolds Averaged Numerical Simulation (RANS) and (b) LES.....	16
Figure 1-3 Sketch of turbulent energy spectrum according to Durbin and Pettersson Reif ¹⁰³	17
Figure 1-4 Representation of the primary and secondary grids for the zonal two-layer wall model ⁸⁹	19
Figure 1-5 Organization of the thesis (from left to right)	21
Figure 3-1 2D Grid partitioning with 1 process (top left), 2 processes (top right), 4 processes (bottom left) and 8 processes (bottom right)	37
Figure 3-2 Ratio of computational time costs in data communication with different numbers of processes	38
Figure 3-3 Computational domain of a representative unit structure; the depth is H . .	41
Figure 3-4 Velocity profiles at the outlet for grid independence check for flow through an REV with impermeable square rods with (a) FLUENT (b) IB method	44
Fig. 3-5. A comparison of streamwise velocity contours between (a) FLUENT and (b) the IB method.....	46
Fig. 3-6. The parallel speedup with different numbers of processes.....	47
Figure 3-7 Sketch of the configuration of the system involving only one cylinder.	48
Figure 3-8 C_p on the top surface of a stationary cylinder at $Re = 40$. Compare the current result with $\delta t = 256^{-1}$ to the results from Zheng & Zhang ⁶³	49

Figure 3-9 Time-periodic variation of the lift coefficient between two RK3 schemes.	51
Figure 3-10 Time-periodic variation of the lift coefficient among three temporal schemes:	52
Figure 3-11 Time-periodic variation of the lift coefficient among three temporal schemes:	53
Figure 3-12 The variation of the response amplitude with the reduced velocity for a single vortex-induced vibrating cylinder and its comparison with previous studies ^{83, 139, 140}	54
Figure 3-13 Comparison of pressure components of drag coefficient.	56
Figure 3-14 Comparisons of wake axis distributions of average streamwise velocity and its root-mean-square (r.m.s.) for the flow over a sphere at $Re = 300$	57
Figure 3-15 Comparisons of wake axis distributions of average streamwise velocity and its root-mean-square (r.m.s.) for flow over a sphere at $Re = 3700$	60
Figure 4-1 Basic pitch-up, pitch-down kinematics (with $k = 0.7$ shown here) from Eldredge <i>et al.</i> ¹⁵¹	64
Figure 4-2 Comparisons of vorticity fields for the flat plate cases for $k = 0.7$, among the current simulation (left), Eldredge <i>et al.</i> ¹⁵¹ (center), and Ol ¹⁵² $Re=10k$ (right).	65
Figure 4-3 Same as previous figure but for $k = 0.2$, and Row 6 is for the results of 0.875 time units after completion of pitch-down.....	66
Figure 4-4 Lift and drag coefficient comparisons of the $k = 0.2$ cases between the current simulation (left) and Eldredge <i>et al.</i> ¹⁵¹ (right).	68
Figure 4-5 Comparisons of lift and drag coefficients between the current simulation and Theodorsen's theory for the cases of $k = 0.7$ (left) and $k=0.2$ (right).	72

Figure 4-6 Comparisons of lift coefficient between the current simulation and Theodorsen's theory for the cases of $k = 0.7$ (left) and $k=0.2$ (right).	73
Figure 5-1 Definition sketch of set-up of simulations in this study	75
Figure 5-2 Vorticity contours for the case of $k = 10$, $h = 0.12$, and $Re = 400$.	77
Figure 5-3 The pairing competition among the first few vortices of a heaving airfoil, (a) with an initially upward motion and (b) with an initially downward motion.	79
Figure 5-4 Parameters used in calculating the effective phase velocities	80
Figure 5-5 Streamwise velocity profiles downstream of the airfoil with $h = 0.12$, $k = 9$ (dash-dot lines) and $h = 0.24$, $k = 5$ (solid lines).	83
Figure 5-6 The vertical location of the maximum value of downstream x-direction velocity profiles for cases with $Re = 500$, where $y = 0$ is the mean location of the heaving airfoil and $x = 0$ is the location of the trailing edge of the airfoil.	84
Figure 5-7 Vorticity contours of cases with the same $V_p=1.2$, (a) $h = 0.12$, $k = 10$ and (b) $h = 0.24$, $k = 5$.	85
Figure 5-8 Deflection angle and effective phase velocities versus the reduced frequency for cases presented in Fig. 7. (a) $h = 0.12$ and (b) $h = 0.16$	86
Figure 5-9 Deflection angle and the difference between the symmetry-breaking and symmetry-holding effective phase velocities versus the reduced frequency k and heaving amplitude h for the case of $Re = 500$.	88
Figure 5-10 Vorticity contours of the beginning of the down-stroke for the case of $h = 0.12$, $k = 10$ with $Re = 200$ (a) and $Re = 400$ (b).	89
Figure 5-11 Deflection angle comparisons with different Reynolds numbers	91

Figure 5-12 Deflection angle and effective phase velocities versus the Reynolds number	92
Figure 5-13 Deflection trends of the cases of $V_p = 1.2$ and $Re = 500$ at different reduced frequencies and amplitudes	94
Figure 5-14 Vorticity contours of the case with $V_p = 1.2$, $k = 20$, and $Re = 500$	96
Figure 5-15 Vorticity contours of the case with $V_p = 1.2$, $k = 14$, and $Re = 500$ at the end of an upstroke. The contour color range is from -20 to 20.	97
Figure 5-16 Vorticity contours of the case with $V_p = 1.3$, $k = 14$ and $Re = 500$	98
Figure 5-17 Vorticity contours of the case with $V_p = 1.3$, $k = 14$, and $Re = 300$ at the end of an upstroke.	99
Figure 5-18 Schematic view of parameters used in calculating the effective phase velocities	101
Figure 5-19 The history of the difference of the effective phase velocity of two consecutive vortex dipoles in the case of $V_p = 1.3$, $k = 14$, $Re = 500$ along with a 2nd-order polynomial fitting curve.	102
Figure 5-20 Trend lines illustrating (a) the effect of the two terms in Eq. (5.4)	105
Figure 5-21 Individual effects of Γ ratio and $1/\xi$ ratio on the ratio of dipole velocity	107
Figure 5-22 Comparisons of the histories of ξ	107
Figure 5-23 Schematic view of parameters for calculating the Biot-Savart induced velocities	109
Figure 5-24 Expected locations of vortices based on the Biot-Savart law	110
Figure 5-25 Histories of $\Delta\xi$ of the two consecutive dipoles	111

Figure 5-26 (a) The individual effect of $\sin\alpha$ of ‘A&B’ and ‘B&C’ (b) Comparisons of α between ‘A&B’ and ‘B&C’	113
Figure 5-27 Histories of $\Delta\alpha$ of “A” and “B” predicted by the Biot-Savart Law.....	114
Figure 6-1 Sketch of the configuration of the system of a cylinder and a foil.....	117
Figure 6-2 Histories of lift and drag coefficients acting on the stationary airfoil at $L = 5$, angle of attack = 30° ; and $d = 0$ [the 1st row], 1 [the 2nd row], and -1 [the 3rd row]. The left column shows the results from the current simulation, and the right column shows these from Liao et al. ¹⁶²	118
Figure 6-3 (a) The suppressing mode of the LEV occurs in the case of $h_a = 0.1$ and $\phi = 225^\circ$, and (b) The reinforcing mode of the LEV occurs in the case of $h_a = 0.1$ and $\phi = 45^\circ$. A quarter cycle of the airfoil down stroking motion is experienced from “the current moment” to “the next moment” in this figure.....	121
Figure 6-4 A sketch of the complex potential theory and coordinate transformation	122
Figure 6-5 (a) Vorticity contours for the case with a heaving airfoil $h_a = 0.1$, $\phi = 0^\circ$ (b) A sketch of the relative locations of the vortices in the potential theory	125
Figure 6-6 While the CCW vortex is approaching, the distribution of the pressure coefficient in the vicinity of the leading edge and trailing edge of an airfoil on its (a) lower surface and (b) upper surface. The motions of the leading edge and trailing edge in this figure are both $2\pi f_a \times 0.4$ downward. For the lower surface, the degree increases counter-clockwise from zero at the leading edge to 180 degree at the trailing edge of the airfoil. For the upper surface, the degree increases clock-wise from zero at the leading edge to 180 degree at the trailing edge.	127

Figure 6-7 While the CW vortex is approaching, the distribution of the pressure coefficient in the vicinity of the leading edge and trailing edge of an airfoil on its (a) lower surface and (b) upper surface.....	128
Figure 6-8 While the CCW vortex is approaching, the distribution of the pressure coefficient in the vicinity of the leading edge and trailing edge of an airfoil on its (a) lower surface and (b) upper surface.....	129
Figure 6-9 While the CW vortex is approaching, the distribution of the pressure coefficient in the vicinity of the leading edge and trailing edge of an airfoil on its (a) lower surface and (b) upper surface.....	130
Figure 6-10 Input and output powers for the cases with different heaving amplitudes and phase differences.....	134
Figure 6-11 Input and output powers for the cases with $h_a = 0.1$	136
Figure 6-12 Lift and thrust coefficients, translational velocity, and vorticity contours of the airfoil over the half cycle of downstroke for the case of $h_a = 0.1$ and $\phi = 45^\circ$	137
Figure 6-13 Lift and thrust coefficients, translational velocity, and vorticity contours of the airfoil over the half cycle of downstroke for the case of $h_a = 0.1$ and $\phi = 225^\circ$	140
Figure 6-14 Lift coefficients, translational velocity, and vorticity contours of the airfoil over the half cycle of downstroke for the case with $h_a = 0.4$ and $\phi = 45^\circ$	144
Figure 6-15 Lift coefficients and translational velocity and vorticity contours of the airfoil over the half cycle of downstroke for the case with $h_a = 0.4$ and $\phi = 225^\circ$	146
Figure 6-16 Input and output powers for the cases with different pitching amplitudes and phase differences.....	148

Figure 6-17 Moment coefficients and angular velocity and vorticity contours of the airfoil over the half cycle of downstroke for the case with $A_a = 12.5^\circ$ and $\phi = 135^\circ$	150
Figure 6-18 Moment coefficients, angular velocity, and vorticity contours of the airfoil over the half cycle of downstroke for the case with $A_a = 12.5^\circ$ and $\phi = 315^\circ$	154
Figure 6-19 Moment coefficients, angular velocity, and vorticity contours of the airfoil over the half cycle of downstroke for the case with $A_a = 60^\circ$ and $\phi = 135^\circ$	157
Figure 6-20 Moment coefficients, angular velocity, and vorticity contours of the airfoil over the half cycle of downstroke for the case with $A_a = 60^\circ$ and $\phi = 315^\circ$	160
Figure 6-21 Histories of vertical positions for all the cases with varying h_c but same $L = 7$	165
Figure 6-22 FFT for the histories of y_a for different cases with $L = 7$	167
Figure 6-23 Comparison of (a) energy harvesting efficiency and (b) input power among all cases	168
Figure 6-24 The history of approximate foil positions and vorticity contours over the oscillating cycle of the foil for the case with $h_c = 0.25$	170
Figure 6-25 The history of approximate foil positions and vorticity contours over the oscillating cycle of the foil for the case with $h_c = 0.4$	172
Figure 6-26 The history of approximate foil positions and vorticity contours over the oscillating cycle of the foil for the case with $h_c = 0.1$	173
Figure 7-1 Summary of the dissertation.	175

List of Tables

Table 1 The relation between incoming vortex positions and interaction modes with an airfoil undergoing a downstroke heaving motion.	131
Table 2 The relation between incoming vortex positions and interaction modes with an airfoil undergoing an upstroke heaving motion.	132

List of Publications

Portions of the material presented here have appeared in the following publications:

Journal Articles:

1. Zheng, Z.C., and **Wei, Z.**, "Study of Mechanisms and Factors That Influence the Formation of Vortical Wake of a Heaving Airfoil," *Physics of Fluids*, Vol. 24. 103601, 2012
2. **Wei, Z.**, and Zheng, Z.C., "Mechanisms of Wake Deflection Angle Change behind a Heaving Airfoil", *Journal of Fluids and Structures*, (accepted)
3. **Wei, Z.**, Zheng, Z.C., and Yang, X. "Computation of flow through a three-dimensional periodic array of porous structures by a parallelized immersed-boundary method", *Journal of Fluids Engineering*, Vol. 136 (4), 040905, 2014
4. **Wei, Z.**, Zheng, Z.C., Bennett, J.S. and Yang, X. "Turbulent simulation and comparison of particle injection in an indoor environment using the species transport and discrete phase/parcel Models", *Journal of Fluids Engineering*, (submitted)
5. **Wei, Z.**, Zheng, Z.C. "Energy harvesting of a flapping airfoil in a vortical wake", (In preparation)
6. **Wei, Z.**, Zheng, Z.C. "Energy harvesting of a purely passive heaving foil in a vortical wake", (In preparation)

Peer-Reviewed Conference Publications

1. **Wei, Z.** and Zheng, Z.C, "Mechanisms of Deflection Angle Change in the Near and Far Vortex Wakes behind a Heaving Airfoil", *51st AIAA Aerospace Sciences Meeting Including the New Horizons Forum and Aerospace Exposition*, January 7-10, 2013, Grapevine, Texas. *AIAA paper* 2013-0840.
2. Zheng, Z.C. and **Wei, Z.**, "Effects of Surface Roughness and Patterns on a Surface-Approaching Pair of Aircraft Wake Vortices", *51st AIAA Aerospace Sciences Meeting Including the New Horizons Forum and Aerospace Exposition*, January 7-10, 2013, Grapevine, Texas. *AIAA paper* 2013-0364.
3. **Wei, Z.** and Zheng, Z.C, "Parallel Implementation and performance of an immersed boundary method", *ASME 2012 Fluid Engineering Summer Meeting*, July 8-12, 2012, Puerto

Rico, USA, *FEDSM* 2012-72318.

4. Zheng, Z.C., **Wei, Z.**, J.S. Bennett and X. Yang, “Simulation and comparison of particle injection in an indoor environment using the species transport and discrete phase models”, *ASME 2012 Fluid Engineering Summer Meeting*, July 8-12, 2012, Puerto Rico, USA, *FEDSM* 2012-72014
5. Zheng, Z.C. and **Wei, Z.**, “Energy Harvesting of a Moving Airfoil in a Vortical Wake,” *50th AIAA Aerospace Sciences Meeting and Exhibits*, January 9-12, 2012, Nashville, TN. *AIAA paper* 2012-0183.
6. Zheng, Z.C., **Wei, Z.** and Zhang, N., “Immersed-Boundary Simulation of a Fast Pitching Airfoil”, *AIAA 40th Fluid Dynamics Conference and Exhibit*, June 28- July 1, 2010, Chicago, IL. *AIAA paper* 2010-4380.
7. Zheng, Z. C., Zhang, N. and **Wei, Z.**, 2009, “Low-Reynolds Number for Flow over a Flapping Wing: Comparisons to Measurement Data”, *39th AIAA Fluid Dynamics Conference*, June 22-25, 2009, San Antonio, TX. *AIAA paper* 2009-3691.

1 Introduction

This introduction discusses the background of the current research, the methods used to meet the objectives, and the organization of this thesis.

1.1 Research Objectives and Background

1.1.1 Asymmetric Wakes Downstream of Heaving Airfoils

Flow around oscillating airfoils has received a lot of attention because of its wide variety of applications in the area of micro-aerial vehicles. At the beginning of last century, it was found that flapping airfoils were able to create a normal force to produce both lift and thrust¹. Flapping wings can therefore be used as an alternative of conventional propeller. In the following decades, aerodynamics of flapping airfoils was studied systematically for heaving and pitching motions. Garrick³ and Theodorsen⁴ analytically proved that plunging airfoils generate thrust over a wide frequency range, while pitching only airfoils do so only for high frequencies. Koochesfahani⁵, Jones *et al.*⁶, Lua *et al.*⁷, and Bratt⁸ explored the vortex patterns of flapping airfoils both experimentally and numerically.

An interesting phenomenon, a deflected vortex wake, was observed in the flow downstream of a heaving symmetric airfoil by Jones *et al.*⁶. Although the heaving motion was symmetric and periodic, the wake deflected to one side of the airfoil rather than locating symmetrically along the line of the mean plunging location of the airfoil. Deflected wakes were also recorded earlier by Bratt⁸ in experiments of flow over a symmetrically pitching NACA0015 airfoil. Unsurprisingly, similar deflected wakes were found in flow with asymmetric sinusoidal airfoil motions⁹. However, unlike the cases

with asymmetric airfoil motions, this phenomenon, with a pure symmetric sinusoidal heaving motion, only occurred at high Strouhal number that Lai and Platzer¹⁰ defined as $2\pi f^* h^* / U_\infty$, where f^* and h^* are the dimensional frequency and amplitude of the heaving motion, respectively. It was noted⁶ that the direction of deflection did not change in numerical simulation, whereas in experiment, small disturbances might influence the flow and randomly change the direction of the deflected wake. Heathcote and Gursul¹¹ presented that the switching of direction of the deflected wake was quasi-periodic in experiments.

Recently, a number of studies have concentrated on the deflected wake. Lewin and Haj-Hariri¹² showed that the direction of the deflected wake could even be altered in the middle of simulation. Blondeaux *et al.*¹³ found a chaotic flow pattern when the heaving amplitude was large, which might be another way to explain the observation in Lewin and Haj-Hariri¹². Zhang *et al.*¹⁴ studied the effect of the geometric shape on the trend of the deflected wake and found that it is easier and faster for slender foils to form an asymmetric downstream wake. In addition, Lua *et al.*⁷ experimentally showed the interactions between leading edge vortices (LEV) and trailing edge vortices (TEV) might lead to a deflected wake. To quantify the deflection angle, the location of the maximum streamwise velocity in the wake was used to determine the deflection angle^{11, 15, 16}. Godoy-Diana *et al.*¹⁷ proposed a vortex dipole model to provide a quantitative prediction of the symmetry-breaking wake based on two consecutive counter-rotating vortices in the wake. A symmetry-breaking criterion based on the phase velocity and an idealized self-advection velocity of vortex dipole was discussed. More recently, Liang *et al.*¹⁸ found that

the wake of a heaving airfoil with a larger Reynolds number would form a larger deflection angle.

Lately, a number of studies have concentrated on the vortex-dipole patterns in the deflected wake. It is recognized¹⁸ that the vortex dipole pattern is the major reason for the asymmetric wake. A vortex dipole model was proposed to quantitatively provide a symmetry-breaking criterion based on the two counter-rotating vortices in the dipole. It related the onset of the asymmetric wake to the strength of the vortices and distances among them. The effect of vortex strength on the asymmetric wake was also evident^{19, 20} where numerical studies showed that a larger deflection angle was formed in the wake of a heaving airfoil with a larger Reynolds number. The effect of distance among vortices was readily supported by the conclusions made in previous papers^{6, 15}. Recently, Zheng & Wei²⁰ extended the model of Godoy-Diana *et al.*¹⁷ by considering two consecutive dipoles, which consist of three vortices, in the calculation of the symmetry-breaking criterion. One of these two consecutive dipoles tends to break the symmetry of the wake, while the other one is inclined to hold it. Zheng & Wei²⁰ not only confirmed the criterion for the onset of the asymmetric wake by Godoy-Diana¹⁷ but also fulfilled a more general purpose in addressing other quantities of the asymmetric wake and the variation of the deflection.

In the present study, deflected wakes of a symmetric heaving airfoil with a zero angle of attack are investigated numerically in 2D. Factors that influence the near wake deflection, including deflection direction and vortex pairing mechanisms, Strouhal number, frequency, amplitude, and Reynolds number, are investigated in detail. The deflection angle is found to be correlated with the symmetry-breaking and symmetry-

holding effective phase velocities. Later, it is found that the near wake deflection angle changes in the far wake. In order to explain this phenomenon, the effective-phase velocity concept is extended to the cross-flow direction of an already deflected wake. The vortex dynamics mechanisms that cause the effective-phase velocity changes are investigated by employing a vortex dipole model. Finally, a vortex dynamic model based on the Biot-Savart law is proposed to explain why the distance between the vortices and the direction of self-induced velocity of the vortex dipole varies from the near wake to the far wake. These mechanisms pertaining to the far wake behaviors can provide important information on far-wake signal detection and how following objects in the far wake region interact with the wake.

1.1.2 Energy Harvesting of Flapping Foils

In addition to the force generation, the topic of energy consumption for MAVs becomes attractive since they need to cover sufficient distances on their own power supplies. Most importantly, the potential renewable energy for MAVs –wind power- is abundantly stored in their operational environments.

As a bio-inspired masterpiece, MAVs often adopt the flapping wing as it is the most common force generator of natural flyers or swimmers. Studies of marine animals^{21, 22} also inspired the concept of extracting energy from ambient flows through the flexible dynamo. The ocean, as a sustainable energy supplier, provides abundant and consistent power. Aquatic animals harvest energy from their living environments with their foils or undulating bodies to enhance their swimming performance²³ or even detect their prey²⁴. In analogy to the ocean, the atmosphere also contains an appreciable amount of energy

resulting in possible improvement in the mechanical efficiency of MAVs. The capability of a single flapping airfoil extracting energy from the uniform freestream has been widely discussed with either forced motions²⁵⁻²⁹ or vortex excited motions³⁰⁻³². Moreover, for unsteady incoming flows, Wu³³ theoretically proved that oscillating foils obtain the energy extraction potential in surface waves. Similar capabilities were discovered for fish to exploit vortices to decrease their muscle activities while swimming³⁴. Gopalkrishnan *et al.*³⁵ carried out experiments with flapping foils in the wake of an oscillating D-cylinder. Interaction modes were identified corresponding to different streamwise distances between the cylinder and airfoil, and the relationship between the different modes and energy harvesting was discussed. Hydrodynamic performances of a flapping airfoil or a fishlike undulating foil downstream of a D-cylinder, later, have been numerically investigated by Shao and Pan³⁶ and Shao *et al.*³⁷, respectively. In addition, Streitlien *et al.*³⁸ established an inviscid analysis and revealed that the phase between foil motion and the arrival of inflow vortices is a critical parameter to tune the efficiency of the energy extraction. Furthermore, Beal *et al.*²³ emphasized that the energy extraction is achieved when the harvester resonates with incoming vortex wakes. Last but not the least, the size of the energy harvester is not negligible as it may substantially influence the energy extraction under certain circumstances^{39, 40}.

Among biologists, similar issues have been broadly discussed for natural flyers with tandem wings, i.e. dragonflies^{41, 42}. Such a configuration with a forewing and a hindwing was reported to obtain better aerodynamic performance compared with that of a single wing^{43, 44}. The phase difference of the motions between the two foils has the capability to tune types of force production for the sake of fulfilling flying tasks in different conditions,

and a trade-off between the propulsion and lift forces was observed⁴³⁻⁴⁶. It is further concluded^{44, 45, 47, 48} that the phase relationship between the fore- and hindwing primarily influences the formation of the LEV, which is directly related to the sign of the interacting vortex and the local flow conditions, i.e. local speeds and angles. Akhtar et al.⁴⁹ further reported that the local effective angle of attack near the LE resulting from the interactions predominantly determines the formation of the LEV.

In this study, energy extraction of a flapping airfoil in the wake of an oscillating D-cylinder is investigated with two-dimensional simulations. Interaction modes between the incoming vortices and flapping airfoils are categorized into two types: suppressing mode and reinforcing mode; their relevance to the formation of both LEVs and TEVs are quantitatively demonstrated by a potential theory proposed in the current study. The topology of the incoming vortices corresponding to the airfoil was found to be of critical importance in activating different interaction modes. The importance of the topology will also be emphasized in order to explain the distinctions between heaving and pitching airfoils in terms of their influence on the interaction modes and the capacity of energy extraction.

Similar phenomena occur for passively heaving foils in the wake of the cylinder. LEVs and TEVs are usually induced to help extract energy from the wake. However, different widths of the incoming vortical wake impact the dynamic responses of the passively mobile energy harvester. The relationships between properties of the vortical wakes and performance of the energy harvesters are discussed.

1.2 Numerical Methods

1.2.1 Immersed Boundary Method

Immersed-boundary methods were first introduced by Peskin⁵⁰ to investigate a flow field around the flexible leaflet of a human heart. It exhibits powerful evidence for this method to predict the flow phenomena in low Reynolds numbers with complicate moving or morphing objects. The advantages of using IB methods are primarily 1) only simple Cartesian grids are needed, 2) no conforming mesh is required to simulate an object in motion, and 3) the shape/arrangement of the objects can be arbitrary. The computation is performed as if there are no solid objects in the flow field. In order to achieve these advantages, a proper artificial forcing term is essential for the Navier-Stokes equation to represent the effect of immersed boundaries in the simulation. In addition, the approach to implement this artificial forcing term identifies different types of the IB methods. Since the emergence of the IB methods, numerous modifications and improvements have been introduced and many variations have been developed. The IB methods can be primarily categorized into four types: feedback forcing methods, direct forcing methods, sharp interface methods, and penalization methods⁵¹.

The original IB method by Peskin^{50, 52} falls into the first category, the feedback forcing method. In this method, a set of elastic fibers are used to represent the immersed boundaries. These fibers numerically are a collection of massless points that move with the local fluid velocity and their locations are tracked in a Lagrangian frame. This method is very attractive for flows with immersed elastic boundaries, including biological⁵²⁻⁵⁷ and multiphase flows^{58, 59}. However, such a forcing term specifically designed for elastic boundaries generally does not perform well in the rigid limit, i.e. for rigid bodies. Early

researchers, e.g. Goldstein *et al.*⁶⁰, circumvented this problem by introducing a spring with a restoring force, $\mathbf{f}(t)$, attached to an equilibrium location.

$$\mathbf{f}(t) = \alpha \int_0^t \mathbf{u}(\tau) d\tau + \beta \mathbf{u}(t) \quad (1.1)$$

This system provides feedback control of the velocity near the surface but brings in two case-dependent empirical parameters, α and β . Although promising results of simulating low Reynolds number flows has been exhibited, the feedback forcing IB method has potential to encounter stability problems for highly unsteady flows because of those empirical parameters. In addition, since the choice of α and β completely depends on the physical problems, the robustness of the feedback forcing IB method is intrinsically limited.

To remedy this drawback of the feedback forcing IB method, the direct forcing IB method was proposed for problems involving rigid bodies; pioneers include Mohd-Yusof⁶¹, Uhlmann⁶², and among others. In this type of IB methods, the forces at immersed boundaries are directly calculated from numerical solution based on the temporally discretized momentum equation.

$$\frac{\mathbf{u}^{n+1} - \mathbf{u}^n}{\delta t} = RHS + \mathbf{f} \quad (1.2)$$

where the right-hand-side (RHS) includes the convective, viscous and pressure gradient. On the immersed boundary, the forcing term in Eq. (1.2) can be obtained by enforcing the physical velocity of the boundary \mathbf{V}^{n+1} to the background grid node for the next time, i.e. $\mathbf{u}^{n+1} = \mathbf{V}^{n+1}$.

$$\mathbf{f} = \frac{\mathbf{V}^{n+1} - \mathbf{u}^n}{\delta t} - RHS \quad (1.3)$$

In each time step, the forcing term acts as a velocity compensator in order to correct the error between the desired (physical) boundary velocity and the computed velocity on the boundary surface. It is apparent that the absence of user-specified parameters in Eq. (1.3) helps the direct forcing IB method eliminate the stability constraints and improve the robustness. With this considerable progress, the direct forcing IB methods are widely used in simulating unsteady flow problems, e.g. Zhang & Zheng⁶³ and Fadlun *et al.*⁶⁴. In addition, the direct forcing concept is successfully implemented in not only the velocity fields but also other flow variables, such as streamfunction⁶⁵. However, no matter if it is the feedback forcing, i.e. Eq. (1.1), or direct forcing, i.e. Eq. (1.3), the forcing terms exhibited above are only valid when the background grid nodes coincide with the immersed boundary. If the coincidence is not there, the force at the interface need to be distributed to the background grid nodes using discrete delta functions, which is expressed as follows

$$\mathbf{f}(\mathbf{x}) = \sum \mathbf{f}(\mathbf{x}_s) \delta_h(\mathbf{x} - \mathbf{x}_s) \Delta \mathbf{x}_s \quad (1.4)$$

where δ_h is a discrete delta function and \mathbf{x}_s is Lagrangian points representing the immersed boundary. With this delta function, the effect of the immersed boundaries is distributed to the neighboring background grid nodes. As a result, the real interface is slightly diffused. This diffused interface issue decreases the accuracy near the boundary, which is less desirable for simulations with high Reynolds number flows.

In order to treat the immersed boundary as a “sharp” interface with no spreading, the sharp interface IB method is developed with the emphasis on the local accuracy near the IB. The concept of the sharp interface IB method is to modify the computational stencil near the immersed boundary and directly impose the boundary condition on the IB. The sharp interface IB method, strictly speaking, belongs to the type of the direct forcing IB method since it as well constructs the forcing term directly from the existing flow field. The fundamental distinction is that the sharp interface IB method does not involve any discrete delta function; therefore, the direct forcing IB method discussed in the previous paragraph sometimes is called discrete direct forcing IB method. The boundary condition on the immersed boundary in the sharp interface IB method is enforced through the use of “ghost points”, i.e. “G” in Fig. 1-1, which is defined in the solid but has at least one neighbor in the fluid.

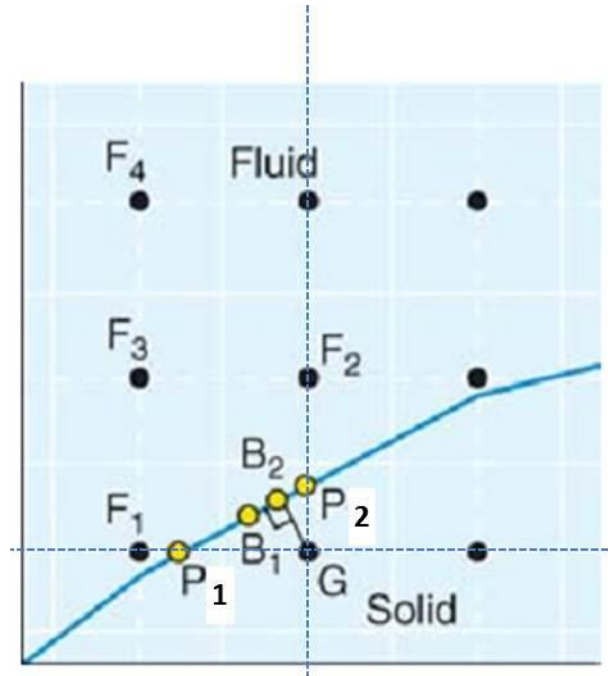


Figure 1-1 Representation of the points in the vicinity of an immersed boundary used in the sharp interface IB method.

It is according to Mittal & Iaccarino⁵¹. F_i are fluid points, G is the ghost point, and B_i and P_i are locations where the boundary conditions can be applied. P_i is the immersed boundary intercept with grid edge between F_i and G . B_1 is the midway between P_1 and P_2 . B_2 is the normal intercept from the ghost node, G , to the immersed boundary.

The flow variable, ϕ , for the ghost points is obtained by the interpolation schemes. A simple option is bilinear (trilinear in 3D) which reads

$$\phi = C_1xy + C_2x + C_3y + C_4 \quad (1.5)$$

The ϕ of “G” can be evaluated by Eq. (1.5) and the four coefficients can be obtained corresponding to the information of F_1 , F_2 , F_3 and B_2 . The point B_1 can be a good alternative of B_2 since it is easier to find the former in the geometrical sense. With the Eq. (1.5), the boundary condition for the sharp interface IB method can be precisely specified; therefore, this type of IB methods improves the local resolution in the vicinity of the boundary compared with the discrete direct forcing IB method, and the boundary layers on the surface can be resolved better. The linear reconstruction is successfully applied to simulate high Reynolds number flows^{66, 67} as the first grid point is located in the viscous sub-layer. The higher-order interpolation^{68, 69}, is also developed in case the resolution near the boundary is marginal for high Reynolds number flows. In addition, the sharp interface IB method can be easily implemented with finite volume approach and conservation laws for the cells in the vicinity of the IB can be satisfied by the cut-cell methodology⁷⁰⁻⁷². As a consequence, further refined local resolutions near the immersed boundary can be achieved.

The penalization method, which can also be considered as a direct forcing IB method, is usually employed to model porous media. The forcing term is constructed to allow some convection and diffusion existing in the immersed boundaries.

$$\mathbf{f}(\mathbf{x}) = \lambda \chi_s (\mathbf{u}^p(\mathbf{x}) - \mathbf{u}(\mathbf{x})) \quad (1.6)$$

where χ_s is the mask function, which is 1 inside the porous media and 0 outside, λ is the penalization parameter, and \mathbf{u}^p is the fluid velocity allowable in the porous media. It is not mandatory to smoothly distribute the forcing term near the immersed boundaries; however, the smooth distribution can help improve numerical stability and avoid numerical oscillations^{73, 74}.

The current study primarily employs the discrete direct forcing IB method, which is developed by Zhang & Zheng⁶³. This IB method can arbitrarily tune the number of points to represent the immersed boundary, which provides the robustness to achieve high resolution of the immersed boundary interpolation. The penalization IB method is also used when the immersed objectives involve porous media.

1.2.2 Parallel Computation

It is not a trivial task to develop a parallel solver with the immersed boundary method. The pressure Poisson equation included in this algorithm costs the most computational time. Several powerful scientific computing libraries are available. Hypre⁷⁵ is well-known for its multigrid preconditioners and FEniCS⁷⁶ is famous for the automated error control and adaptation. PETSc⁷⁷, a Portable Extensible Toolkit for Scientific computation, is employed in the current study because its linear solvers based on the Krylov subspace methods have outstanding performance and scalability in parallel computation. PETSc is developed in Argonne National Laboratory. It provides a powerful set of tools for the numerical solutions of partial differential equations. It consists of a variety of libraries based on FORTRAN, C, and C++, which provides an easy way for code reuse and

flexibility. The foundation of all inter-processes communication in PETSc is MPI; however, many details of message passing within PETSc are shielded from users by default. This creates the possibility for agile programming of large scale applications. In addition, PETSc provides tools to assist in the management of parallel data. A good example is the distributed array (DA). The distributed array (DA) object is adopted for delivering the information required in data parallelization and communication between processes. In the current work, numerical tools with multilevel Krylov subspace methods⁷⁸ for solving a large sparse algebraic linear system of equations are used for the Poisson equation. Multiple previous researchers studied and revealed its power in computational fluid dynamics, i.e. Bozkurtas *et al.*⁷⁹, Hicken *et al.*⁸⁰, and Hsu *et al.*. Indeed, it is a very tedious job to implement the IB method in a parallel fashion. Small improvements could speed up the computation dramatically. The details of the implementation will be demonstrated in detail in the next chapter.

1.2.3 Fluid-Structure Interactions and Temporal Schemes

To capture fluid-structure interactions (FSI) for passively mobile objects, the dynamic model is essential, which can be broadly separated into two categories: the monolithic (strongly-coupled) approach^{81, 82} and the partitioned (weakly/loosely-coupled) approach. The former treats the fluid and structure dynamics in the same mathematical framework and develops equations for a single strongly coupled system solved simultaneously by a unified algorithm. Therefore, iterations between the fluid field and dynamic system are required. This approach has the capability of being more accurate for a multidisciplinary problem, but it may require substantially more computational resources. Moreover, since

the governing equations for the structure domain are implicitly integrated in time, the strongly-coupled approach has a considerable overhead to solve large implicit linear matrices in parallel computation. The strongly-coupled FSI has been successfully coupled with the IB method in previous studies^{83, 84}. Lately, Yang and Stern⁸⁵ proposed to calculate the forces exerted on the immersed boundary by the fluid using the direct forcing concept. They further detected that the pressure gradient near the immersed boundary does not affect the forcing term at all. As a consequence, the Poisson equation involved in the IB methods to couple the velocity and the pressure fields is only required to be solved once in one time step regardless of the number of iterations between the flow field and the dynamic system. The computational resources can be substantially saved since obtaining the solution of the Poisson equation is usually the most expensive part for the flow solver.

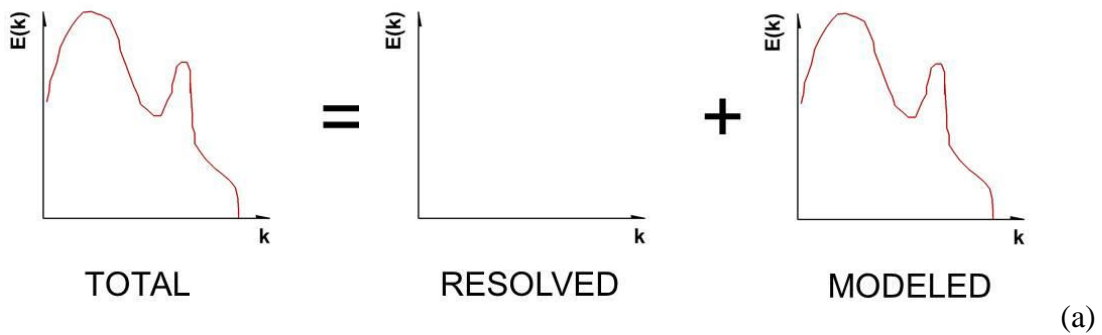
On the other hand, the partitioned approach solves the fluid and the structure separately with respect to different mesh and numerical algorithms. The structure solver can be built upon any existing solver. The interfacial information exchange between fluid and solid is explicit, which is easily implemented for parallel computations. However, the loosely-coupled approach suffers from numerical stability issues, especially when the added-mass effect overcomes the natural mass of the structure⁸³. In addition, van Brummelen⁸⁶ found that the added mass in the incompressible flow asymptotes to a constant as the time step approaches to zero, which implies that the FSI scheme may not be stable with incompressible flows no matter how small the time step size is. The loosely-coupled FSI was successfully coupled with IB methods^{87, 88} and Uhlmann⁶²

demonstrated a stable loosely-coupled scheme for density ratio of the structure to fluid as low as 1.2.

In order to achieve better real-time feedback of forces for the FSI model and more relax numerical stability, a temporal scheme with a higher order of accuracy is desirable. A good example is the predictor-corrector scheme of the low-storage third order Runge-Kutta (RK3) scheme, where all terms in the right-hand-side of the momentum equation are advanced explicitly. Similar RK3-schemes have also been employed in several previous studies for immersed boundary methods. However, their approaches to construct the forcing term may exacerbate the spurious force oscillations for immersed boundary methods, especially for moving body problems, although some of the studies also discussed special techniques to alleviate such a numerical error.

1.2.4 Turbulence Model

In order to simulate flow with moderate to high Reynolds numbers, turbulence models are required. Two major types of turbulence models are popular nowadays: the Reynolds Averaged Numerical Simulation (RANS) and the Large Eddy Simulation (LES).



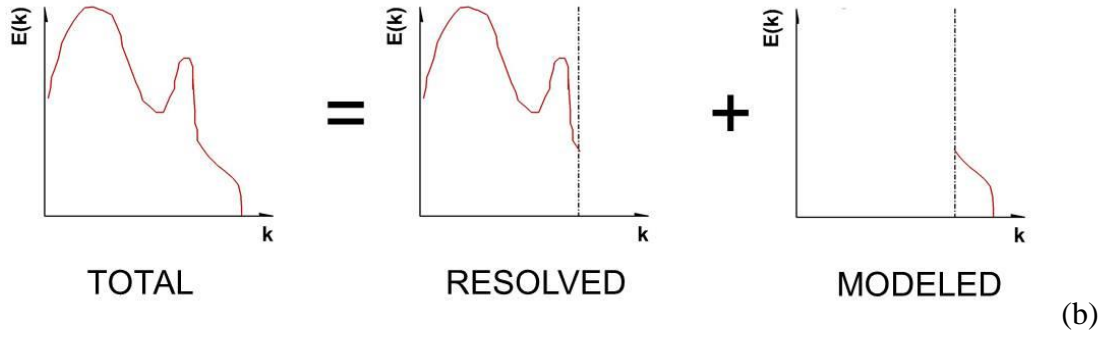


Figure 1-2 Decomposition of the energy spectrum of the solution associated with the (a) Reynolds Averaged Numerical Simulation (RANS) and (b) LES.
It is according to Sagaut⁸⁹. $E(k)$ is the turbulent energy and k is the wavenumber.

RANS models, e.g. k - ϵ models, k - ω models, and the Spalart-Allmaras model, have been widely employed in engineering applications⁹⁰⁻⁹⁴. However, RANS models only resolve the averaged flow field and employ mathematical models to obtain all wavenumber modes in the energy spectrum, as shown in Fig. 1-2. Unsteady RANS models may resolve certain low wavenumber energy modes but still model the rest of it. Therefore, RANS models highly rely on the mathematical models to describe physical behaviors in turbulent flow. However, those mathematical models often involve multiple empirical parameters, which are sensitive to different physical problems⁹⁵⁻¹⁰¹. On the other hand, LES resolves most of the wavenumber modes, which represent the larger three-dimensional unsteady turbulence motions¹⁰², whereas the effects of the smaller-scale motion associated with higher wavenumber modes are modeled. Because the large-scale unsteadiness is directly simulated, LES is expected to be more accurate and robust than RANS models. It offers a suitable method for solving complex flow problems dominated by large scale phenomena, especially for three-dimensional unsteady flows, i.e. the flow over bluff bodies with flow separations, reattachments, and vortex shedding. In addition, unlike direct numerical simulation (DNS), which resolves all of the scales of

flow field solution, LES only resolves large scales of the solution but models the fine scale turbulence, which is the most expensive part in DNS. Therefore, the computational expense of LES lies between that of RANS and DNS.

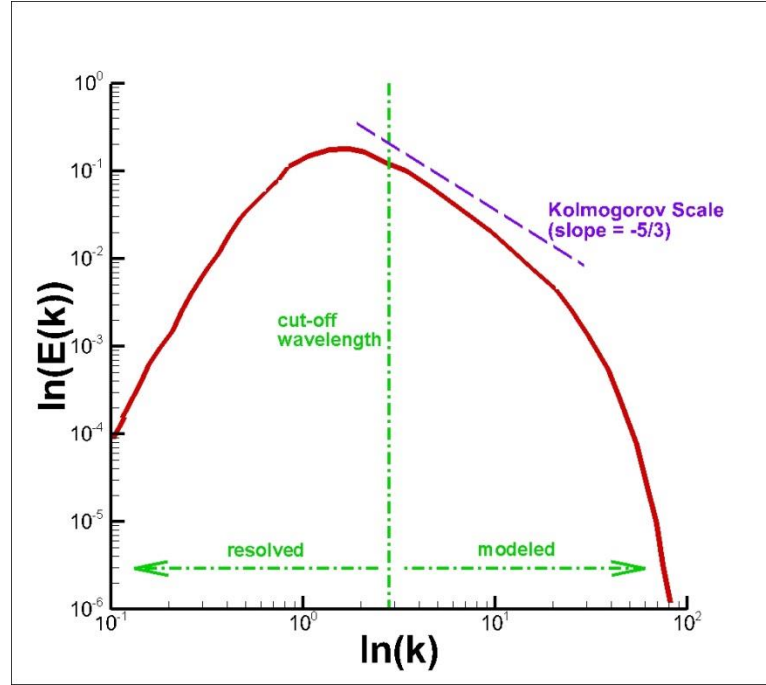


Figure 1-3 Sketch of turbulent energy spectrum according to Durbin and Pettersson Reif¹⁰³

The principal operation in LES is low-pass filtering. The filtered flow field obtains no effect on higher wavenumber modes, which requires to be modeled by mathematical model, e.g. the Smagorinsky model¹⁰⁴. One empirical parameter, the Smagorinsky coefficient, is involved in the Smagorinsky model. Lily¹⁰⁵ theoretically derived the value of this parameter under the condition that the high wavenumber modes all fall into the Kolmogorov scale of the turbulence energy spectrum¹⁰². It implies that the size of the filter in LES needs to be small enough to resolve the all wavenumber modes which are larger than the Kolmogorov scale. In other words, the cut-off wavelength associated with the filter should be inside of the Kolmogorov scale region in the turbulent energy

spectrum shown in Fig. 1-3. Since the computational grid size is usually used as the LES filter, high resolution of mesh is desired for LES^{106, 107}.

It is worth noting that the standard Smagorinsky model obtains nonzero eddy viscosity at solid boundaries. It contradicts the fact that the eddy viscosity should be zero where there is no turbulence, i.e. at the wall. The dynamic Smagorinsky model proposed by Germano *et al.*¹⁰⁸ revisited the Smagorinsky coefficient and treated make it as a variable rather than a constant. The variable Smagorinsky coefficient can automatically be reduced to zero near solid boundaries, which results in zero eddy viscosity. Although the dynamic Smagorinsky model improves the robustness of LES, it dramatically increases the complexity of the implementation and requirement of the computational resources. An alternative is to use the van Driest damping function¹⁰⁹, i.e. Eq. (1.7).

$$D = \left[1 - \exp\left(-y^+ / 25\right)^3 \right]^{0.5} \quad (1.7)$$

It is based on the turbulent logarithmic law (log-law)¹¹⁰ and has the capacity to damp out the eddy viscosity at the wall as well. However, the use of van Driest damping formulation requires the accurate computation of wall shear, which has generally been accomplished by high grid resolution in the near-boundary regions. When the mesh resolution is marginal, the wall function is essential. The simplest wall function again follows the logarithmic law¹¹⁰ for the near-wall velocity profile, i.e. Eq. (1.8).

$$\frac{u_{//}}{u_\tau} = \frac{1}{\kappa} \ln \frac{yu_\tau}{\nu} + C^+ \quad (1.8)$$

where μ is the dynamic viscosity of the fluid, $u_{//}$ is the flow velocity parallel to the wall, κ is the Karman constant and its value is 0.41, and C^+ is a constant with a value of 5.0 for smooth walls. With the log-law, the first off-boundary grid outside the viscous sub-layer can be used to calculate the wall shear. The approach with van Driest damping function and log-law model is an algebraic wall model; although it is very simple and widely used in engineering problems^{111, 112}, its limitation is obvious and inherent since the log-law is derived from fully developed turbulence flow over a flat plate. In other words, it would not perform very well with highly-curved surfaces. The zonal two-layer wall model proposed by Balaras and Benocci¹¹³ provides a good solution to this problem.

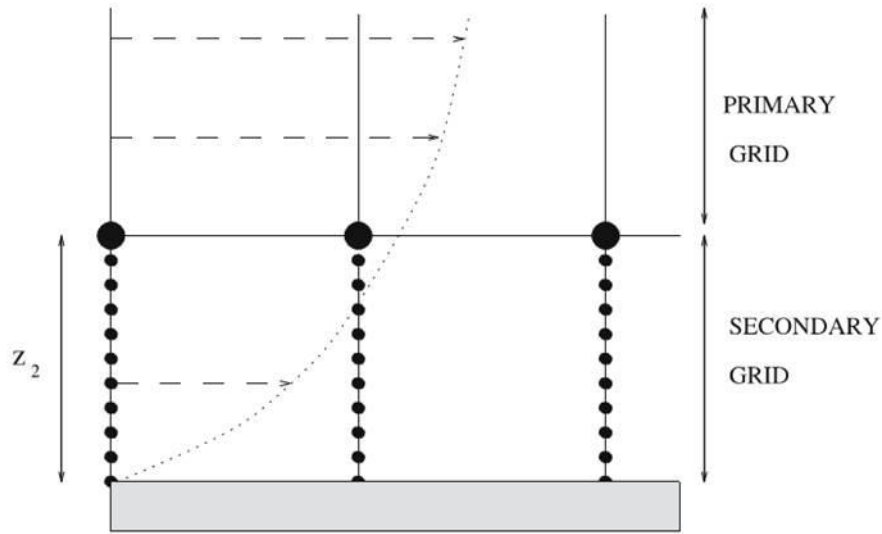


Figure 1-4 Representation of the primary and secondary grids for the zonal two-layer wall model⁸⁹

The zonal two-layer wall model assumes that all first off-boundary grids are located in the buffer layer or logarithmic zone. It only employs LES to solve up to the first off-boundary grid (the large dots in Fig. 1-4) and establishes the secondary grids (the small dots in Fig. 1-4) to compute a simplified turbulent boundary-layer equation, i.e. Eq. (1.9).

$$\frac{\partial \bar{u}_i}{\partial t} + \frac{\partial \bar{u}_i \bar{u}_n}{\partial x_i} = -\frac{\partial \bar{p}}{\partial x_i} + \frac{\partial}{\partial x_n} \left[(\nu + \nu_t) \frac{\partial \bar{u}_i}{\partial x_n} \right] \quad (1.9)$$

The subscript n in Eq. (1.9) stands for the wall-normal direction, i.e. $x_n = y$ following the convention of Eq. (1.8). The van Driest damping function can be used to obtain the turbulent eddy viscosity, ν_t , in Eq. (1.9). Other options are also available, i.e. Eq. (1.10) used in Wang & Moin¹¹⁴ and Tessicini *et al.*¹¹⁵

$$\frac{\nu_t}{\nu} = \kappa y^+ \left[1 - \exp\left(-y^+ / 19\right) \right]^2 \quad (1.10)$$

Last but not least, as reviewed in the IB method section, the linear interpolation of IB forcing term is only valid while the near boundary resolution is fine enough to ensure the first off-boundary grids locating inside the viscous sub-layer. With a marginal grid resolution near the boundary, the higher-order interpolations of IB method are required^{116, 117}. However, an interpolation of IB method that can reproduce the log-law near the boundary is infeasible. Instead, with the linear interpolation of the IB method, Ji *et al.*¹¹⁸ recommended to generate a fictitious velocity on the boundary based on the wall shear obtained from the wall function. This modification makes the scheme preferably preserve the Neumann boundary of the wall shear rather than the no-slip boundary condition. It makes sense since the wall shear is of pivotal importance for wall-bounded turbulent flow.

1.3 Organization of Thesis

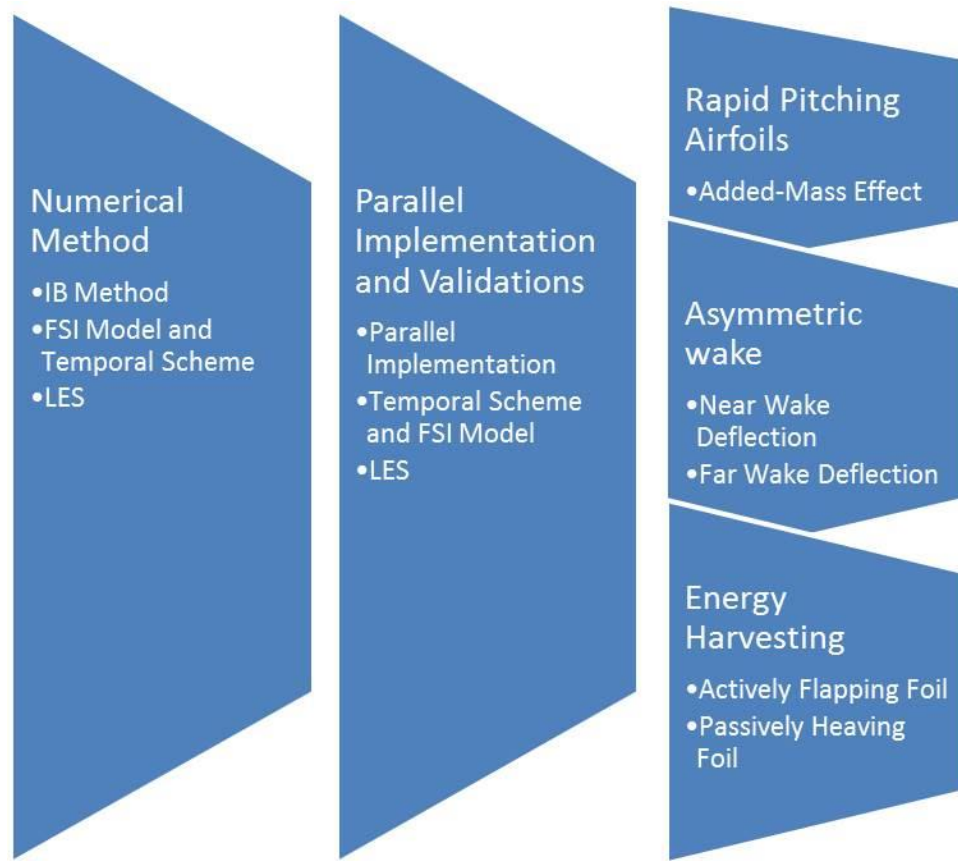


Figure 1-5 Organization of the thesis (from left to right)

Details and formulations of the immersed boundary method, FSI model and large eddy simulations are demonstrated in Chapter 2. The special treatment of the RK3 for IB method is also discussed.

Chapter 3 is about the coupling of the immersed boundary method, different numerical schemes, and fluid dynamic models. Details of parallel implementation of the IB method are also discussed and the performance is studied. The first order temporal scheme was found to be adequate for most cases, yet, the 3rd-order RK3 scheme is necessary for the FSI model and LES since these two fluid dynamic models require a higher temporal

resolution and better numerical stability. In addition, the less restrictive time step size of the RK3 scheme is also advantageous for 3D simulations for the sake of saving computational resources. Benchmark validation cases are carried out and good agreements are achieved. It is also attempted to couple LES with the IB method. Although the implementation is not completed, comments and suggestions are made correspondingly for future research.

Chapter 4 focuses on the added-mass effect with the flow over rapid pitching airfoils. The IB method is validated and obtains good agreement with other results, including simulations, experiments and theories. It was found that the added-mass effect becomes inevitable when the swift acceleration/deceleration is present. Since the loosely-coupled FSI model is coupled with IB method in the current work, the sudden change of the motion is not desirable for the studying objectives.

In Chapter 5, the asymmetric wake downstream of the single two-dimensional heaving airfoil is investigated. The mechanism of near wake deflection is firstly discussed and that of the far wake deflection is then demonstrated. Theoretical fluid dynamics is highly involved. The vortex dipole model and point vortex model based on the Biot-Savart law are greatly helpful for obtaining in-depth comprehension of those mechanisms.

Chapter 6 concentrates on the energy harvesting with either an actively or passively flapping foil in the vortical wake of a cylinder. The vortex/foil interactions are important for understanding and improving energy harvesting capacity of the foil. The potential theory is also used as a guideline to analyze the modes of vortex-foil interactions.

Finally, conclusions are listed in Chapter 7.

2 Numerical Method

2.1 Governing Equations Without Turbulence Models

The immersed-boundary method is an effective way to simulate flow around a moving structure. A direct-forcing IBM in the light of Zhang and Zheng is selected for simulation in this study. However, some major changes have been applied in the implementation procedure, which will be explicitly discussed in this section.

The governing equations for incompressible fluid flow are used:

$$\frac{\partial \mathbf{u}}{\partial t} + \mathbf{u} \cdot \nabla \mathbf{u} = -\nabla p + \frac{1}{\text{Re}} \nabla^2 \mathbf{u} + \mathbf{f} \quad (2.1)$$

$$\nabla \cdot \mathbf{u} = 0 \quad (2.2)$$

where \mathbf{f} is the body forcing term representing the virtual boundary force. The definition of the forcing term is

$$\mathbf{f} = \frac{1}{\Delta t} (\mathbf{V} - \mathbf{u}) - \mathbf{u} \cdot \nabla \mathbf{u} + \nabla p - \frac{1}{\text{Re}} \nabla^2 \mathbf{u} = \frac{1}{\Delta t} (\mathbf{V} - \mathbf{u}) - \text{RHS} \quad (2.3)$$

where \mathbf{V} is the velocity vector of the solid object, Re is the Reynolds number defined based on incoming flow velocity (U_∞) and the characteristic length. Different characteristic length was chosen based on different objects in the flow, i.e. chord length for airfoils or wings, diameter for cylinder and spheres.

The boundary force has non-zero values only on the boundary surface, while zero anywhere else. For immersed boundary points, \mathbf{x}_s , on solid objects, the forcing term is obtained by

$$\mathbf{f} = \begin{cases} \mathbf{f}_G & \text{for the internal-layer grid points} \\ 0 & \text{elsewhere} \end{cases} \quad (2.4)$$

$$\mathbf{f}^n(\mathbf{x}_s) = \frac{\mathbf{V}^n - \mathbf{u}^{n-1}}{\delta t} - RHS \quad (2.5)$$

This equation is only valid when the forcing mesh point coincides with the immersed boundary points \mathbf{x}_s . However, practically, the forcing point exists not only on the immersed boundary but inside the body, i.e. on the internal layer. Thus an interpolation procedure is required. The bilinear weighting functions, $D(\mathbf{x})$, are widely used and the current study employed the one from Zhang & Zheng, of which the two-dimensional format reads

$$\mathbf{U}(\mathbf{x}_s) = \sum_{i,j,k}^{i+1,j+1,k+1} D_{i,j,k}(\mathbf{x}_s) \mathbf{u}_{i,j,k} \quad (2.6)$$

and

$$\mathbf{f} = D(\mathbf{x}_s) \mathbf{f}(\mathbf{x}_s) \quad (2.7)$$

A penalization immersed boundary method has been implemented in the study of flow through/around porous media. For the immersed boundary point in the porous media, the forcing terms are constructed based on Zwicker-Kosten (ZK) model, which has been used previously for numerical calculations of sound propagations in porous media^{119, 120}. The ZK type of source term is applied in place of the forcing term in Eq. (2.4)

$$\mathbf{f} = \begin{cases} 0 & \text{outside the microporous medium} \\ -\sigma \mathbf{u} & \text{inside the microporous medium} \end{cases} \quad (2.8)$$

where σ is the dimensionless flow resistivity of the porous medium (non-dimensionalized by $\rho \langle u \rangle / H$). The flow resistivity is inversely proportional to the porosity of the microporous material.

The momentum equation, Eq. (2.1), is solved on a staggered Cartesian grid by using a 2nd order differencing scheme. Three different types of temporal discretization will be discussed later. Regardless of temporal schemes, the predictor-corrector process is essential to obtain a divergence-free flow field under the condition of incompressibility.

2.2 Temporal Discretization

The temporal scheme exactly following Zhang and Zheng⁶³ obtains the 1st-order accuracy with the 2nd order Adams-Bashforth scheme for convection.

The velocity predictor equation is:

$$\hat{\mathbf{u}}^n = \mathbf{u}^{n-1} + \delta t \left\{ \frac{3}{2} (\mathbf{u}^n \cdot \nabla \mathbf{u}^n) - \frac{1}{2} (\mathbf{u}^{n-1} \cdot \nabla \mathbf{u}^{n-1}) - \nabla P^* + \frac{1}{\text{Re}} \nabla \mathbf{u}^n + \mathbf{f}^n \right\} \quad (2.9)$$

The pressure can be determined by Eq. (2.10) ,

$$\nabla^2 P^* = -\nabla \left[(\mathbf{u}^n \cdot \nabla) \mathbf{u}^n - \mathbf{f}^n \right] \quad (2.10)$$

Then, the correction steps involve a pressure corrector, ϕ , and the equation in the 1st-order temporal scheme is

$$\nabla^2 \phi^n = \nabla \hat{\mathbf{u}}^n / \delta t \quad (2.11)$$

$$\mathbf{u}^n = \hat{\mathbf{u}}^n - \delta t \nabla \phi \quad (2.12)$$

$$P^n = P^* + \phi^n \quad (2.13)$$

Such a temporal scheme needs to solve the Poisson equation twice, i.e. Eqs. (2.11) and (2.12). The flow chart associated can be found in Appendix I. It requires substantial computational resources to obtain solutions of the Poisson equation, including memory and time. Therefore, it would be a wiser choice if the Poisson equation is only required to be solved one time. The alternative method has been presented in multiple previous studies^{66, 121}. They simply skip calculating the pressure field with Eq. (2.10) and time-marching the pressure from the time n to $n+1$ corresponding to the pressure corrector; The flow chart is in Appendix II.

$$P^n = P^{n-1} + \phi^n \quad (2.14)$$

For numerical stability, both of these 1st-order schemes requires,

$$\begin{aligned} \delta t &< \min \left[\frac{h^2 \text{Re}}{4}, \frac{2}{(u^2 + v^2) \text{Re}} \right] \quad \text{in 2D} \\ \delta t &< \min \left[\frac{h^2 \text{Re}}{6}, \frac{2}{(u^2 + v^2 + w^2) \text{Re}} \right] \quad \text{in 3D} \end{aligned} \quad (2.15)$$

where h is the computational grid size¹²². The first method will be called the 1st-order temporal scheme with pressure, and the second one will be named as the 1st-order temporal scheme without pressure. The 1st-order temporal scheme without pressure seems to save lots of computational resources especially the simulation time. However, it does not always perform better than the one with pressure, which will be demonstrated later.

As mentioned before, in order to improve the accuracy of the real-time flow field, force calculations, and numerical stability, the low-storage 3rd-order Runge-Kutta (RK3) scheme¹²³ is employed for simulations involving the FSI model or turbulence model. The velocity predictor is obtained by

$$\frac{\hat{\mathbf{u}}^k - \mathbf{u}^{k-1}}{\delta t} = \gamma_k \mathbf{H}(\mathbf{u}^{k-1}) + \rho_k \mathbf{H}(\mathbf{u}^{k-2}) - \alpha_k \nabla P^{k-1} + \mathbf{f}^k \quad (2.16)$$

where

$$\mathbf{H}(\mathbf{u}^k) = -(\mathbf{u}^k \cdot \nabla) \mathbf{u}^k + \frac{1}{\text{Re}} \nabla \mathbf{u}^k \quad (2.17)$$

where the RK3 coefficients are α_k , ρ_k , and γ_k ; their values will be given later. Then, under the incompressibility condition, the following correction steps are carried out in order to achieve divergence-free flow quantities.

$$\nabla^2 \phi^k = \nabla \hat{\mathbf{u}}^k / \alpha_k \delta t \quad (2.18)$$

$$\mathbf{u}^k = \hat{\mathbf{u}}^k - \alpha_k \delta t \nabla \phi \quad (2.19)$$

$$P^k = P^{k-1} + \phi^k \quad (2.20)$$

The condition for the numerical stability for two-dimensional flow is

$$CFL = \delta t \left\{ \frac{u + v + w}{h} \right\}_{\max} \quad (2.21)$$

The value of CFL is theoretically equal to $\sqrt{3}$ but varies in practical problems¹²⁴. Although this temporal scheme requires solving the Poisson equation, i.e. Eq. (2.18), three times for each time steps, it provides a more relax numerical stability.

In Eqs. (2.18)-(2.20), k is the stage index, which ranges from 1 to 3; $\hat{\mathbf{u}}^k$ is the intermediate velocity. In order to temporally match flow quantities from time step n to $n+1$, the following relations are also essential:

$$\mathbf{u}^k \Big|_{k=0} = \mathbf{u}^n \quad (2.22)$$

$$\mathbf{u}^{n+1} = \mathbf{u}^k \Big|_{k=3} \quad (2.23)$$

The coefficients for this RK3 scheme are

$$\begin{aligned} \alpha_1 &= 8/15 & \gamma_1 &= 8/15 & \rho_1 &= 0 \\ \alpha_2 &= 2/15 & \gamma_2 &= 5/12 & \rho_2 &= -17/60 \\ \alpha_3 &= 1/3 & \gamma_3 &= 3/4 & \rho_3 &= -5/12 \end{aligned} \quad (2.24)$$

It is noted that, since $\rho_1 = 0$, Eq. (2.24) at the 1st stage does not require any information from time step $n-1$. In each substep of the RK3-scheme, the forcing term is obtained by rearranging Eq. (2.16).

$$\mathbf{f}^k(\mathbf{x}_s) = \frac{\mathbf{V}^k - \mathbf{u}^{k-1}}{\delta t} - \gamma_k \mathbf{H}(\mathbf{u}^{k-1}) - \rho_k \mathbf{H}(\mathbf{u}^{k-2}) + \alpha_k \nabla P^{k-1} \quad (2.25)$$

In Eq. (2.25), \mathbf{V}^k is the desired boundary velocity. This equation is only valid when the forcing mesh point coincides with the immersed boundary point \mathbf{x}_s . However, practically, the forcing point exists not only on the immersed boundary but also inside the

body, i.e. on the internal layer. Thus an interpolation procedure is required. With the bilinear weighting function stated in Eqs. (2.6) and (2.7), the forcing term becomes

$$\mathbf{f}^k = \frac{1}{\delta t} \frac{1}{N_b} \sum_{n=1}^{N_b} D_{i,j}(\mathbf{x}_s) [\mathbf{V}^k - \mathbf{U}^{k-1}(\mathbf{x}_s)] - \gamma_k \mathbf{H}(\mathbf{u}^{k-1}) - \rho_k \mathbf{H}(\mathbf{u}^{k-2}) + \alpha_k \nabla P^{k-1} \quad (2.26)$$

Notice the weighting function used in Eq.(2.26) is the two-dimensional version. The three-dimensional version is not used here to avoid the ambiguity of k . Only considering those forcing points, the momentum equation, i.e. Eq. (2.16), turns out to be

$$\frac{\hat{\mathbf{u}}^k - \mathbf{u}^{k-1}}{\delta t} = \frac{1}{\delta t} \frac{1}{N_b} \sum_{n=1}^{N_b} D_{i,j}(\mathbf{x}_s) [\mathbf{V}^k - \mathbf{U}^{k-1}(\mathbf{x}_s)] \quad (2.27)$$

Both sides of Eq. (2.27) have the term $1/\delta t$; therefore Eq. (2.27) can be reduced to

$$\hat{\mathbf{u}}^k - \mathbf{u}^{k-1} = \frac{1}{N_b} \sum_{n=1}^{N_b} D_{i,j}(\mathbf{x}_s) [\mathbf{V}^k - \mathbf{U}^{k-1}(\mathbf{x}_s)] \quad (2.28)$$

Interestingly, no time-marching term explicitly appears in Eq. (2.28). This indicates that the temporal accuracy of the velocity on the forcing points is not directly influenced by any high-order time-matching schemes, in this case the RK3 scheme.

Equation (2.28) can be further rearranged into Eq. (2.29) by plugging in the weighting function:

$$\hat{\mathbf{u}}^k = \mathbf{u}^{k-1} + \frac{1}{N_b} \sum_{n=1}^{N_b} D_{i,j}(\mathbf{x}_s) \mathbf{V}^k - \frac{1}{N_b} \sum_{n=1}^{N_b} D_{i,j}(\mathbf{x}_s) \left[\sum_{i,j}^{i+1,j+1} D_{i,j}(\mathbf{x}_s) \mathbf{u}_{i,j}^{k-1} \right] \quad (2.29)$$

The temporal accuracy of $\hat{\mathbf{u}}^k$ on the forcing points hence primarily depends on that of \mathbf{u}^{k-1} , which is, in fact, not guaranteed to be 2nd-order accurate in time. For example, the 1st stage of this RK3 scheme is apparently a forward Euler method with an effective time step of $\alpha_{k=1}\delta t$, which can only ensure 1st-order temporal accuracy for the intermediate velocities of the corresponding stage. The weighting function, in the 3rd term of the RHS of Eq. (2.29), brings the 1st-order error into the interpolation of the forcing term. This would introduce an additional source of error for spurious pressure oscillations. Furthermore, the choice of \mathbf{V}^k becomes of pivotal importance to the accuracy of $\hat{\mathbf{u}}^k$ as well because of the correction required by the continuity equation. One option for \mathbf{V}^k could be the reconstructed intermediate velocity based on the effective time step in each substep of Eq. (2.18), $\alpha_k\delta t$ ¹²⁴. This approach projects $\hat{\mathbf{u}}^k$ by the intermediate physical velocity and flow velocity; hence, a few potential defects and several difficulties of implementation exist. First, it is not trivial to obtain intermediate physical velocity for a non-prescribed motion. Even for a prescribed motion, once the intermediate physical velocity is determined, the intermediate position of the object is also required. Since the forcing points vary in terms of the position of the object, each substep, then, has to identify its own set of forcing points, which is additional overhead, especially for parallel computation¹²⁵. Finally, the effective time step for a substep, which is smaller than the actual computational time step size, would increase spurious pressure oscillations, according to the discussions by Lee *et al.*¹²⁶.

The alternative approach proposed in the current study is to obtain $\hat{\mathbf{u}}^k$ for forcing points only at the 1st stage of the RK3-scheme with $\mathbf{V}^{k=1} = \mathbf{V}^n$. In other words,

$$\hat{\mathbf{u}}^1 = \mathbf{u}^{n-1} + \frac{1}{N_b} \sum_{n=1}^{N_b} D_{i,j}(\mathbf{x}_s) \mathbf{V}^n - \frac{1}{N_b} \sum_{n=1}^{N_b} D_{i,j}(\mathbf{x}_s) \left[\sum_{i,j}^{i+1,j+1} D_{i,j}(\mathbf{x}_s) \mathbf{u}_{i,j}^{n-1} \right] \quad (2.30)$$

and,

$$\hat{\mathbf{u}}^k = \mathbf{u}^{k-1} \quad (\text{if } k > 1) \quad (2.31)$$

This concept is originated from the fact that the velocity field for the forcing points is not directly related to the time integration as discussed before. The procedure involving Eqs. (2.30)-(2.31), which is illustrated in the flow chart in Appendix III, directly projects the forcing points corresponding to the physical velocity on the next time step, which requires only one set of forcing points for one stage of the object's position. Most importantly, it only adopts the velocity field in the last time step, which guarantees the 2nd-order temporal accuracy and satisfying the continuity. On the other two stages, the intermediate velocities and pressures for the forcing points are only updated to meet the incompressibility condition.

Another alternative was to apply Eq. (2.29) for all three substeps with $\mathbf{V}^k = \mathbf{V}^n$, which as well needs only one stage of physical location. However, the intermediate pressure corrector, ϕ^k , would introduce another source of error by doing that. Consider that after the intermediate velocities for the forcing points are obtained by Eq. (2.29) at the 1st stage, their values were corresponding to the physical velocity on the next time step. However, the intermediate velocities for the fluid points immediately next to the forcing points are only advanced $\alpha_k \delta t$ in time. Since the velocity gradient between these two types of mismatching velocities was involved in Eq. (2.18), the intermediate pressure correctors would not guarantee an accurate final velocity for the corresponding stage, \mathbf{u}^k , near the

boundary. This inaccurate velocity would be an additional source of spurious pressure oscillations if it was used to construct the forcing term in the next stage.

2.3 Fluid-Structure Interaction Model

In the current study, only the translational (vertical) motion of the foil along the cross flow direction is allow. Assuming the mass is concentrated at the center of the objective, the motion equation of the body can be formulated in the inertial frame of reference as

$$\frac{\partial^2 Y}{\partial t^2} + 4\pi\xi \frac{1}{U_{red}} \frac{\partial Y}{\partial t} + 4\pi^2 \frac{1}{U_{red}^2} Y = \frac{1}{2M_{red}} C_Y \quad (2.32)$$

The non-dimensional coefficients in the above equation are defined corresponding to mass, M , damping factor, C , and stiffness of the spring, K . The variable Y is the vertical displacement of the object.

The dimensionless damping coefficient is

$$\xi = \frac{C}{C_{cr}} \quad (2.33)$$

where the critical damping factor is

$$C_{cr} = 2\sqrt{MK} \quad (2.34)$$

The reduced velocity is

$$U_{red} = \frac{U}{fD} \quad (2.35)$$

where the structure natural frequency is

$$\omega = 2\pi f = \sqrt{\frac{K}{M}} \quad (2.36)$$

The reduced mass is defined as

$$M_{red} = \frac{M}{\rho D^2} \quad (2.37)$$

The solution of Eq. (2.32) is obtained by a loosely-coupled FSI implementation⁸³ with the scheme:

$$\frac{\dot{Y}^{n+1} - \dot{Y}^n}{\delta t} + 4\pi\zeta \frac{1}{U_{red}} \dot{Y}^n + 4\pi^2 \frac{1}{U_{red}^2} Y^n = \frac{1}{2M_{red}} C_Y^n \quad (2.38)$$

Then, the location of the object is updated based on

$$\frac{Y^{n+1} - Y^n}{\delta t} = \frac{1}{2} (\dot{Y}^{n+1} + \dot{Y}^n) \quad (2.39)$$

2.4 Large Eddy Simulation

The governing equations are filtered Navier-Stokes equation:

$$\frac{\partial \bar{u}_i}{\partial t} + \frac{\partial \bar{u}_i \bar{u}_j}{\partial x_j} = -\frac{\partial \bar{p}}{\partial x_i} + \frac{1}{\text{Re}} \frac{\partial^2 \bar{u}_i}{\partial x_j \partial x_j} - \frac{\partial \tau_{ij}}{\partial x_j} + f_i \quad (2.40)$$

$$\frac{\partial \bar{u}_i}{\partial x_i} = 0 \quad (2.41)$$

where $\overline{u_i}$ is the velocity component of the resolved scales, and \overline{p} is the corresponding pressure. The non-resolvable subgrid scale stresses, τ_{ij} , describe the influence of the small-scale structures on the larger eddies, which have to be modeled by a subgrid scale model. The well-known Smagorinsky model^{89, 102} is often used for LES. In analogy to Newton's law of friction (or viscous stresses in laminar flows), the turbulent stresses, based on the Boussinesq hypothesis¹¹⁰, are proportional to the mean velocity gradient, or more specifically, to the large-scale strain rate tensor $\overline{S_{ij}}$:

$$\begin{aligned}\tau_{ij} &= -2\nu_T \overline{S_{ij}} \\ \overline{S_{ij}} &= \frac{1}{2} \left(\frac{\partial \overline{u_i}}{\partial x_j} + \frac{\partial \overline{u_j}}{\partial x_i} \right)\end{aligned}\tag{2.42}$$

The eddy viscosity, ν_T , is a function of the strain rate tensor and the Smagorinsky length-scale (or subgrid length) l :

$$\nu_T = l^2 \sqrt{2\overline{S_{ij}}\overline{S_{ij}}}\tag{2.43}$$

The Smagorinsky length-scale l is assumed to be proportional to the filter width $\overline{\Delta}$, which typically is correlated with the grid spacing by the cube root of the cell volume:

$$l = C_s \overline{\Delta} = C_s (\Delta x \Delta y \Delta z)^{1/3}\tag{2.44}$$

Taking into account the reduction of the subgrid length near the solid walls, it is suggested^{127, 128} that the length scale should be multiplied by a Van Driest damping function as

$$l = C_s \bar{\Delta} \left[1 - \exp\left(-y^+ / 25\right)^3 \right]^{0.5} \quad (2.45)$$

where C_s is the Smagorinsky coefficient, which is theoretically derived to be around 0.17 for homogenous, isotropic turbulence based on the Kolmogorov spectrum. However, smaller values are usually applied in LES computations of non-homogeneous and non-isotropic flows; $C_s = 0.1$ is suggested as a typical value for practical applications of the Smagorinsky model¹²⁷.

The y^+ in Eq. (2.45) is the dimensionless wall distance for a wall-bounded flow:

$$y^+ = y \frac{u_\tau}{\nu} \quad (2.46)$$

y is the distance to the nearest wall, ν is the local kinematic viscosity of the fluid, and u_τ is the friction velocity or wall shear, which is related to wall shear stress τ_w . The approach to obtain the friction velocity is not trivial, which will be explicitly discussed in the corresponding section in the next chapter.

3 Parallel Implementation and Validations

3.1 Parallel Implementation

Notice that the computational cost for solving the Poisson equation is the most expensive part of the current numerical scheme. In order to fully speed up this method, a Poisson equation solver has been obtained based upon PETSc, which is a scientific parallel computational library. In a parallel implementation, the right-hand side of the Poisson equation is calculated in all sub-domains separately. The domain is decomposed in all directions automatically by the PETSc function in the process of establishing a uniform coordinate system. One extra layer of ghost points is generated manually to fulfill the task of communicating data with neighbor processes to construct the 2nd-order partial differential equation with the 2nd-order accurate computational scheme. While distributing immersed objects to each sub-domain, the immersed boundary points, which contain non-zero forcing terms, should be separated corresponding to the ghost layer to distinguish them from the genuine boundary of sub-domains. In other words, the immersed boundary points can be overlapped with the aid of ghost layers between two neighbor processes if the genuine boundary of these two neighbor processes cuts through the immersed object. The data communication among processes is done with MPI derived data type. This approach can minimize the fixed overhead of MPI traditional sending and receiving procedures, especially for non-homogenous large scale data that are not contiguous in memory.

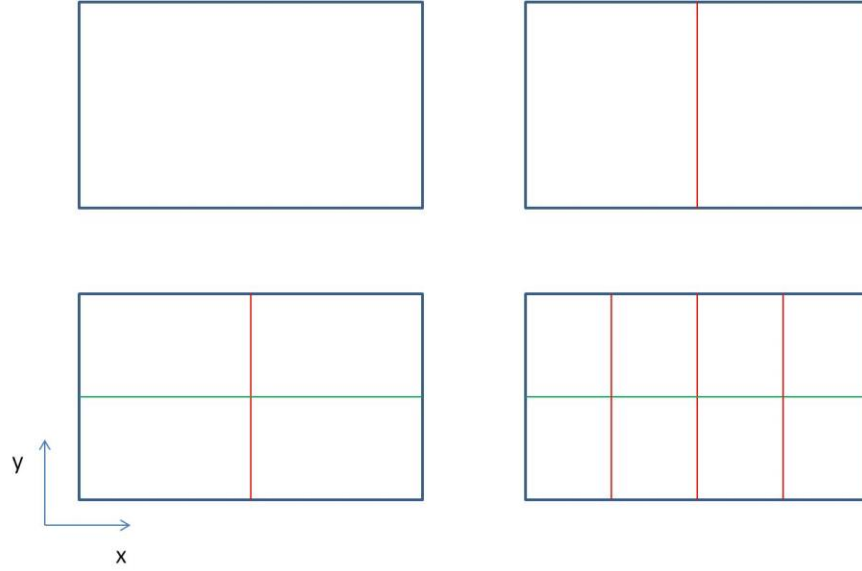


Figure 3-1 2D Grid partitioning with 1 process (top left), 2 processes (top right), 4 processes (bottom left) and 8 processes (bottom right)

Primitive variables to be transferred among processes are velocities in different directions, pressure, and pressure correctors. A single data communication follows the conventional MPI mechanism. Since arrays are defined along the x-direction in this study, values along the green lines in Fig. 3-1 can be treated as a series of data stored in arrays, which can be communicated all together in MPI. On the other hand, each value of two overlapping layers of ghost points along the red lines in Fig. 3-1, needs to be sent and received one after another as they are not contiguous in arrays. If we only use the y-direction mesh partitioning (green lines), the number of data in the overlapping region will be much more than the case with mesh partitioning in both directions. This problem becomes severe when the number of grids is large. It should be noted that without changing the number of processes, the total number of grids leads to an increment of ghost points assigned in the overlapping region. In order to resolve the issue of non-contiguous data communication, all data which need to be transferred among processes

can be pre-packed into an additional local array and be communicated as contiguous ones. In the current study, this method has not implemented. It apparently requires more memory to operate data communication.

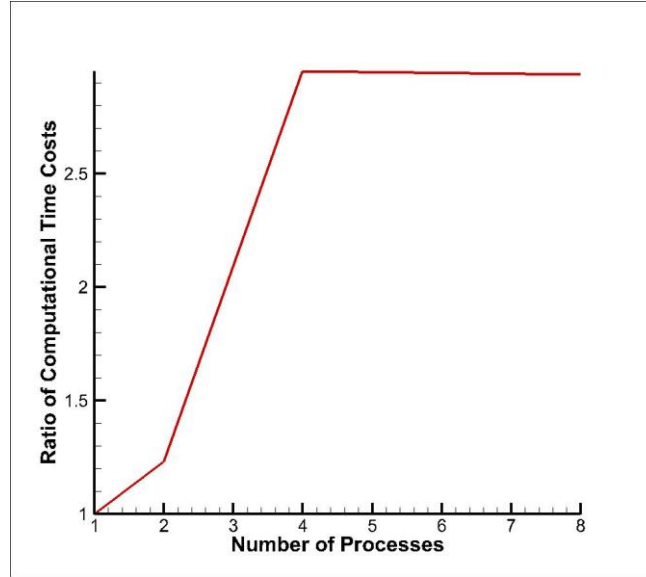


Figure 3-2 Ratio of computational time costs in data communication with different numbers of processes

Following MPI derived data types, the current computational program pre-defines customary data types in MPI. It is similar to the data packing method, but it uses pointers rather than physically allocated additional arrays so that much less memory is required. It, moreover, reduce communication time cost compared to single data commutation with MPI, as shown in Fig. 3-2. The ratio of computational time costs in Fig. 3-2 is defined as T_2/T_1 , where T_2 is the data communication time cost when using the conventional single data communication and T_1 is the one when using the MPI derived data type. In Fig. 3-2, it was found that the latter method gives access to reduce waiting, sending, and receiving times between neighbor processes and achieve better parallel synchronization. A ratio value of around “2” happens in the simulation with 4 and 8 processes. This shows a good

speed-up by using MPI data type replacing conventional methods. It can be concluded that the MPI derived data type has the capability to reduce both the communication time cost and memory requirements in data communication. All the tests in this section are based on validation simulation with a stationary cylinder.

Once the right-hand side is constructed, the Poisson equation can be solved in the serial manner with MUDPACK or parallel manner with the assistance of PETSc. PETSc is recognized as a good portable parallel library for solving partial differential equations (PDEs). The mathematical theory of PETSc is thoroughly summarized in Smith *et al.* . The soul of PETSc is predefined tools dealing with the preconditioned Krylov subspace problems. The solution of a nonsingular system of $Ax = b$ can be determined in multiple ways in PETSc, including parallel and sequential, direct and iterative. The iterative approaches are often well-known for their outstanding performance in massively parallel computations with large scale problems. The conjugate gradient (CG) method is one of the best in the family of iterative linear solvers. The CG method requires matrices to be symmetric positive definite, which limits its use for many applications in computational fluid dynamics. However, this method was mentioned to be optimal for the symmetric positive definite class of problems because it minimizes the residual over a Krylov subspace . On account of the advantage of the IB method, uniform Cartesian mesh is usually used to solve the Poisson equation, which results in a symmetric positive definite matrix. Consequently, the CG method is selected as the linear solver in the current work.

Moreover, a great number of preconditioners are ready in PETSc. Preconditioners are typically used to alter the spectrum of the linear system and hence accelerate the convergence rate of the iterative technique, because the rate of convergence of the Krylov

projection method for a particular linear system is strongly dependent on its spectrum. The preconditioner adopted by the current study is the algebraic multigrid method (AMG). This approach has been proved quite effective on scalar equations. A native algebraic multigrid method in PETSc works well with moderately non-symmetric matrices; therefore, it is always coupled with the CG method to solve the symmetric positive definite problem. A good reference is edited by McCormik¹²⁹ showing the mathematical theory behind the AMG and its applications.

The parallel implementation of the IB method is firstly developed to validate flow over a spatially periodic porous matrix. The geometry of the structures can be square rods, circular rods, cubes and spheres. Square and circular rods are considered as two-dimensional patterns, while cubes and spheres are three-dimensional patterns. An example of an REV in a periodic array of square rods is shown in Fig. 3-3. The flow is from left to right and perpendicular to all arrays of rods.

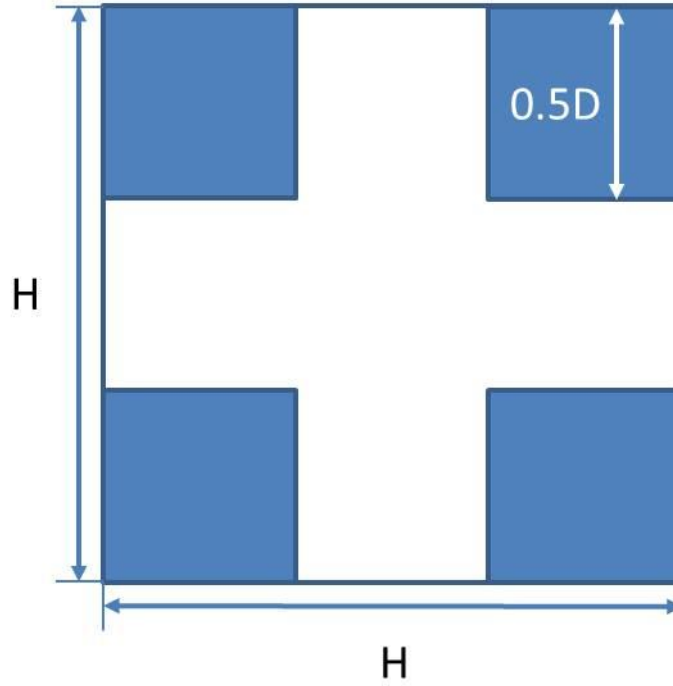


Figure 3-3Computational domain of a representative unit structure; the depth is H .

The REVs with the impermeable structures are considered a unit with solid objects, namely a solid REV unit, which only have macroscopic porosity, or porosity for short, in this study. On the other hand, if the objects have smaller-scale material porosity, the REV is called a microporous REV unit. The macroscopic porosity (ϵ) is determined by two length parameters of the unit: the length scale of the REV (H) and the objects (D). In the current study, the three-dimensional computational domain is a unity cube; therefore, the length scale of the REV (H) is fixed and assigned as the side length of the cube. The length scale of objects (D) is different in terms of different types of structures: the side length is for cubes or square rods and the diameter for spheres or circular rods. Since the macroscopic porosity represents a volume blockage of the structures in an REV, its formula varies with the geometry of the structures^{130, 131}.

By using the REV unit and appropriate boundary conditions, the computational domain ensures the periodicity of flow in all of the x-, y- and z-directions. Because under

most circumstances of interest, flow inside porous media is of low speed, only laminar, low Reynolds number flows are considered in this study, where the Reynolds number, $Re = \rho H \langle u \rangle / \mu$, is based on the fluid density ρ , viscosity μ , length scale of the REV H , and the volume averaged velocity $\langle u \rangle$. The volume for averaging the velocity in the current work is H^3 , which is the total volume of an REV. For non-dimensional computation in this study, the side length H acts as a characteristic length and is always chosen as 1, and the Reynolds number is selected as 10, for which the Darcy-Forchheimer law holds¹³¹⁻¹³³.

Periodic boundary conditions are specified in all three directions for velocity components^{134, 135}. The periodic boundary conditions are also applied to the pressure equation, Eq. (3.1), except for the streamwise direction (the x-direction):

$$\begin{aligned} p|_{(0,j,k)} &= p|_{(H,j,k)} + \Delta p \\ p|_{(i,0,k)} &= p|_{(i,H,k)} \\ p|_{(i,j,0)} &= p|_{(i,j,H)} \end{aligned} \tag{3.1}$$

where Δp is a constant related to the total mass flow rate in an REV unit. The dimensionless flow rate through the periodic cell was set equal to unity by tuning the value of Δp . In most of the studies in the literature, the non-periodic pressure condition in the flow direction was transformed to a periodic boundary condition by adding a global pressure gradient to the pressure, resulting in a source term in the momentum equation. In the present numerical solution procedure, that approach would not be applicable because the all-direction periodic pressure boundary conditions do not work with the Poisson solver.

In this study, we concentrate on the impermeable square rods cases. The fluid/solid interaction problem in this unique structure is already interesting and was selected to be the validation case before further investigations were conducted. We also use this study to investigate the effectiveness of the parallel implementation of the IB method.

All square rods have the size $D = 0.5H$, and the corresponding porosity that the REV represents is $1-(D/H)^2 = 0.75$. Simulations in the commercial CFD solver, FLUENT¹⁷, are all two-dimensional; boundary conditions are the same as used in the IB method, including the periodicity and the pressure drop in the streamwise direction. A value of $\sigma = 10^4$ is used for the impermeable material in the solid REV.

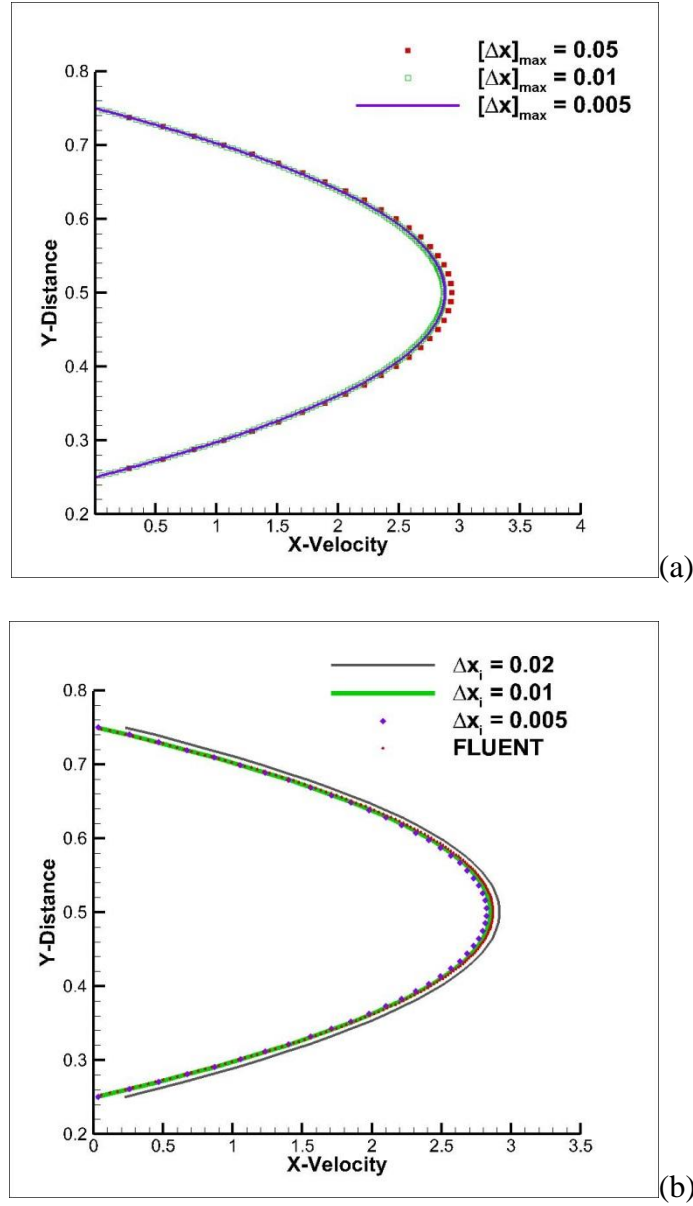


Figure 3-4 Velocity profiles at the outlet for grid independence check for flow through an REV with impermeable square rods with (a) FLUENT (b) IB method

First of all, the grid independent study is carried out for the commercial CFD solver. Since a nearly structured Cartesian mesh is used in FLUENT, all grid cells in the mesh are approximately squares, and the size is very close to the maximum cell size, which is indicated as $[\Delta x]_{\max}$ in Fig. 3-4(a). Figure 3-4(a) illustrates that the discrepancy of the results between the case with the mesh of $[\Delta x]_{\max} = 0.01$ and the one with the finest mesh

of $[\Delta x]_{\max} = 0.005$ is very small; therefore, the mesh of $[\Delta x]_{\max} = 0.01$ is chosen for further simulations with the commercial solver.

Furthermore, a similar grid independence study is performed with the IB method. It was found in Fig. 3-4(b) that the result with the mesh of $\Delta x_i = 0.01$ not only achieves a grid independent convergence for the IB method but also provides a reasonable result which has a good agreement with the result from the commercial software. Additionally, contours of streamwise velocity shown in Fig. 3-5 from these two approaches are very close to each other. This good comparison of contours reinforces the validity of the result with this mesh. The mesh with $\Delta x_i = 0.01$, hence, is used in the further study for all simulation cases of the IB method. In order to achieve the numerical stability of the IB method, the time step size is 0.0001, based on Eq. (2.15).

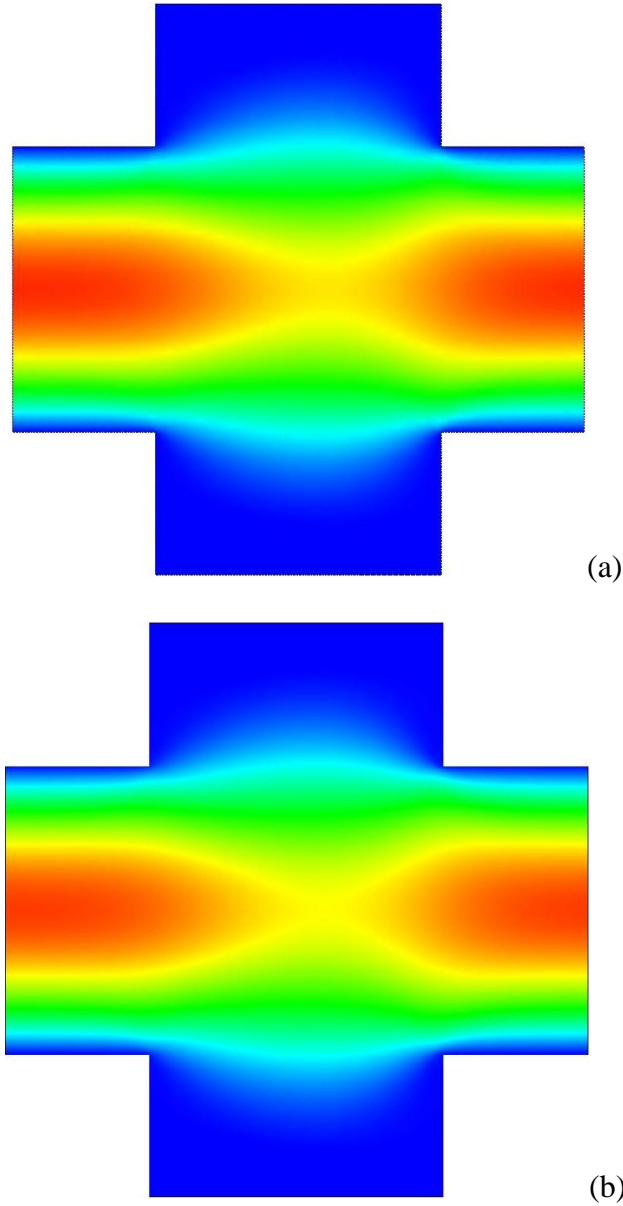


Fig. 3-5. A comparison of streamwise velocity contours between (a) FLUENT and (b) the IB method. The contour level is 0~3 for both pictures.

The total grid number in the IB method, with the selected mesh size, is $100 \times 100 \times 100$; for this validation case, around 25% of them are flagged as inside the objects, which need to be applied with the forcing term for Eq. (2.8). As most IB applications with uniform meshes usually involve around 1~5% grids with the “inside” flag, the 25% is a relatively large fraction of total computational grids inside the objects. This requires a lot of

memory and computational sources. In order to access more memory and speed up the computational rate, the IB method is implemented in a parallel fashion. The parallel scalability is also tested with the flow through impermeable square rods with one million grids for ten-thousand time steps.

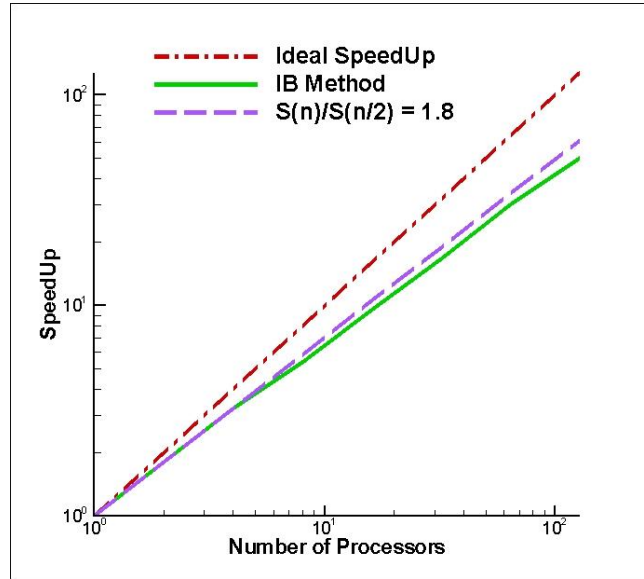


Fig. 3-6. The parallel speedup with different numbers of processes.

The value of speedup in Fig. 3-6 is determined by a ratio of T_1/T_n , where T_n indicates the time cost for the program with “n” processes. The ideal speedup with ‘n’ processes ($S(n)$) is obtained from Amdahl’s Law, Eq. (3.2), with 100% parallel fraction of the code (Φ).

$$S(n) = \frac{1}{1 - \Phi + \Phi/n} \quad (3.2)$$

The scalability is tested in a supercomputing cluster with Intel E5-2650 Dual 8 core CPU. Figure 3-6 shows that the computational time is reduced by an order of 1.8 when the number of processes is doubled. This indicates a good scalability of the IB method in

the current work. However, if the number of processes keeps increasing and exceeds 8, the scalability would suffer from overhead of inter-node communication. Since the computation with 8 processes provides acceptable speed, all cases in the current tests were simulated with 8 processes.

3.2 Temporal Schemes and the FSI Model

The following numerical examples are conducted to simulate flow over 2D cylinders with prescribed motions and vortex-induced vibrations. The grid-size independence test is performed for all the cases with uniform grid sizes of 0.05, 0.025, and 0.0125. Based on these test results, the grid size of 0.025 is selected. The computational domain size, 25.6×12.8 , is tested to assure an independent solution to domain size. The total number of immersed boundary points of 1280 is selected, as recommended in Zhang & Zheng⁶³.

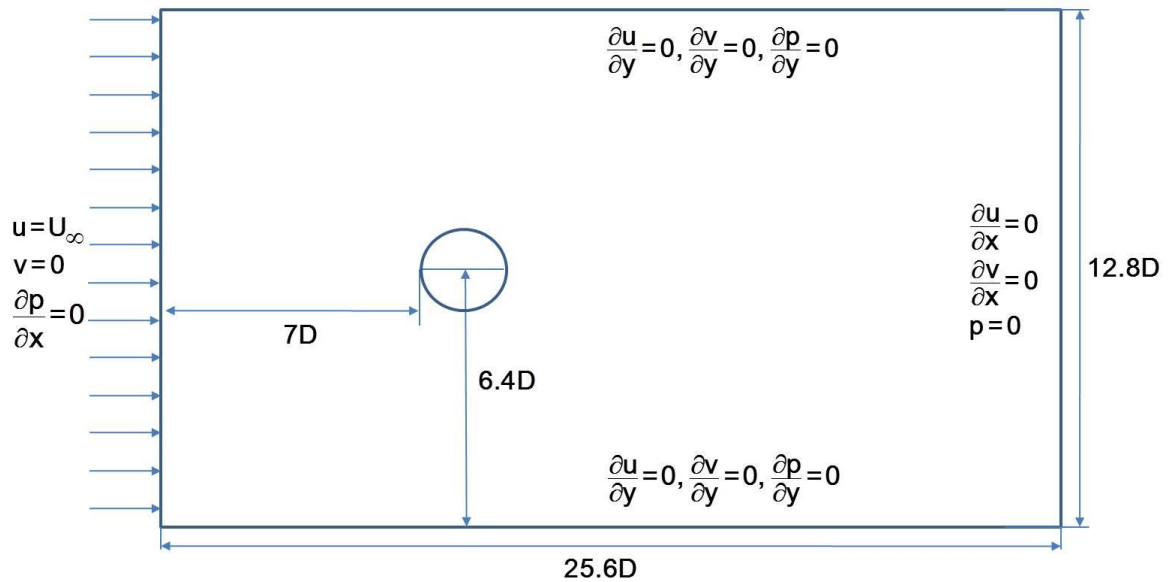


Figure 3-7 Sketch of the configuration of the system involving only one cylinder.

Accordingly, the center of the cylinder is located at 7-unit from the inlet in order to avoid inlet boundary effects. All boundary conditions are shown in Fig. 3-7.

3.2.1 Stationary Cylinder

The flow over a stationary cylinder at $Re = 40$ is the threshold case to validate the IB method with RK3-scheme employed in the current study. Firstly, the steady state solution, as shown in Fig. 3-9, preserves good agreements on comparisons of pressure coefficients against previous studies. The convergence criterion is 10^{-10} corresponding to L_2 -norm of u-velocity for the entire computational domain

$$\text{Residual} = \sqrt{\sum_{i=1}^{N_{grid}} (u_i^n - u_i^{n-1})^2 / N_{grid}} \quad (3.3)$$

where N_{grid} is the total number of grids and n represents the time step.

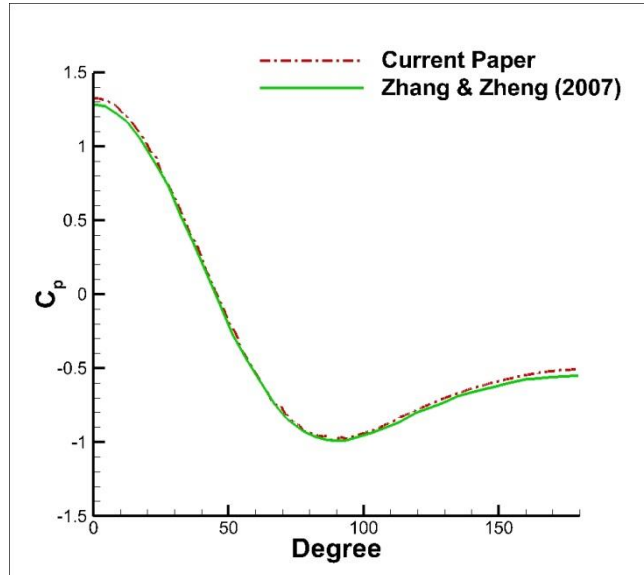


Figure 3-8 C_p on the top surface of a stationary cylinder at $Re = 40$. Compare the current result with $\delta t = 256^{-1}$ to the results from Zheng & Zhang⁶³.

In addition, the cases with $\delta t = 256^{-1}$, 512^{-1} , and 1024^{-1} are simulated to one unit time for the sake of obtaining the order of temporal accuracy for the current scheme. The order of temporal accuracy, γ , is calculated as

$$\gamma = \ln \left(\frac{E_{\delta t=256^{-1}}}{E_{\delta t=512^{-1}}} \right) / \ln(2) \quad (3.4)$$

The L_2 -norm of u-velocity is defined corresponding to the result with the finest time step size, i.e. $\delta t = 1024^{-1}$.

$$E_{\delta t=\tau} = \sqrt{\sum_{i=1}^{N_{grid}} (u_i|_{\delta t=\tau} - u_i|_{\delta t=1024^{-1}})^2} / N_{grid} \quad (3.5)$$

The value of γ obtained by this set of tests is 1.83, which is a reasonable value to demonstrate a 2^{nd} -order temporal accuracy for the current scheme.

It is worth to notice that two assumptions are made for the above method of determining the temporal order of accuracy. The first assumption is, as all the cases were matched $t = 1$, none of them should really converge to the steady state, since the steady state solutions are time-independent. If this assumption holds, the results at $t = 1$ can be treated as solutions of “unsteady” simulations, which allows the potential to obtain the temporal order of accuracy. In the current test, the residual of all cases at $t = 1$ is $O(10^{-5})$, which is far from the true steady solution. The second assumption is the result from the case with the finest δt can represent the exact solution for the “unsteady case” at $t = 1$, which is also valid in the test based on its comparison against the case with $\delta t = 2048^{-1}$.

3.2.2 Oscillating Cylinder with Prescribed Motions

Since spurious pressure oscillations often occur for the IB method with moving objects^{126, 136}, cases with a two-dimensional transversely-oscillating cylinder is simulated. The motion of the cylinder is prescribed as

$$y_c(t) = h_c \sin(2\pi f_c t) \quad (3.6)$$

To facilitate comparisons, the dimensionless amplitude, 0.15, and frequency, 0.18, are chosen to be the same as those in Zheng & Zhang¹³⁷, and the Reynolds number is 200. The time step, δt , is fixed to be 256^{-1} unless specifically pointed out otherwise.

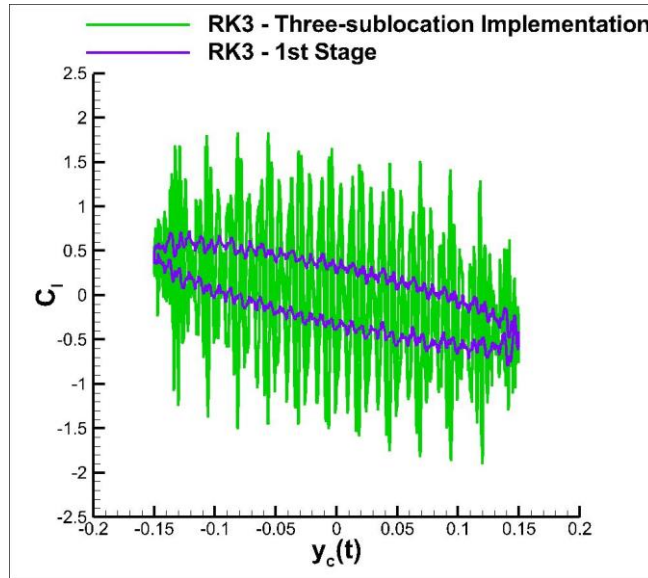


Figure 3-9 Time-periodic variation of the lift coefficient between two RK3 schemes.

RK3 – Three-sublocation implementation: The \mathbf{V}^k in Eq. (20) is reconstructed as intermediate physical velocities corresponding to the substep physical positions, based on the effective time step, $a_k \delta t$.

RK3 - 1st stage: It is proposed by the current study, which only applies the momentum equation with non-zero forcing terms for forcing points at the 1st stage of the RK3 scheme.

As mentioned before, the reconstructed \mathbf{V}^k corresponding to intermediate physical velocities based on the effective time step has the potential to introduce much more

spurious pressure oscillations, as illustrated in Fig. 3-9. The effective time step, which is smaller than the actual computational time step, can possibly amplify the non-physical behaviors of the pressure near the IB points¹²⁶. Some techniques to reduce such oscillations have been discussed in the literature, e.g. the “field extension” in Yang & Balaras¹²³ and “artificial mass” in Kim *et al.*¹³⁸. Nonetheless, they require extra computational resources to either extrapolate the fluid field near the IB or construct additional mass terms. Consequently, the method proposed by the current study could be an efficient alternative or augment.

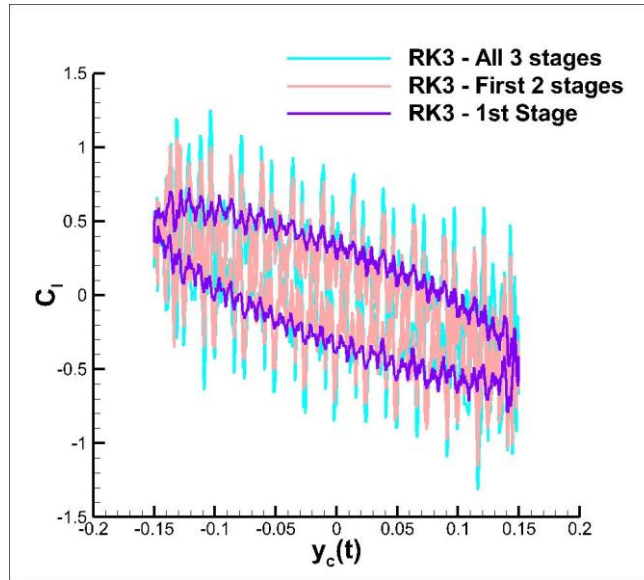


Figure 3-10 Time-periodic variation of the lift coefficient among three temporal schemes:
RK3 – All 3 stages: the flow quantities for forcing points are interpolated with $V^k = V^n$ for all three stages of the RK3 scheme;
RK3 – First 2 stages: the flow quantities for the forcing points are interpolated with $V^k = V^n$ for the 1st two stages of the RK3 scheme;
RK3 – 1st stage: the RK3 scheme proposed in the current study $\delta t = 256^{-1}$

Figure 3-10 demonstrates that the more substeps used to construct the forcing term, the worse spurious pressure oscillations there will be. The intermediate velocities of the RK3 scheme is neither physical nor guaranteed 2nd-order accurate; therefore, involving them in the forcing term introduces an additional source of error for flow quantities near

the IB. The RK3 scheme presented in the current work only implements the forcing term at the first stage. In other words, it only uses the final velocities of the RK3 scheme that are ensured 2nd-order accurate and divergence-free.

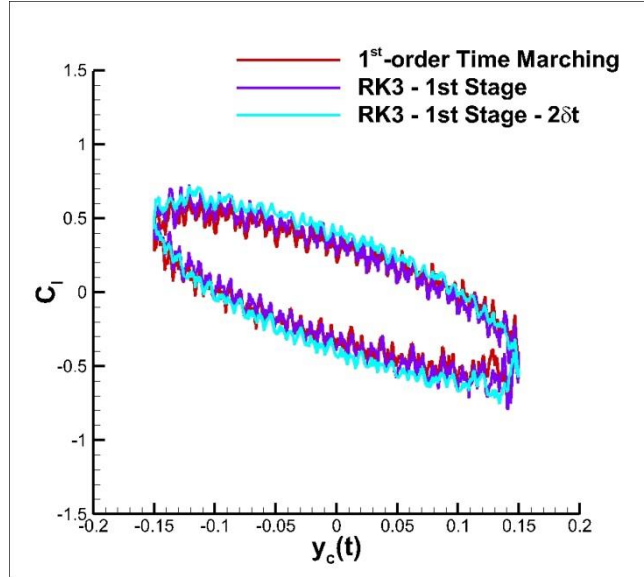


Figure 3-11 Time-periodic variation of the lift coefficient among three temporal schemes:
The 1st-order Time Marching: The time marching scheme follows Zhang & Zheng⁶³ (the 1st-order temporal scheme with pressure), which obtain an overall 1st order temporal accuracy;
RK3 – 1st stage: the RK3 scheme proposed in the current study $\delta t = 256^{-1}$
RK3 – 1st stage - $2\delta t$: the RK3 scheme proposed in the current study with $2\delta t = 128^{-1}$

The spurious pressure oscillations showed with the current RK3 scheme are almost the same amplitude as that from the simulation with the 1st-order temporal scheme if other computational settings are the same. This demonstrates that the spurious pressure oscillations of the IB method are not exacerbated by the current multi-stage temporal scheme; it is still primarily caused by spatial discretization errors of the linear weighting functions¹²⁶. A local smoothing technique for those discrete weighting functions¹³⁶, may further reduce this type of non-physical behavior. However, since the current scheme allows larger computational time step sizes, it can be an alternative relief for spurious pressure oscillations. The simulation with $2\delta t = 128^{-1}$ obtains a distinctly smaller pressure

oscillations compared with that of $\delta t = 256^{-1}$, as shown in Fig. 3-11. The time step size of $2\delta t$ cannot provide computational stability for the testing case with the 1st-order scheme; consequently, the corresponding result is not plotted.

3.2.3 Validation Cases for FSI Model – Vortex-Induced Vibration

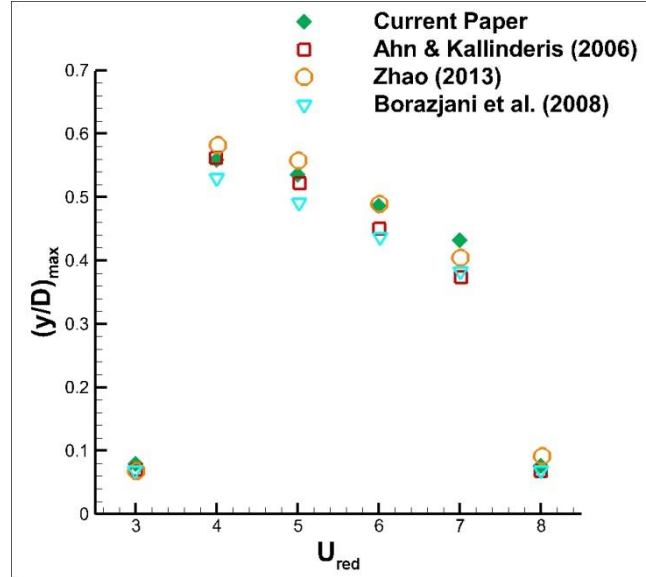


Figure 3-12 The variation of the response amplitude with the reduced velocity for a single vortex-induced vibrating cylinder and its comparison with previous studies^{83, 139, 140}.

In order to validate the fluid-structure interaction model, the vortex induced vibration problem with a single two-dimensional cylinder at $Re = 150$ is studied. This is accomplished by varying the reduced velocity, U_{red} , with increments of 1 from 3 to 8. The damping coefficient is zero and the reduced mass, M_{red} , is fixed at 2. The comparisons between the current study and previous literature, as shown in Fig. 3-12, are in good agreement. Note that it requires a very long time to achieve a quasi/periodic solution for simulations with high reduced velocity since their dimensional dynamic frequency is relatively low, according to Eq. (2.35). The reduction of time step size by the RK3

scheme is greatly helpful to save computational resources. The computational time step size is, again, 256^{-1} for all the validation cases.

3.2.4 Other Comments on Temporal Schemes

Although the power of RK3 has been demonstrated, its weakness is also observed. Similar to the 1st-order temporal scheme without pressure, RK3 does not directly obtain pressure fields, yet the pressure is accumulated by time integration of a pressure corrector. This may require higher resolution on the spatial discretization.

A set of tests is carried out for the flow over a three-dimensional sphere at $Re = 300$. The sketch of the domain in the center plane of z-direction and the boundary conditions are similar to Fig. 3-7 except the computational domain is $16 \times 9.6 \times 9.6$. Uniform Cartesian meshes are used with a grid size of either 0.05 or 0.025. Three different temporal schemes are coupled with the IB method respectively and the results are compared against Johnson & Patel¹⁴¹. The time step size for all tests remains at 0.005.

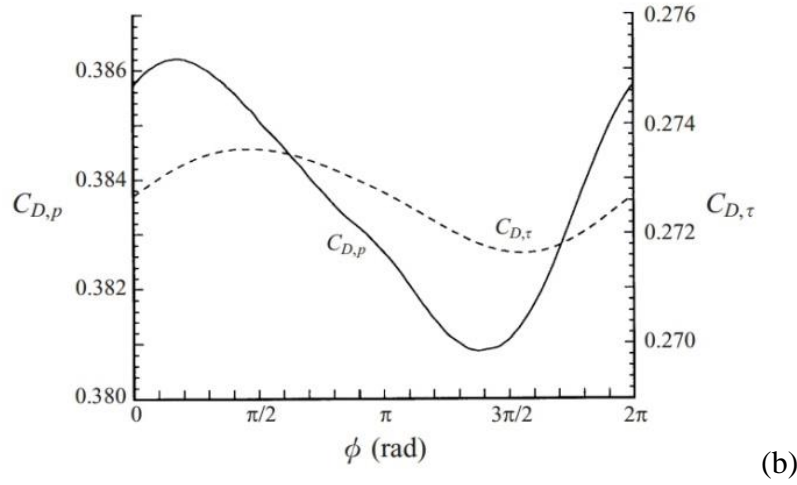
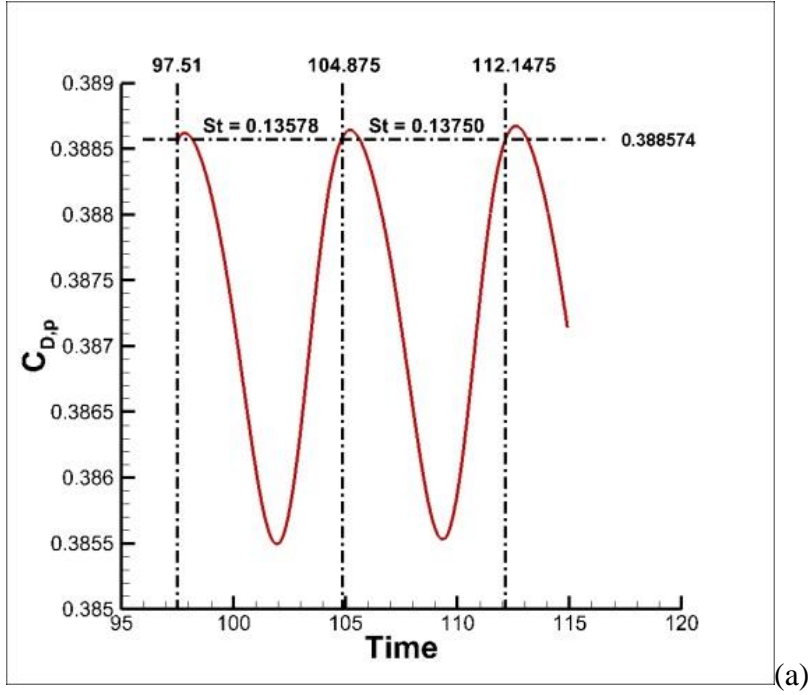


Figure 3-13 Comparison of pressure components of drag coefficient.

(a) the current simulation with the 1st-order temporal scheme without pressure and $dx = 0.025$.

(b) Johnson & Patel¹⁴¹, phase angle ϕ from 0 - 2π corresponds to an arbitrary beginning and end of one period of flow.

Figure 3-13 demonstrates that the 1st-order temporal scheme without pressure had a good agreement with the previous study if the $dx = 0.025$. The Strouhal number reported in Fig. 3-13 (a) is around 0.136, which agrees well with the value of 0.137 found by Johnson & Patel¹⁴¹.

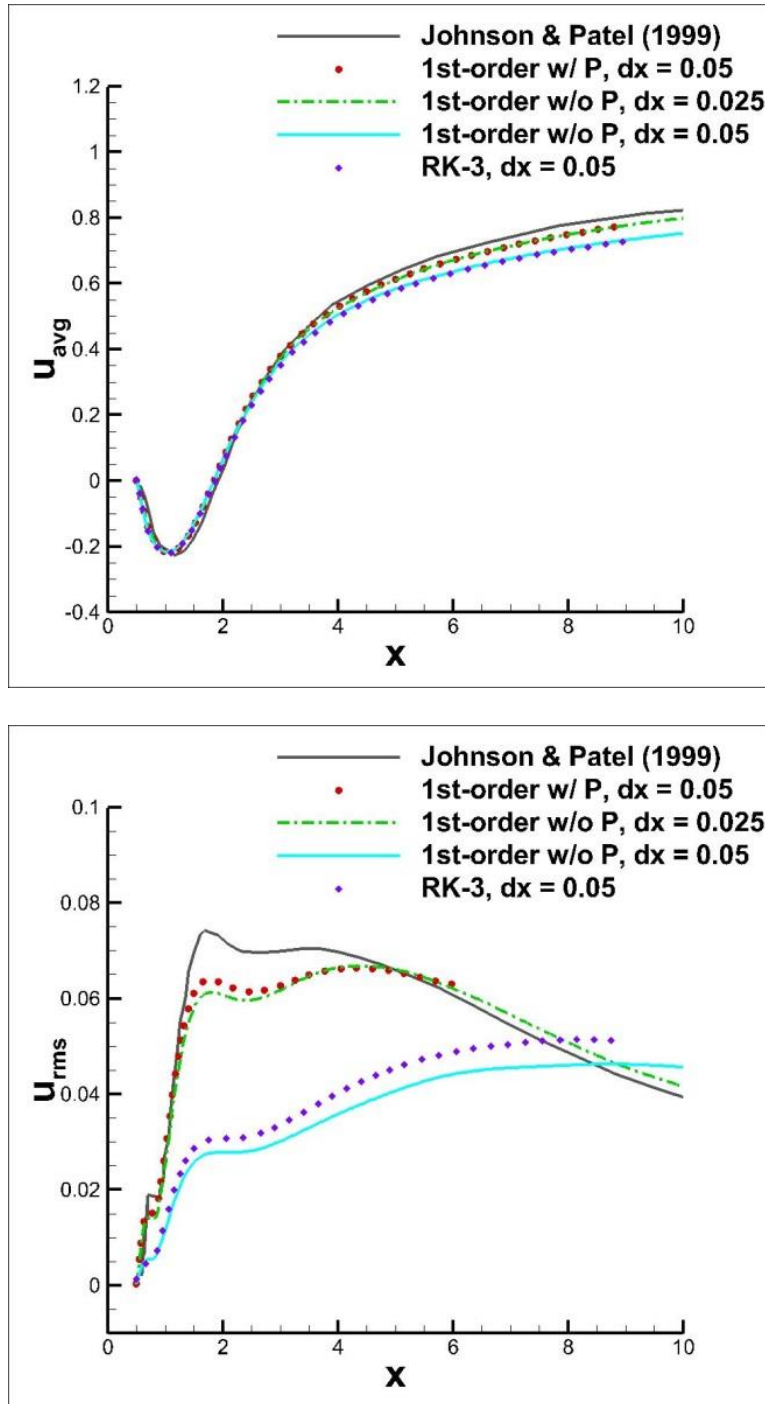


Figure 3-14 Comparisons of wake axis distributions of average streamwise velocity and its root-mean-square (r.m.s.) for the flow over a sphere at $Re = 300$

Figure 3-14 exhibits the wake axis distribution of the average streamwise velocity and its r.m.s. The $x = 0$ in the figure indicates the center of the sphere. The time periods to

average the result or calculate the r.m.s. is corresponding to the Strouhal number discussed in Fig. 3.13. It is very obvious that neither method, without directly obtaining pressure, i.e. the 1st-order w/o pressure and RK-3, can achieve any acceptable agreements in the u_{rms} with the coarse mesh, i.e. $dx = 0.05$. Refining the mesh definitely improves their results, though they can only obtain comparably good results with finer meshes as in the simulation with the 1st-order temporal scheme with pressure and the coarse mesh. Similar behaviors are detected in the comparison of u_{avg} .

This indicates that by skipping the step of calculating pressure, a higher requirement of computational mesh is desired. My suggestion is that if enough computational power, i.e. computing units, is accessible, then the 1st-order temporal scheme without pressure could be adopted; otherwise, the one with pressure should be employed. Nonetheless, if the RK3 scheme has to be used for the sake of higher temporal accuracy, the better resolution on the computational mesh is mandatory.

3.3 Large Eddy Simulation

As mentioned before, it is attempted to couple LES with the current IB method. The objective is the flow over a three-dimensional sphere at $Re = 3700$. The computational setup is exactly the same as the one for the flow over the sphere at $Re=300$. The dx remains at 0.05 and time step size is 0.001. There are several difficulties in the implementation of the turbulence model with the IB method.

The threshold one is the friction velocity in Eq. (2.46). The general form of the friction velocity reads

$$\begin{aligned}
u_\tau &= \sqrt{\frac{\tau_w}{\rho}} \\
\tau_w &= \mu \left(\frac{\partial u_{//}}{\partial y} \right)_{y=0}
\end{aligned} \tag{3.7}$$

where μ is the dynamic viscosity of the fluid and $u_{//}$ is the flow velocity parallel to the wall. However, the above formula is only valid when the computational grid of $u_{//}$ falls into the viscous sub-layer, i.e. $y^+ < 5$. If not, multiple approaches can be adopted^{114, 142-144}. The simplest way is to obtain the wall shear directly from the logarithmic law¹¹⁰

$$\frac{u_{//}}{u_\tau} = \frac{1}{\kappa} \ln \frac{y u_\tau}{\nu} + C^+ \tag{3.8}$$

where κ is the Karman constant and its value is 0.41. The C^+ is a constant and its value is 5.0 for smooth walls. The value of u_τ can be easily obtained by Eq. (3.8) with the Newton-Raphson method. The test carried out in the current work shows that without using Eq. (3.8) to calculate friction velocity while $y^+ > 5$, the program would blow up very quickly.

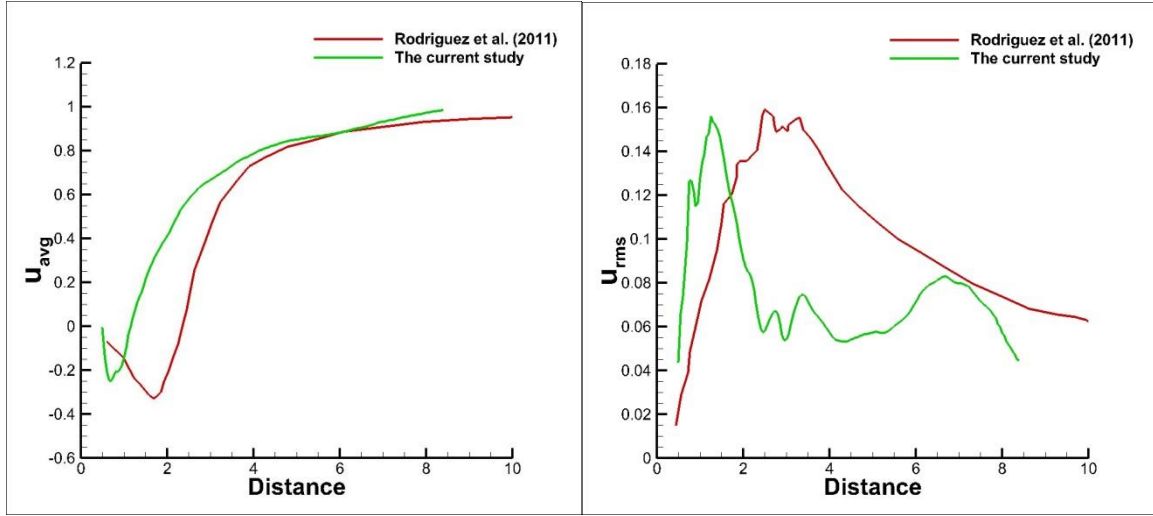


Figure 3-15 Comparisons of wake axis distributions of average streamwise velocity and its root-mean-square (r.m.s.) for flow over a sphere at $Re = 3700$

Figure 3-15 exhibits that the current scheme, although it becomes executable after introducing Eq. (3.8), does not have good agreement with previous literature¹⁴⁵. Ji *et al.*¹¹⁸ recommended modifying the boundary velocities on the IB to fulfill the Neumann boundary condition based on the wall shear; unfortunately, it does not help much with the current IB method.

The idea to improve the results may start with refining the mesh. As discussed in the previous section, the coarse mesh $dx = 0.05$ does not work very well with the RK3 scheme even in laminar flow simulations, let alone LES, which inherently requires high mesh resolutions. However, the program becomes substantially slow with refined mesh, i.e. $dx = 0.025$. This brings an issue of parallel implementation of the IB method. PETSc has very powerful and robust domain decomposition algorithms for structure meshes. It usually divides the total computational domain evenly corresponding to the number of processes; this makes each process obtain an equal same amount of computational loading. However, the load balance in PETSc does not consider the computational cost

required for the IB points. Although divided corresponding to the boundary of the sub-domains, IB points are obtained by very few processors. In other words, only few processors proceed with the calculations related to the IB points in semi-parallel manner while other processors are waiting. This would reduce the stability of the whole program, especially with LES. LES requires a lot more calculations on the IB points, i.e. obtaining friction velocity. In addition, as the total number of IB points should increase as the mesh size decreases⁶³, the issue of not fully parallelizing the calculation of IB points becomes more severe for simulations with the refined mesh. The ultimate way to solve this problem might be using the dynamic loading tools to balance the computational weight of the whole domain, including the IB points.

Furthermore, a better way to refine the mesh is to use the adaptive mesh. Due to the inherent advantage of the IB method, totally unstructured mesh might be a waste, so structured adaptive mesh refinement (S-AMR)¹⁴⁶ would be the best approach. Scientific computing packages that can solve Poisson equations with S-AMR include SAMRAI¹⁴⁷ (Structured Adaptive Mesh Refinement Application Infrastructure), Hypre⁷⁵, and so on. However, it is not a trivial task to couple S-AMR with the IB method. The formulation of the IB forcing term may need to be modified to handle hanging cells¹⁴⁸. Last but not least, inflow conditions involved in LES may not be identical to those without LES, especially for wall-bounded flows^{149, 150}. The influence of LES on the free stream inlet flow has not been discussed yet.

All in all, the current study attempted to couple LES with the IB method, yet not succeeded. In order for those in the future to make better achievements, a few suggestions are stated to my limited knowledge. Firstly, the S-AMR is essential to carry out reliable

computations of LES with the IB method. Previous studies without adaptive mesh cannot employ IB method with LES to handle bluff bodies well; most of them deal with plane flows with non-smooth surface^{66, 116}. Even though few literature¹¹⁸ exhibited results of the IB method and LES simulating flow over the cylinder in the turbulence region, only comparisons of averaged flow quantities are shown, and the agreement with experimental results are not perfectly acceptable. Secondly, the computation for IB points needs to be implemented in a fully parallel manner. Since dynamic load balancing is necessary for S-AMR, it is not hard to take the IB points into account to balance the load of the entire computational domain. Finally, one should be aware of the inflow condition, especially for wall-bounded flows.

4 Rapid Pitching Airfoils

Since most applications in this work are related to flapping foils, this section will further validate the current numerical scheme with a two-dimensional airfoil in a pitch-up and pitch-down maneuver with a foil and compare it with previous simulations¹⁵¹, experiments¹⁵², and canonical theories^{3, 153}. The added-mass effect will be studied.

4.1 Comparisons of Vorticity and Forces

The foils used in the current work are a flat plate, SD0073, and an ellipsoidal foil with a ratio of 10:1. The pivoting point for all simulation is at the quarter chord from the leading edge. The motion function is the same as in Eldredge et al.¹⁵¹, shown in Fig. 4-1.

$$\alpha(t) = \frac{k}{A} \ln \left[\frac{\cosh(AU_{\infty}(t-t_1)/c) \cosh(AU_{\infty}(t-t_4)/c)}{\cosh(AU_{\infty}(t-t_2)/c) \cosh(AU_{\infty}(t-t_3)/c)} \right] \quad (4.1)$$

where k is the reduced frequency, A is a coefficient for speed of transition, selected as 100 in the present work, and c is the chord length.

The airfoil remains at a zero angle of attack until ΔT_s . A linear pitch-up reaches a maximum angle of $\alpha_m=40^\circ$. A hold-on period at this angle has a duration of ΔT_h . Finally, the airfoil pitches down linearly back to a zero angle of attack. Equation is an explicit function of the motion. In all simulation cases, the same values of ΔT_s and ΔT_h are used. However, the value of ΔT_p varies with different cases because of the different reduced angular velocity. Two reduced angular velocities are considered, i.e. $k = 0.2$ and 0.7 . In the present validation, the start-up interval, ΔT_s , is $1.0 c/U_{\infty}$. The duration of pitch-down

and pitch-up, ΔT_p , is $\alpha_m / \dot{\alpha}$, where $\dot{\alpha}$ is the angular velocity. The hold interval, ΔT_h , is $0.5 c/U_\infty$.

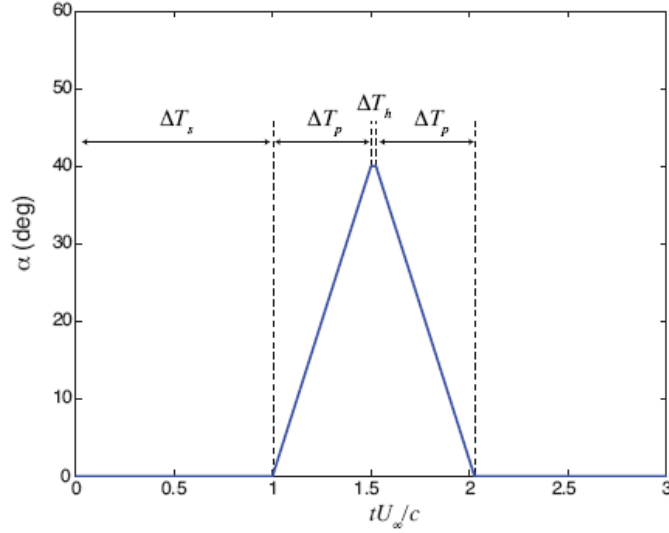


Figure 4-1 Basic pitch-up, pitch-down kinematics (with $k = 0.7$ shown here) from Eldredge *et al.*¹⁵¹

Eldredge et al.¹⁵¹ gave the vorticity contours of flat plate cases for $k = 0.2$ and 0.7 from their simulation at $Re=1000$. In addition, Ol¹⁵² exhibited the vortex pictures based on his dye injection experiments at $Re = 10k$.

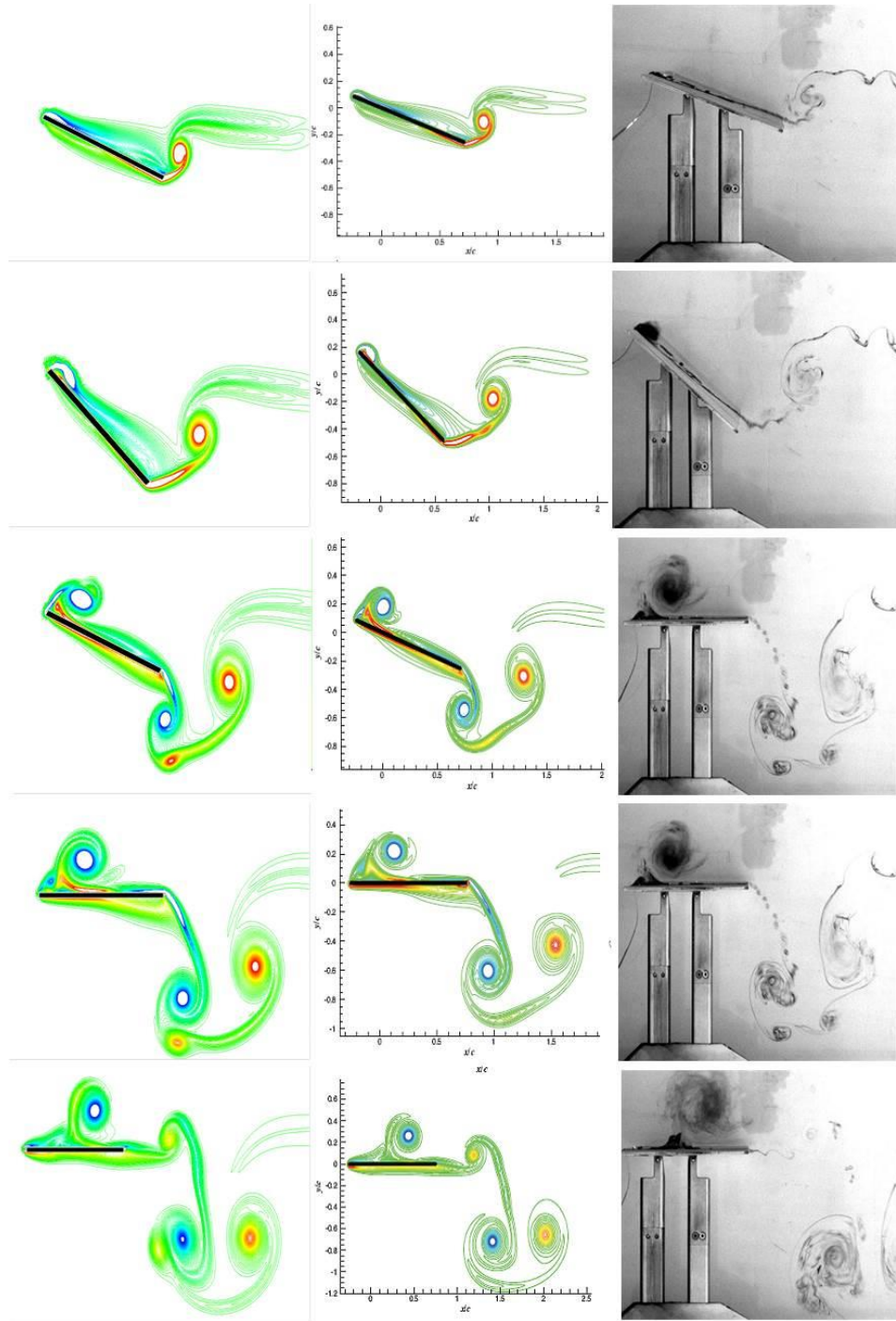


Figure 4-2 Comparisons of vorticity fields for the flat plate cases for $k = 0.7$, among the current simulation (left), Eldredge et al.¹⁵¹ (center), and OI¹⁵² $Re=10k$ (right).
 From the top to bottom rows: halfway to pitch-up; the moment reaching the maximum angle of attack; halfway to pitch-down; at the end of pitch-down; 0.5 time units after completion of pitch-down.

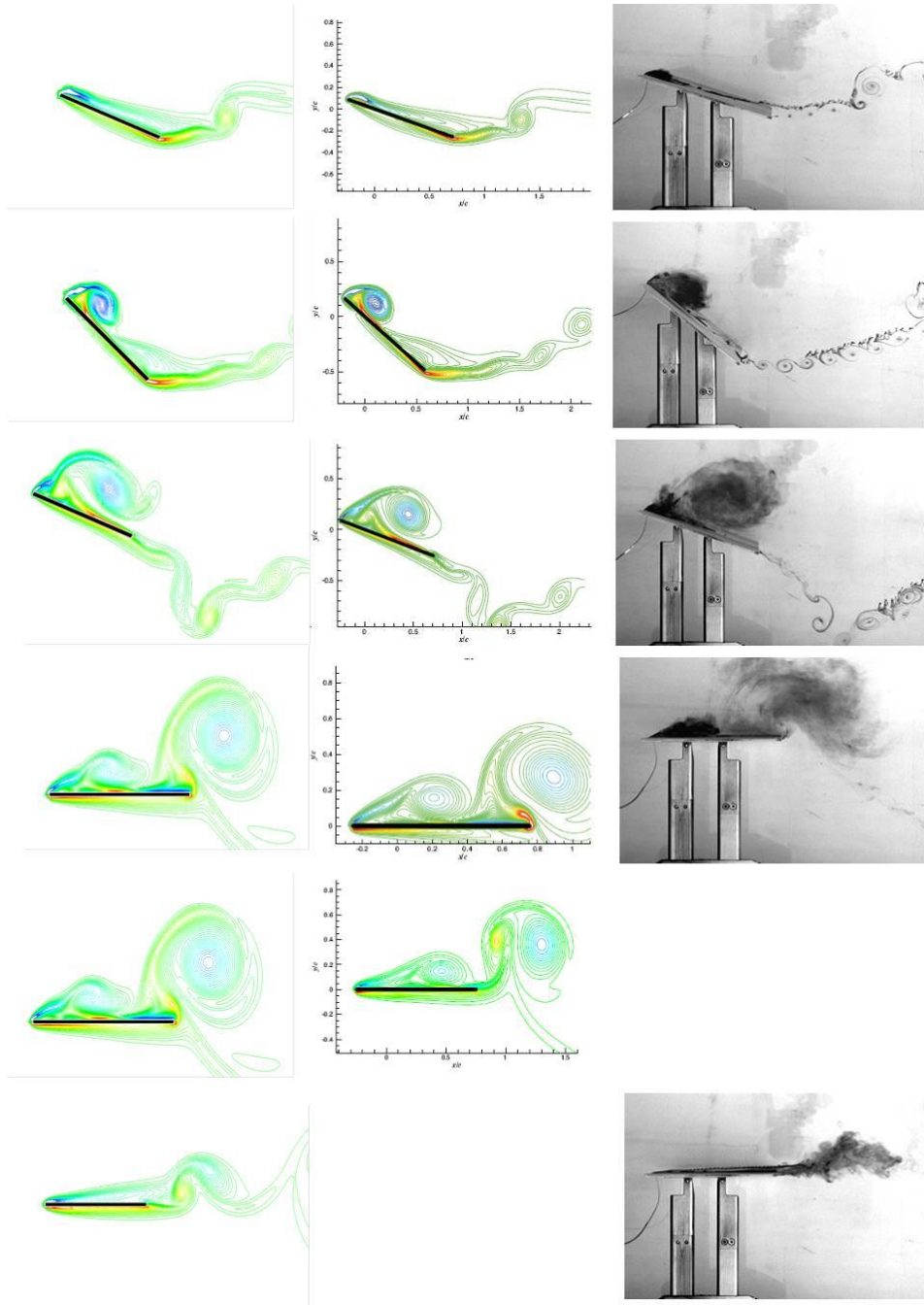


Figure 4-3 Same as previous figure but for $k = 0.2$, and Row 6 is for the results of 0.875 time units after completion of pitch-down.

Figures 4-2 and 4-3 depict comparisons for flat plate cases with $k = 0.7$ and 0.2 , respectively. Pictures in these two figures have the same color scale. The moments of time to capture the vorticity field are the same as the previous two studies, except for the last two rows of Fig. 4-3. Because the previous two studies do not have any common

instant for vorticity contours after the plate goes back to a zero angle of attack, two images are captured from the current simulation, each corresponding to one of the two data sets. In general, the results from the current simulation have a good agreement with these two studies. At the beginning of the motion, a clockwise leading edge vortex is generated. This small vortex plays a very important role in producing lift in all cases. It keeps attaching with the flat plate until the pitch-down motion.

The current simulation gives more detailed vortex structures than the results of Eldredge et al¹⁵¹, in comparison to the experiment¹⁵², especially for the $k = 0.7$ case. For example, the experimental results in rows 3~5 of Fig. 4-2 show a small shedding vortex under the clockwise trailing edge vortex, which starts to form approaching half-way to pitch-down (row 3 of Fig. 4-2) and eventually attaches to the clockwise trailing edge vortex after some time at the end of pitch-down (row 5 of Fig. 4-2). This process is clearly captured in the current simulation.

However, in Figs. 4-2 and 4-3, very small vortex structures in the experiment are not resolved in either of the simulations because of the Reynolds number limit in the simulations, which is ten times smaller than that in the experiment.

Figure 4-4 shows a good comparison between the current simulation and previous work¹⁵¹. At the beginning, when the angle of attack is zero, the lift coefficient remains zero with a very small drag coefficient. There are several short-lived spikes that are due to forces generated by non-circulatory flow (i.e. added mass force, to be explained in the next section). These forces are particularly significant in high acceleration rate motion. Moreover, based upon discussions on the vorticity field in the previous section, the “hump” region of the lift coefficient for the lower pitch rate case is shown in Fig. 4-3

during pitch-down at the time unit 3-3.7 because of the second leading edge vortex for the case of relatively low pitch rate. For the same reason, the lift coefficient for this case does not reach zero immediately after the motion is completed. On the other hand, for the case with a faster pitch rate, because of the stronger vortex and delayed detach time near its leading edge, the negative drag coefficient for this case has a “cave-up” region during time units 1.6~1.9 in Fig. 4-4.

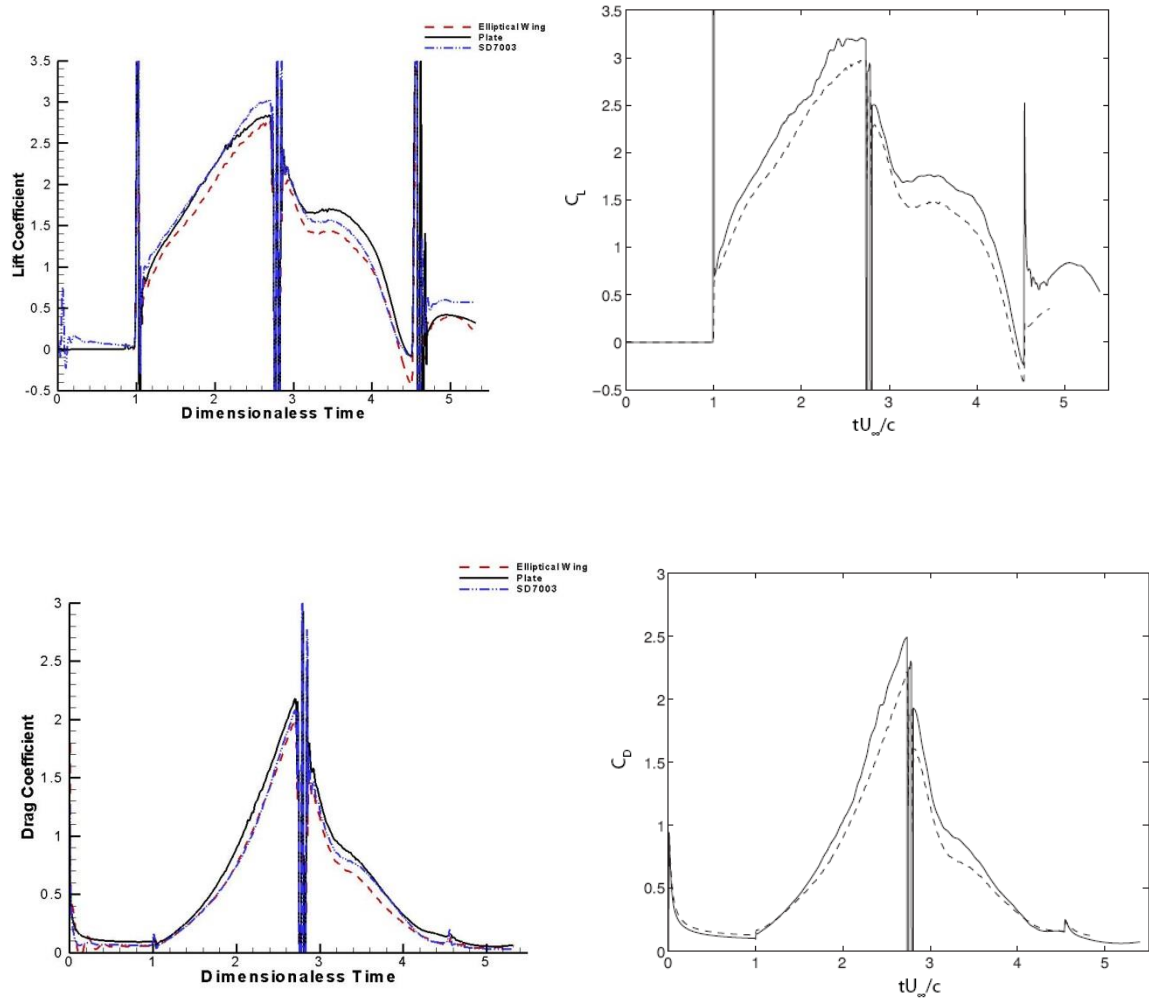


Figure 4-4 Lift and drag coefficient comparisons of the $k = 0.2$ cases between the current simulation (left) and Eldredge *et al*¹⁵¹ (right).

The solid line is for the flat plate, dashed line for the elliptical airfoil, and dash-solid line for SD7003 (which was not simulated by Eldredge *et al*¹⁵¹)

4.2 Added-Mass Effect

It was mentioned above that the short-lived spikes appearing in Fig.4-2 may be due to forces generated by non-circulatory flow. Theodorsen's theory¹⁵³ suggests that the lift on an unsteady airfoil can be generated by non-circulatory and circulatory flow components. The former part generally does not have a significant effect on slow airfoil motion in air flow because of the low rate of the motion and the small density value of the air property. In contrast, it plays a more important role in water. It is studied here because of rapid pitch motions involved, which indeed show evidence of forces generated by non-circulatory flow.

A recent summary of the theory can be found in McGowan et al.¹⁵⁴ and Leishman¹⁵⁵. A lift coefficient can be separated into two parts:

$$C_l = C_{lss} + C_{lpitch} \quad (4.2)$$

The first part is the steady-state contribution, C_{lss} , resulting from the mean angle of attack. By integrating the angle of attack of the airfoil following the motion in Eq. (4.1) from time 0 to infinity, this part turns out to be zero. The second part is the pitch contribution, C_{lpitch} , resulting from the instantaneous pitch motion.

The lift coefficient contributed by the pitch has also two parts: (1) the non-circulatory flow contribution, the first term on the right hand side of Eq. (4.3), resulting from high rate acceleration of the motion described in Theodorsen's work¹⁵³; (2) the circulatory flow contribution, the second term on the right hand side of Eq. (4.3), resulting from the effect of vortex distribution on the flow. Following Leishman¹⁵⁵, the lift coefficient can be expressed as

$$C_l = C_{lpitch} = \pi b \left(\frac{\dot{\alpha}}{U_\infty} - ba \frac{\ddot{\alpha}}{U_\infty^2} \right) + 2\pi C(k) \left[\alpha + b \left(\frac{1}{2} - a \right) \frac{\dot{\alpha}}{U_\infty} \right] \quad (4.3)$$

where $C(k)$, called Theodorsen's function, is a complex function that takes into consideration the effect of the wake vorticity on the flow. Based on McGowan et al¹⁵⁴, the expression for Theodorsen's function is

$$C(k) = \frac{K_1(ik)}{K_0(ik) + K_1(ik)} \quad (4.4)$$

where the argument, k , is originally the reduced frequency for harmonic oscillation motion. However, for the problem of the current study, this parameter has, strictly speaking, an ambiguous meaning. Wagner's theory is thus used here for the circulatory part. This theory has a solution for the indicial lift on a thin airfoil undergoing a step change in the angle of attack¹⁵⁵. Hence, the total lift coefficient consists of the non-circulatory part from original Theodorsen's theory and the circulatory part from Wagner's theory:

$$C_l = C_{lpitch} = \pi b \left(\frac{\dot{\alpha}}{U_\infty} - ba \frac{\ddot{\alpha}}{U_\infty^2} \right) + 2\pi \left[\alpha(s_0)\phi(s) + \int_{s_0}^s \frac{d\alpha(\sigma)}{d\sigma} \phi(s-\sigma) d\sigma \right] \quad (4.5)$$

where ϕ is the Wagner function. For simplicity of calculation, an exponential approximation of the Wagner function, which was found to agree with the exact solution with accuracy within 1%¹⁵⁵, is used here:

$$\phi(s) \approx 1.0 - 0.165e^{-0.0455s} - 0.335e^{-0.3s} \quad (4.6)$$

The drag coefficient is deduced following the propeller theory of Garrick³ that was originated from Theodorsen's theory:

$$C_d = \pi S^2 + \alpha C_{lpitch} \quad (4.7)$$

$$S = \frac{\sqrt{2}}{2} \left[2C(k)Q - b \frac{\dot{\alpha}}{U_\infty} \right] \quad (4.8)$$

$$Q = \alpha + b \left(\frac{1}{2} - a \right) \frac{\dot{\alpha}}{U_\infty} \quad (4.9)$$

Since the first term of Eq. (4.7) is derived from vorticity distribution, it is recognized as a contribution from circulatory flow. Additional drag contributed by circulatory flow is in the circulatory part of the lift (i.e. the second term of Eq. (4.7)). Consequently, the only non-circulatory part of the drag is brought about by the non-circulatory part of the lift.

Notice there is still a Theodorsen Function in Eq. (4.8). It has a real part and an imaginary part. The real part denotes the calculation associated with the motion as a cosine function, and the imaginary part as a sine function. In the following calculation, the imaginary part has been employed for calculation of the pitch-up interval since the attack angle is zero at the beginning (i.e. a sine motion), while the real part has been used for calculation of the pitch-down interval.

We select the flat plate airfoil cases for comparisons. Figure 4-5 shows the comparisons of lift and drag coefficients between the current simulation and the theoretical results from Theodorsen's theory. As the motion here is non-periodic, k in the Theodorsen function is simply selected as the reduced angular velocity. However, this may cause some discrepancies in the results of the circulatory part of the drag coefficient, especially in the case of $k = 0.2$. In the case of $k = 0.7$, since the ramp time is relatively

short, the simulation results still show a good agreement with the theoretical results. It should be noted that Theodorsen's theory is suitable for small angles of attack, and therefore the comparison is apparently always better for smaller angles of attack.

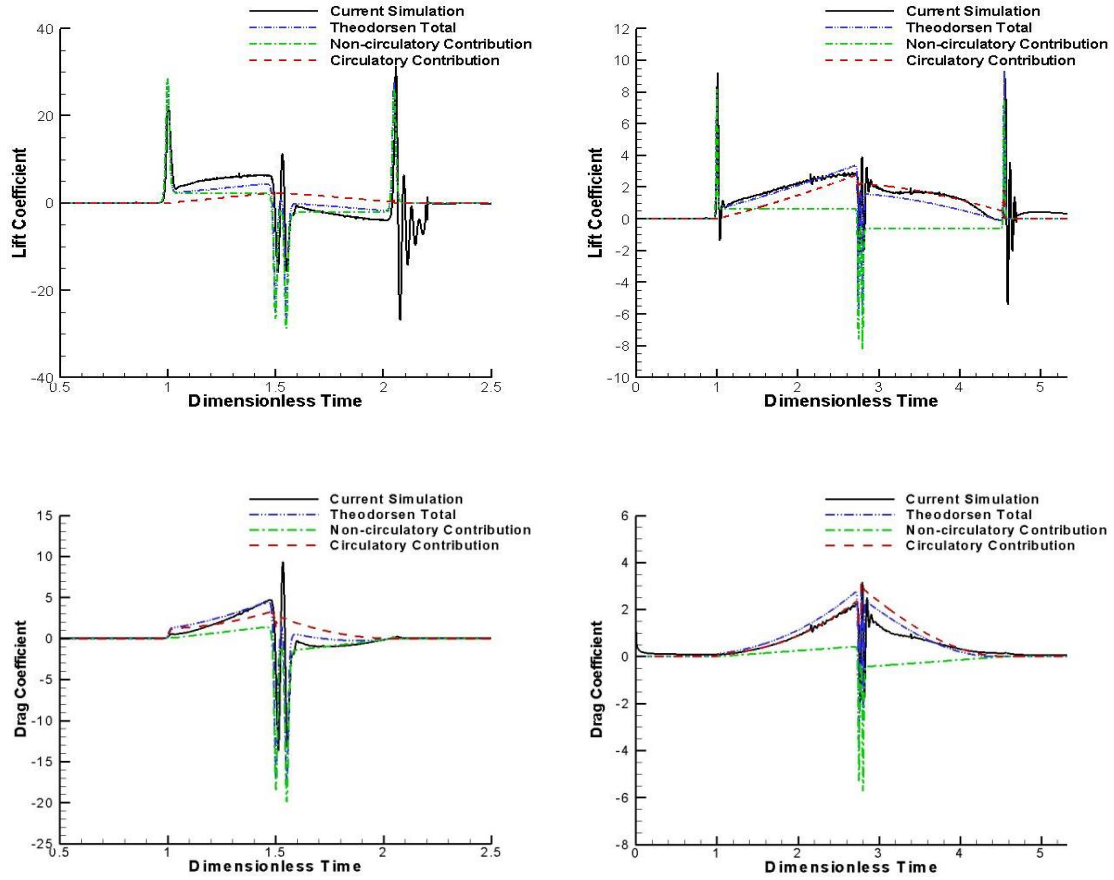


Figure 4-5 Comparisons of lift and drag coefficients between the current simulation and Theodorsen's theory for the cases of $k = 0.7$ (left) and $k=0.2$ (right).

In Fig. 4-6, we zoom into high-acceleration-rate time intervals to show detailed lift coefficient comparisons of the cases of $k=0.7$ and $k=0.2$. The non-circulatory part has a significant effect on these times due to the high acceleration of the angle of attack. Especially when the angle of attack is small (i.e. rows 1 and 3 in Fig. 4-6), both the simulation and theoretical results show that the lift is contributed entirely from the non-circulatory part, though there is a small time shift between the two results. On the other

hand, the circulatory part barely has an effect during the high-rate acceleration and keeps its value almost the same before and after the acceleration.

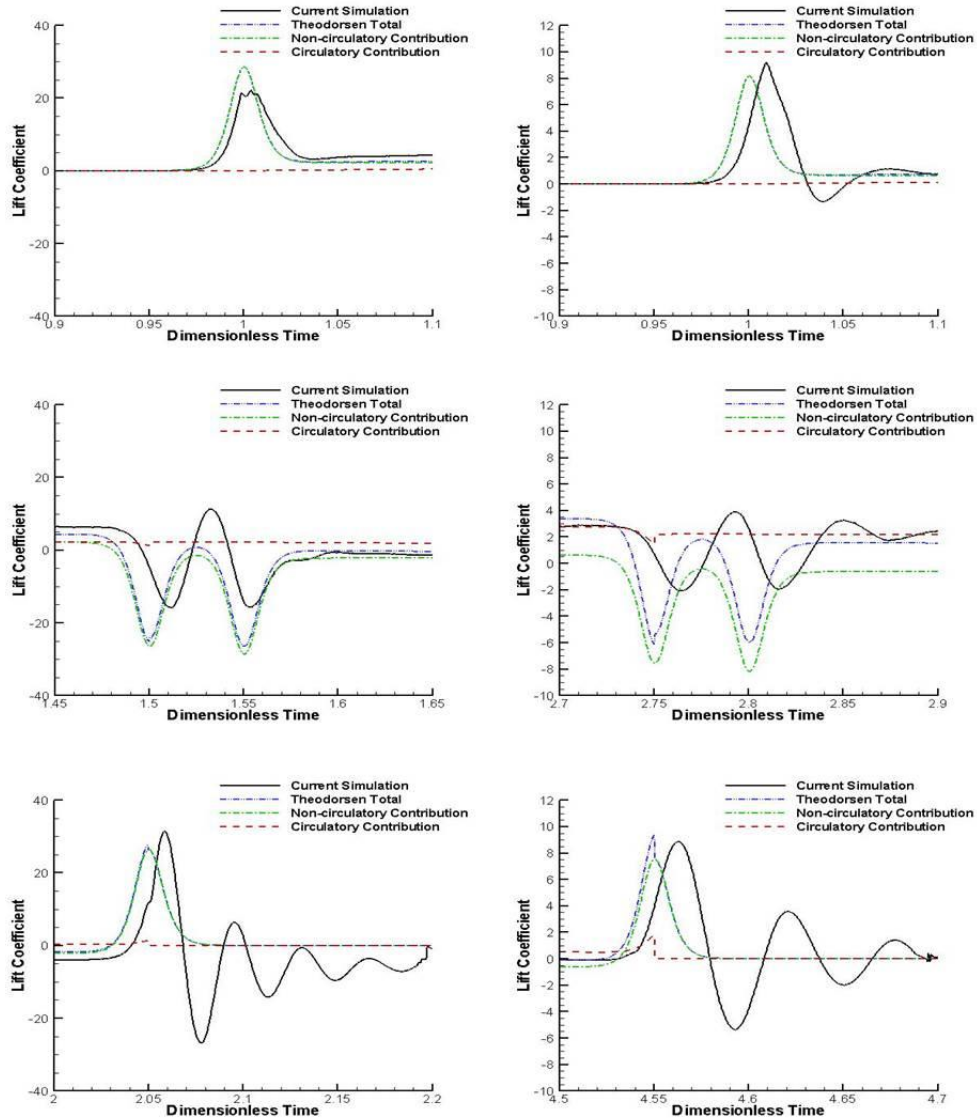


Figure 4-6 Comparisons of lift coefficient between the current simulation and Theodorsen's theory for the cases of $k = 0.7$ (left) and $k=0.2$ (right).

Top row: at the beginning of pitch-up; middle row, in the interval of hold; bottom row: at the end of pitch-down motion.

4.3 Summary for the Rapid Pitching Airfoil

The IB method is used to simulate the canonical pitch-hold-return cases for flat plate, elliptical, and SD 7003 airfoils. The IB method is validated and good agreements in comparison with other numerical methods, experiments and canonical theories were obtained. By using Theodoren's theory for unsteady airfoils, the non-circulatory contribution (added-mass effect) to the lift and drag has been found to be the major component when the airfoil experiences a high-rate acceleration or deceleration. Since the loosely-coupled FSI employed in the current work suffers from the added-mass effect, the high-rate change of motion is not preferable.

5 Asymmetric Wakes

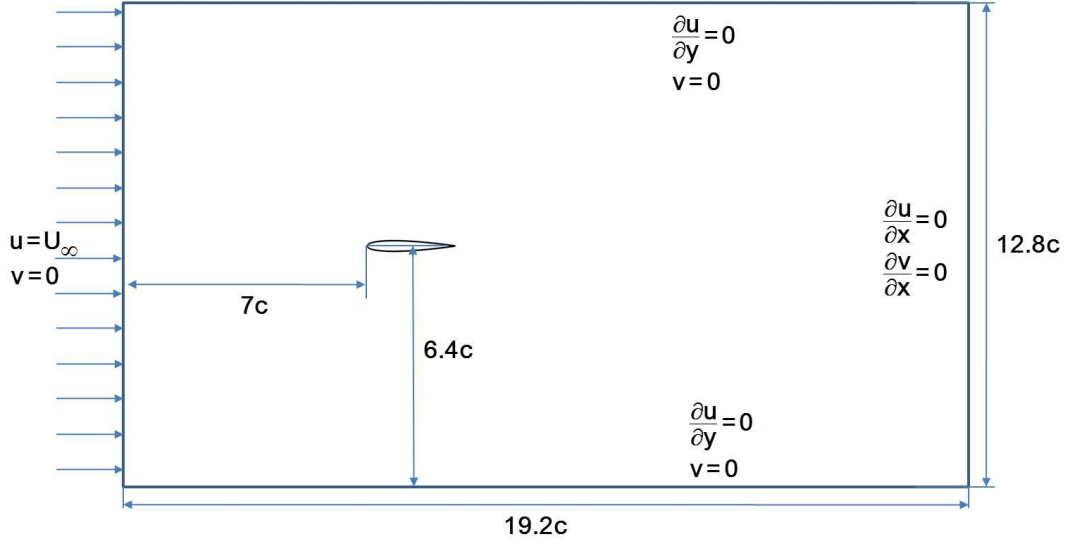


Figure 5-1 Definition sketch of set-up of simulations in this study

The sinusoidal heaving motion of a symmetric airfoil, a NACA0012 airfoil, is specified as

$$\begin{aligned} y(t) &= h \sin(kt) \\ k &= 2\pi f \end{aligned} \quad (5.1)$$

Again, all the equations and variables are dimensionless. The characteristic length and velocity are the airfoil chord length and the free stream velocity, respectively. The frequency, f , and reduced frequency, k , in Eq. (5.1) are respectively, $f = f^* c / U_\infty$ and $k = 2\pi f = 2\pi f^* c / U_\infty$. The simulation is performed for a heaving airfoil under four different Reynolds numbers ($Re = 200, 300, 400$ and 500) and three Strouhal numbers ($V_p = 2\pi f^* h^* / U_\infty = kh = 0.96, 1.08, 1.2$ and 1.3). The Strouhal number, which is the product of

reduced frequency and dimensionless heaving magnitude, is considered a primary factor that influences the wake of a heaving airfoil^{6, 7, 9, 10, 12, 15}.

The computational domain size selected for this study is 19.2×12.8 , shown in Fig. 5-1. This mesh setup provides an acceptable grid-resolution-independent solution for all the computational cases in this study. Although the immersed-boundary method is not limited to a uniform grid mesh, the uniform grid implemented in the simulation provides good results for the objectives of the current study. In addition, the physical phenomena corresponding to the subject of this study do not change if the computational domain size is enlarged in both streamwise and cross-flow directions. The size of the computational domain is selected so that the size of the domain does not influence the results. The airfoil is located at 7-unit lengths downstream of the inlet flow boundary to leave sufficient space for reducing the effect of the inlet boundary condition. The grid size is $\Delta x = \Delta y = 0.0125$, which provides an acceptable grid-resolution-independent solution for all computational cases in this study after a grid-size convergence study. The Dirichlet-type boundary condition is employed at the inlet for velocity; the symmetry boundary condition is used for both the upper and lower boundaries; and the outlet is specified with the Neumann-type boundary condition. All velocity profiles presented in this study were averaged over four airfoil oscillation cycles after the simulation results became periodic.

5.1 Near Wake Deflections

An interesting phenomenon was observed in the flow of a heaving airfoil by Jones *et al.*⁶, where the wake vortex street after a symmetric airfoil, with a symmetric periodic

sinusoidal heaving motion, deflected to one side of the airfoil rather than locating symmetrically along the line of the mean plunging location of the airfoil.

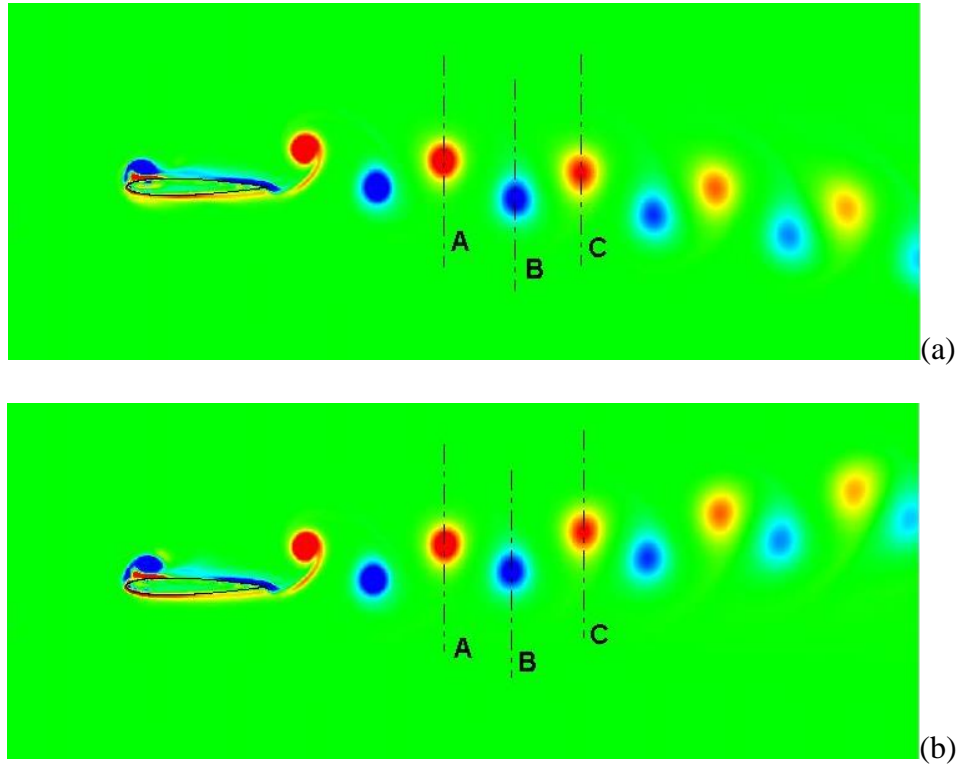


Figure 5-2 Vorticity contours for the case of $k = 10$, $h = 0.12$, and $Re = 400$. (a) the heaving starts with an upward motion; (b) the heaving starts with a downward motion. The dashed lines indicate the approximate center of a vortex. The contour color range is from -30 to 30

Previous studies reported that the vortex deflection direction is affected by the initial direction of the heaving motion^{6, 10, 15}. This is also confirmed in the current study, as shown in Fig. 5-2. When the airfoil starts moving upward at the beginning of the heaving motion, the wake deflects downward, and vice versa.

This phenomenon is attributed to the pairing pattern of the wake vortices downstream of the airfoil. Figure 5-2 (a) is a case when the airfoil starts periodic heaving with an initially upward motion. Figure 5-2(a) shows that the distance between vortices

“A” and “B” is longer than that between vortices “B” and “C”. According to the Biot-Savart vortex induction law, a shorter distance amounts to a stronger vortex interaction. Therefore, vortices “B” and “C” are recognized as a pair instead of “A” and “B”, indicating a strong interaction between “B” and “C”. Since the negative vortex (darker gray - blue line in Fig. 5-2) is rotating clockwise and the positive vortex (lighter gray - red online in Fig. 5-2) counter-clockwise, such a pairing pattern induces a downward motion. This downward motion thus results in a downward vortex wake deflection. The situation in Fig. 5-2(b) is when the airfoil starts with a downward motion. The wake deflection is then in the direction opposite to the case in Fig. 5-2(a). The vortex pair now formed by “A” and “B” in Fig. 5-2(b), with a positive vortex on the left and a negative vortex on the right, causes an upward wake vortex deflection.

Following the vortex pairing argument stated above, if the distances between two adjacent vortices are equal, no deflection should be detected. Several no-deflection cases shown later in the study will confirm this claim.

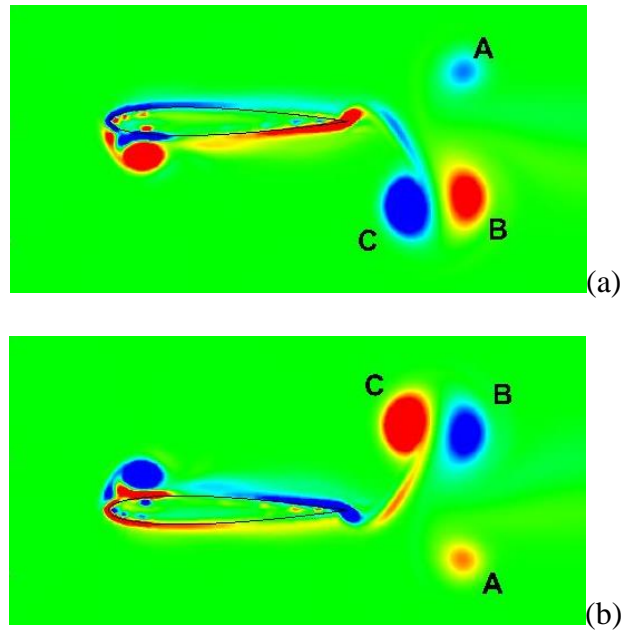


Figure 5-3 The pairing competition among the first few vortices of a heaving airfoil, (a) with an initially upward motion and (b) with an initially downward motion.

Now the follow-up question is why the different vortex pairing patterns occur when the starting motion is upward versus downward. Figure 5-3 shows the vorticity field at the nascent stages after the airfoil starts to move. It can be seen when the airfoil starts with an upward motion in Fig. 5-3 (a), a starting vortex “A” in the negative sense (clockwise) is generated at the trailing edge. This is because the total lift on the airfoil is negative during the initial upward motion, which is created by an overall circulation around the airfoil in the positive sense. A strong positive sign vortex “B” is generated in the consecutive downward motion, followed by a strong vortex negative sign vortex “C” generated during a later upward motion shown in Fig. 5-3(a). Due to its lower strength, the starting negative vortex “A” loses the pairing competition with the positive vortex “B” in the wake against the stronger negative vortex “C”. Such a pairing, as discussed in the previous paragraph, leads to a downward deflection of the wake. Vice versa, the opposite

pairing pattern and thus deflection direction can be seen in Fig. 5-3(b) when the airfoil starts with a downward motion.

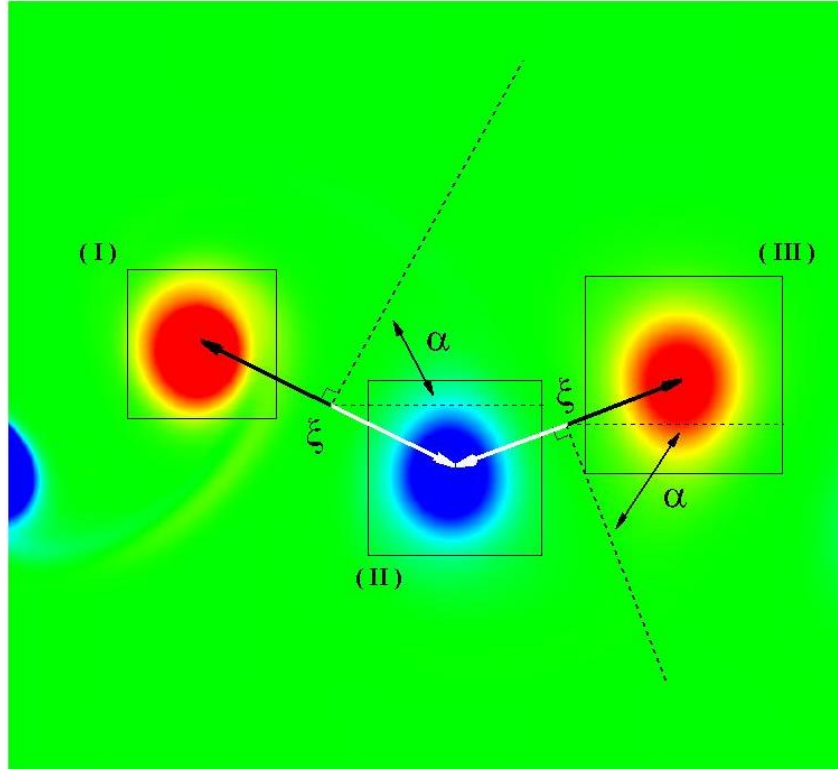


Figure 5-4 Parameters used in calculating the effective phase velocities

To detect the wake deflection trend quantitatively, Godoy-Diana¹⁷ proposed a symmetry-breaking condition depending on the vortex pair (the dipole) structure and the vortex phase speed. We extend this condition by making use of the effective phase velocity to quantitatively define the trends of symmetry breaking and symmetry holding. In the dipole structures (between I and II, and II and III) shown in Fig. 5-4, the wake tends to deflect downward. The effective phase velocity for a vortex dipole, U_p^* , is then defined as

$$U_p^* = U_{dipole} - (U_{phase} - U_{\infty}) \cos \alpha \quad (5.2)$$

As the deflection is downward in this case, the symmetry-breaking effective phase velocity is calculated based on a dipole that induces the downward motion on the pair of vortices in the dipole. In this case, the symmetry-breaking dipole is represented by vortices II and III, which is the same as the pair selection stated previously. The other pair, vortices I and II, which induces an upward motion in the dipole, is to produce a symmetry-holding effective phase velocity and considered a symmetry-holding dipole. The definition of the variables in Eq. (5.2) follows those in Godoy-Diana¹⁷. Specifically, U_{phase} , in Eq. (5.2), is the averaged x -direction velocity of the motion of the two vortex centers in dipole. The center of a vortex is defined as the location of the local maximum vorticity. And U_{dipole} is calculated as

$$U_{dipole} = \frac{\Gamma}{2\pi\xi} \quad (5.3)$$

and ξ and α are defined in Fig. 5-4. The circulation of the dipole, Γ , is calculated using the method of vorticity area integration in the rectangular area indicated in Fig. 5-4. The choice of rectangular integration contours, instead of the elliptical ones that would have better followed the vortex shape, was made in order to avoid errors from interpolation of the velocity data¹⁷. The size of the rectangular area is determined by using Gaussian fits, $\exp(-x_i^2/\sigma_i^2)$, along the vertical and horizontal axes centered on positions of the maxima and minima of vorticity. The sizes of the vortex along the x - and y -direction are defined as $2\sigma_i$. The circulation value is the average circulation of the two vortices in the dipole.

We calculated the effective phase velocities of symmetry-breaking and symmetry-holding for the cases shown in Fig. 5-3. When the wake is deflected either downward (Fig. 5-3a) or upward (Fig. 5-3b), for both cases, the effective symmetry-breaking phase

velocity is 0.32, while the effective symmetry-holding phase velocity is 0.21. This is primarily due to the fact that ξ in the symmetry-breaking dipole is smaller than that in the symmetry-holding dipole, which is the same factor to determine vortex pairing as discussed earlier. Since the symmetry-breaking effective velocity is greater than the symmetry-holding effective phase velocity, the wake deflects. Subsequent discussions will make rigorous use of this criterion.

5.2 Discussions of the Factors Influencing Near Wake Deflection

5.2.1 Effects of the Strouhal Number versus the Individual Effects of the Reduced Frequency and Amplitude

In the discussion of the magnitude of the wake deflection angle, previous work put more concentration on the effect of the Strouhal number only^{10, 15}. The current study is the first that has investigated the effect of amplitude and frequency individually on the wake deflection angle. A general consensus in the previous work^{7, 10, 12, 15} was that a larger value of V_p is related to a larger deflection angle. However, it was reported^{6, 7} that in some cases, a flow with larger Strouhal number might not show any wake deflection. Another exception, illustrated in Fig. 5-5, is that the case with $h = 0.12$ and $k = 9$ has a larger deflection angle than the case with $h = 0.24$ and $k = 5$, although the latter has a larger Strouhal number ($V_p = 1.2$) than the former ($V_p = 1.08$).

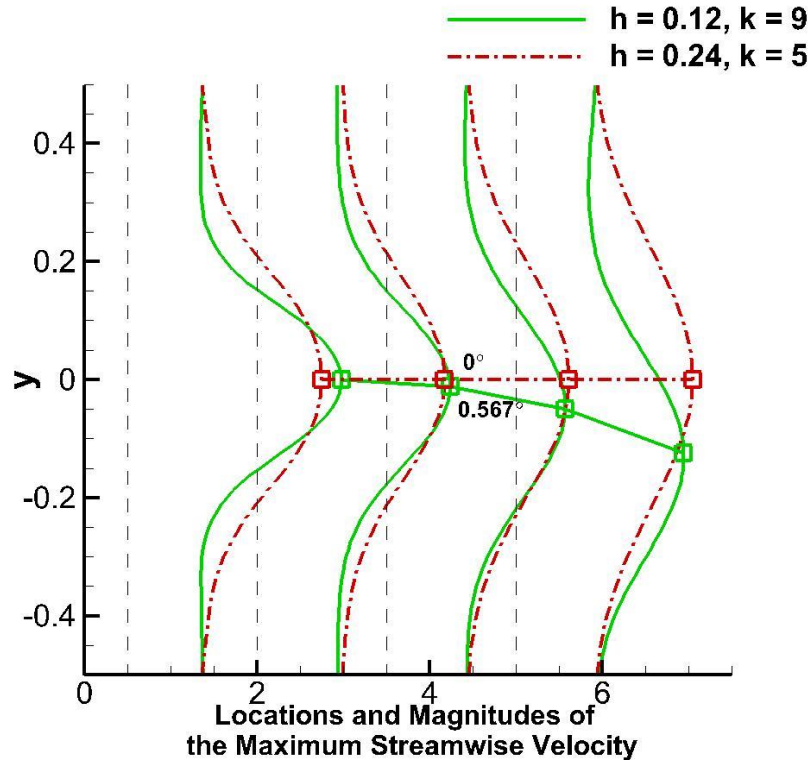


Figure 5-5 Streamwise velocity profiles downstream of the airfoil with $h = 0.12$, $k = 9$ (dash-dot lines) and $h = 0.24$, $k = 5$ (solid lines).
Dashed lines indicate four locations in the flow direction (x-direction) for the downstream distances from the airfoil TE to where the velocity profiles are recorded. Rectangular symbols imply locations of maximum velocity.

The way to express the deflection angle in terms of maximum values in velocity profiles in Fig. 5-5 follows that of Ref. 16. The zero value in the y axis is the mean position of the airfoil heaving motion. Four vertical dashed lines indicate the downstream distances from the trailing edge of the airfoil to where the velocity profiles are recorded. These locations are 0.5, 2, 3.5, and 5 in the x -direction downstream of the trailing edge. The shape of the velocity profiles in Fig. 5-5 indicates the velocity magnitude at a particular location. Rectangular symbols, which show the locations of maximum value of each profile, are formed to represent the wake deflection angle. Numerical values of the deflection angle (i.e. 0° and 0.567° in Fig. 5-5) are calculated based on the vertical and

horizontal location differences of maximum values sampled at the two locations of 0.5 and 2. The type of graph as in Fig. 5-5, with omitted curves for velocity profiles, will be frequently employed in the following discussion to compare the wake deflection angles. It is noted that the symbol at $x = 0.5$ is defined as a marker to identify the near wake deflection, while the symbol at $x = 5$ denotes the far wake deflection.

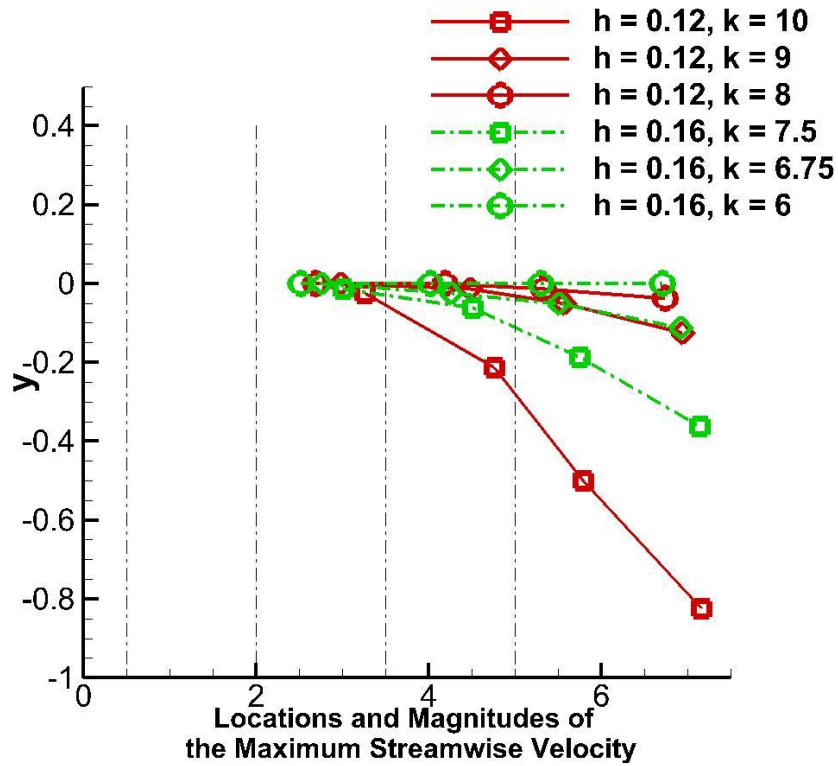


Figure 5-6 The vertical location of the maximum value of downstream x-direction velocity profiles for cases with $Re = 500$, where $y = 0$ is the mean location of the heaving airfoil and $x = 0$ is the location of the trailing edge of the airfoil.

Figure 5-6 shows that the deflection angle increases as V_p increases by increasing the reduced frequency, k , at a fixed heaving amplitude^{10, 15} ($h=0.12$ and 0.16 , respectively). In this case, the magnitude of maximum downstream velocity also increases as the symbols on curves with the same line type (solid or dot-dash, indicating $h=0.12$ and 0.16 , respectively) from the same location increase their magnitudes in the abscissa direction.

The increasing velocity magnitude is consistent with the fact that higher heaving frequency leads to higher input power from the airfoil, which provides more propulsive force^{9, 12}.

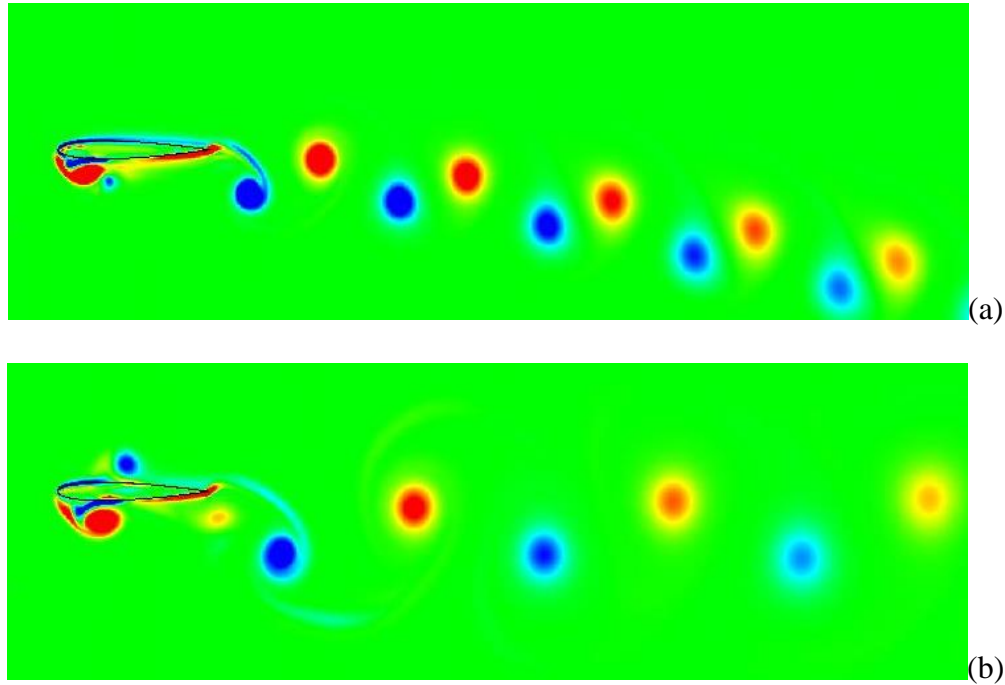


Figure 5-7 Vorticity contours of cases with the same $V_p=1.2$, (a) $h = 0.12$, $k = 10$ and (b) $h = 0.24$, $k = 5$.

Figure 5-6 also confirms the individual effect of reduced frequency and magnitude at the same V_p that is the product of these two factors. Each of the cases is represented by square, diamond, or circle symbols, and has the same V_p values of 1.2, 1.08, and 0.96 respectively. Note the symbols with solid lines have a lower magnitude and higher frequency than the ones with dash-dot lines. The closer distance between the two vortices in a dipole, which appears in the cases of higher frequency such as in Fig. 5-7(a), gives rise to stronger interactions between the vortices that therefore create a larger angle of deflection in the wake. The cases with higher frequency generate more vortices within the same distance downstream of the airfoil. In Fig. 8, the frequency in the higher frequency

case is twice the low frequency case, while the V_p value remains the same as 1.2, the highest V_p value among the cases in Fig. 5-6. In this particular case, the lower frequency case, with $h=0.24$ and $k=5$, even does not have a deflected wake. As stated earlier, the pairing of the vortices into a dipole and their interactions are the reason that the wake deflects. Such a pairing pattern does not appear in the lower frequency case in Fig. 5-7(b), where the vortices are evenly distributed like a symmetric, reversed von Karman vortex street^{7, 17}.

At the same time, by comparing the two wakes in Figs. 5-7(a) and 5-7(b), each individual vortex at the same distance downstream the airfoil has almost the same strength in both the higher frequency and lower frequency cases. However, the higher frequency case has twice the number of vortices in the wake as a non-symmetric pairing pattern. This again proves that the vortex pairing pattern is the reason for the wake deflection, not just the vortex strength itself that is somehow related to the Strouhal number (when then Reynolds number is fixed).

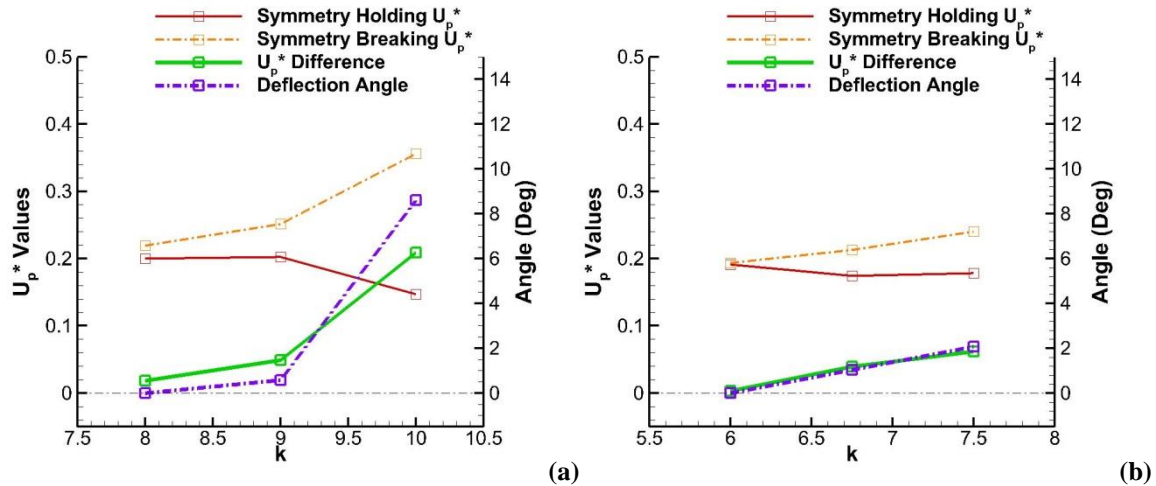
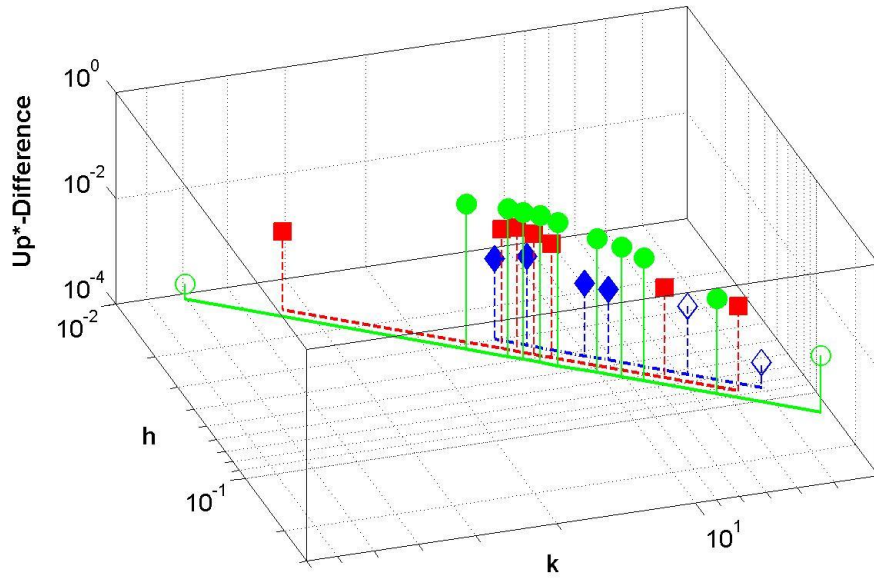
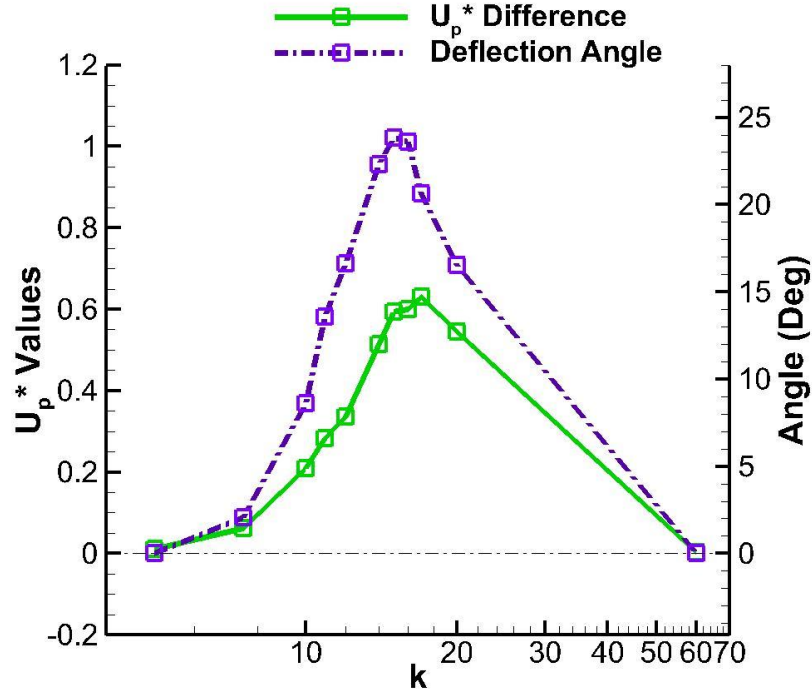


Figure 5-8 Deflection angle and effective phase velocities versus the reduced frequency for cases presented in Fig. 7. (a) $h = 0.12$ and (b) $h = 0.16$

The criterion based on the effective phase velocities presented in the previous section has been applied in the cases here to check its applicability. Figures 5-8 contain the plots of the deflection angles and the effective phase velocity versus the reduced frequency for the cases presented in Fig. 5-6 with $h=0.12$ and $h=0.16$, respectively. In both cases in Fig. 5-8, when the deflection angle increases with the reduced frequency, the symmetry-breaking effective phase velocity apparently increases while the symmetry-holding phase velocity either decreases slightly or remains almost the same. This result shows that when the difference between the two effective phase velocities increases, the deflection angle increases. Such a trend reaffirms the use of effective phase velocity to correlate with the deflection angle¹⁷.



(a)



(b)

Figure 5-9 Deflection angle and the difference between the symmetry-breaking and symmetry-holding effective phase velocities versus the reduced frequency k and heaving amplitude h for the case of $Re = 500$.

(a) Solid lines with circle markers: $V_p = 1.2$; Dash lines with square markers: $V_p = 1.08$; Dash-dot lines with diamond markers: $V_p = 0.96$. Solid markers: deflected wakes; Hallow markers: symmetry wakes. (b) A particular case of $V_p = 1.2$.

Figure 5-9(a) presents the results from a study of the deflection behavior in a wider range of reduced frequencies and heaving amplitude at three Strouhal numbers, $V_p=0.96$, 1.08, and 1.2. It confirms that the deflection occurs in a regime of moderate heaving amplitude and frequency^{7, 12, 15, 156}.

Furthermore, it should be noted that some of previous work^{7, 10, 15} showed that, for a certain value of V_p , the wake does not have any deflection for very small or large values of k , while it has quite a significant deflection at moderate values of k . Figure 5-9(b) illustrates the relationship between the deflection angle and the difference between the symmetry-breaking and symmetry-holding effective phase velocities at a fixed Strouhal

number $V_p = 1.2$. The reduced frequency increases in the range of $5 < k < 60$, with a correspondingly decreasing h value. The results in Fig. 5-9(b) indicate that the deflection angle occurs when the value of k is greater than 7.5. For large values of k , such as 60, with an extremely small h of 0.02 for the same V_p value of 1.2, the flow exhibits a nicely symmetric wake. Therefore, the deflection angle increases to a maximum value at a moderate value of k and reduces towards zero, as the results show in Fig. 5-9(b). This trend can also be correlated to the difference between symmetry-breaking and symmetry-holding effective phase velocities. In Fig. 5-9(b), the deflection angle increases when the difference between the two effective phase velocities increases.

5.2.2 Reynolds number effect on the deflection angle

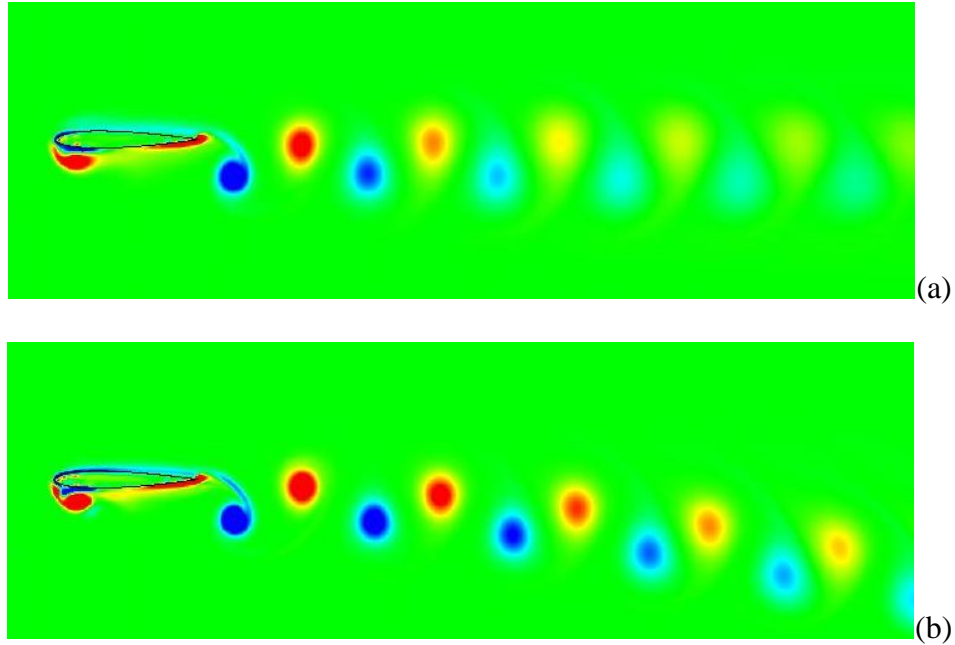


Figure 5-10 Vorticity contours of the beginning of the down-stroke for the case of $h = 0.12$, $k = 10$ with $Re = 200$ (a) and $Re = 400$ (b).

Liang *et al.*¹⁹ claimed that, to their knowledge, they were the first to find the increment of the deflection angle when the Reynolds number increases. The current study has further studied the mechanism for this phenomenon. The results in Figs. 5-10 and 5-11 are for the cases at different Reynolds numbers but at the same V_p value of 1.2. Figure 5-10 compares contours of cases with $Re = 200$ and 400. Apparently, the case with $Re = 400$ has a larger deflection angle in its wake than the case with $Re = 200$. The primary factor is the stronger vortices associated with the higher Reynolds number. It is then easily understood that the stronger the vortex pairs, the larger the resultant deflection angles, because the induced motion in the vortex pairs directly causes the deflection. As a higher Reynolds-number flow results in lower vorticity dissipation, Figure 5-11 illustrates that vortices in the wake of the higher Reynolds number case ($Re = 400$) decay more slowly than those of the lower Reynolds number case ($Re=200$). The vortex pairing pattern also disappears in the lower Reynolds number case, resulting in an almost non-deflecting wake.

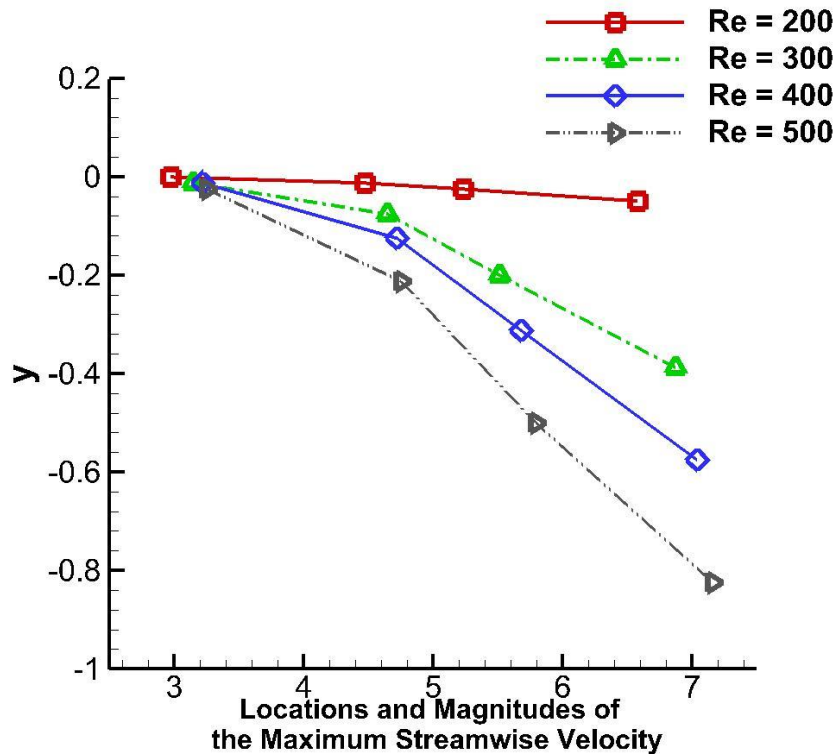


Figure 5-11 Deflection angle comparisons with different Reynolds numbers

The increment of the deflection angle as the Reynolds number increases between 200 and 500 is illustrated in Fig.5-11. It also shows that the increase of the Reynolds number causes the increase of the magnitude of the maximum velocity, as the symbols indicating the maximum velocity from the same location shift further right in the abscissa direction for larger Reynolds numbers. The correlation between the effective phase velocities and the deflection angle is again presented in Fig. 5-12. The symmetry-breaking effective phase velocity increases and the symmetry-holding effective phase velocity decreases with the increase of the Reynolds number. This once more correlates the increase of the difference between the two effective phase velocities with the increase of the deflection angle.

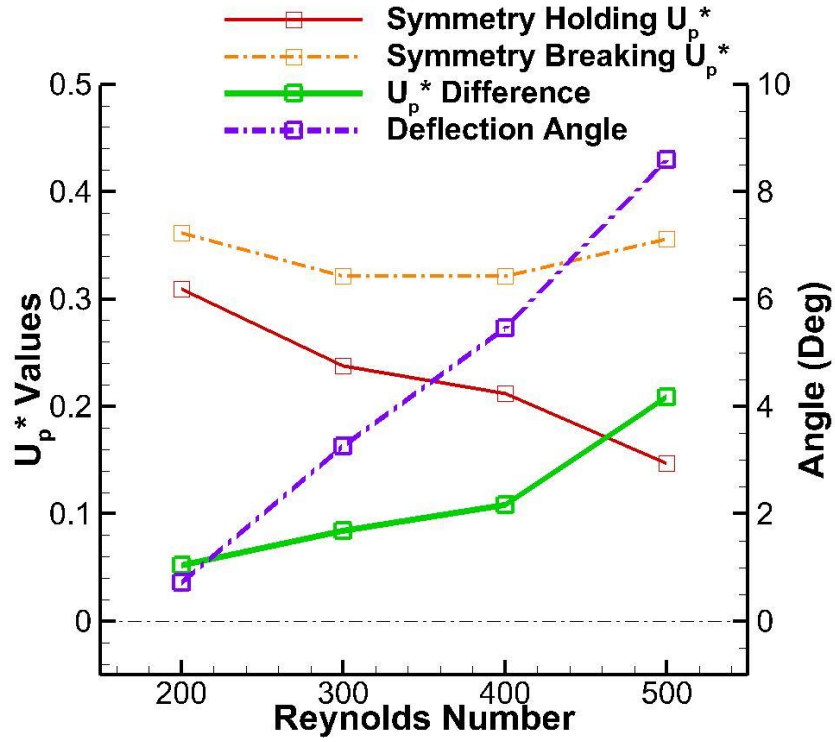


Figure 5-12 Deflection angle and effective phase velocities versus the Reynolds number

5.3 Summary of the Near Wake Deflections

In this section, the formation of deflected wakes downstream of a heaving airfoil has been studied numerically. The reason for the deflection is attributed to the vortex pairing pattern in the wake, which causes a downward deflection wake if the airfoil starts the heaving motion upward, and vice versa. The deflection trend is determined by the competing mechanism between the symmetry-breaking and symmetry-holding effective phase velocities. These velocities are defined and calculated according to the vortex pairing pattern. At the same Strouhal number, the deflection angle achieves its maximum value at a moderately reduced heaving frequency. Particularly, at a very small or very large reduced frequency, the pairing pattern that causes the wake deflection disappears, and a symmetric, reversed von Karman street wake is generated. In addition, the

Reynolds number also influences the wake deflection. For a fixed Strouhal number, the deflection angle increases with the Reynolds number. This is because the vortex strength in the wake is stronger in a high Reynolds number flow, which exacerbates the pairing pattern that causes the wake deflection. In the low Reynolds number cases, the vortices are weaker and the pairing pattern may no longer exist, resulting in a weak, non-deflected wake. Based on this study, it is evident that the size of the deflection angle is proportional to the difference between the symmetry-breaking effective phase velocity and the symmetry-holding effective phase velocity. Although this conclusion is based on the results of changing one variable at a time in this study, such as reduced frequency or the Reynolds number, the trend should remain the same even under a multi-variable situation.

5.4 The Phenomena of Far-Wake Deflection and Switching of Vortex Pattern

The previous section deliberately discussed the wake deflection in the near wake region, and this section will focus more on the deflection angle, which can change from the near wake to the far wake regions.

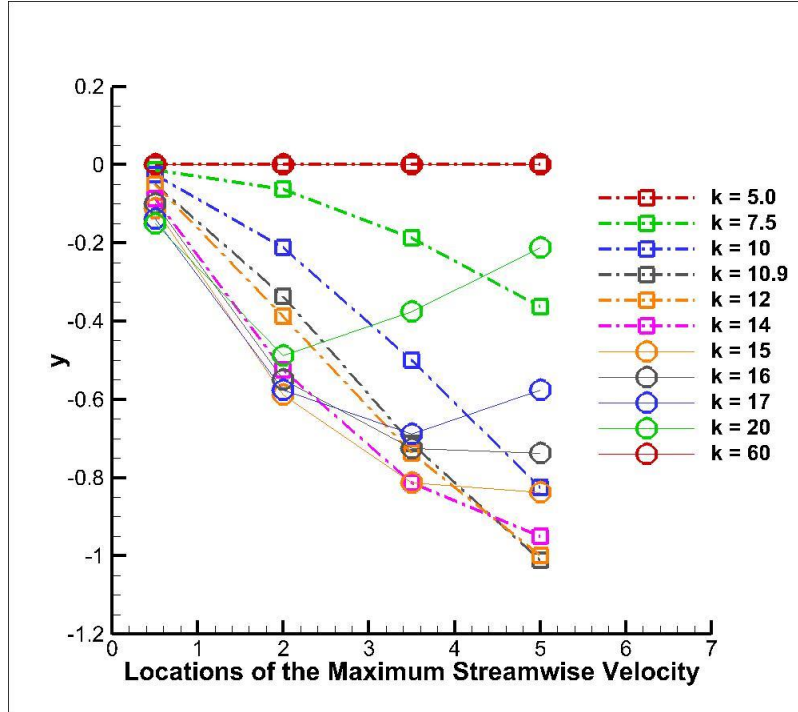


Figure 5-13 Deflection trends of the cases of $V_p = 1.2$ and $Re = 500$ at different reduced frequencies and amplitudes

In the current study, the trend of change of the deflection from the trailing edge of the airfoil to the far wake field is represented by the cross-flow locations of the maximum streamwise velocities in the wake. It is very similar to the idea of the deflection angle used in the previous studies^{15, 16, 20, 157}.

The onset of the asymmetric wake and the formation of the deflected wake were areas of concentration for most previous studies^{7, 10-12, 15, 17, 18, 20, 156}. Few of them investigated the variation process of the deflected wake at different downstream locations. In this study, cases with different frequencies and amplitudes restricted to a fixed Strouhal number of 1.2 were first simulated. It is shown in Fig. 5-13 that the deflection of the wake keeps enlarging as the heaving frequency goes from a very low value ($k = 5.0$) to a moderate number ($k = 15$ for the near wake region and $k = 10.9$ for the far wake region), and then decreases monotonously to zero. It not only confirms a conclusion made by

earlier studies^{7, 12, 17, 18, 20} that the asymmetric wake only occurs at moderate heaving frequencies and amplitudes, but also evidently exhibits that a maximum deflection exists at a reduced frequency value for a fixed Strouhal number. Furthermore, it illustrates that the deflection initially increases swiftly with the frequency in both the near wake (i.e. $x = 0.5$ markers) and far wake regions (i.e. $x = 5$ markers) once the onset of the asymmetric wake occurs in the low frequency range (i.e. $k = 7.5$). Then, the far wake deflection angle firstly starts to decrease with the increment of frequency (i.e. from $k = 12$ to $k = 15$), although the near wake deflection, in the meanwhile, is still amplified with the increase of frequency and about to reach its peak value (i.e. at $k = 15$). Later, as the heaving frequency continues to increase, the near wake deflection eventually begins to decline until a symmetric wake reappears at a very high frequency (i.e. $k = 60$). A similar trend has been reported in Ref.¹² that, for a fixed Strouhal number, the symmetric wake appears at very small reduced frequencies and reappears at very large ones; in between, asymmetric wakes show up at moderate reduced frequency. It can also be observed from Fig. 5-13 that the wake deflection downstream of a heaving airfoil develops faster as well as vanishes earlier in the far wake than in the near wake. The fact that the deflection increases faster with the increasing frequency in the far wake region at relatively low frequencies is not difficult to explain, as vortices shed from the airfoil need a certain distance to fully develop from zero deflection at the airfoil trailing edge to a non-zero deflection.

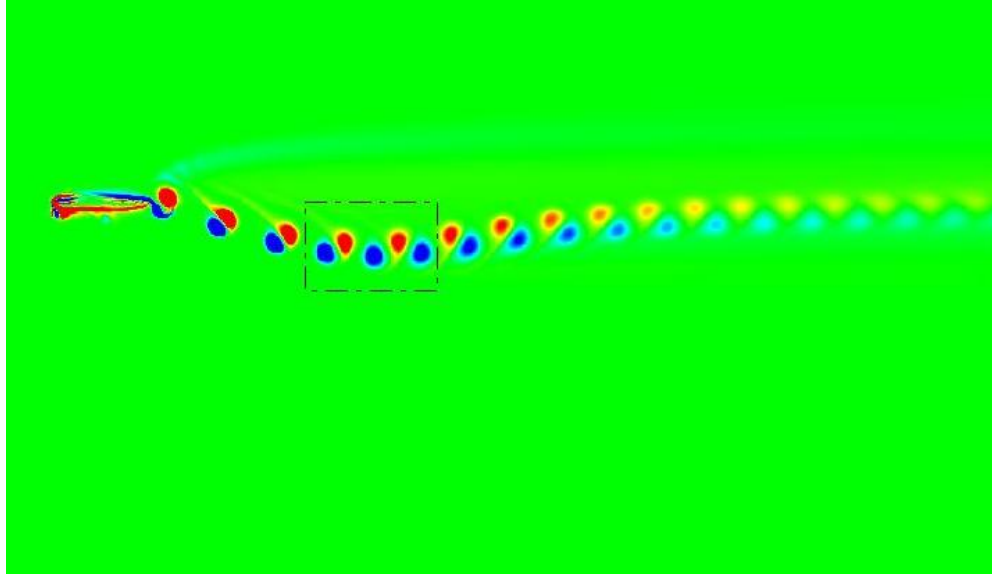


Figure 5-14 Vorticity contours of the case with $V_p = 1.2$, $k = 20$, and $Re = 500$

However, the reason that the far wake deflection starts to decrease when the heaving frequency further increases is a little more complicated. The vortex pairing mechanism in the far wake, although different from that in the near wake, is again recognized as the key reason in the current study. The relationship of the vortex pairing mechanism and formation of the asymmetric wake was discussed in the literature^{17, 18, 20}. However, only vortex pairs in the near wake region have been investigated carefully. Fig. 5-14 shows that, in the near wake, the two counter-rotating vortices in a vortex dipole stay close to each other, while the distance between the neighboring vortex dipoles is relatively large. This type of vortex pairing pattern triggers the formation of the asymmetric wake downstream of the heaving airfoil. The two proximal counter-rotating vortices, in the near wake region of Fig. 5-14, can be simply considered as an isolated vortex dipole, which results in a downward dipole velocity; it implies a downward deflection. The deflection in the far wake region, however, is much less than that in the near wake region. In Fig. 5-14, in the region located about two chord lengths from the airfoil trailing edge,

the characteristic vortex pairing pattern that evokes the asymmetric wake disappears. Alternatively, an opposite vortex pairing pattern (a counter-clockwise vortex closely followed by a clockwise vortex) emerges (see the dash-dot box in Fig. 5-14), which turns the downward deflected wake back to upward in the far wake region. A similar phenomenon has been recorded in Ref.¹⁵⁸. However, the vortices are extensively dissipated before the switch of the vortex pattern in their experiments. To our knowledge, the current study is the first to document clear views of vortex switching. The reason that initiates the swap of vortex patterns will be discussed in a quantitative sense later. Interestingly, among all the cases in the current study, only a maximum of one time switching is observed (and some cases have none). This is because of the low Reynolds number in the studied cases so that the vortices dissipate quickly after just one switch and are not able to maintain sufficient strength to make another one.

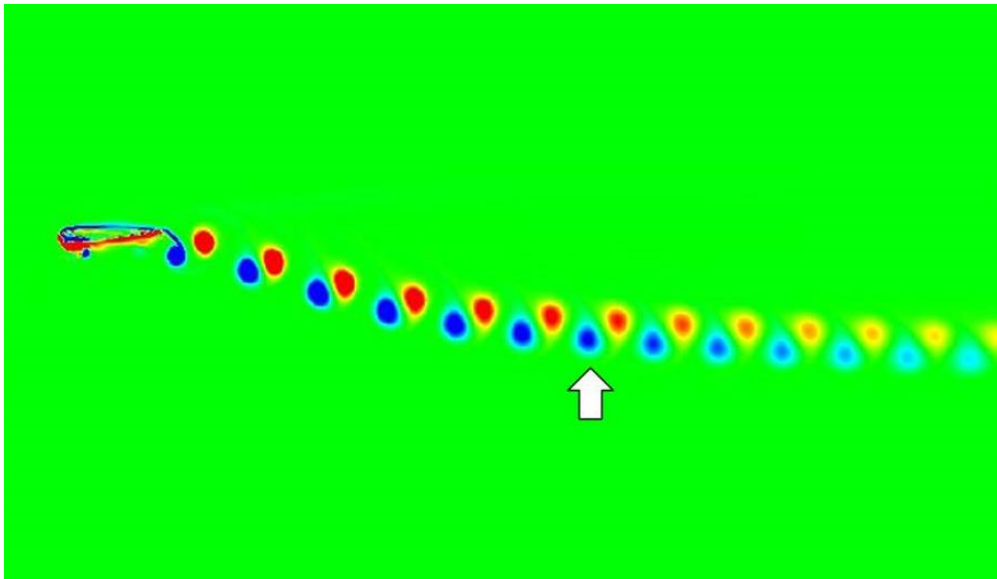


Figure 5-15 Vorticity contours of the case with $V_p = 1.2$, $k = 14$, and $Re = 500$ at the end of an upstroke. The contour color range is from -20 to 20.

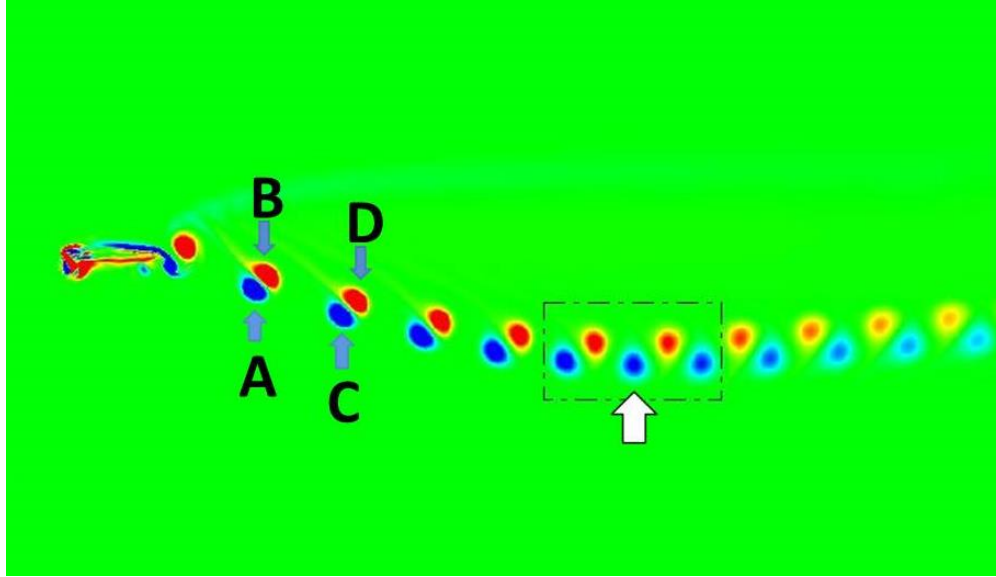


Figure 5-16 Vorticity contours of the case with $V_p = 1.3$, $k = 14$ and $Re = 500$.

The dissipation of vortices may also be the reason that the cases with a low heaving frequency do not show any switch of the vortex pattern. By comparing Fig. 5-15 against Fig. 5-14, the lower frequency case in Fig. 5-15 exhibits fewer vortices in the wake, which prolongs the distance for the vortices to possibly trigger the switch. If their strengths have already dissipated before reaching the condition for the pattern switch, the switch may not be activated. When there is no switch, the wake of the far wake region is nevertheless deflected less than the wake of the near wake region. Another example to demonstrate the relationship between the vortex strength and the vortex-pattern switch is seen by comparing Fig. 5-15 with Fig. 5-16. Fig. 5-16 is a case for a slightly higher Strouhal number ($V_p = 1.3$) with the same heaving frequency. The same heaving frequency ensures that the number of vortices in the wake is about the same for these two cases. The larger Strouhal number results in larger heaving amplitude, which indicates stronger vortices generated at the trailing edge of the airfoil in Fig. 5-16. A vortex-pattern switch apparently occurs in Fig. 5-16 (the dash-dot box in Fig. 5-16). The stronger

vortices in the case of $V_p = 1.3$ dissipate relatively more slowly and trigger the switch at the 12th vortex (the white arrow in Fig. 5-16). It is shown that the 13th vortex in Fig. 5-16 is much stronger than the one in Fig. 5-16 (the white arrow in Fig. 5-16). Hence, there is a switch with $V_p = 1.3$, but no switch with $V_p = 1.2$.

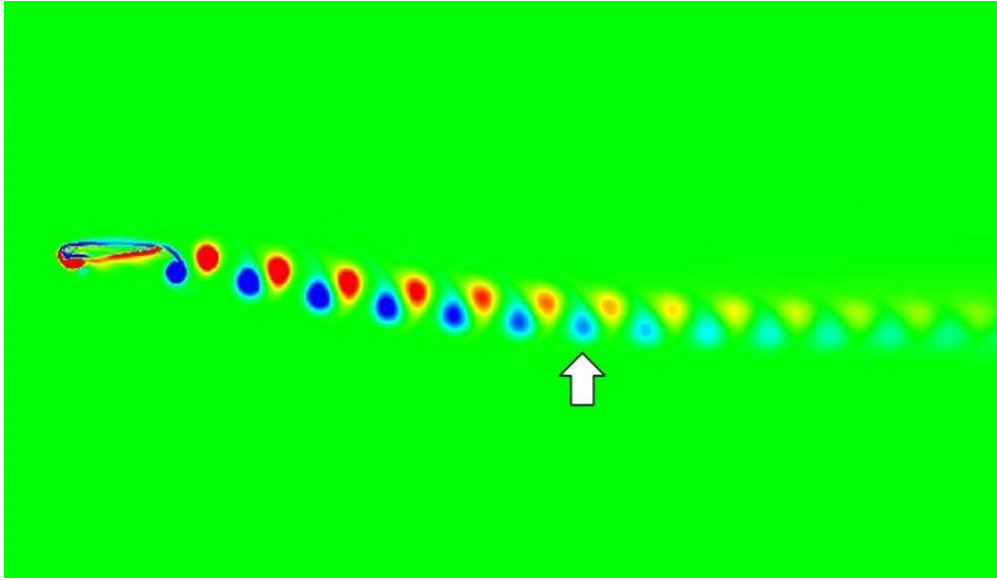


Figure 5-17 Vorticity contours of the case with $V_p = 1.3$, $k = 14$, and $Re = 300$ at the end of an upstroke.

It is noted that the Reynolds number has a strong influence on the vortex strength and its dissipation. Similar to the effect of the Strouhal number, the weaker vortices in Fig. 5-17 with the lower Reynolds number dissipate relatively faster than vortices with the higher Reynolds number in Fig. 5-16. The 12th vortex in the low Reynolds-number case (the white arrow in Fig. 5-17) is much weaker than the one in Fig. 5-16. Consequently, the vortex-pattern switch occurs with $Re = 500$ in Fig. 5-16, but not with $Re = 300$ in Fig. 5-17.

5.4.1 The Cross-flow Effective Phase Velocity

To quantitatively reveal the factors inducing the vortex-pattern switch, a model based on the vortex dipole analysis, which is in light of the method of Godoy-Diana¹⁷ and Zheng & Wei²⁰, has been further developed. Here, a cross-flow effective phase velocity of a vortex dipole is defined as

$$U_p^* = U_{\text{dipole}} \sin \alpha - V_{\text{phase}} \quad (5.4)$$

where

$$U_{\text{dipole}} = \frac{\Gamma_{\text{avg}}}{2\pi\xi} \quad (5.5)$$

Following the concept originally introduced by Godoy-Diana *et al.*¹⁷, the “symmetrizing” effect of the subsequent vortices on the target vortex dipole, which is represented by the effective phase velocity, is still the key factor. However, the effective phase velocity defined in Eq. (5.4) only considers the effect that is projected to the cross-flow direction rather than to the direction of the vortex-dipole velocity as in Godoy-Diana¹⁷ and Zheng & Wei²⁰. In their studies, for the purpose of discussing the onset of wake deflection, the criterion based on the effective phase velocity projected to the direction of the vortex-dipole velocity can also be considered as a criterion based on the effective phase velocity projected to the streamwise direction. However, the purpose of the present study is to quantify the magnitude of the local deflection of an already-formed asymmetric wake. Therefore, the effective phase velocity used for the criterion in the current case needs to be projected to the cross-flow direction, which is the direction of the

local deflection. The terms representing the dipole phase velocity in the streamwise direction and the free stream velocity in the previous studies^{17, 20} are not included in Eq. (5.4) because their projections in the cross-flow direction are zero. It will be shown later that the effective phase velocity in the cross-flow direction provides an effective quantitative criterion to indicate the switching of the vortex wake deflection direction.

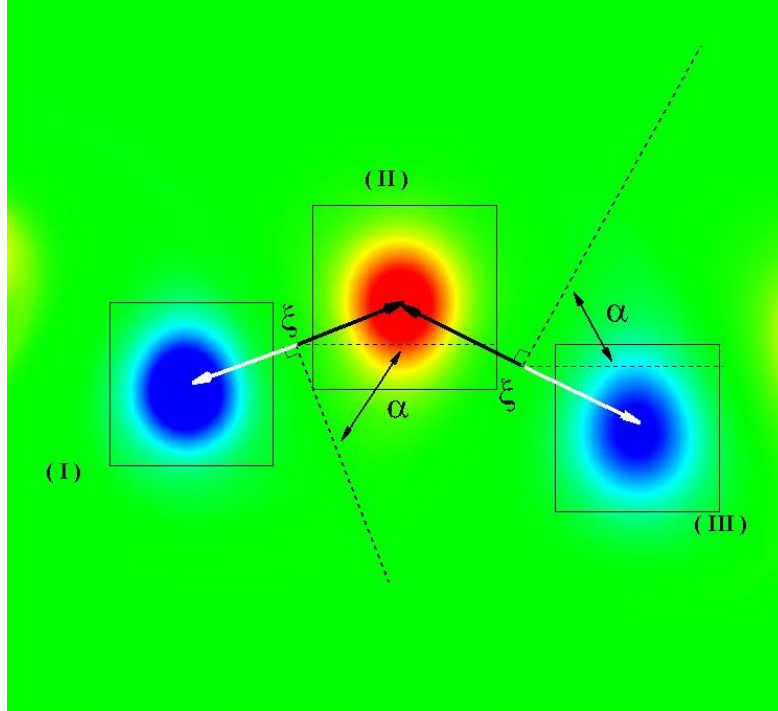


Figure 5-18 Schematic view of parameters used in calculating the effective phase velocities

The method to obtain the circulation of each vortex in Godoy *et al.*¹⁷ has been implemented in the current study. More detailed procedures can be found in Zheng & Wei²⁰. The approach to measure the dipole velocity angle, α , is illustrated in Fig. 5-18. Without losing generality, we consider only the cases with downward deflected wakes in the near wake region, as the upward deflected wakes can be discussed in a vice-versa way. In Fig. 5-16, the vortex dipole carrying a self-induced velocity towards the downward direction, i.e. the vortex pair with vortices “A” and “B”, act as the symmetry-breaking

vortex dipole. Conversely, the vortex dipole having an upward self-induced velocity, i.e. the vortex pair with vortices “B” and “C” in Fig. 5-16, behaves like the symmetry-holding one. Zheng & Wei²⁰ suggested that the difference in the effective phase velocity between these two consecutive vortex dipoles indicates the trend of the deflection. In other words, the competition of the effective phase velocity between the symmetry-breaking and symmetry-holding dipoles determines the local deflection of the wake. Nonetheless, only the near-wake deflection of the heaving airfoil has been deliberately explained in Zheng & Wei²⁰ since only the behaviors of vortex dipoles in the near wake region were investigated.

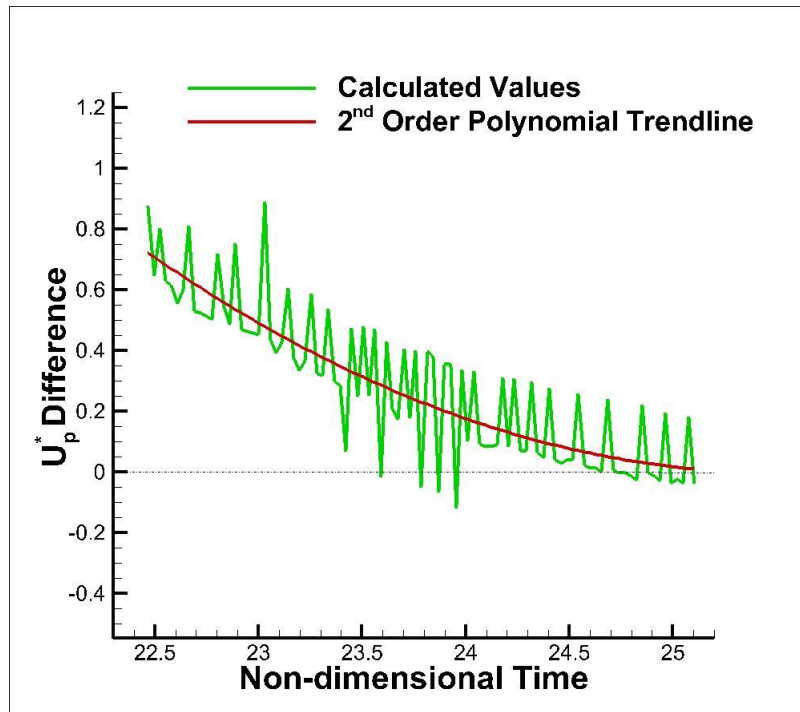


Figure 5-19 The history of the difference of the effective phase velocity of two consecutive vortex dipoles in the case of $V_p = 1.3$, $k = 14$, $Re = 500$ along with a 2nd-order polynomial fitting curve.

In the interest of unfolding the mechanisms of the wake deflection pattern switching, the approach in Zheng & Wei²⁰ is extended to record the histories of the effective-phase-

velocity difference while these two vortex dipoles (“A&B” and “B&C” in Fig. 5-16) travel from the near wake to the far wake. This difference at each instant represents the moving trend of these two consecutive vortex dipoles at that moment. If the effective phase velocity of the symmetry-breaking dipole is larger than that of the symmetry-holding dipole at a certain moment, these two consecutive vortex dipoles are inclined to follow the near wake deflection direction and keep moving away from the mean position of the heaving airfoil. On the other hand, if the symmetry-breaking dipole has a smaller effective phase velocity than the symmetry-holding dipole, this vortex pattern has the tendency to break the near wake deflection trend and move upwards.

Fig. 5-19 shows the history of the difference of the effective phase velocity between the two consecutive vortex dipoles in the case of $V_p = 1.3$, $k = 14$, and $Re = 500$, with the vorticity contours for this case already shown in Fig. 5-16. The difference of the effective phase velocity is a subtraction of the effective phase velocity of the vortex dipole “B&C” from that of “A&B”.

It is readily seen in Fig. 5-19 that the 2nd-order polynomial fitting curve captures the primary trend of the changing difference of the effective phase velocity over the time and smoothes out the noise generated in the unsteady simulation and post-processing during the calculation of the effective phase velocity. For this reason, fitted curves of the histories of effective-phase-velocity difference are selected hereafter for determining the deflection tendency. We call these fitted curves “trend lines” for this study. The trend line in Fig. 5-19 shows that the difference of the effective phase velocity between the two consecutive vortex dipoles reduces as they travel towards the far wake. In particular, the difference of the effective phase velocity begins to have negative values around $t = 24.7$,

when the three pertaining vortices (A, B and C) reach the deflection switching region (marked as the dash-dot box in Fig. 5-16). As the time goes on, the difference of the effective phase velocity tends to be more negative. This proves the fact that the two consecutive vortex dipoles tend to change their moving direction to cause a local deflection switch inside the region of the dash-dot box in Fig. 5-16. Therefore, the difference of the effective phase velocity is recognized as an indicator of deflection switching. In what follows, we will reveal the mechanisms that cause such a change in the difference of the effective phase velocity over time in the wake.

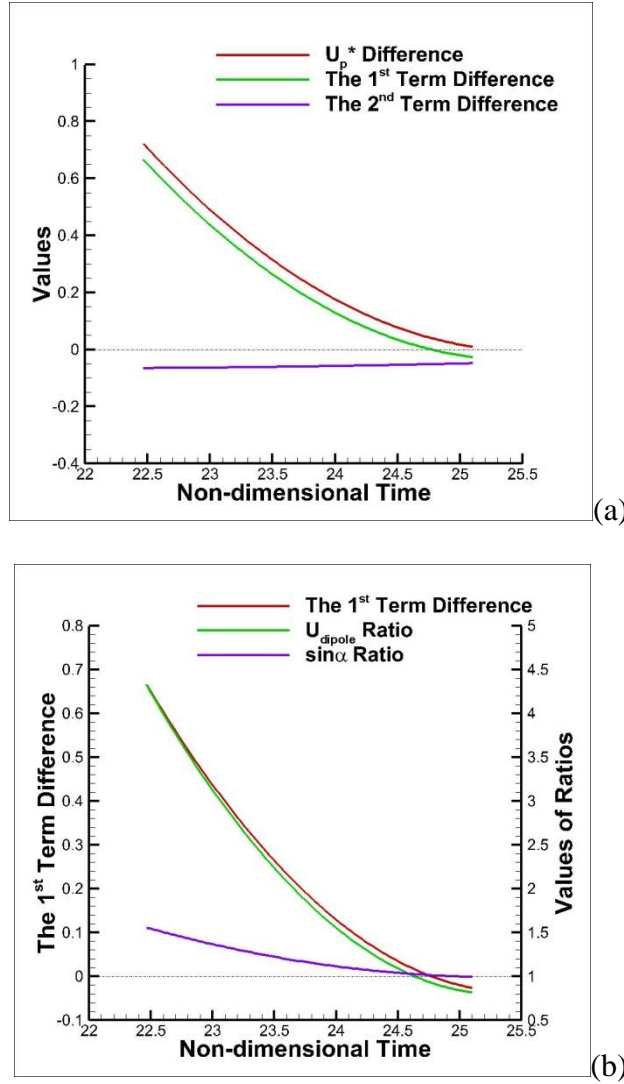


Figure 5-20 Trend lines illustrating (a) the effect of the two terms in Eq. (5.4)
 1st term: $U_{dipole} \sin \alpha$; 2nd term: $(-V_{phase})$;
 (b) individual effects of U_{dipole} and $\sin \alpha$ ratio on the difference of the 1st term in Eq. (5.4).

The details are actually in the individual effects of each of the two terms in Eq. (5.4). Fig. 5-20(a) evidently illustrates that the effective-phase-velocity difference due to the 1st term of Eq. (5.4) plays the dominant role. The curve of the difference of the 1st term has almost the same shape as the curve of the effective-phase-velocity difference; the discrepancy between these two curves is nearly a constant, which is the contribution from the difference of the vortex phase velocity in the cross-flow direction. Additionally, the

individual effects of the self-induced dipole velocity and $\sin\alpha$ in the 1st term of Eq. (5.4) have been separated and plotted in Fig. 5-20(b). Since the 1st term in Eq. (5.4) is a production of self-induced dipole velocity and $\sin\alpha$, the ratios of these two quantities between the two dipoles are used to facilitate the discussion. The ratio of a quantity is defined as the ratio between the quantity of the dipole “A&B” and that of the dipole “B&C” in Fig. 5-16. It is noticed in Fig. 5-20(b) that the effect of U_{dipole} , which symbolizes the difference of the self-induced dipole velocities between the symmetry-breaking and symmetry-holding vortex dipoles, is the primary driving factor for the variation of the 1st term in Eq. (5.4).

Consequently, it can be concluded that the change in the difference of the effective phase velocity between the two consecutive vortex dipoles is mainly due to the difference of their self-induced dipole velocity. In the following two sections, we will first discuss the change in the self-induced dipole velocity from the near wake to the far wake and then comment on the minor factor of the dipole angle, α .

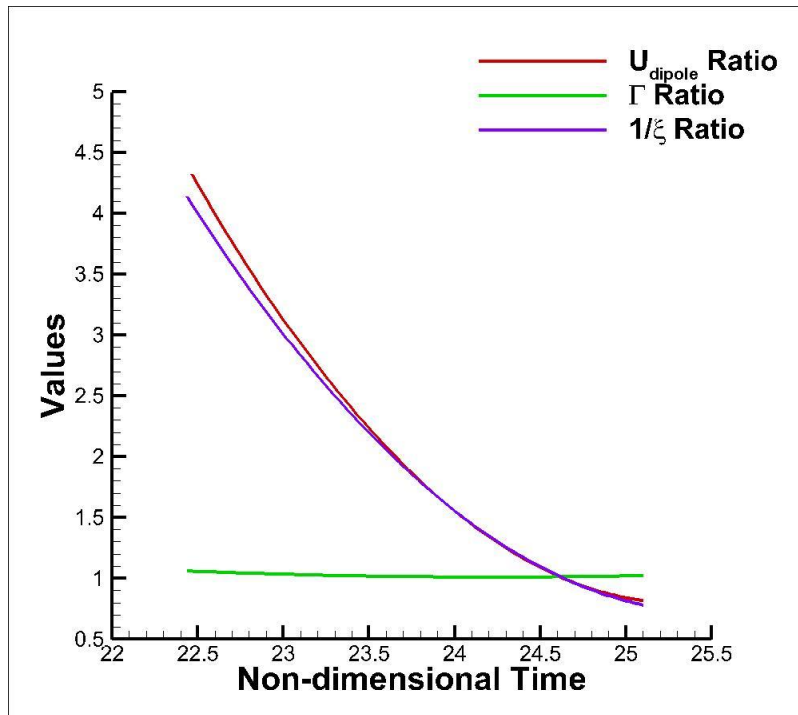


Figure 5-21 Individual effects of Γ ratio and $1/\xi$ ratio on the ratio of dipole velocity

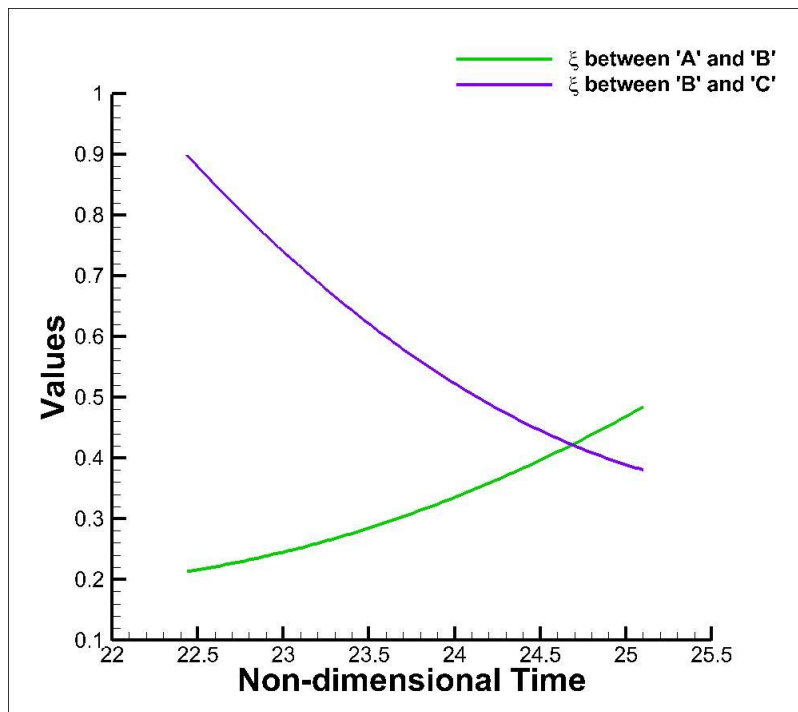


Figure 5-22 Comparisons of the histories of ξ

5.4.2 The Change of the Self-Induced Dipole Velocity

A further question is what leads to the change in the difference of dipole velocities in the far wake. As the Biot-Savart law shows in Eq. (5.5), the dipole velocity is obtained by dividing the vortex strength by the distance between the two vortices in the dipole. Therefore, the ratios of these two quantities between the two successive dipoles are plotted in Fig. 5-21, which are similar to the plots in Fig. 5-10. Fig. 5-11 exhibits that the vortex dipoles with “A&B” and “B&C” have almost the same average dipole strength all the time. However, there is a significant drop of the $1/\xi$ -ratio that obviously results in the reduction of the ratio of the dipole velocity. Fig. 5-22 illustrates the history of the two ξ 's. The ξ between vortices “A” and “B” starts with a very small value when these two vortices just detach from the trailing edge of the airfoil, and it keeps increasing as these two vortices travel farther downstream. The ξ between vortices “B” and “C” has a reversed trend: it has a very large initial value when vortices “B” and “C” are in the near wake and continue to decrease as the vortices move far downstream. The two ξ values of “A&B” and “B&C” reach an identical value around $t = 24.7$. The same phenomenon can also be qualitatively observed in Fig. 5-16. The distance between the vortices of dipole “A&B” is apparently shorter than that between the vortices of dipole “B&C” in the near wake. In the far wake region, near where the dash-dot line box is indicated, the distances between any two consecutive vortices among three vortices of the two dipoles become approximately the same.

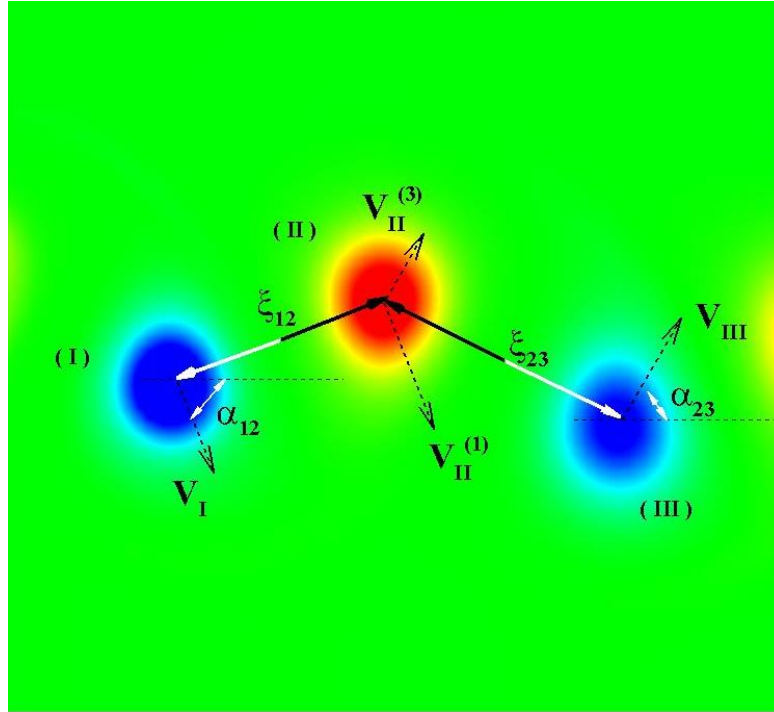


Figure 5-23 Schematic view of parameters for calculating the Biot-Savart induced velocities

The final questions are what causes the change of the distance between the two vortices in a dipole, and why does the size of the symmetry-breaking dipole increase as it travels from the near wake to the far wake while the size of the symmetry-holding dipole is decreasing during the time? To answer these two questions we start by looking at the influence of each individual vortex on other vortices in the vicinity based upon the Biot-Savart law. For example, V_I in Fig. 5-23 is the induced velocity by vortex “II”, and it tends to move vortex “I” to the direction of “ V_I ” in an infinitesimal time Δt . After this infinitesimal time, the expected location of the center of vortex “I”, as shown in the dash-dot-dot circle in Fig. 5-24, can be calculated based upon the location of vortex “I” at the current moment and $V_I \Delta t$. A similar procedure can be applied to vortex “II” and vortex “III”. It should be noted that vortex “II” has two induced velocities – one is due to vortex “I” and the other is vortex “III”.

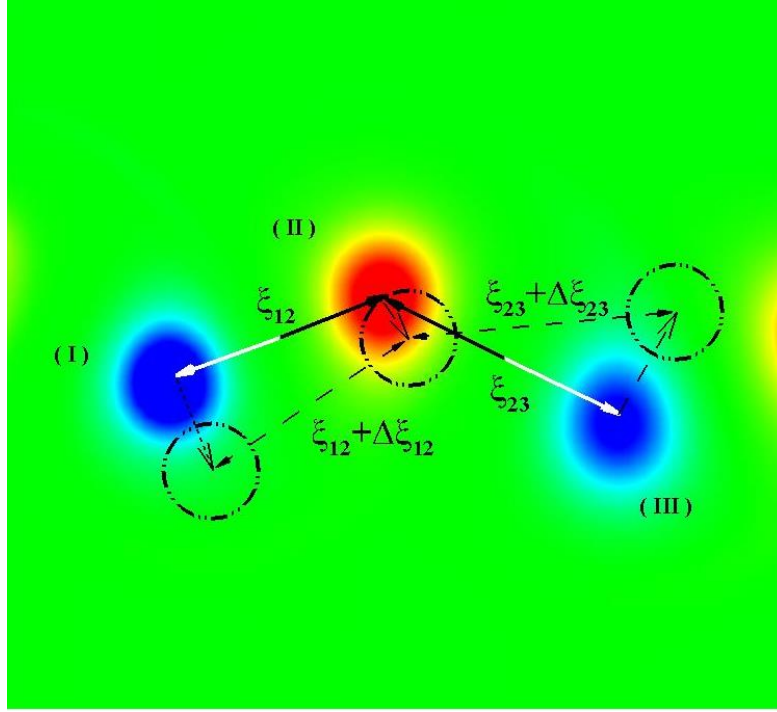


Figure 5-24 Expected locations of vortices based on the Biot-Savart law

The fact that no other vortices need to be considered will be carefully discussed at the end of this section. Moreover, for simplicity, the influence from vortex “III” on vortex “I” is neglected, since the distance between these two vortices is large enough that the induced velocity is negligible. After the expected locations of vortices “I”, “II” and “III” are obtained, as shown in Fig. 5-24, the expected distances between the two vortices in a dipole can be calculated. Then the change of this distance, $\Delta\zeta$, can be determined by the difference between the expected ζ and the original ζ obtained by the numerical simulation. This $\Delta\zeta$ indicates a predicted tendency of the change of ζ in the dipole. A positive $\Delta\zeta$ means the distance between the two vortices in the dipole is expected to be increasing and the two vortices tend to get away from each other, and vice-versa. The vortices “A”, “B” and “C” in Fig. 5-16 are denoted as vortices “I”, “II” and “III” in the Biot-Savart law described in Fig. 5-23. It is noted that Fig. 5-23 illustrates a general vortex model rather

than specifically only for vortices “A”, “B”, and “C” in Fig. 5-16, the notations in Fig. 5-24 are different from that in Fig. 5-16. (This same statement also applies to Fig. 5-18, which indicates a general definition rather than what is shown in Fig. 5-16).

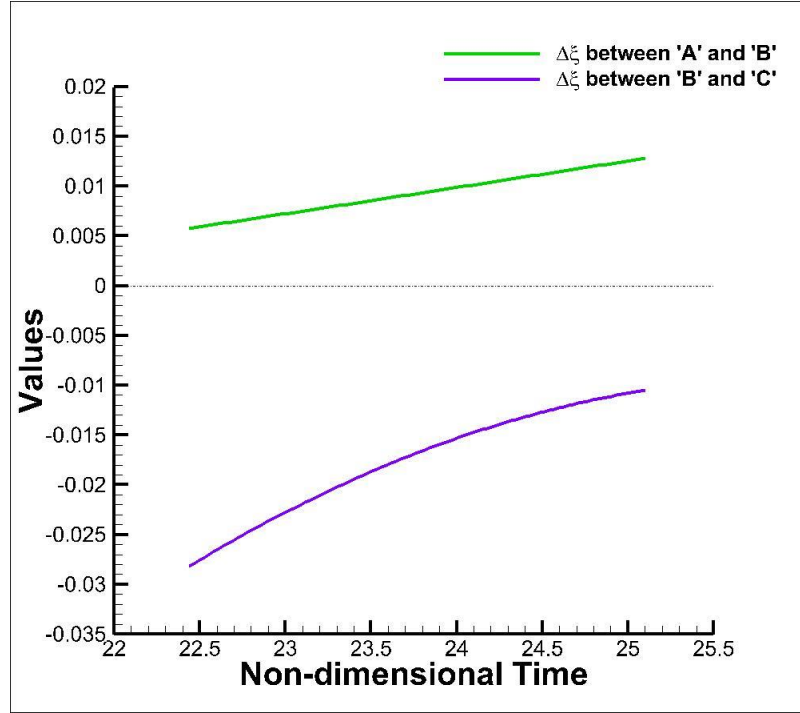


Figure 5-25 Histories of $\Delta\xi$ of the two consecutive dipoles

Fig. 5-25 shows that $\Delta\xi$ in dipole “A&B” is always positive, which explains why ξ of dipole “A&B” in Fig. 5-22 keeps increasing. In addition, the value of $\Delta\xi$ keeps growing over the time in Fig. 5-25, which confirms that the rate of change of ξ of “A&B”, in Fig. 5-22, is getting larger. On the other hand, for $\Delta\xi$ of dipole “B&C”, Fig. 5-25 shows its value is always negative. This explains why ξ of dipole “B&C”, in Fig. 5-22, remains decreasing. Likewise, the magnitude of $\Delta\xi$ of “B&C” decreases with time, providing the reason why the rate of change of ξ of “B&C”, in Fig. 5-22, is getting smaller over the time. Another interesting phenomenon is that the magnitude of $\Delta\xi$ of “B&C” is larger than that of “A&B” at the beginning in Fig. 5-24 ($t = 22.5$). This means that the rate of ξ

decrease of “B&C” is larger than the rate of ζ increase of “A&B”, a phenomenon also shown in Fig. 5-22. It is worth noticing that the vortex model described in Figs. 5-23 and 5-24 can theoretically predict the motion of vortices described in these two figures and the trend is consistent with that shown in Fig. 5-25; details can be found in the Appendix IV.

Now, we come back to explain why the effect of other vortices is excluded. If the vortices are far away from the considered unit (the two vortex dipoles of “A&B” and “B&C”), their effect can be neglected because of the reciprocal-distance influence of the Biot-Savart law. There are two neighboring positive vortices whose effect has been neglected: one near the right boundary of the considered unit and the other near its left boundary in Fig. 5-16. Here we discuss the effect of the one near the right boundary, vortex “D”, and the one near the left boundary can be discussed in the same way. If the effect of vortex “D” is involved in calculating the expected location of the center of vortex “C”, vortex “D” will actually push “C” away from “D”, because the structure combining “C” and “D” is very similar to dipole “A&B”. Fig. 5-24 has already exhibited that such a pattern between vortices “A” and “B” causes them to push each other away. Therefore, the effect of vortex “D” on vortex “C” actually reinforces the effect of vortex “B” on vortex “C” since vortex “B” tends to attract vortex “C” moving towards vortex “B”. Consequently, the effect of vortex “D” on vortex “C” does not change the way that vortex “C” moves in the original discussion. Therefore, for simplicity and the purpose of understanding the trend, the effect of vortex “D” can be excluded when calculating the expected location of the center of vortex “C”. The same reason can be applied to the

calculation of the expected position of vortex “A” involving a positive vortex near the left boundary of the considered unit.

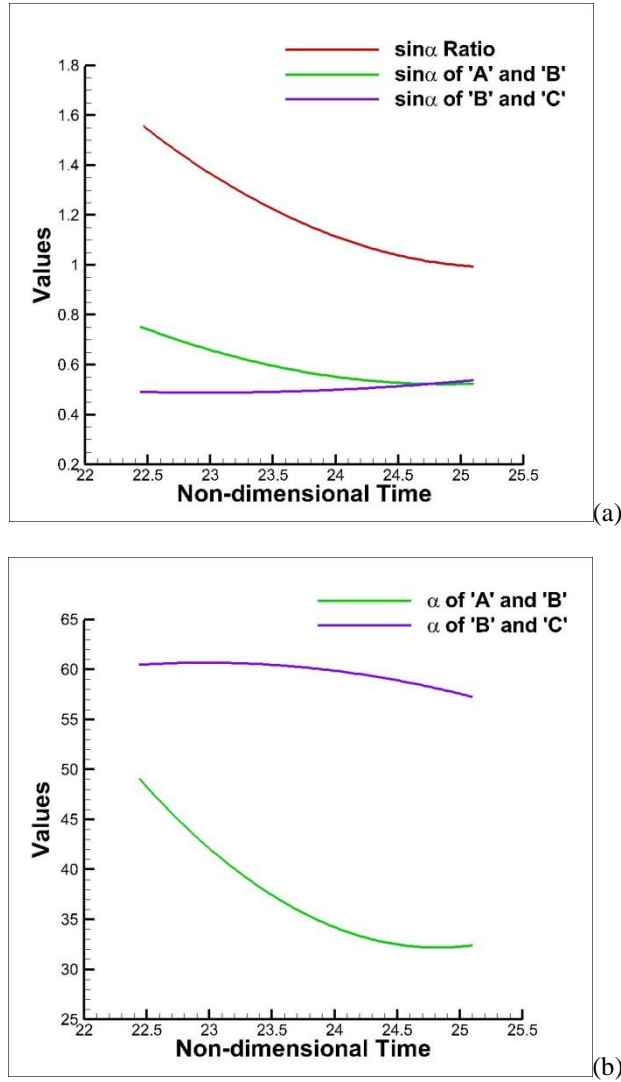


Figure 5-26 (a) The individual effect of $\sin \alpha$ of 'A&B' and 'B&C' (b) Comparisons of α between 'A&B' and 'B&C'

5.4.3 The Effect of the Dipole Angle, α

As is plotted in Fig. 5-20(b) and mentioned previously, the change of ratio of $\sin \alpha$ has some minor contributions to the variation of the 1st term in Eq. (5.4). Fig. 5-26(a) shows

that the change of $\sin\alpha$ over time is primarily due to the change of $\sin\alpha$ of “A&B”. The variation of that of “B&C” is very small. This is also confirmed by Fig.5-26 (b). In order to investigate the physics behind the change of α of “A&B” over time, the Biot-Savart law has been employed here again.

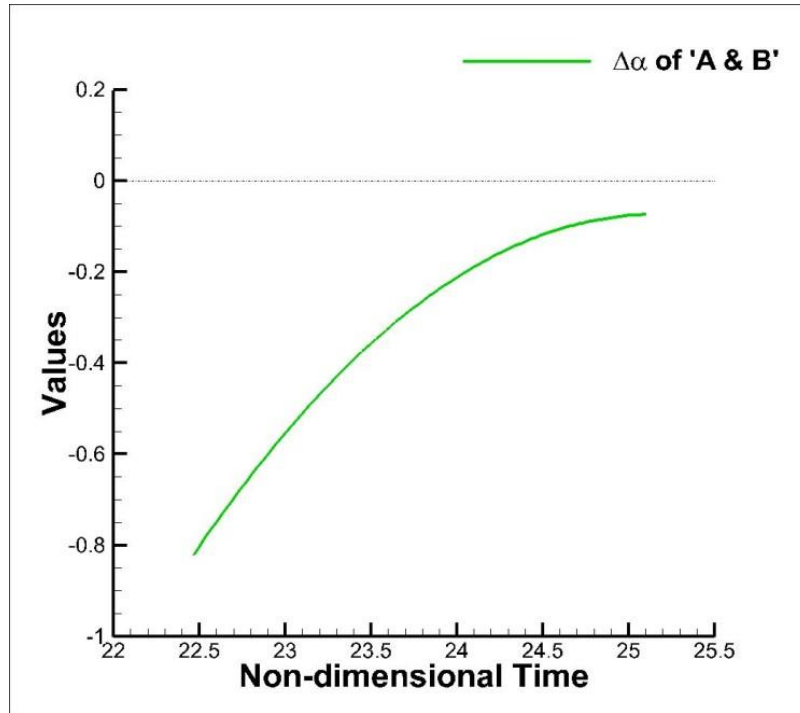


Figure 5-27 Histories of $\Delta\alpha$ of “A” and “B” predicted by the Biot-Savart Law

Fig. 4-27 shows that $\Delta\alpha$ of “A&B” is always negative. Therefore, the angle of dipole “A&B” is expected to decrease with time, which is consistent with what Fig. 5-26(b) exhibits. In addition, the magnitude of the $\Delta\alpha$ of “A&B” decreases with time, which is also shown in Fig. 5-26(b) that the slope of the curve of α of “A&B” reduces as the vortices propagate from the near wake to the far wake. Since the change of α has the opposite tendency from the change of ζ , it therefore further enhances the change of the effective phase velocity, because the 1st term of Eq. (5.4) is proportional to $\sin\alpha/\zeta$.

5.5 Summary of the Far Wake Deflection and Vortex Switching

Asymmetric vortical wakes downstream of a two-dimensional heaving airfoil have been studied numerically. The results confirm that a heaving airfoil with an extremely high amplitude or frequency does not produce asymmetric wakes. A switch of vortex pairing patterns was found to be the key factor that reduces the asymmetry of the vortex wake in the cases of high heaving frequencies or amplitudes. Due to this type of vortex pattern switching, the deflection trend develops faster but disappears earlier in the far wake than in the near wake as the frequency increases at a fixed Strouhal number. The vortex strength and its dissipation were revealed to be the primary reason why the switch of the vortex pattern only occurs in the cases with a relatively high Strouhal number or a high Reynolds number.

The mechanisms of the switch of the vortex pairing pattern were carefully investigated by a vortex dipole model. This model is different from that in Godoy-Diana *et al.*²²⁰ in the sense that the cross-flow effective phase velocity was introduced to analyze the already-formed asymmetric wake behind the airfoil. The change of the distance between the vortices was the key factor leading to the toggle condition of the switching in the far wake. The change of the angle of U_{dipole} enhanced the effect of the change in the distance between the vortices to cause switching of the vortex pattern. A vortex dynamics model based on the Biot-Savart law was employed to support the argument that the distance between the vortices and the angle of U_{dipole} vary from the near wake to the far wake. The theoretically predicted trends of the change for these two quantities were consistent with the numerical simulation results. Furthermore, the changing orientation of the vortex-

dipole self-induced velocity also enhances the effect of the changing distance between the vortices on the switch of the vortex pattern.

6 Energy Harvesting

6.1 Energy Harvesters with Active Heaving/Pitching Motions

This section numerically studies the response of a two-dimensional flapping airfoil in the wake downstream of an oscillating D-shape cylinder. The airfoil has either heaving or pitching motions. The leading edge vortex (LEV) and trailing edge vortex (TEV) of the airfoil are ascertained to be critical to energy harvesting. Two major interaction modes between the airfoil and incoming vortices, the suppressing mode and the reinforcing mode, are identified, which are of pivotal importance to the formation of LEVs and TEVs. However, distinctions exist between the heaving and pitching motion in terms of their contributions to the interaction modes and the efficiency of the energy extraction. A potential theory and related fluid dynamics analysis are developed to quantitatively demonstrate that the topology of the incoming vortices corresponding to the airfoil is the primary factor that determines the interaction modes. Finally, the trade-off between the input and output is discussed. It is found that appropriate operational parameters for the heaving motion are preferable in order to preserve acceptable input power for energy harvesters, while appropriate parameters for the pitching motions are essential to achieve decent output power.

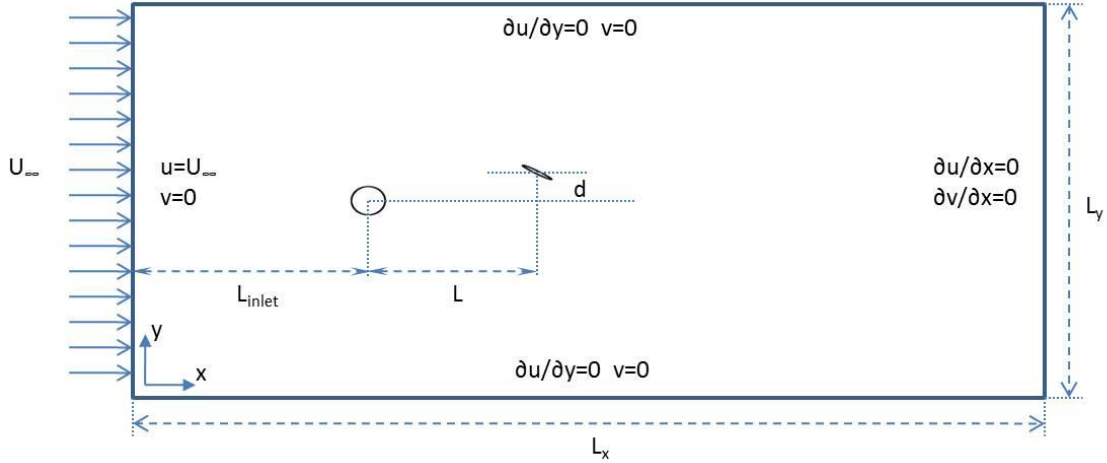


Figure 6-1 Sketch of the configuration of the system of a cylinder and a foil.

The IB scheme has been extensively proved capable of dealing with unsteady flow problems involving single or multiple bodies^{20, 159-161}. It is further validated with the configuration of a circular cylinder and elliptical airfoil, as shown in Fig. 6-1. In the validation case, the diameter of the cylinder is identical to the chord length of the airfoil, and both them are stationary. The angle of attack of the airfoil keeps at 30°, and its streamwise distance from the center of the cylinder is 5-unit lengths. The transverse positions of the airfoil vary at $d = -1, 0$, and 1 , and the Reynolds number remains 500. The comparisons in Fig. 6-2 show good agreements with the results in Ref.¹⁶² for the analysis of histories of forces on the airfoil downstream of the cylinder.

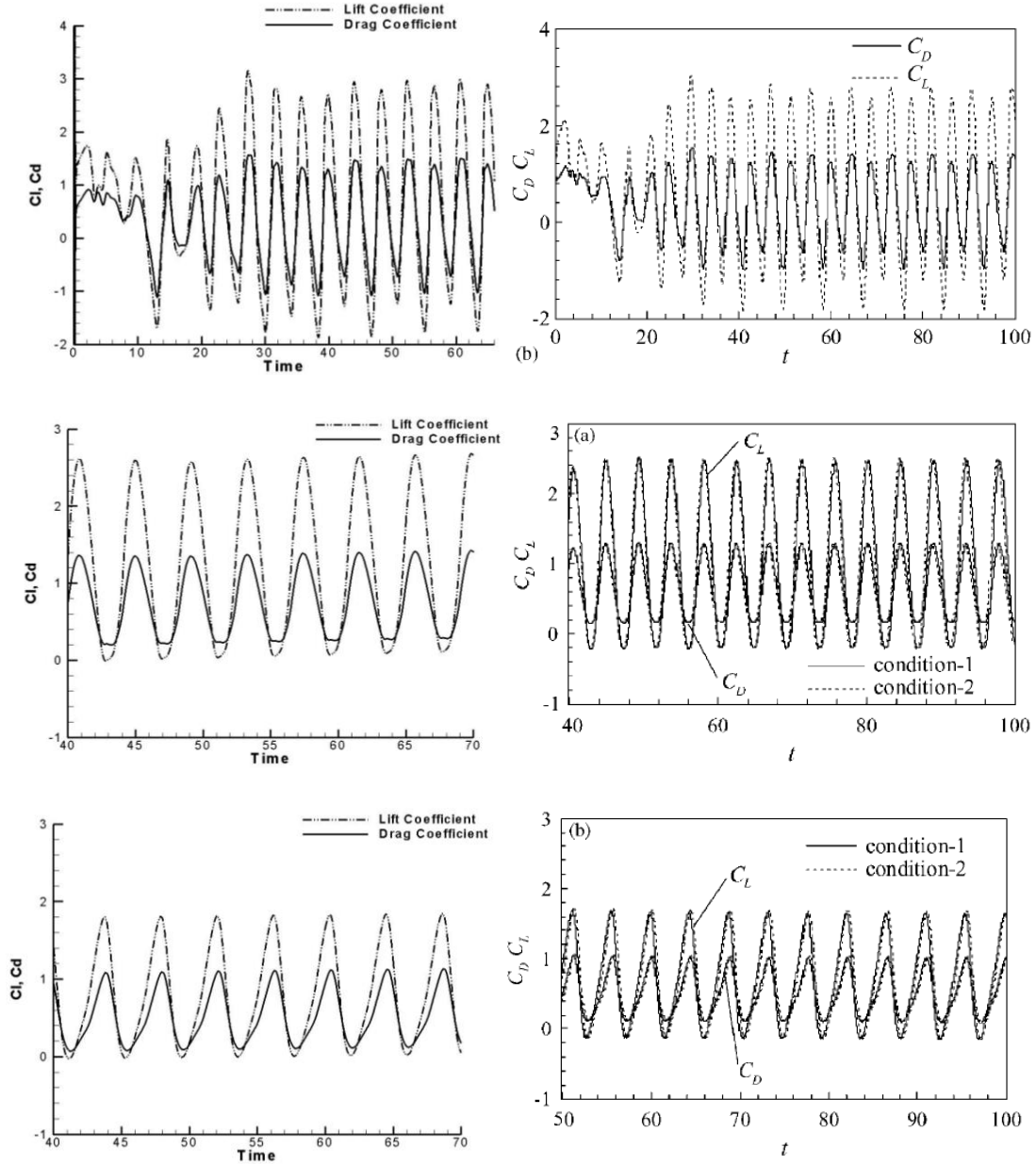


Figure 6-2 Histories of lift and drag coefficients acting on the stationary airfoil at $L = 5$, angle of attack $= 30^\circ$, and $d = 0$ [the 1st row], 1 [the 2nd row], and -1 [the 3rd row]. The left column shows the results from the current simulation, and the right column shows these from Liao et al.¹⁶²

In the following investigation of energy harvesting, as suggested in previous studies^{21, 23, 38, 40, 163} a heaving D-shape cylinder is chosen to be located upstream. Its motion is specified as

$$y_c(t) = h_c \sin(2\pi f_c t) \quad (6.1)$$

where h_c and f are the heaving amplitude and frequency, respectively. Their values are fixed at $h_c = 0.25$ and $f = 0.2$ in order to obtain identical wakes upstream of the airfoil for all the cases. Moreover, an elliptical airfoil with either heaving or pitching motion is used. The heaving motion is defined as

$$y_a(t) = h_a \sin(2\pi f t - \phi) \quad (6.2)$$

and the pitching one is

$$\alpha_a = A_a \sin(2\pi f t - \phi) \quad (6.3)$$

Notice that the frequency of the airfoil for either motion is equal to that of the cylinder, because the resonance between the airfoil and the cylinder is required for good response of energy harvesting^{23, 38}. Moreover, ϕ in Eqs. (6.2) and (6.3) indicates the phase difference between the moving cylinder and the purely heaving/pitching airfoil. The value of ϕ increases from 0° to 360° with an interval of 45°. The h_a is selected as 0.05, 0.1, 0.2, 0.4, 0.8 and A_a are 12.5°, 25°, 60°. The pivoting point in the pitching motion is at half chord and α_a is positive in the clockwise direction. The distance between the airfoil and the cylinder is 7-unit lengths in order to ensure a fully developed vortex street upstream of the airfoil¹⁵⁹. The Reynolds number in all the cases of for the investigation of energy harvesting is fixed at 200.

Following the literature³⁸, the efficiency of the energy extraction is defined as the ratio of average output power, $T_F U_\infty$, and average input power, P_F

$$\eta = \frac{T_F U_\infty}{P_F} \quad (6.4)$$

where T_F is the average thrust force coefficient. The instantaneous input power is

$$P = -L \times \frac{dh_a}{dt} - M \times \frac{d\alpha_a}{dt} \quad (6.5)$$

The moment coefficient, M , is positive in the clockwise direction, which is in the same sign convention as α_a . In the current study, the discussions mostly focus on individual values of input and output power rather than their ratio – the efficiency. Basically, low or negative input power is favorable, so is a high and positive output power.

The computational domain is 25.6×12.8 , and the grid size of 0.0125 is determined to provide an acceptable grid-resolution-independent solution for all computational cases in this study after a careful grid-resolution-convergence check. All mean values of the power presented in this work were averaged over three airfoil oscillation cycles after the simulation results became periodic. In order to explicitly identify primary vortices, the color range of all vorticity contours in this study is from -3 to 3.

6.1.1 Interaction Modes and A Potential-Theory Analysis

In order to expressly investigate the effect of interaction modes between the incoming vortices and the LEVs/TEVs of the airfoil, the distance between the center of the cylinder and the airfoil is fixed, while the phase between the motion of the cylinder and that of the airfoil varies. It has a notable advantage of doing this over changing the distance between the two as in the previous studies¹⁵, because the incoming vortices interacting with the airfoil in all the cases studied here would have similar strengths. Consequently, the

differences in the resultant powers are primarily led by the interaction modes. The relation between the interaction modes and the energy harvesting performance of the airfoil will be deliberately demonstrated in the next section. In the following context of this section, the two primary interaction modes will be illustrated, and a potential-theory analysis that assists to comprehend the onset of the interaction modes is presented here.

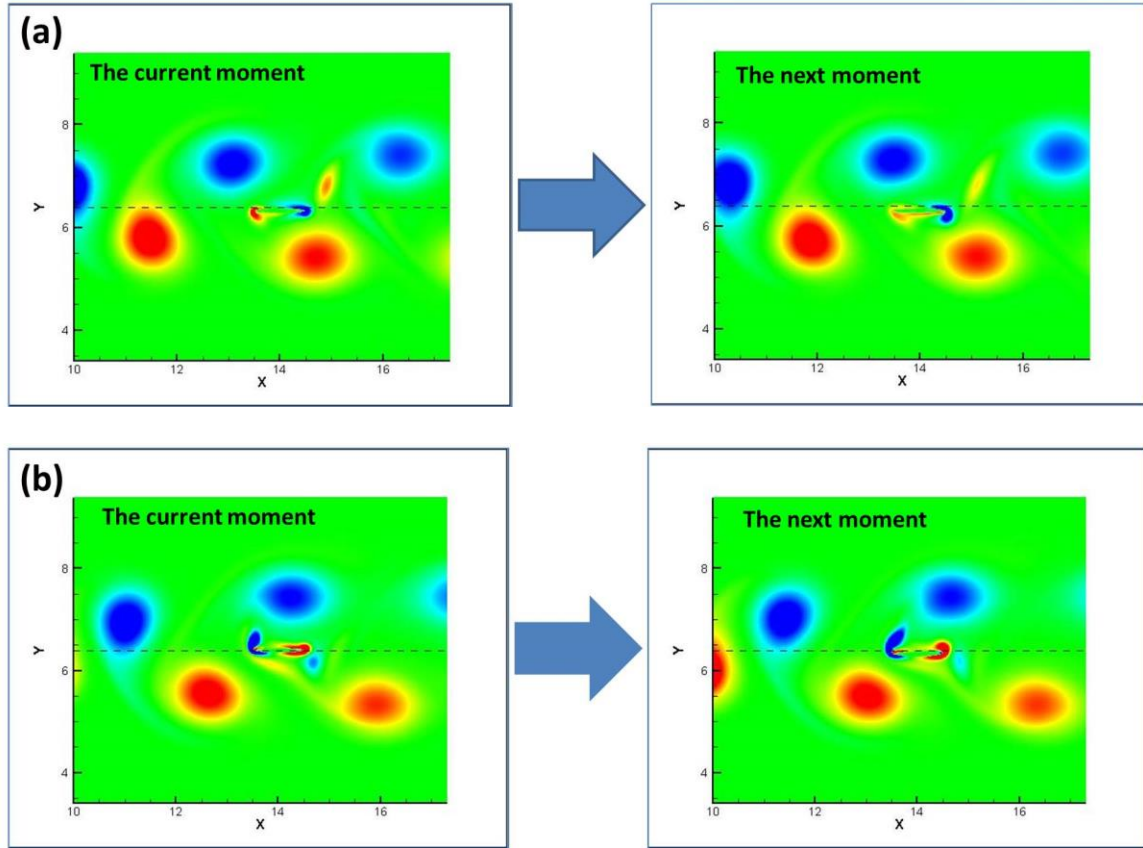


Figure 6-3 (a) The suppressing mode of the LEV occurs in the case of $h_a = 0.1$ and $\phi = 225^\circ$, and (b) The reinforcing mode of the LEV occurs in the case of $h_a = 0.1$ and $\phi = 45^\circ$. A quarter cycle of the airfoil down stroking motion is experienced from “the current moment” to “the next moment” in this figure.

The two primary interaction modes are the suppressing mode and the reinforcing mode. They are possibly formed with either heaving airfoils or pitching ones for the LEV or the TEV. Figure 3 illustrates a pair of typical interaction modes for the LEV observed in the cases with heaving airfoils. In Fig. 3(a), there is an LEV attached to the lower

surface of the airfoil at “the current moment”. The strength of this LEV is apparently reduced in “the next moment” of Fig. 3(a). Therefore, this LEV is suppressed and the suppressing mode of the LEV occurs in Fig. 3(a). In the contrast, the strength of LEV is enhanced from “the current moment” to “the next moment” in Fig. 3(b). In other words, this LEV in Fig. 3(b) is reinforced and the reinforcing mode of the LEV occurs in Fig. 3(b). In addition, by comparing Figs. 3(a) & 3(b), one may easily observe that the topology of the incoming vortices corresponding to the airfoil is very different for different interaction modes. In order to better comprehend the connection between the topology of the incoming vortices and the interaction modes, a potential theory for inviscid incompressible flow is developed.

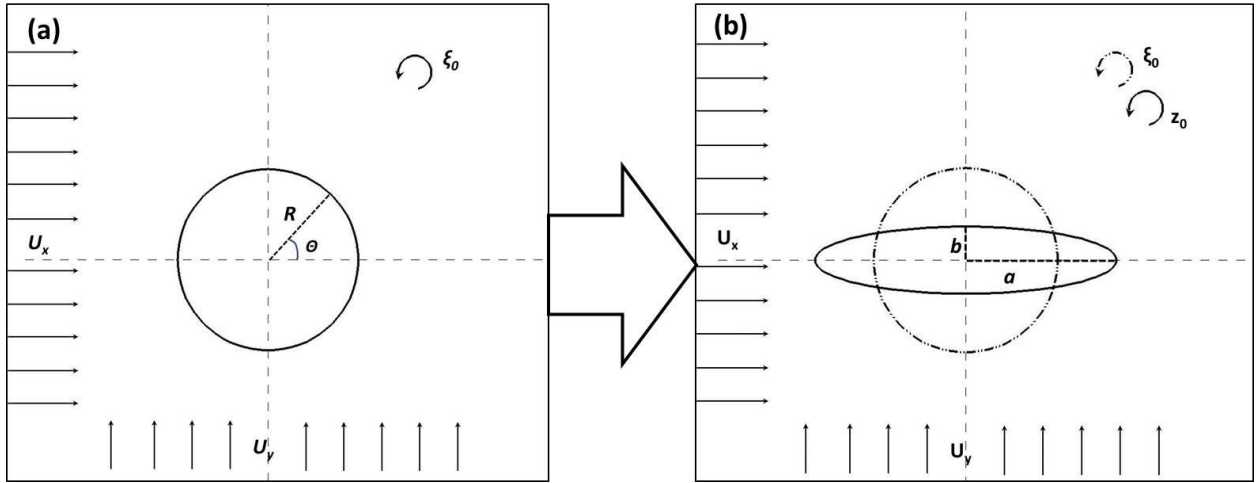


Figure 6-4 A sketch of the complex potential theory and coordinate transformation

Based on the method of images¹⁶⁴⁻¹⁶⁶, the complex velocity potential on a circular cylinder with a point vortex outside can be established in a complex plane $\zeta = R e^{i\theta}$. Because only quantities on the cylinder are concentrated on in the current study, the R is the cylinder radius, and the origin is on the center of the cylinder. The angle, θ , increases counter-clockwise from zero at the trailing edge of the cylinder. In addition, a complex

potential of the free stream velocity, U_x , and vertical velocity, U_y , are superimposed. The full equation of velocity potential for the flow field described in Fig. 6-3(a) is expressed as

$$F(\xi) = \underbrace{U_x \xi + U_x \frac{R^2}{\xi}}_{\text{Freestream Velocity}} - \underbrace{iU_y \xi + iU_y \frac{R^2}{\xi}}_{\text{Vertical Velocity}} - \underbrace{\frac{i\Gamma}{2\pi} \ln(\xi - \xi_0) + \frac{i\Gamma}{2\pi} \ln\left(\frac{R^2}{\xi} - \bar{\xi}_0\right)}_{\text{Point Vortex}} \quad (6.6)$$

In Eq.(6.6), Γ stands for the circulation of the point vortex. Its location is $\xi_0 = \gamma + \delta i$ and its conjugate $\bar{\xi}_0$ is $\gamma - \delta i$. The components of the complex velocity field can be directly obtained from the complex potential by differentiation.

$$\frac{dF(\xi)}{d\xi} = U_x - U_x \frac{R^2}{\xi^2} - iU_y - iU_y \frac{R^2}{\xi^2} + \frac{i\Gamma}{2\pi} \frac{1}{\xi - \frac{R^2}{\bar{\xi}_0}} - \frac{i\Gamma}{2\pi} \frac{1}{\xi} - \frac{i\Gamma}{2\pi} \frac{1}{\xi - \xi_0} \quad (6.7)$$

In order to map the cylinder in the ξ plane to an elliptic airfoil in the physical plane $z = x' + y'i$, the Joukowski transformation is employed:

$$z = \xi + \frac{a^2 - b^2}{4\xi} \quad (6.8)$$

Therefore, the complex velocity field in the z -plane is

$$\frac{dF(z)}{dz} = \frac{dF(\xi)}{d\xi} \frac{d\xi}{dz} \quad (6.9)$$

Finally, the pressure can be calculated from the Bernoulli equation

$$p = -\frac{1}{2} \frac{dF(z)}{dz} \frac{\overline{dF(z)}}{d\bar{z}} \quad (6.10)$$

It should be noted again that only the pressure along the surface of the elliptic airfoil is important to the current study.

It is well known^{110, 167-169} that there is a very high possibility to have a flow separation when the boundary layer travels far enough against an adverse pressure gradient. Therefore, in this study, the value of adverse pressure gradient will be employed as an indication for possible flow separation to occur on the airfoil surface to form LEVs and TEVs.

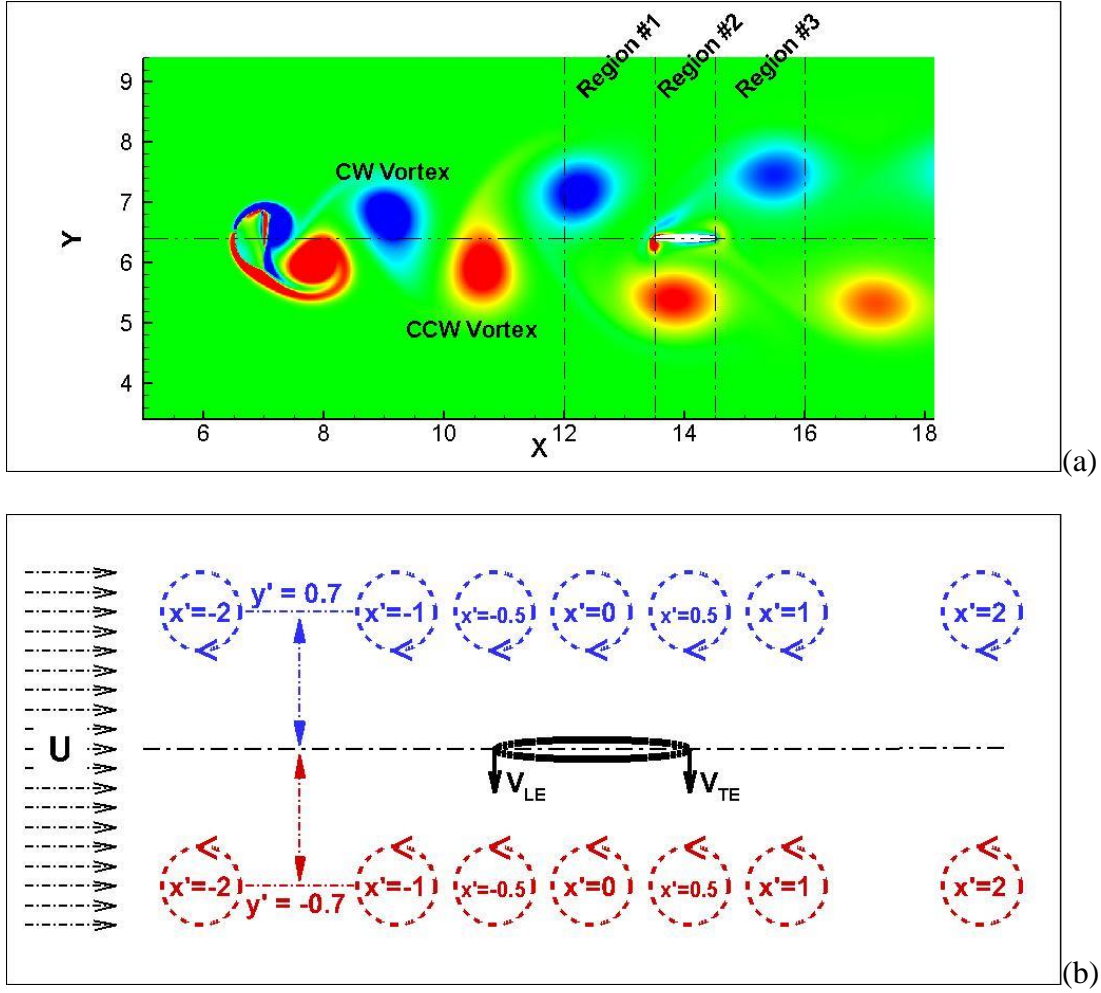


Figure 6-5 (a) Vorticity contours for the case with a heaving airfoil $h_a = 0.1$, $\phi = 0^\circ$ (b) A sketch of the relative locations of the vortices in the potential theory

To avoid ambiguity, several terminologies need to be clarified here for the description and discussion in the current study. For example, in Fig. 6-5(a), the blue vortices are negative, which are recognized as clockwise (CW) vortices, while red ones are positive, and counter-clockwise (CCW) vortices. Likewise, the LEVs and TEVs are also distinguished by CW and CCW. In the vicinity of the airfoil, three important regions will often be mentioned in the following contents, which differ by their streamwise distances. Their ranges are $x = 12 \sim 13.5$ for region #1, $13.5 \sim 14.5$ for region #2, and $14.5 \sim 16$ for region #3. The positions of vortices are identified by the streamwise location of their

centers. The vortices are recognized as “in front of the airfoil” if their centers are in the region #1, “in the airfoil region” if in region #2 and “behind the airfoil” if in region #3. Regions upstream of region #1 and downstream of region #3 are neglected, since the following potential theory shows that the vortices in region #1~3 play the most important roles in interaction modes with the airfoil.

Figure 6-5(b) illustrates the vortex locations in the potential theory analysis, where $x' = x - l/4$. A positive U_y in the potential theory indicates that the airfoil is undergoing a downstroke heaving in the simulation. The vortices at $x' = -2$ & -1 are in front of the airfoil, with $x' = -0.5, 0$ & 0.5 in the airfoil region and $x' = 1$ & 2 behind the airfoil. The magnitude of y' is always 0.7, which is the position of the incoming vortices in the cross-flow direction in the numerical simulation and thus the theoretical analysis is about this value after they entering region #1. Moreover, the circulation of vortices is calculated based on a vorticity area integration method²⁰ and the values are nearly π ; therefore, the Γ is selected as π in the potential theory. Moreover, the interaction modes are identified corresponding to their influences on the formation of LEVs and TEVs compared with the case of a single airfoil in a uniform flow without any incoming vortices. This baseline case, which is only involved in the potential theory analysis here, will be called as “single airfoil case” in the following content.

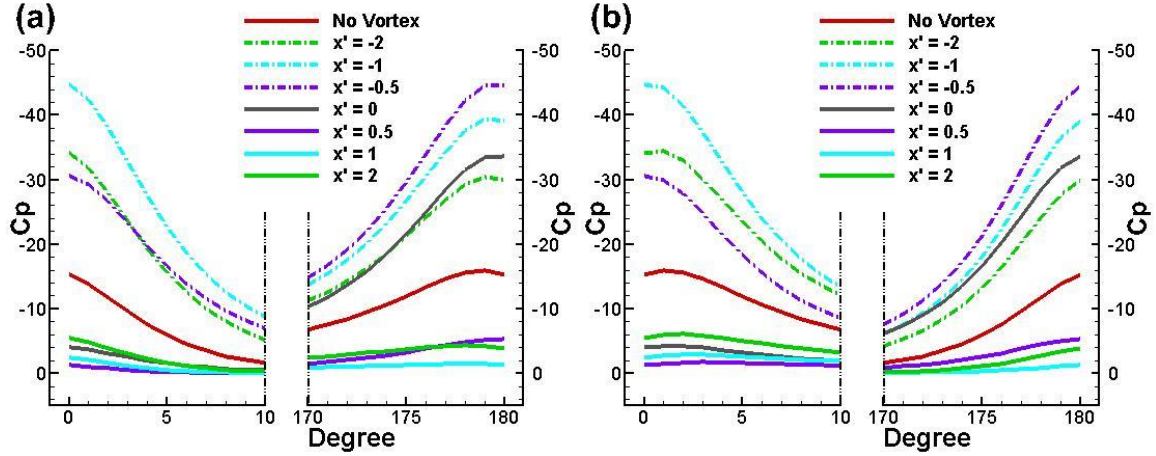


Figure 6-6 While the CCW vortex is approaching, the distribution of the pressure coefficient in the vicinity of the leading edge and trailing edge of an airfoil on its (a) lower surface and (b) upper surface. The motions of the leading edge and trailing edge in this figure are both $2\pi f_a \times 0.4$ downward. For the lower surface, the degree increases counter-clockwise from zero at the leading edge to 180 degree at the trailing edge of the airfoil. For the upper surface, the degree increases clock-wise from zero at the leading edge to 180 degree at the trailing edge.

Without incoming vortices, the single airfoil case with $V_{LE} = V_{TE} = 2\pi f_a \times 0.4$ (see Figs. 6-6), obtains a relatively high adverse pressure gradient near the leading edge (LE) of the airfoil. In addition, the lowest pressure near the LE occurs on the upper surface. These indicate that the flow is possible to form an LEV on the upper surface of the airfoil. Interestingly, near the trailing edge (TE) of the airfoil, an adverse pressure gradient and a low pressure value exist on the lower surface, whose magnitudes are comparable to those on the airfoil upper surface near the LE. However, the distance from the lower pressure point to TE might be too short for flow to travel long enough with the adverse pressure gradient. Therefore, it is expected that the lower surface has less chance to form a TEV than the upper surface to form a LEV; nevertheless, the possibility might not be negligible.

When the positive CCW vortex enters region #1, i.e. $x' = -2$ in Fig. 6-7, the magnitude of the adverse pressure gradient increases in the vicinity of the LE on both the upper and

lower surface of the airfoil compared with that in the single airfoil case. Moreover, the lowest pressure still exists on the upper surface. Consequently, it has more possibility to form an LEV on the upper surface than in the single airfoil case. This possibility increases as the CCW vortex approaches the airfoil and achieves a higher adverse pressure gradient at $x'=-1$, yet it begins to decrease after that and reaches a relatively lower value at $x'=-0.5$. As the CCW vortex keeps moving horizontally, i.e. $x'>-0.5$, the magnitudes of the adverse pressure gradient and lowest pressure for both LE and TE are substantially reduced compared with the single airfoil case. Since the LEV on the upper surface and TEV on the lower surface are usually clockwise and counter-clockwise, respectively, during the downstroke heaving motions, it can be concluded that the incoming CCW vortex strongly reinforces the formation of the CW LEV and CCW TEV while it is in region #1 and strongly suppresses them while in regions #2 & #3. Alternatively, the former vortex obtains a strong reinforcing mode for the latter two vortices in region #1 and a strong suppressing mode in regions #2 & #3.

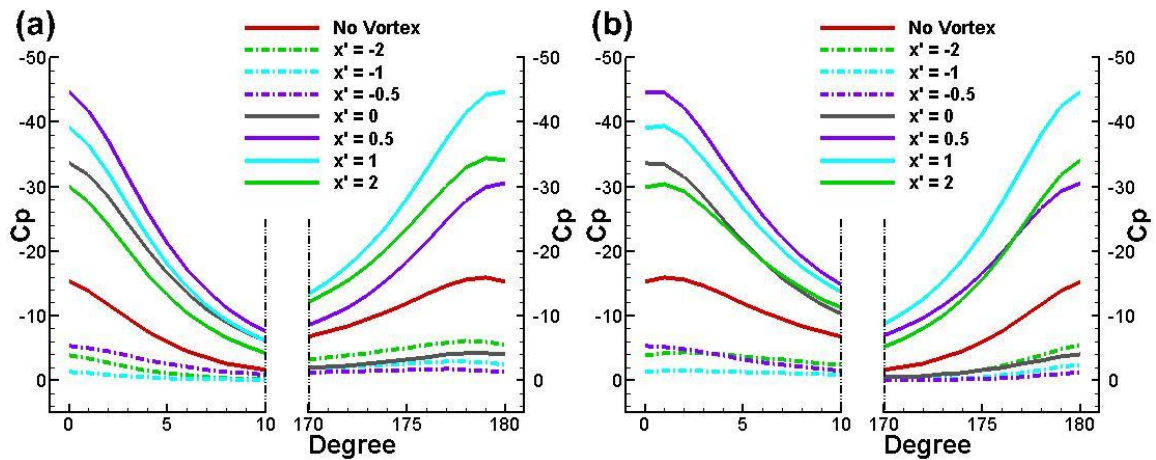


Figure 6-7 While the CW vortex is approaching, the distribution of the pressure coefficient in the vicinity of the leading edge and trailing edge of an airfoil on its (a) lower surface and (b) upper surface.

The motions of the leading edge and trailing edge in this figure are both $2\pi f_a \times 0.4$ downward. The degree increases counter-clockwise from zero at the leading edge of the airfoil.

The situation is opposite while a CW vortex is getting close to the airfoil, i.e. Fig. 6-7. Compared with the single airfoil case, the magnitudes of both pressure and its gradient in the vicinity of either LE or TE are tremendously reduced due to the presence of the CW vortex in front of the airfoil; however, they are noticeably boosted while the CW vortex is inside the airfoil region or behind the airfoil. Consequently, the CW vortex has a strong suppressing mode for the CW LEV and CCW TEV in region #1, but a strong reinforcing mode in regions #2 &3.

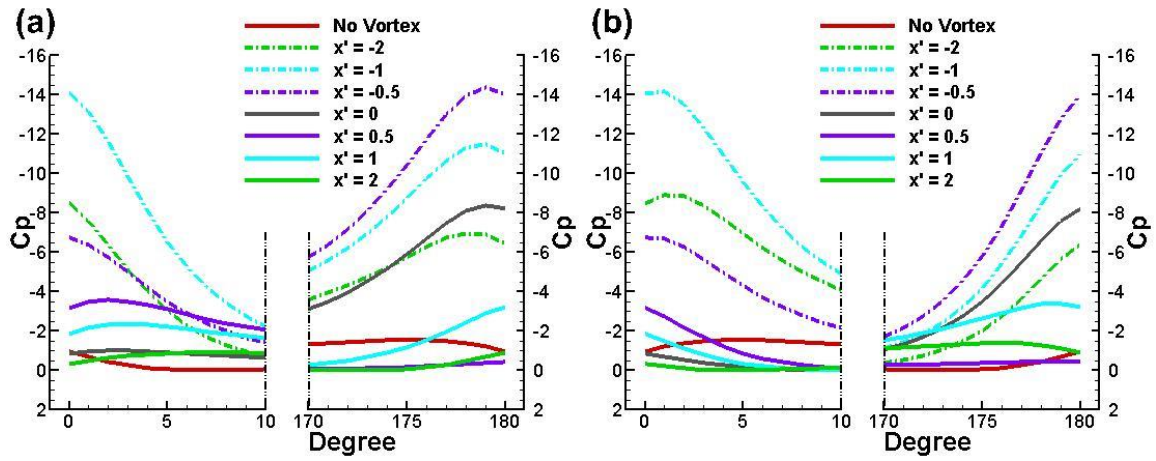


Figure 6-8 While the CCW vortex is approaching, the distribution of the pressure coefficient in the vicinity of the leading edge and trailing edge of an airfoil on its (a) lower surface and (b) upper surface.

The motions of the leading edge and trailing edge in this figure are both $2\pi f_a \times 0.1$ downward. The degree increases counter-clockwise from zero at the leading edge of the airfoil.

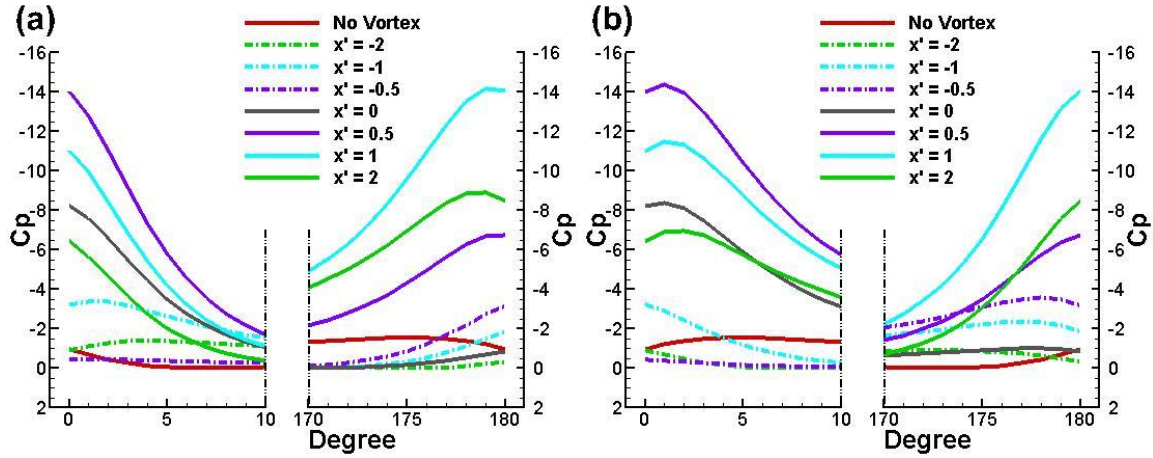


Figure 6-9 While the CW vortex is approaching, the distribution of the pressure coefficient in the vicinity of the leading edge and trailing edge of an airfoil on its (a) lower surface and (b) upper surface.

The motions of the leading edge and trailing edge in this figure are both $2\pi f_a \times 0.1$ downward. The degree increases counter-clockwise from zero at the leading edge of the airfoil.

Figures 6-8 and 6-9 illustrate the pressure distributions on the airfoil with smaller heaving velocities; they are very similar to Figs. 6-6 and 6-7, yet a few differences exist. The first one happens for the single airfoil case. The single airfoil case obtains relatively small magnitudes of pressure and its gradient in Figs. 6-6 and 6-7. It indicates that the single airfoil heaving under such a low speed motion rarely generates any LEVs or TEVs, which is reasonable. This directly results in another primary distinction between Figs. 6-6 & 6-7 and Figs. 6-8 & 6-9. For example, the lowest pressure always occurs on the upper surface near the LE wherever the CW vortex is in Fig. 6-7; however, in Fig. 6-9, its location switches to the lower surface as the CW vortex stays in region #1. In addition, the magnitudes of the pressure and its gradient, with this condition, are larger than that of the single airfoil case. This implies that a CW vortex in region #1 may trigger an onset of an LEV on the lower surface of the airfoil. This is acceptable because of the following reasons. Figure 7 concluded that a CW vortex in region #1 preserves the strong suppressing mode for the LEV on the upper surface of the airfoil, while the airfoil has a

strong tendency to generate this LEV if the CW vortex is absent. Suppression on one side may reinforce the other side. Especially, with a very small possibility to form any LEVs in the single airfoil case with low speed motions, this strong suppressing mode for the LEV on the upper surface may eventually conduces to be a weak reinforcing mode for the LEV on the lower surface. Similar phenomena occur for the CW vortex influencing the formation of the TEV in Fig. 6-9 and CCW vortex impacting the formation of both the LEV and TEV in Fig. 6-8.

The summary of locations of the vortices and the interaction modes is tabulated in Table 1. The “weakly influenced” in Table 1 indicates that suppression of one side would weakly reinforce the other side and vice versa. Such a weak influence can usually be ignored in the cases involving incoming vortices interacting with airfoils undergoing high speed flapping motions, but not for those with low speed motions.

Table 1 The relation between incoming vortex positions and interaction modes with an airfoil undergoing a downstroke heaving motion.

		CW LEV on upper surface	CCW LEV on lower surface	CCW TEV on upper surface	CW TEV on lower surface
CCW Vortex	Region #1	+	*	*	+
	Region #2	-	*	*	+
	Region #3	-	*	*	-
CW Vortex	Region #1	-	*	*	-
	Region #2	+	*	*	-
	Region #3	+	*	*	+
+: reinforcing mode or onset;					

∴: suppressing mode or no influence;

*: weakly influenced or only the magnitude of the pressure gradient increases, yet the lowest pressure occurs on the other side of the airfoil;

The rule-of-thumb can be briefly extracted from Table 1. Basically, an upstream vortex suppresses the LEVs with the same sign in region #1 yet reinforces them in the other two regions; similarly, it reinforces the TEVs with the same sign in region #3 but suppresses them in the other two regions.

It should be emphasized again that interaction modes deduced from the potential theory only provide a guideline. High possibilities may not guarantee existence. Moreover, the amplitude of the heaving motion is intentionally chosen to be small to avoid substantial interactions with the cores of the vortices for the validity of the potential theory. In the next section, the cases with airfoils tremendously interacting with the vortices exhibit bad resultant power, which makes the discussion of interaction modes become less valuable under such circumstances. Moreover, the interaction modes in Table 1 are only for the airfoil experiencing a downstroke heaving motion. In analogy to this table, Table 2 is made for the airfoil undergoing an upstroke heaving motion.

Table 2 The relation between incoming vortex positions and interaction modes with an airfoil undergoing an upstroke heaving motion.

		CW LEV on upper surface	CCW LEV on lower surface	CCW TEV on upper surface	CW TEV on lower surface
CCW Vortex	Region #1	*	-	-	*
	Region #2	*	+	-	*
	Region #3	*	+	+	*

CW Vortex	Region #1	*	+	+	*
	Region #2	*	-	+	*
	Region #3	*	-	-	*
+: reinforcing mode or onset; -: suppressing mode or no influence; *: weakly influenced or only the magnitude of the pressure gradient increases, yet the lowest pressure occurs on the other side of the airfoil;					

The extra value of making Table 2 is for the cases with a purely pitching airfoil. A purely heaving motion should maintain a $V_{LE}=V_{TE}$ in Fig. 6-5, yet a purely pitching motion with the half chord as the pivoting point can be recognized as having $V_{LE}=-V_{TE}$. Since only 10 degrees is considered near the LE and TE for interaction modes in Figs. 6-6~6-9, it is acceptable to assume that the speeds are constant near the end of the airfoil for a pitching motion. Furthermore, as discussed above for Figs. 6-6~6-9, the strongest suppression or reinforcement often occurs when the vortices are located around $x' = -1$ and 1, which will be called “critical positions” in the later discussion. The effect of vortices on the airfoil is gradually reduced as they are far away from the airfoil, i.e. $x' < -2$ or $x' > 2$. Therefore, the impacts on vortices to the flapping airfoil in those regions are neglected in the current study.

The interaction modes in the potential theory are identified by looking at individual incoming vortices. In reality, multiple vortices may fall into region #1~3 and simultaneously interact with the airfoil. Therefore, the overall leading interaction modes should be determined by the competition among those vortices in the numerical simulations. Since the histories of coefficients and the heaving/pitching velocity are periodic and symmetric corresponding to zero, only a half cycle, i.e. the downstroke

heaving or the counter-clockwise pitching, is plotted out in the following contents for analysis. The demonstration of the other half should be very similar. Finally, $t/T = 0$ is assumed to be the moment that the airfoil reaches its maximum vertical displacement for heaving or its maximum angle of attack for pitching.

6.1.2 Purely Heaving Motions

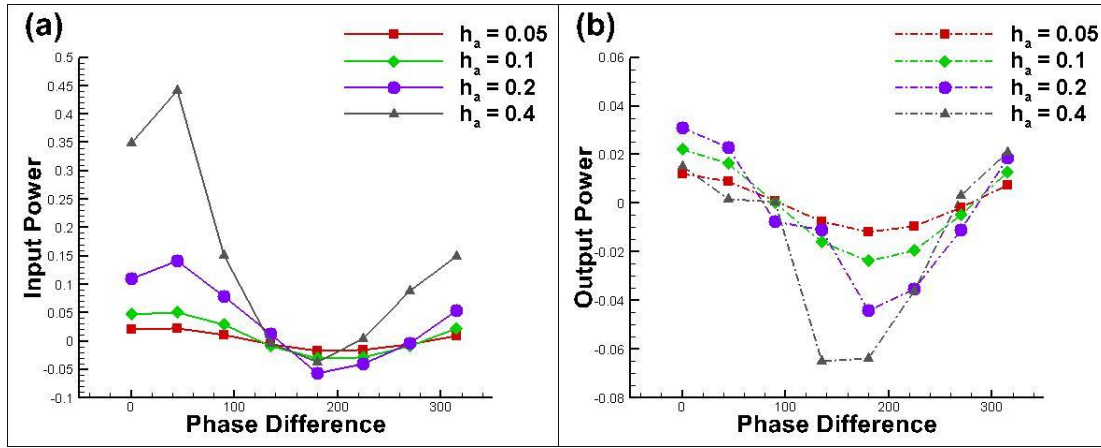


Figure 6-10 Input and output powers for the cases with different heaving amplitudes and phase differences.

As mentioned in the section on potential theory analysis, the half width of the incoming vortex street in front of the airfoil is around 0.7, based on which the choice of the heaving amplitude can be roughly categorized into three types. The first type is for small amplitudes, i.e. $h_a = 0.05, 0.1, 0.2$, which provides a relatively safe region for the airfoil to heave rather than substantially interacting with the cores of the incoming vortices. Among these cases, the changing trends of either input power or output power are very similar, as shown in Fig. 6-10. The peak values are obtained at $\phi = 45^\circ$ and 255° . The best result input power always comes with the worst output power. Most importantly, the magnitude of the peak values increases as the amplitude of the airfoil motion enlarges.

The second type is for intermediate amplitudes, i.e. $h_a = 0.4$; the heaving airfoil gradually has stronger interaction with the cores of the incoming vortices as the amplitude increases. There is a possibility for the airfoil to interfere with the shape and the travel path of the incoming vortices. The potential theory can only be partially employed to interpret the flow phenomena under this circumstance, which will be demonstrated later. With the operation parameters in this category, the resultant powers usually are not comparably with that of the small amplitude type. For example, the worst scenario of both input and output power of the case with $h_a = 0.4$ are much worse than that with $h_a = 0.2$, whereas the best scenario in the former cases is not better than that in the latter cases. The last type is for amplitudes larger than 0.7, i.e. $h_a = 0.8$, which guarantees significant interactions with incoming vortices and may noticeably deform them or change their paths. The potential theory is totally not valid. Particularly, the resultant powers for $h_a = 0.8$ are not plotted in Fig. 6-10, since even the lowest input power is as high as 0.47 at $\phi = 180^\circ$; the range of the output power is comparable to that of the cases in Fig. 6-10 (b). These badly resultant powers make the discussion of the interaction modes less valuable with the large heaving amplitudes. In the following contents, the case with $h_a = 0.1$ and 0.4 will be brought out as examples for the first and second types of heaving amplitudes, respectively, in order to demonstrate the relationship between the interaction modes and their influences on the resultant powers under different circumstances.

6.1.2.1 Small heaving amplitudes

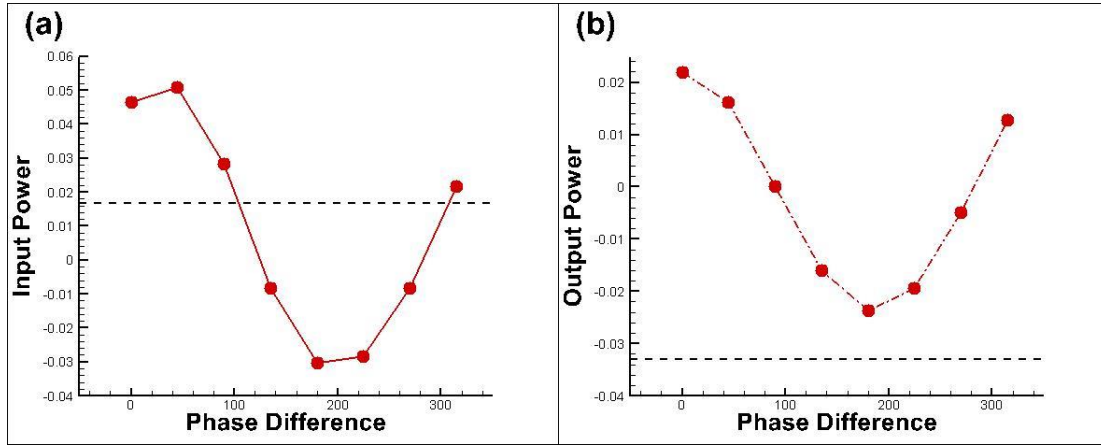


Figure 6-11 Input and output powers for the cases with $h_a = 0.1$. Dashed lines in the figures indicate the input/output power for a single elliptical airfoil with the absence of the upstream cylinder

A typical case of small amplitude is exhibited in Fig. 6-11, which shows, with different phase differences, the resultant powers vary. The output power in the presence of incoming vortices is always enhanced against the single airfoil case. It may be caused by the reserved von-Karman vortex street generated by the heaving cylinder in the current study¹⁷⁰, which embeds the thrust force in its wake. On the other hand, the incoming vortices have the capability to either increase or decrease the input power of the airfoil. Those distinctions will be explicitly revealed by the analysis corresponding to the interaction modes in the following sections.

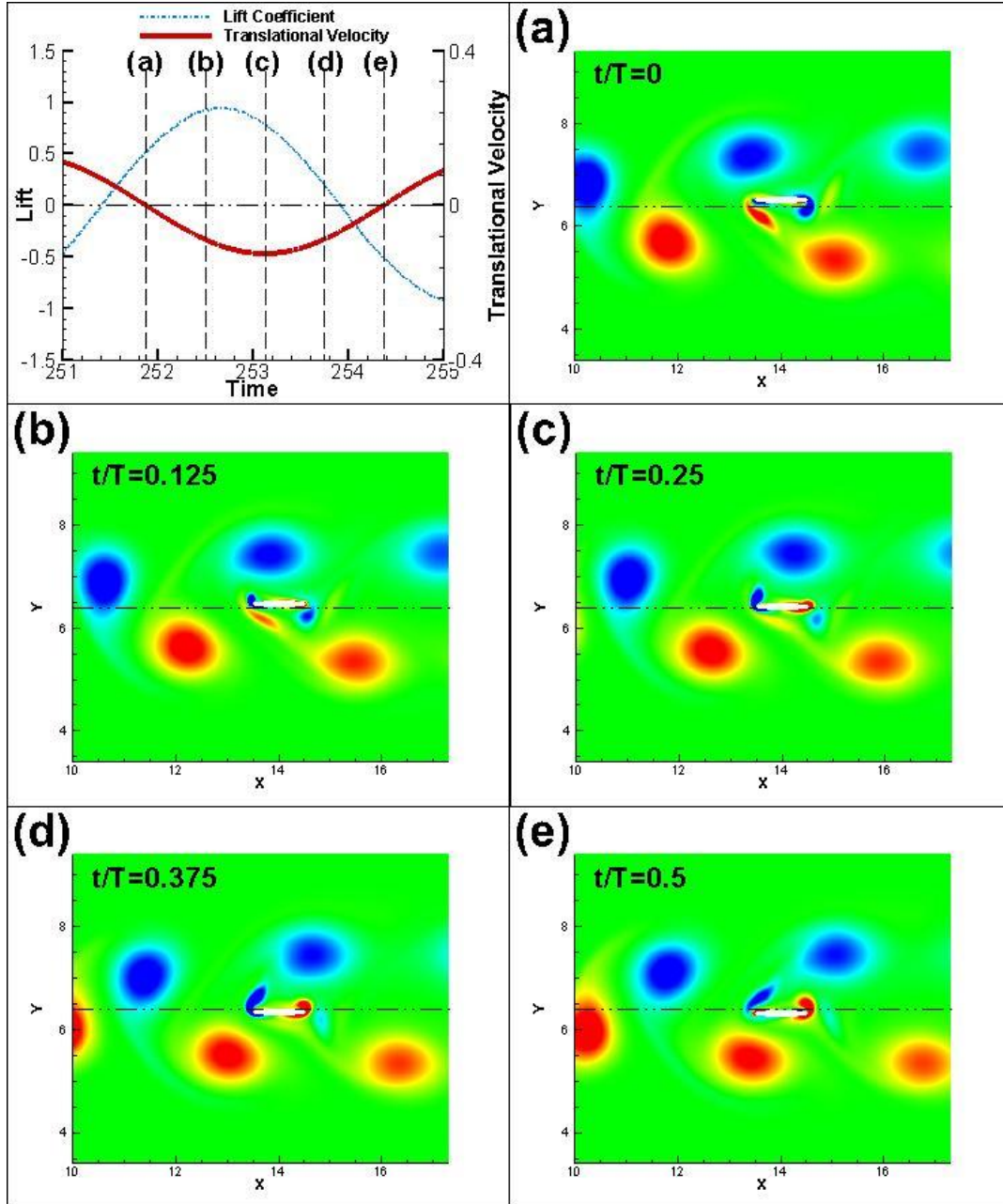


Figure 6-12 Lift and thrust coefficients, translational velocity, and vorticity contours of the airfoil over the half cycle of downstroke for the case of $h_a = 0.1$ and $\phi = 45^\circ$.

Figure 6-12 illustrates the case of an unfavorable input power. At the beginning of the downstroke, in Fig. 6-12(a), a CW vortex is in the airfoil region, a CCW vortex is in front of the airfoil, and another CCW one is behind. Based on the potential theory in Table 1, the CCW vortex in the front of airfoil produces the reinforcing mode for the CW LEV

which slightly suppresses the CCW LEV. This effect may be cancelled by that of the CCW vortex behind the airfoil, which is near its critical position, i.e. $x' = 1$. However, the CW vortex above the airfoil falls into the airfoil region, which brings about a reinforcing mode for the CW LEV and hence a suppressing one for the CCW LEV. Consequently, at this moment $t/T = 0$, the existing CCW LEV is being suppressed. From $t/T = 0 \sim 0.25$, the CCW vortex in front of the airfoil gradually travels to its critical position, i.e. $x' = -1$, and the one behind the airfoil moves away from $x' = 1$; the reinforcing mode for the CW LEV from the former vortex overwhelms the suppressing mode from the latter one. In addition, the CCW vortex on the top of the airfoil stays in the airfoil region. Therefore, the CCW LEV is obviously enervated, yet a CW LEV is formed, as shown in Fig. 6-12(c). This CW LEV keeps growing till the end of this stroke.

In terms of the CW TEV, both the CCW vortex behind the airfoil and the CW one in the airfoil region suppress it, and only the CCW vortex in front of the airfoil reinforces it with limited strength; hence, this CW TEV is being suppressed. As suggested in the potential theory, in the conditions with small heaving amplitudes, a CCW TEV may be triggered on the other side of the airfoil during the consecutive downstroke heaving due to the strong suppressing mode for the CW TEV, which is confirmed by Figs. 6-12 (d) & 13(e). This phenomenon will be further demonstrated in the discussion for the next figure.

The mapping between the input power and the LEV and TEV can also be investigated by Fig. 6-12. At $t/T = 0$, although a small CCW LEV and a small CW TEV remain from the last half cycle of the upstroke, the lift coefficient is positive due to the presence of the CW vortex closely staying above the airfoil. Therefore, at this initial stage, the input power is unfavorably positive since the sign of lift coefficient and airfoil heaving velocity

is different. With the development of both the LEV and TEV on the upper surface of the airfoil, the lift coefficient stays positive. Particularly at $t/T = 0.375$ (Fig. 6-12 (d)) the CCW vortex is about to enter the airfoil region while the CW one is about to leave; therefore, their direct contributions to the normal force on the airfoil could be cancelled. However, an obvious positive lift coefficient still exists which should be primarily attributed by the well-formed CW LEV and CCW TEV on the upper surface of the airfoil. Although, from this moment to the end of the downstroke, the lift coefficient becomes negative because of the rising influence of the CCW vortex below the airfoil, the magnitude of the negative lift coefficient and the airfoil heaving velocity are both very small; hence, the resultant favorably negative input power is limited compared to the total amount of positive input power generated in the previous part of this half cycle.

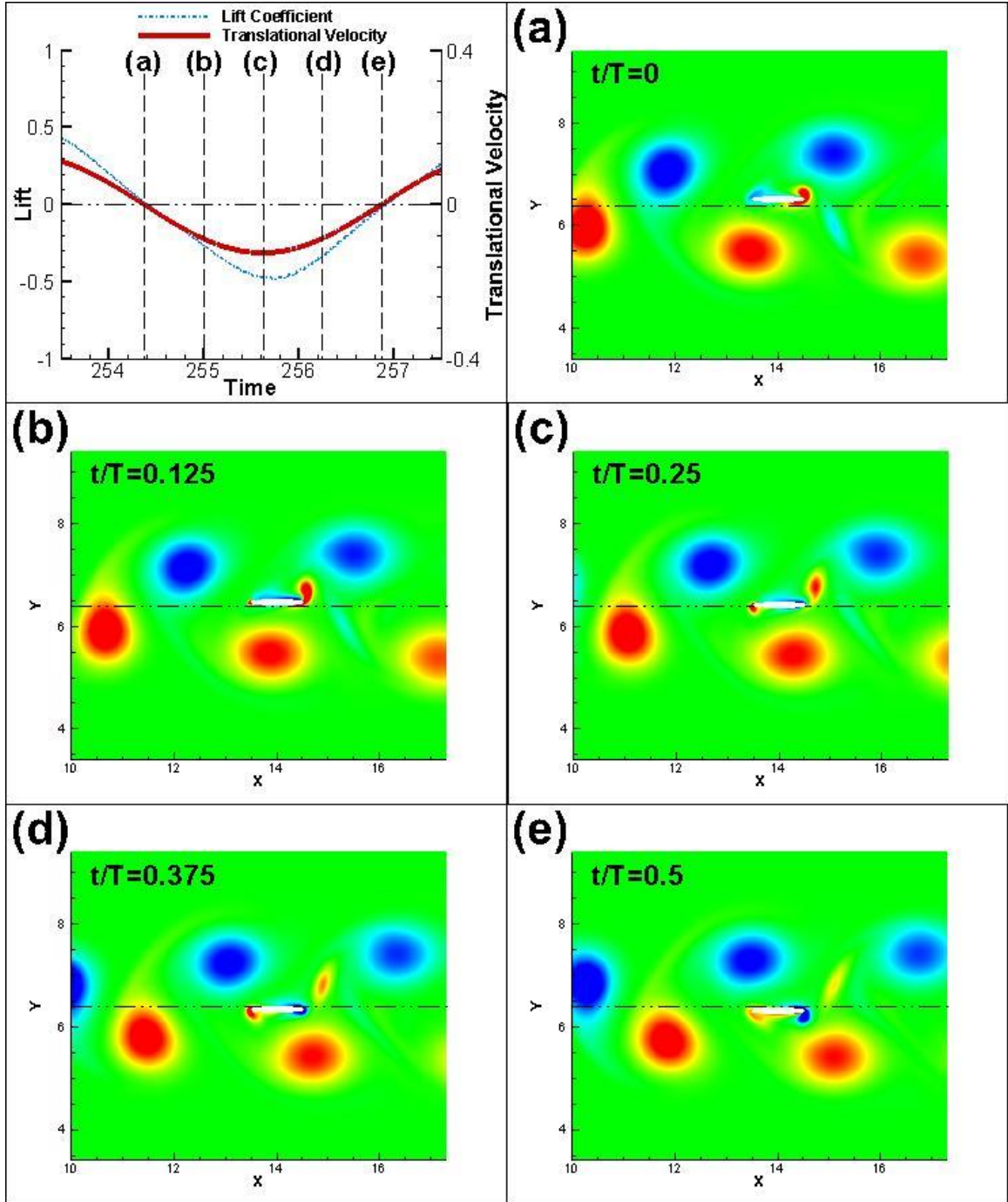


Figure 6-13 Lift and thrust coefficients, translational velocity, and vorticity contours of the airfoil over the half cycle of downstroke for the case of $h_a = 0.1$ and $\phi = 225^\circ$.

The situation is opposite for the case of $\phi = 225^\circ$, which produces a negative total input power. At the beginning of the downstroke (Fig. 6-13(a)) a negligible CW LEV and

a small CCW TEV remain on the top of the airfoil. The suppressing impact from the CW vortex in front of the airfoil for the CW LEV is comparable to the reinforcing one from the CW vortex behind the airfoil. Nonetheless, the strong suppressing mode for the CW LEV from the CCW vortex in the airfoil region results in no CW LEVs apparently formed in the duration of $t/T = 0 \sim 0.125$. Instead, a CCW LEV is generated on the bottom of the airfoil around $t/T = 0.25$. This phenomenon is again predicted by the potential theory, which has been distinctly pointed out in the discussion for Figs. 6-8 and 6-9. At this moment in Fig. 6-13(c), the CW vortex in front of the airfoil reaches the critical position, and the CCW vortex is under the TE; both these vortices have strong suppressing modes on the CW LEV, which, as mentioned in the section on the potential theory, have a tendency to trigger the onset of the CCW LEV on the other side of the airfoil if a low speed heaving motion is applied. Although the CW vortex behind the airfoil has a weak suppressing mode on this CCW LEV, this LEV has been developed from $t/T = 0.25 \sim 0.375$ in the numerical simulation. Interestingly, the situation is completely changed in the interval of $t/T = 0.375 \sim 0.5$. With another CCW vortex freshly entering the region in front of the airfoil and producing a suppressing mode to the CCW LEV, the reinforcing mode from the CCW vortex under the airfoil is balanced. Furthermore, once the centroid of the CW vortex above the airfoil passes the LE of the airfoil, its interaction mode for the CCW LEV shifts from the reinforcing mode to the suppressing one. As a consequence, these swift switches in a very short period weaken the strength of the CCW LEV in Fig. 6-13(e) right after its full development in Fig. 6-13(d). Fortunately, this procedure is of pivotal importance in preventing such an LEV

from making any adverse contributions to the favorable input power for the consecutive upstroke heave.

Likewise, the CCW TEV at $t/T = 0$ is majorly suppressed by the CCW vortex under the airfoil, and the impact from one CW vortex cancels the other. Due to this suppressing mode, the CCW TEV quickly detaches the airfoil from $t/T = 0$ to 0.25. Similarly, a CW TEV is about to be formed at $t/T = 0.375$ as a result of the competition between the reinforcing mode from the CCW vortex under the airfoil and the suppressing mode from the CW vortex in front of the airfoil.

The histories of the lift coefficient and heaving velocity in Fig. 6-13 further demonstrate the importance of the interaction modes for good input power, especially through the formation of the CCW LEV and CW TEV. The lift coefficient is roughly zero at the beginning of the downstroke. Because of the detachment of the TEV and absence of the LEV, the CCW vortex under the airfoil plays a very important role in generating the negative lift coefficient during $t/T = 0 \sim 0.25$, which contributes significantly to the favorable input power. After that, although the CW vortex starts entering the airfoil region and producing a positive lift coefficient, the developing LEV and TEV on the lower surface of the airfoil make their effort to balance the negative impact contributed by the CW vortex to the favorable input power. Particularly, in Fig. 6-13(e), the centroid of the CW vortex is inside the airfoil region and the CCW vortex is outside; because of the presence of the TEV on the lower surface of the airfoil, the lift coefficient becomes almost zero again, making it more than ready to achieve the favorable input power for the consecutive upstroke.

In addition to the input power, the interaction modes also influence the output power. Due to the small heaving amplitude of the airfoil, incoming vortices would not be substantially disturbed by the airfoil motions and the reserved von-Karman vortex street should remain downstream of the airfoil. This indicates that the difference in the output power between the cases in Figs. 6-12 and 6-13 would primarily be contributed by the LEVs and TEVs. Since both cases in these two figures form TEVs and their strengths are comparable, the LEVs become the key to the difference in the output power. In Fig. 6-11, reinforced LEVs create low pressure regions in the vicinity of the LE, which is also illustrated in the potential theory. Such low pressures provide noticeable suction forces and give the airfoil the ability to obtain thrust rather than drag. In contrast, with the absence of the LEV in Fig. 6-12, the airfoil keeps producing drag and results an overall negative output power, as shown in Fig. 6-10.

6.1.2.2 Intermediate Heaving Amplitudes

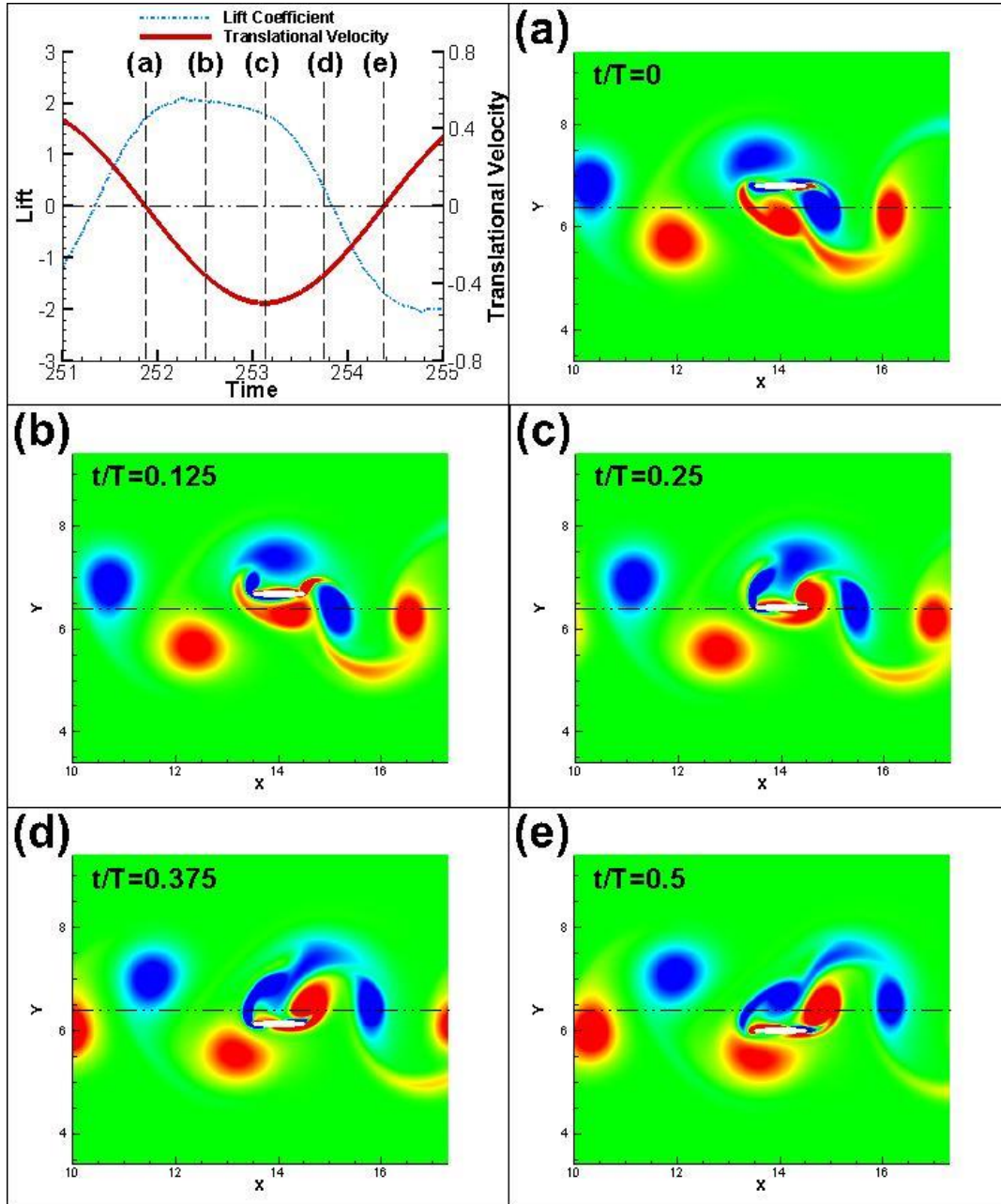


Figure 6-14 Lift coefficients, translational velocity, and vorticity contours of the airfoil over the half cycle of downstroke for the case with $h_a = 0.4$ and $\phi = 45^\circ$.

The first impressions of the vorticity contours in Fig. 6-14 compared to those in Fig. 6-12 are the strong LEVs and TEVs. In addition, the strength of the incoming vortices is weakened by their substantial interactions with the airfoil. As mentioned before, the

potential theory proposed in the current work has some limitations under such a circumstance. A good example is that the theory does not include the effect of one strong LEV/TEV on another LEV/TEV. Therefore, the analysis for Fig. 6-14 does not involve such influences related to developed LEVs and TEVs. Moreover, since the impact of diminished vortices downstream of the airfoil is limited, the vortices in front of the airfoil and in the airfoil region will be mostly concentrated for the current analysis. At $t/T = 0$, both the CW vortex in the airfoil region and the CCW vortex in front of the airfoil carry reinforcing modes for the CW LEV, which suppress the existing CCW LEV in Fig. 6-14 (a). In Fig. 6-14 (b) & 6-14(c), the CW LEV starts to develop and wrap up the CW vortex on the top of the airfoil. This wrapping-up keeps the CW vortex staying in the airfoil region and eventually merging itself with the CW LEV, which strengthens its reinforcing mode for the CCW TEV. Although the CCW vortex in the front of the airfoil obtains a suppressing mode for this TEV, a strong CCW TEV has eventually been formed in the numerical simulation. With the presence of both a strong LEV and TEV, relatively positive large lift coefficients are generated, which make substantially negative contributions to the input power. The situation does not change until Fig. 6-14 (e) while most of the CCW vortex enters the airfoil region and begins to balance the positive lift produced by the fully developed LEV and TEV.

Although strong LEVs are formed, the strong TEVs ruin the output power in this case. Worse still, the weakened vortices behind the airfoil are often located in the mean position of the heaving motion, which induces suction pressure for drag generation. This might explain why the output power for this case is almost zero in Fig. 6-10, which is worse than that for the case in Fig. 6-12.

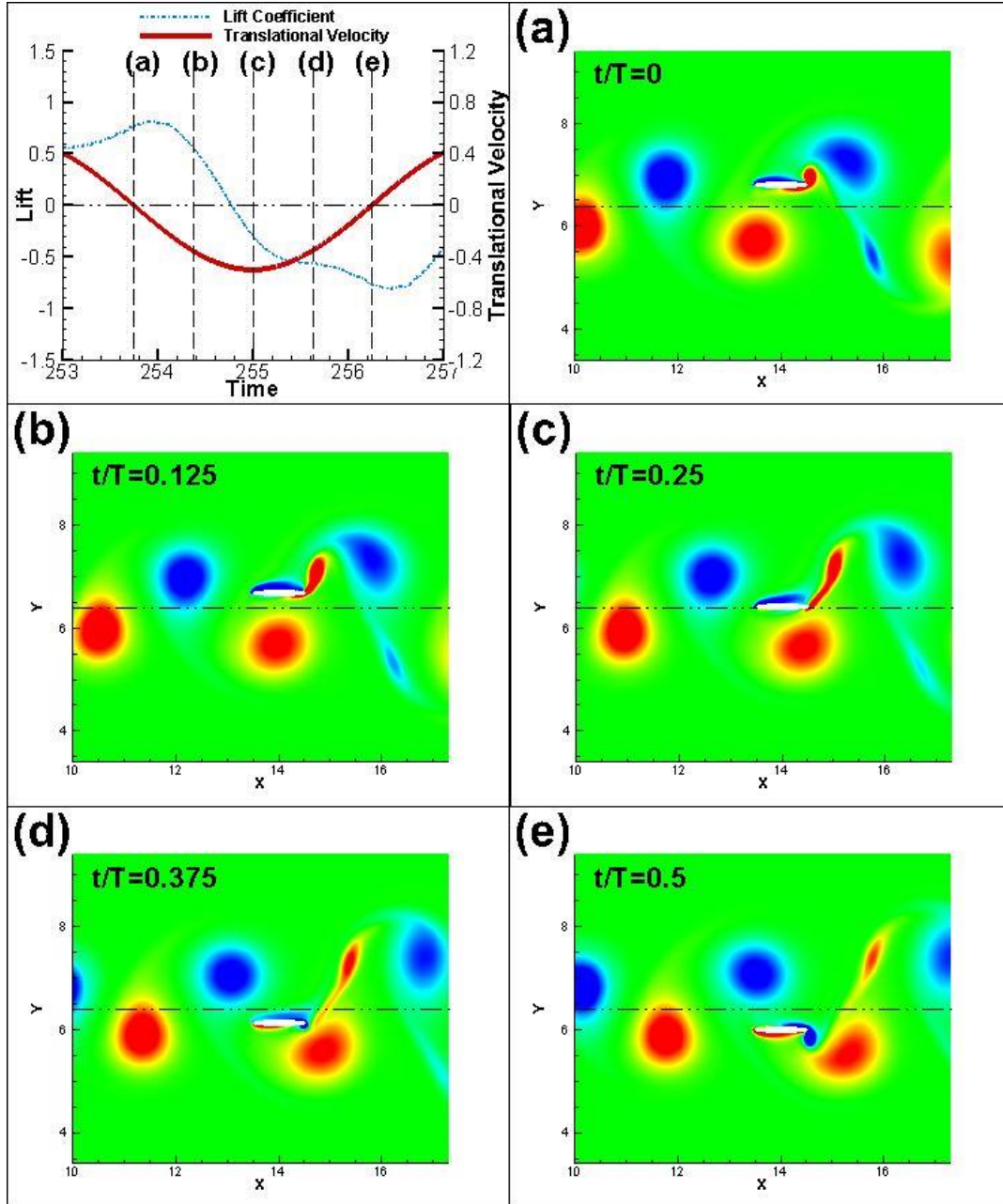


Figure 6-15 Lift coefficients and translational velocity and vorticity contours of the airfoil over the half cycle of downstroke for the case with $h_a = 0.4$ and $\phi = 225^\circ$.

The topology of the vortices and TEVs in Fig. 6-15 is very similar to that in Fig. 6-13. The primary difference between these two figures is the appearance of the CCW LEV. Since the heaving amplitude was small, the CW LEV was not observed in Fig. 6-13 due to the overall suppressing mode from the vortices surrounding the airfoil; instead, a CCW

LEV was formed on the lower surface of the airfoil in Figs. 6-14(c)~(e), which assists producing a favorable input power. In Fig. 4-42, the overall suppressing mode still exists in Figs. 6-15(a) to (c); however, maybe due to the strong tendency of generating a CW LEV for the airfoil with large heaving amplitudes, a thin boundary layer with the negative (CW) vorticity sign is formed rather than a fully developed CW LEV. Although this thin boundary layer results in much smaller positive lift coefficients than the fully developed CW LEV in Fig. 6-14, it still makes adverse contributions to the favorable input power until it is mostly suppressed in the interval between Figs. 6-15(c) and 6-15(d). After that, a thin boundary layer and a strong CW TEV are formed on the lower surface of the airfoil to improve the input power. However, the positive impact from this thin boundary layer and CW TEV emerges too late for the downstroke in Fig. 6-15. As shown in Fig. 4-37, the final averaged input power for this case of Fig. 6-15 is not better than that for the case in Fig. 6-13, whereas the peak lift coefficients in Fig. 6-15 are almost twice as larger as that in Fig. 6-13.

Furthermore, with the relatively large amplitude, there are few moments in Fig. 6-15 when strong vortices are located right behind the TE of the airfoil, i.e. Figs. 6-15 (a) and 6-15(e). This would tremendously destroy the resultant output power. Compared with Fig 6-13 that the vortices behind the airfoil are always far away from the TE and hence the drag is mostly contributed by the small TEVs, it is not unexpected that the case in Fig. 6-15 leads to an apparently worse output power against that in Fig. 6-13 (see Fig. 6-10).

6.1.3 Purely Pitching Motions

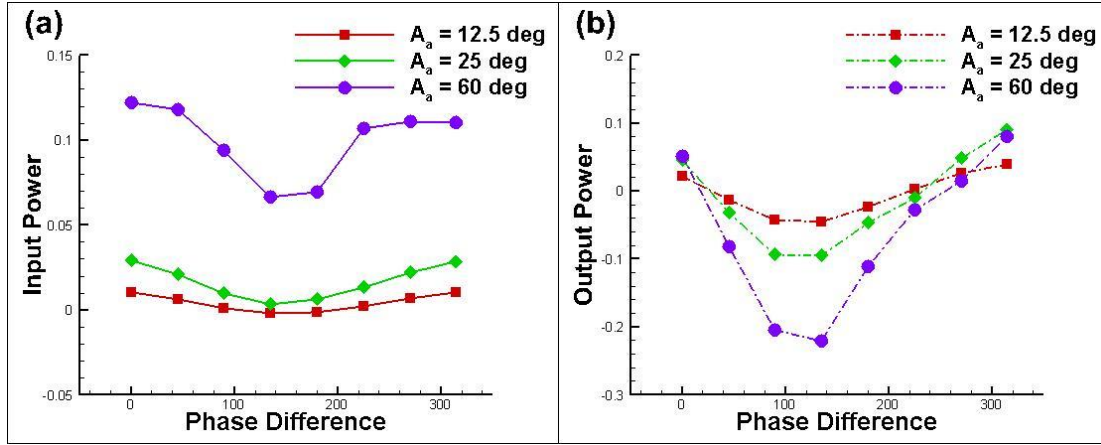


Figure 6-16 Input and output powers for the cases with different pitching amplitudes and phase differences.

For purely pitching motion, the cases with $A_a = 12.5^\circ$ and 25° can be categorized as the small pitching amplitude type, since their corresponding maximum vertical displacements of the LE of the airfoil are 0.108 and 0.211, respectively. The cases with $A_a = 60^\circ$ are the intermediate pitching amplitude type, in which the equivalent vertical amplitude for the LE of the airfoil is around 0.43. Compared with purely heaving motion, the purely pitching motion barely provides negative input powers. The trade-off between the input and output power is still detected. Most importantly, the phase difference in pitching motion primarily tunes the output power rather than input power compared with that in heaving motion. For example, compared with the heaving cases with $h_a = 0.1$ and the pitching ones with $A_a = 12.5^\circ$, both of them obtain comparable vertical displacements for the LE of the airfoil. However, the heaving cases result in a variation of input powers (the maximum value minus the minimum value) to be around 0.1 and of the output powers to be 0.05, while the pitching ones lead 0.02 as the variation of input powers and 0.15 for output powers. This implies that good operational parameters of pitching motions mainly

help to fulfill the requirement for satisfying output power and good ones of heaving motions primarily make contributions to a great input power. Moreover, the phase difference for the best scenarios of resultant powers for the purely pitching motion in Fig. 6-16 is always around 90° away from that for the purely heaving motion exhibited in Fig. 6-10. It confirms the conclusion made by previous studies^{35, 38, 163} that, in order to achieve the best propulsion efficiency with such a cylinder-airfoil configuration, a flapping motion involving both heaving and pitching is necessary; in addition, a phase lag between the heaving and pitching motion is essential and the value of the lag should be around 90° .

6.1.3.1 Small Pitching Amplitudes

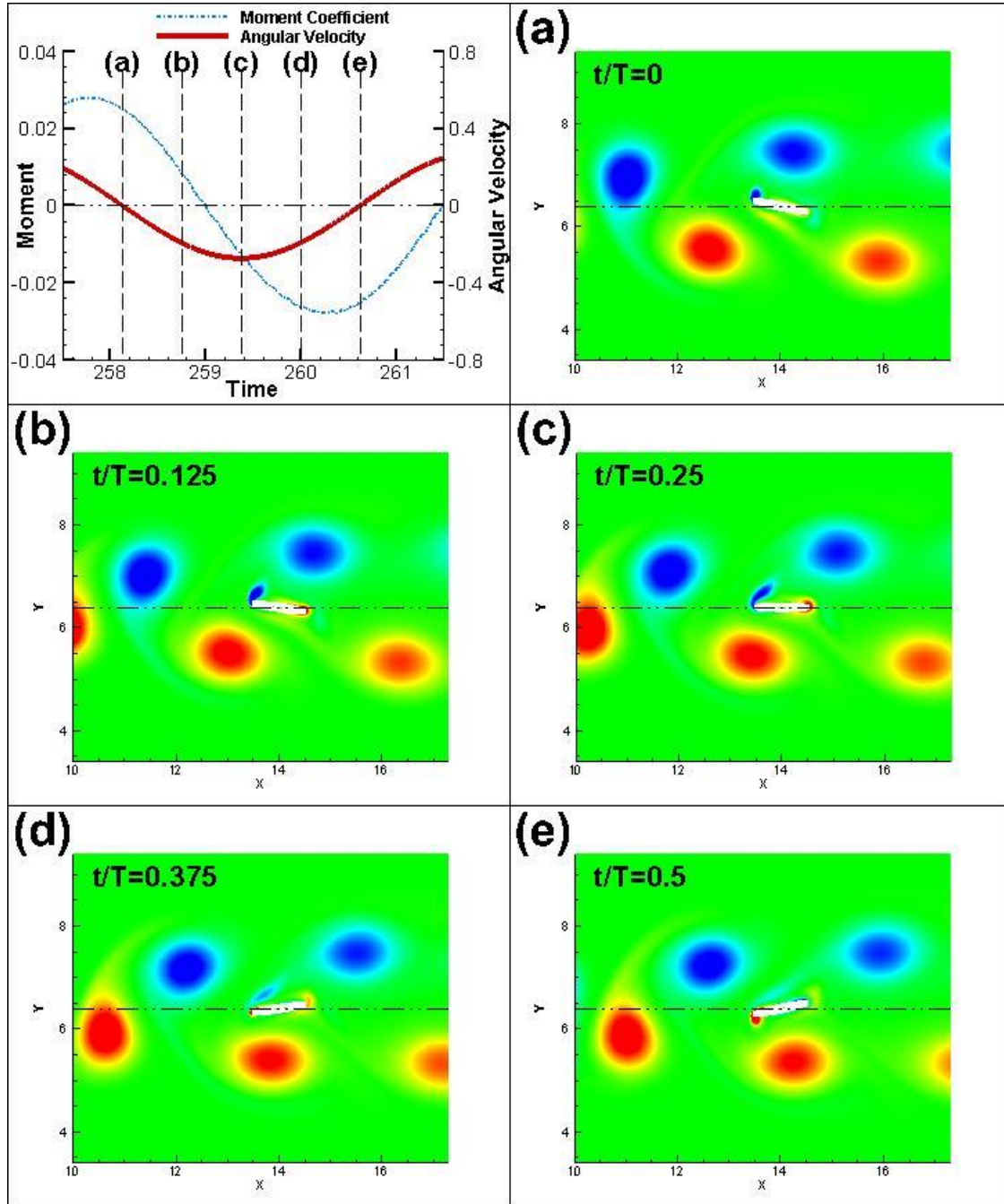


Figure 6-17 Moment coefficients and angular velocity and vorticity contours of the airfoil over the half cycle of downstroke for the case with $A_a = 12.5^\circ$ and $\phi = 135^\circ$.

The chord of the airfoil is considered to be approximately parallel to the streamwise direction in cases with small pitching amplitudes. Therefore, the analysis of interaction

modes for LEVs under such a circumstance is similar to that with purely heaving motions. The remained CW LEV at $t/T = 0$ is associated with reinforcing modes from both the CCW vortex in front of the airfoil and the CW vortex in the airfoil region. Although the suppressing mode from the CCW vortex behind the airfoil exists, the CW LEV, on the whole, is being reinforced from $t/T = 0$ to 0.25. At $t/T = 0.25$, a CW vortex newly enters the region in front of the airfoil, which carries a strong suppressing mode for the CW LEV. In addition, the centroid of the CW vortex under the airfoil just passes the LE of the airfoil and steps into the airfoil region, where it also obtains a suppressing mode to the CW LEV. An overall suppressing mode for the CW LEV is established at $t/T = 0.25$, though the reinforcing mode from the CW vortex behind the airfoil remains. In analogy to the analysis for purely heaving motion with small amplitudes, this suppressing mode for the CW LEV on the upper surface of the airfoil accelerates the onset of the CCW LEV on the lower surface since the pitching amplitude in Fig. 6-17 is very small. This CCW LEV is fully developed at the end of the counter-clockwise pitching motion, i.e. Fig. 6-17 (e), which is about to generate a negative moment coefficient and destroy the input power for the consecutive clockwise pitching.

On the other hand, differing from that with purely heaving motions, the analysis of interaction modes for TEVs with purely pitching motions should employ the conclusions in Table 2. At $t/T = 0$, no TEV is clearly observed. With the counter-clockwise pitching motion, a CW TEV may be formed on the lower surface of the airfoil in the single airfoil case. However, with the vortex topology in Figs. 6-17(a) and (b), the suppressing modes are exerted from both the CW vortex on the top of the airfoil and the CCW vortex behind the airfoil, yet the reinforcing mode is only from the CCW vortex in front of the airfoil.

As a consequence, there is no CW TEV formed in these two figures, yet a very weak CCW TEV appears on the upper surface of the airfoil at $t/T = 0.25$. Unfortunately, the vortex topology since then, i.e. $t/T = 0.25, 0.375$, and 0.5 , preserves an overall suppressing mode for this low strength CCW TEV. Hence, it is swiftly suppressed and almost vanishes at $t/T = 0.375$.

In terms of the moment generation, the interaction modes matter. At $t/T = 0$ (see Fig. 6-17(a)), the CW vortex on the top of the airfoil is approximately aligned on the center of the airfoil with a distance and no other vortex is in the airfoil region. The moment coefficient, only with this vortex, might be close to zero. However, the resultant moment coefficient at $t/T = 0$ almost reaches its largest value in Fig. 6-17. Therefore, it can be speculated that the small CW LEV is critical for producing the positive moment coefficient. Indeed, the presence of this LEV makes adverse contributions to the favorable input power, and the overall suppressing mode is not achieved until $t/T = 0.25$. Fortunately, at the next stage, i.e. $t/T = 0.125$, the CCW vortex in front of the airfoil gets into the airfoil region under the LE, and the CW vortex reaches above the TE. Both of them induce negative moment coefficients, which balance the potential positive value that the CW LEV would produce. Hence, a very small positive moment coefficient is actually obtained from the simulation at $t/T = 0.125$. After that, the CW vortex on the top of the airfoil travels away, and the CCW on its bottom contributes more and more to negative moment coefficients. In Fig. 4-44(e), the CCW vortex may still do no harm to the input power since it is just aligned on the center of the airfoil, yet the developed CCW LEV on the lower surface of the airfoil retains the negative moment coefficient.

It is worth noticing that the CW LEV Fig. 6-17(a) is reinforced by the CCW vortex in front of the airfoil and the CW one above the airfoil. Although the presence of the CW LEV is not good for the favorable input power, its negative impact is immediately alleviated by the positive efforts made by the latter two vortices. This balancing process will often be observed in the future analysis of purely pitching airfoils. With this process, the best input power with purely pitching motions would not be too low and the worst one would not be too high. The situation is just the opposite in the analysis with purely heaving motions. A good example is the CW vortex on the top of the airfoil. Because this vortex is in the airfoil region, it not only reinforces the formation of the CW LEV but also directly produces a positive lift coefficient; both of these consequences make appreciably negative contributions to favorable input power. Therefore, a very bad input power is obtained. All in all, the balancing process could be the key to explain why the variation of the resultant input power with purely pitching motions is much smaller than that with purely heaving motions.

On the other hand, the formed LEVs and TEVs influence the output power of purely heaving airfoils primarily through skin friction, while their impact on the output power of purely pitching airfoils can be directly through pressure, which is an order of magnitude larger than the skin friction. This situation becomes more severe when the pitching amplitude is relatively large. Consequently, it is acceptable that the variation of the resultant output power with purely pitching motions is usually larger than that with purely heaving motions.

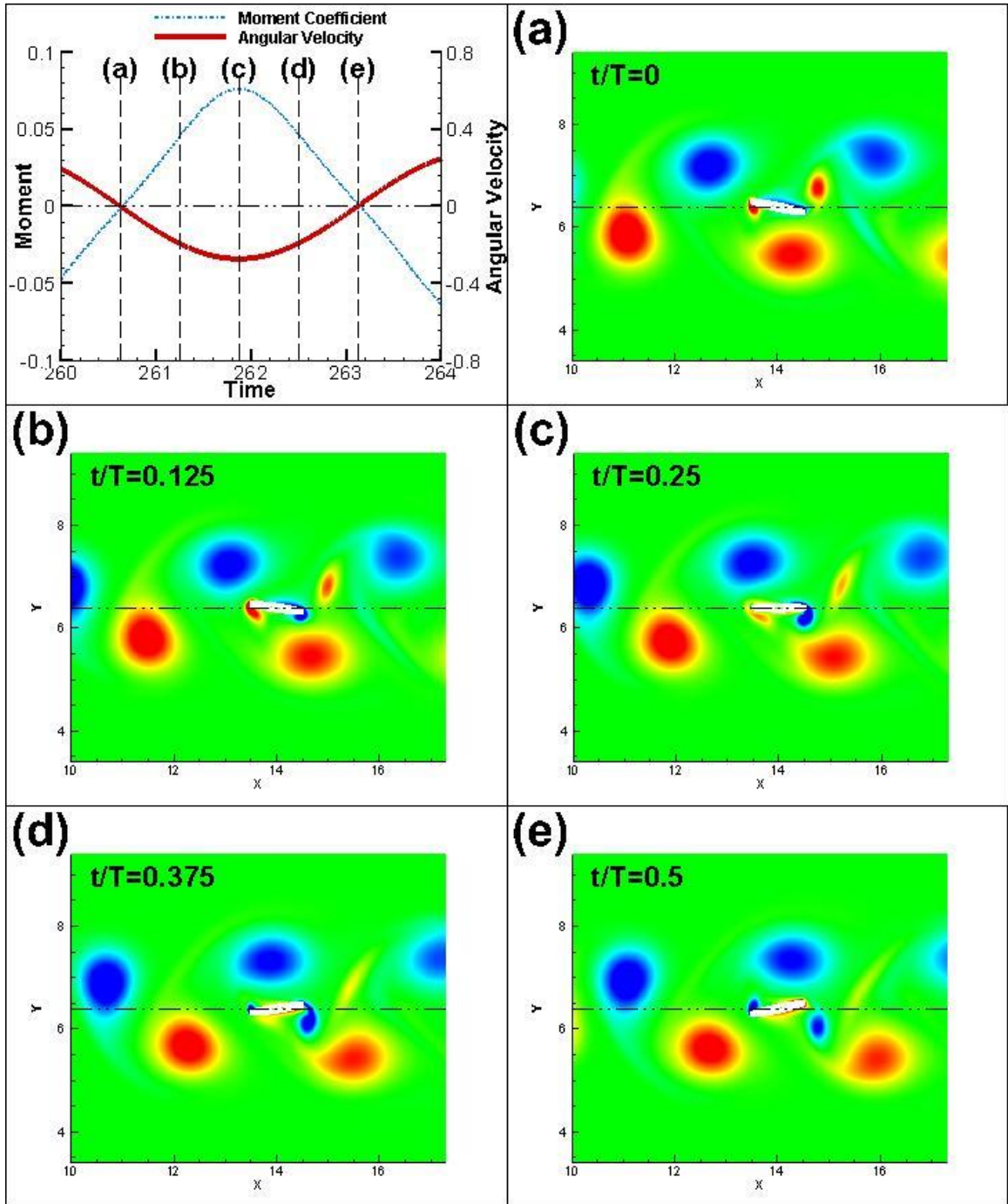


Figure 6-18 Moment coefficients, angular velocity, and vorticity contours of the airfoil over the half cycle of downstroke for the case with $A_a = 12.5^\circ$ and $\phi = 315^\circ$.

The vortex topology in Figs. 6-18 (a) and (b) obtains two reinforcing modes for the CCW LEV on the lower surface of the airfoil from both the CW vortex in front of the

airfoil and the CCW one in the airfoil region. Although one suppressing mode is presented from the CW vortex behind the airfoil, the CCW LEV is reinforced and growing till $t/T = 0.25$. After that, a CCW vortex freshly enters the region, in front of the airfoil, the CW vortex above the airfoil steps into the airfoil region and the CCW below the airfoil travels away from the airfoil, as shown in Fig. 6-18(c). An overall suppressing mode is obtained for the CCW LEV and slightly triggers the formation of the CW LEV on the upper surface of the airfoil, as shown in Fig. 6-17(e).

The vortex topology in Figs. 6-17 (a) and (b) produces an overall suppressing mode with the CCW TEV, which stirs the formation of the CW TEV on the lower surface of the airfoil. However, this CW TEV starts to be suppressed in Fig. 6-17(c), since the vortex topology is substantially changed. Therefore, even though the strength of the CW TEV is not obviously diminished in Figs. 6-17(c)~(e), this TEV is no longer attached to the airfoil.

A balancing process mentioned in the discussion of Fig. 6-16 is again observed for the case in Fig. 6-17. The CCW vortex in the airfoil region in Fig. 6-17 (a) directly induces positive moment coefficients which overwhelm the negative ones potentially produced by the CCW LEV, which is reinforced by the former vortex. The maximum positive moment coefficient is achieved at $t/T = 0.25$ in Fig. 6-17(c). when the CCW LEV is almost suppressed, the CW TEV is fully developed and the CW vortex just reaches the spot above the LE of the airfoil.

In addition, the trade-off between the input and output power is again detected for the cases with small pitching amplitudes, i.e. in Figs. 6-16 and 6-17. Because of the small pitching amplitude, differences of output power are primarily contributed by the LEVs

and TEVs. The LEVs in Fig. 6-16 are always formed on the airfoil surface that does not encounter the flow directly. Therefore, with the absence of any TEVs, the drag is not surprisingly produced, and a bad output power is achieved. On the other hand, both LEVs and TEVs in Fig. 6-17 are formed on the airfoil surface that confronts the flow. Consequently, thrust is generated and a good output is accomplished.

6.1.3.2 Intermediate/Relatively Large Pitching Amplitudes

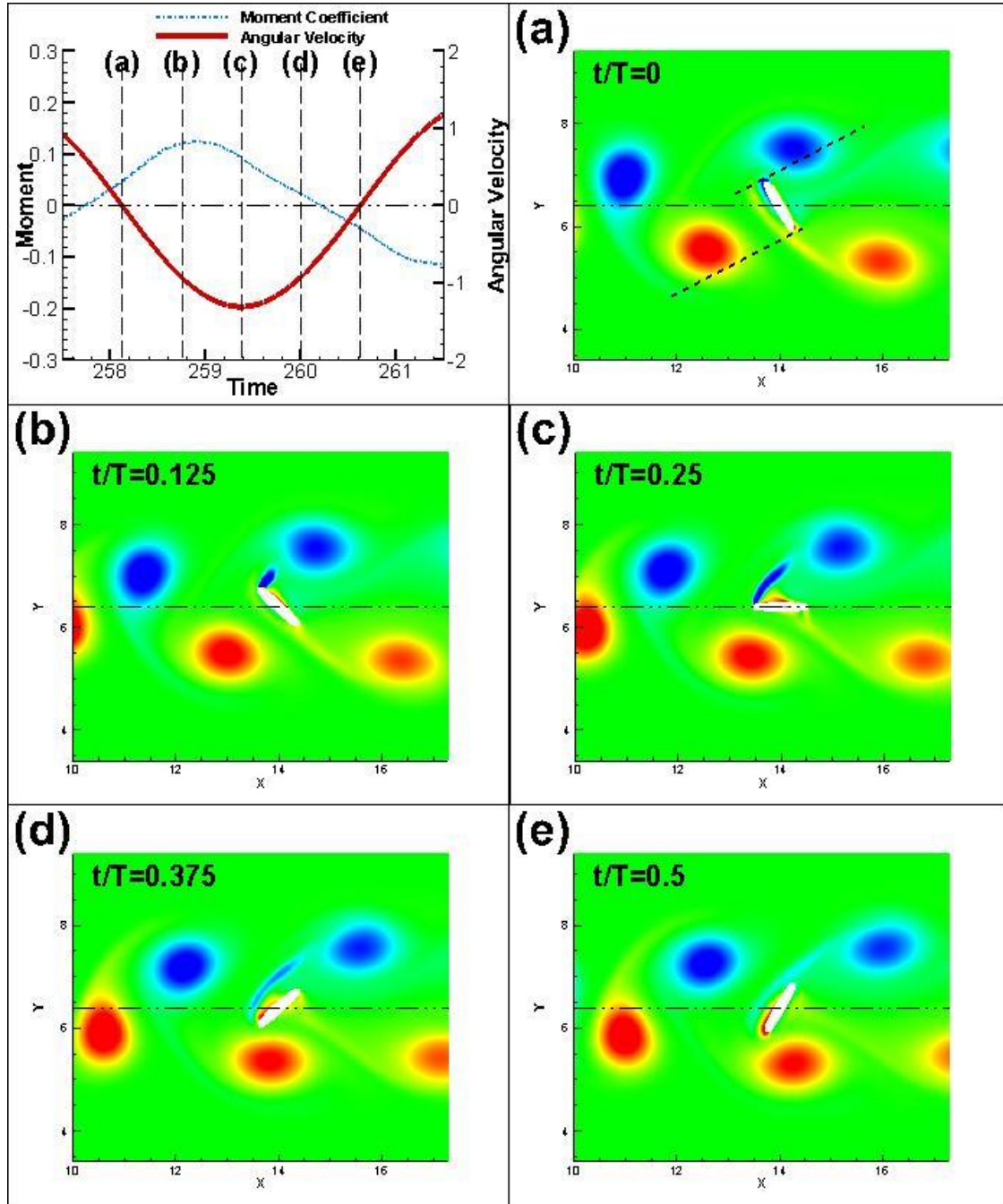


Figure 6-19 Moment coefficients, angular velocity, and vorticity contours of the airfoil over the half cycle of downstroke for the case with $A_a = 60^\circ$ and $\phi = 135^\circ$. Dashed lines in (a) are drawn from LE/TE in the normal direction corresponding to the chord of the airfoil.

The approach to determine interaction modes through the potential theory becomes complicated in the cases with relatively large pitching amplitudes, i.e. Fig. 6-19. Region #1~3 in the potential theory, strictly speaking, is defined corresponding to the airfoil whose chord is aligned with streamwise direction; those regions should be extrapolated very carefully in Fig. 6-19. For example, the CW vortex at $x = 14.5$ should be roughly recognized as “just entering the airfoil region”, the CCW vortex at $x = 12.5$ is “in the airfoil region but below the airfoil” and the CW vortex at $x = 16$ is behind the airfoil. Additional approximations could be added if acceptable. First, the effect of the CW vortex at $x = 16$ is negligible since its distance from the airfoil is too large, i.e. > 2 . Moreover, the reinforcing mode with CW LEV on the upper surface of the airfoil from the CW vortex at $x = 14.5$ might overwhelm the suppressing mode from the CCW vortex at $x = 12.5$, because the distance between the LE and the former vortex is noticeably smaller than the one between the LE and the latter vortex. Consequently, the reinforcing mode is identified for this CW LEV on the upper surface as the reinforcing mode in Fig. 6-19 (a). Notice that the balancing process does not exist yet since both the CW vortex at $x = 14.5$ and its reinforced CW LEV make adverse contributions to the favorable input power. This could be the reason that the cases with relatively large pitching amplitudes achieve much worse input power than that with small pitching amplitudes. Although the presence of the CCW vortex below the LE of the airfoil in Fig. 6-19(c) reduces the moment coefficient from its peak value obtained in Fig. 6-19(b), the moment is still positive until Fig. 6-19(e). Moreover, the CCW vortex located near the $x = 14$ in Fig. 6-19 (d) & (e) is approximately considered as “in the airfoil region” and primarily tends to establish a suppressing mode with the CW LEV. As the LEV on the upper surface of the

airfoil is suppressed and the CCW vortex near $x = 14$ gradually assists generating more negative moment, a negative moment coefficient is finally achieved in Fig. 6-19 (e).

Similar to the discussion above, the overall interaction modes for the CCW TEV in Fig. 6-19 are mostly suppressing modes or nearly negligible influences, which results in no apparently observed TEV with the case in Fig. 6-19.

Last but not least, the CW LEV appearing in Figs. 6-19 (b) and (c) is on the surface of the airfoil that does not encounter the flow directly. In addition, because of the large pitching amplitude, there are some moments that the vortices stay in a region downstream but very close to the airfoil, i.e. the CW vortex at $x = 14.5$ in Fig. 6-19 (a) and the CCW vortex at $x = 14.5$ in Fig. 6-19 (e). Therefore, it can be speculated that the resultant output power for the case in Fig. 6-19 is not good or even worse than that for cases with small pitching amplitudes, which is exactly confirmed by Fig. 6-16.

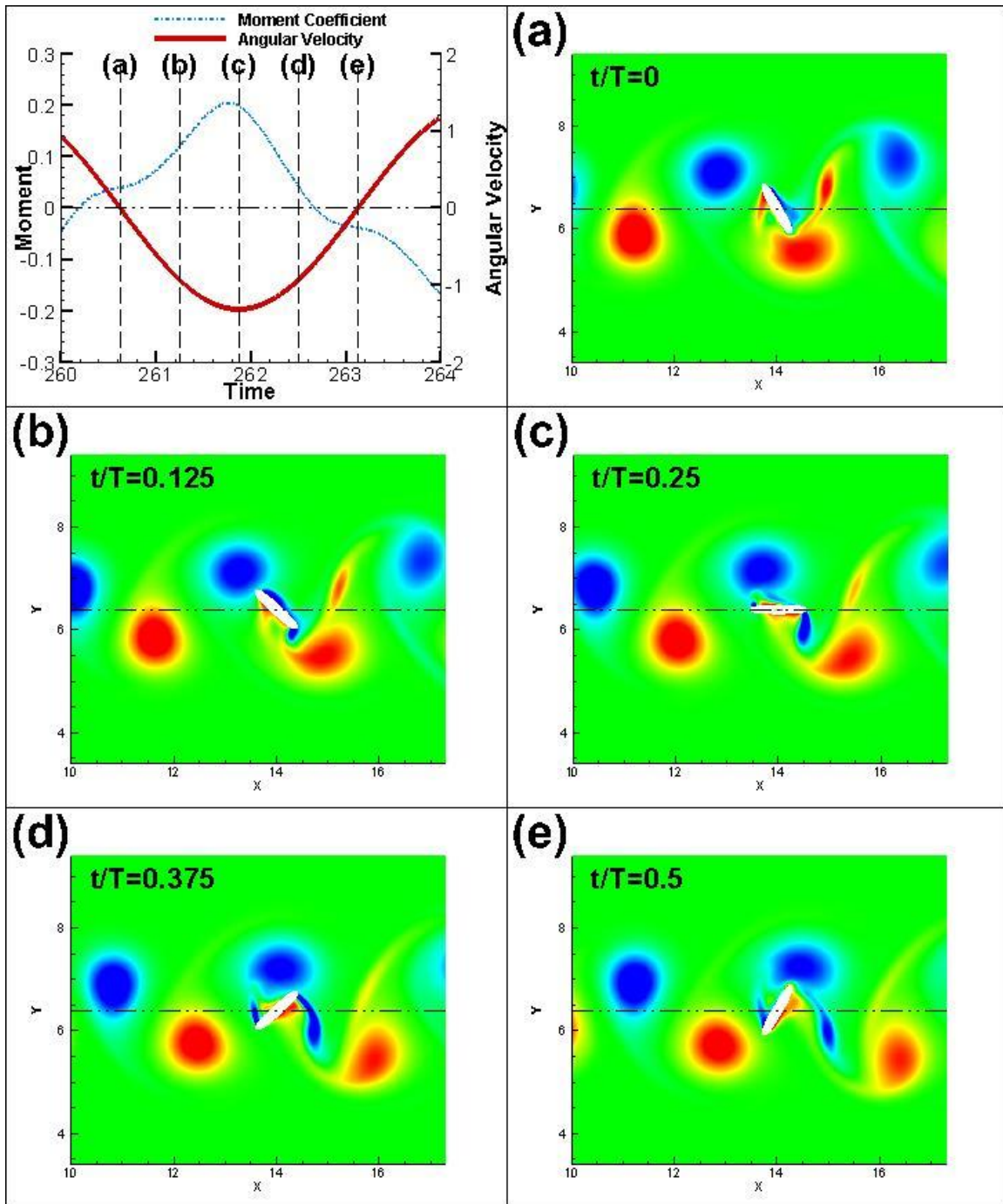


Figure 6-20 Moment coefficients, angular velocity, and vorticity contours of the airfoil over the half cycle of downstroke for the case with $A_a = 60^\circ$ and $\phi = 315^\circ$.

Interaction modes with LEVs and TEVs in Fig. 6-20 are not very clear. However, due to the relatively large pitching amplitudes, the airfoil substantially interacts with incoming vortices and changes their shapes and paths. Additionally, the pitching motion

makes it tougher to identify the “real” positions of the incoming vortices corresponding to the airfoil. The rules-of-thumb from the potential theory concluded in Tables 1 and 2 are not suggested for the analysis under this circumstance.

6.1.4 Summary of Active Energy Harvesters

The energy harvesting of a purely heaving/pitching airfoil in the wake of an oscillating D-cylinder was studied numerically. This configuration including an upstream vortex generator, i.e. a cylinder, and a downstream airfoil can be easily extended to mimic natural flyers with tandem foils, i.e. a dragonfly or an MAV flying in the wake of objects, i.e. building. The phase difference between the motion of the cylinder and airfoil was confirmed to be of pivotal importance for the resultant powers. It was quantitatively demonstrated by the potential theory that the topology of the incoming vortices has the capability to tune the interaction modes between the incoming vortices and the LEVs and TEVs. The latter two edge vortices, then, directly influence the force generation and the resultant powers. Simple rules-of-thumb were made out of the potential theory to expressly comprehend the mapping between the phase difference and the resultant powers. Those theoretical predictions exhibited an acceptable capacity to analyze two-dimensional results from numerical simulations. A trade-off between input and output power was found for both purely heaving and purely pitching airfoils. Also, with purely heaving motions, the input power has the tendency to be negative, which is barely observed in cases with purely pitching motions. Moreover, the phase-lag between the heaving and pitching motions was confirmed to be around 90° in order to achieve the best efficiency of energy extraction with combined flapping motions. Furthermore, under

similar circumstances, i.e. vertical displacements of the LE point of the airfoil, the range of input power that can be tuned by purely heaving motion is larger than that by pitching motions, yet the situation for output power is just the opposite. Particularly, with relatively large purely heaving amplitudes or pitching amplitudes, there are some risks to access very bad input or output powers, respectively. In other words, the choices of operational parameters for flapping airfoils with combined motion are biased. Good operational parameters for the heaving motion have the highest priority when an excellent input power is expected, while good ones for the pitching motion have precedence for requests of substantial output powers. This is particularly true for combined motions involving both relatively large heaving and pitching motions, i.e. some bio-inspired applications⁴³⁻⁴⁶.

Finally, future work could be accomplished to discuss the influence of the advance ratios¹⁷¹ on the capacity of the energy extraction. The conclusions can be used later to interpret the energy extraction of an MAV not only flying in the wake of an object but also approaching it.

6.2 Energy Harvesters with Passive Heaving Motions

A two-dimensional problem similar to the previous section is considered. In order to provide significant incoming vortical wakes, a D-cylinder is chosen to generate the incoming vortices. The D-cylinder is forced to heave as

$$y_c(t) = h_c \sin(2\pi f_c t) \quad (6.11)$$

The frequency, f_c , is fixed at 0.2 for all the cases, and h_c varies from 0.1 to 0.7 with an increment of 0.15. The foil has an elliptical shape with a ratio of 10 and is only mobile in the transverse direction. The pitching motion is not considered in the current study, firstly, for the sake of simplicity. Secondly, as mentioned in previous studies^{31, 172}, the energy extraction from pitching motions is negligible compared to that from heaving motions. The foil is mounted on a spring and a damper; foils with zero damping would not retrieve any energy harvesting capability. The dynamical properties are $M_{red} = 2$, $U_{red} = 4$, and $\xi = 0.5$. The diameter of the cylinder is equivalent to the chord length of the foil, which results in $Re = 200$. The distance between the airfoil and the cylinder are integers from 4 to 7. The presence of the foil would disturb the formation of vortices generated by the D-cylinder if a smaller distance was used⁴⁰.

After the numerical tests with variable domain sizes and grid sizes, the computational domain is selected as 25.6×12.8 and 0.0125 for the grid size. The RK3 scheme is used and the time step size is 256^{-1} . At the beginning of the simulation, the upstream cylinder heaves and the foil remains stationary until its force coefficients achieve periodic states. Then, the fluid-structure interaction model is enabled for the foil only.

In the interest of quantifying the energy harvesting capacity of the passive heaving airfoil, the energy harvesting efficiency is defined as the portion of the incoming flow energy flux through the cross-sectional area covered by the moving foil^{32, 172},

$$\eta = \frac{P_F}{0.5\rho \int_{Y_-}^{Y_+} U^3 dY} \quad (6.12)$$

where Y_+ and Y_- are the highest and lowest vertical positions of the center of the foil and U is the speed profile of the incoming flow. With uniform incoming flows, the efficiency can be calculated with $U = U_\infty$ ^{30, 32}; the same condition is adopted to estimate the efficiency in the current study, since the vortices generated from the cylinder are symmetrically distributed corresponding to the mean position of the foil and approximately propagated with the free stream velocity. The extracted energy, or input power, is represented as P_F , which is the time-averaged value of instantaneous power transfer from the flow to the foil,

$$P_F = C_Y \frac{dY}{dt} \quad (6.13)$$

where C_Y is the force coefficient on the vertical direction, i.e. the lift coefficient.

6.2.1 Types of Foil Responses

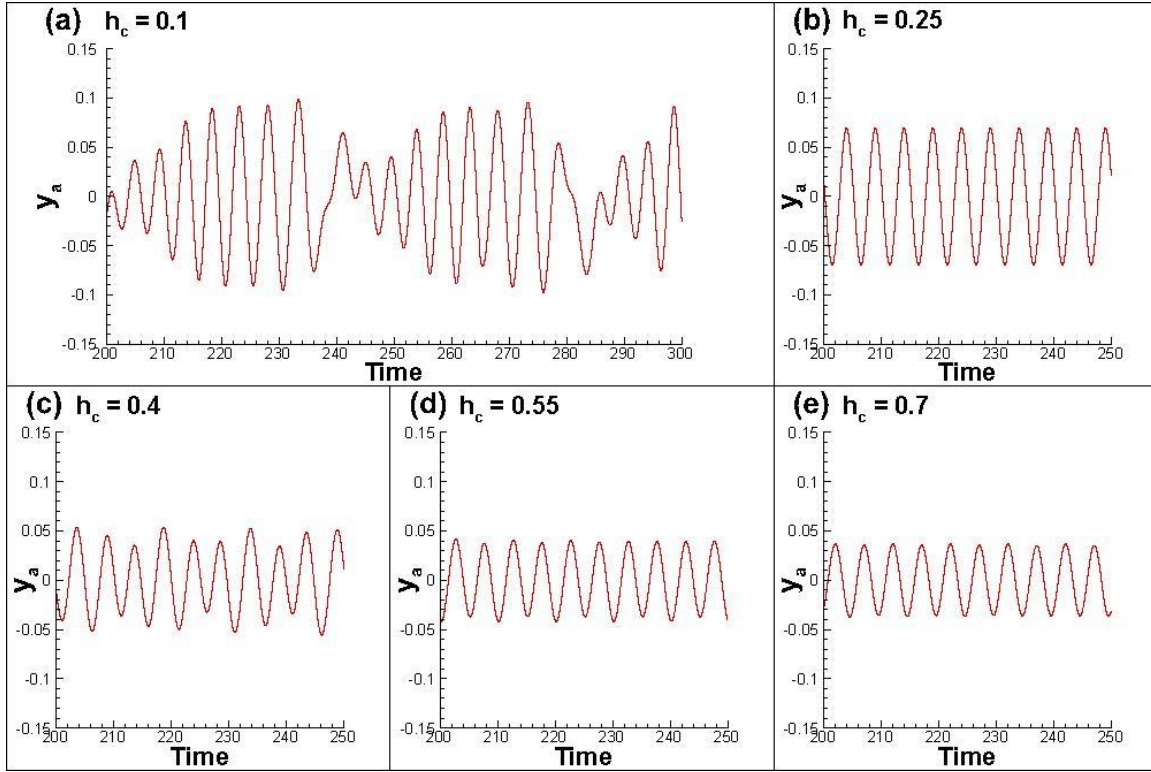


Figure 6-21 Histories of vertical positions for all the cases with varying h_c but same $L = 7$.

Three primary types of dynamic response are identified among all the cases simulated in the current study. Examples are illustrated in Fig. 6-21. Typically, the foil in the cases with very small h_c , e.g. 0.1, undergoes quasi-periodic heaving motions. The second type of response is a semi-periodic motion which occurs at relatively high intermediate h_c , i.e. Fig. 6-21(c). The final type, which is the periodic response, is achieved with either a moderate intermediate h_c , e.g. 0.25, or a very large h_c , e.g. 0.55 and 0.7. It is not difficult to explain the periodic response with a large h_c . If the amplitude of vortex generator is very large, the incoming vortices are away from the foil and their influence on the foil becomes negligible, according to the Biot-Savart law. Then, the foil extracts energy from the flow close to uniform flow and that type of interactions easily shows periodic.

However, it should be noted that with the same dynamic parameters of the studied foil here, no motion has been detected for a single foil with just uniform incoming flow. Therefore, the cases with a large h_c in the current work still retain energy harvesting capability. Our interest is more in the cases with an intermediate h_c , i.e. 0.25. They produce not only periodic responses but also larger foil motion amplitudes, e.g. y_a , compared with those cases with a very large h_c . We call this type of responses the desired periodic response, since larger foil amplitudes in periodic motions usually imply better energy harvesting performance, which will be discussed later.

Since cross-flow distance between the two layers of the incoming vortices is proportional to the heaving amplitude of the vortex generating cylinder, observations detected in Fig. 6-21 can be summarized in the subsequent way. With an increasing vortex street span of incoming vortices, which is due to the increasing amplitude of the vortex generating cylinder, the response of the foil is gradually recovering back to that of a single foil. Before that, non-periodic responses are usually obtained, yet the foil has a chance to achieve the desired periodic response at moderate intermediate span of the incoming vortex street.

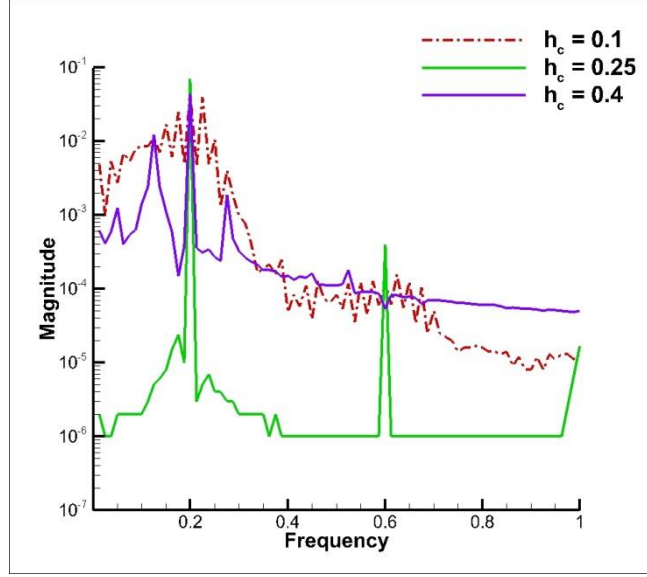


Figure 6-22 FFT for the histories of y_a for different cases with $L = 7$

The primary driven frequency is 0.2, which is the oscillating frequency of the upstream vortex generator, for all of the three kinds of dynamic responses. Cases with periodic responses, i.e. $h_c = 0.25$ in Fig. 6-22, obtains a very clean frequency spectrum. On the other hand, random noises appear in the cases with non-periodic responses, i.e. $h_c = 0.1$ or 0.4 in Fig. 6-22. Therefore, it is not a trivial task to choose the averaging period for the input power, P_F . Based on Figs. 6-21 and 6-22, seven oscillation periods of the upstream cylinder, which is 35 dimensionless computational time, are selected to be the averaging interval for the calculation of energy efficiency.

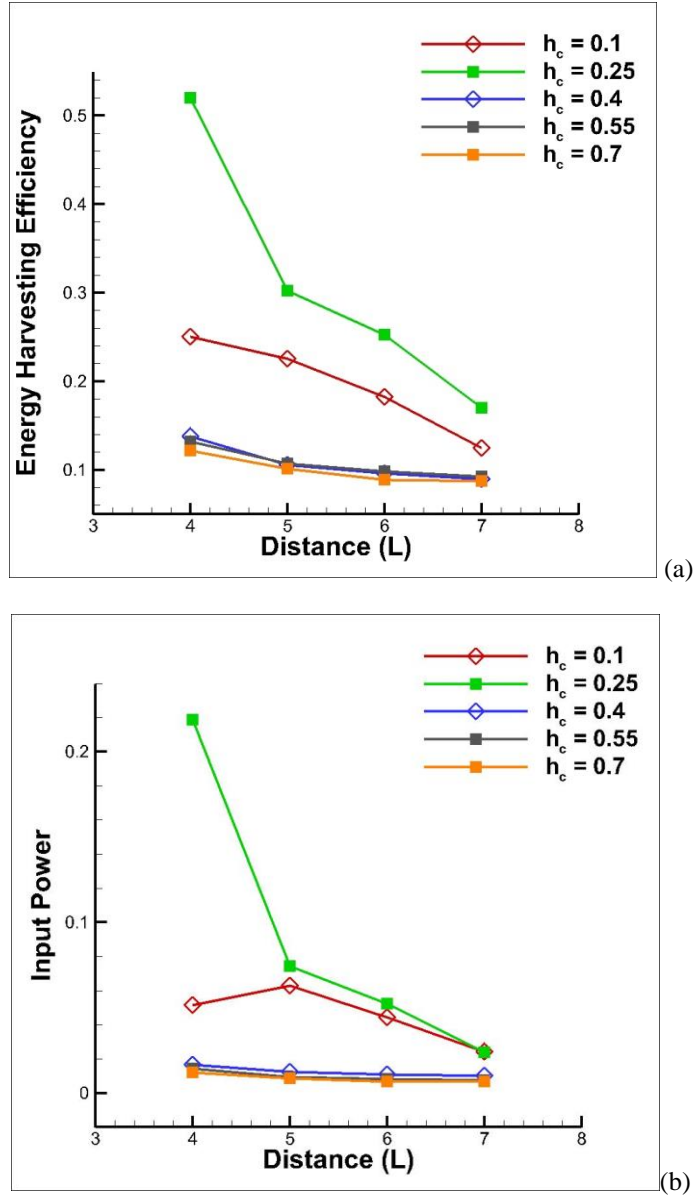


Figure 6-23 Comparison of (a) energy harvesting efficiency and (b) input power among all cases

As discussed before, with a very large h_c , i.e. 0.55 or 0.7, both the energy harvesting efficiency and the input power are very low; this also occurs at a relatively high intermediate h_c , e.g. 0.4. The input power is almost zero, which is the value obtained by the simulation with a single airfoil without incoming vortices. The other two curves in Fig. 6-23, e.g. $h_c = 0.1$ & 0.25, gain more attention. The cases with $h_c = 0.25$ achieve

desired periodic responses with larger maximum y_a compared with other periodic response cases, which are with a very large h_c . Therefore, significantly better energy harvesting efficiency is expected for the former cases, which is consistent with Fig. 6-23. On the other hand, in Fig. 6-21, the maximum y_a of the case with $h_c = 0.1$ is apparently larger than that of the case with $h_c = 0.25$, yet neither the energy harvesting efficiency nor the input power of the former cases is better than that of the latter ones. It confirms that non-periodic responses are not desired for efficient energy harvesters^{30, 32, 172}.

Finally, it is because of the vortex dissipation due to the viscous effect that both the efficiency and input power decrease as the distance between the foil and the cylinder increases for the cases with certain heaving amplitude of the cylinder.

6.2.2 Vortex Topology

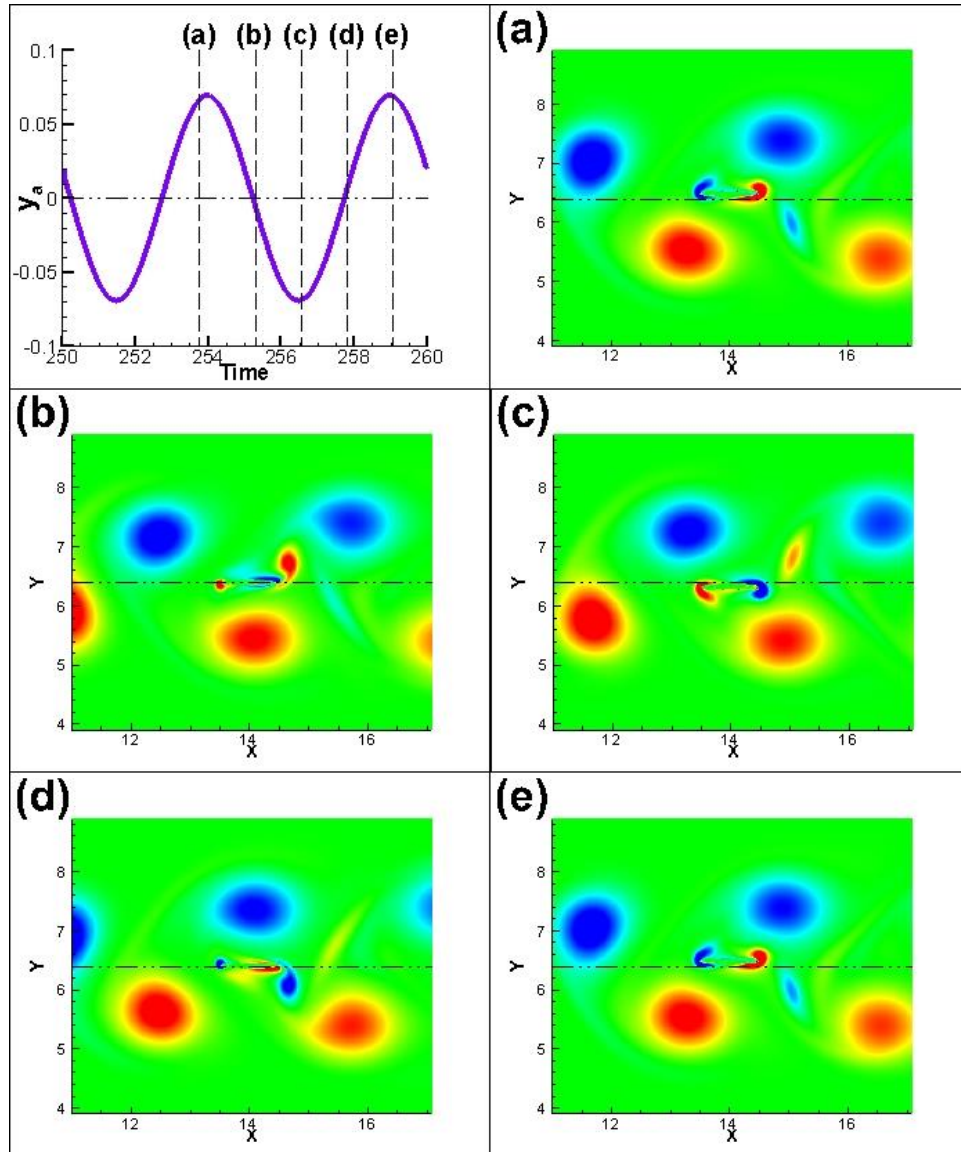


Figure 6-24 The history of approximate foil positions and vorticity contours over the oscillating cycle of the foil for the case with $h_c = 0.25$

The vortices shown in Fig. 6-24 are very clean, which is the case of the moderate intermediate amplitude case. Both incoming vortices and induced vortices on the surface of the foil make positive contributions to the dynamic response of the foil. A good example is illustrated in Fig. 6-24 (b). At this moment, the foil is in the middle of stroking

downwards. Not only is an incoming positive vortex under the foil, but also a leading edge vortex (LEV) is induced on its lower surface and no trailing edge vortex (TEV) is attached. Both of these vortices are obligated to produce the negative lift coefficient, which reinforces the foil's down-stroking motion. In Fig. 6-24 (b) and (c), the positive vortex under the foil is travelling away from the region of the foil, which is defined as the streamwise area from the leading edge to the trailing edge of the foil in the current work, and the negative incoming vortex above the foil has not arrived yet. However, the topology of incoming vortices in these two figures has the tendency to reinforce the formation of the positive LEV and the negative TEV; the strong induced surface vortex on the bottom of the foil still helps generate negative lift force until the end of the period. A good discussion of the impacts of incoming vortices on the formation of the LEVs and TEVs of the foil can be found in the last section or Wei & Zheng¹⁷³. Interestingly, although the LEV and TEV that remain in Fig. 6-24 (c) are strong, at the next moment, e.g. Fig. 6-24 (d), the strength of the positive LEV on the lower surface of the foil is quickly suppressed, and instead, a negative LEV is formed on its top surface. In addition, the TEV is detached from the foil. Most importantly, the negative incoming vortex enters the foil region and is located very close to the foil. The vortex topology swiftly shifts and becomes favorable to assist the foil in stroking upwards, which is consistent with the moving trend of the foil at this moment according to y_a history plotted in Fig.6-24.

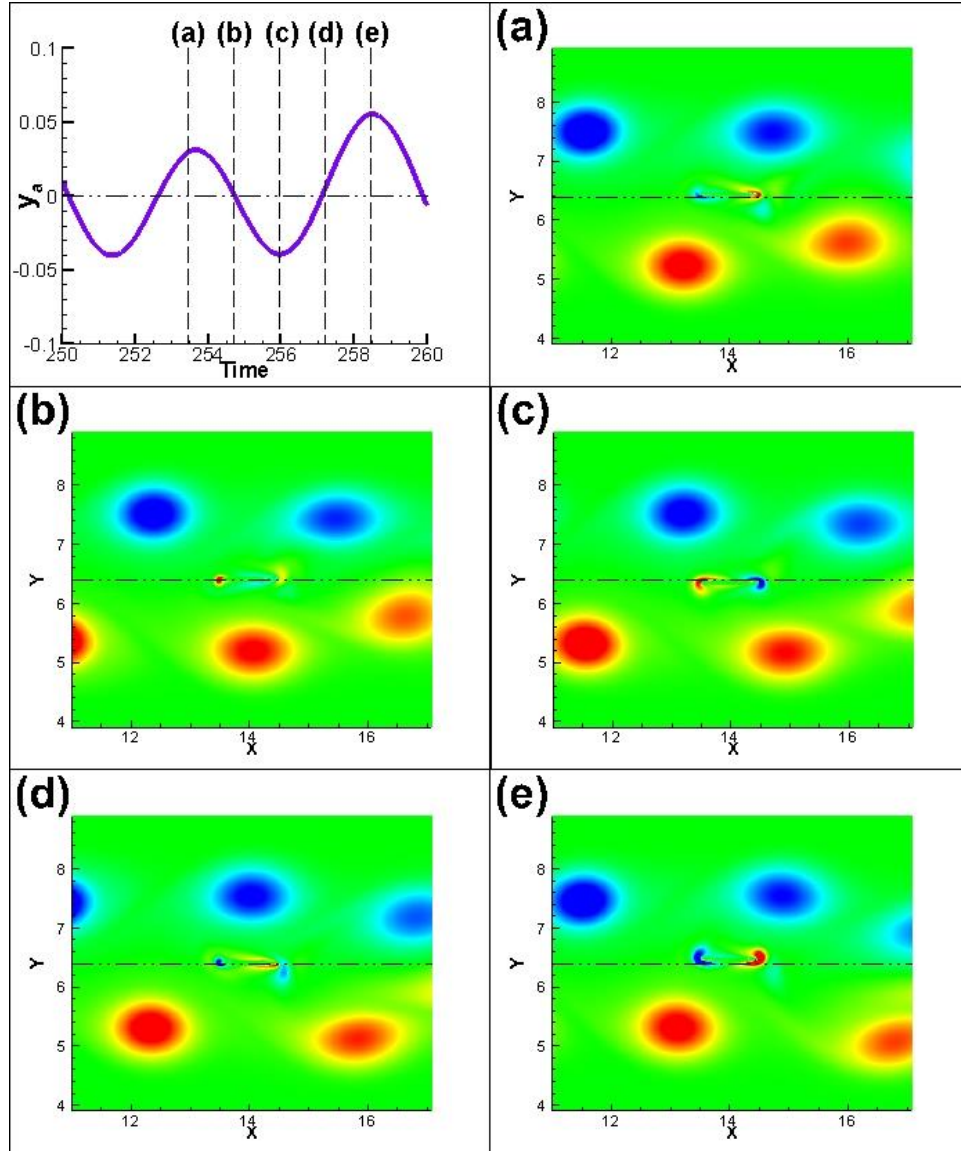


Figure 6-25 The history of approximate foil positions and vorticity contours over the oscillating cycle of the foil for the case with $h_c = 0.4$

The vortices and their topologies exhibited in Fig. 6-25 for the high intermediate amplitude case are very similar to those in Fig 6-24. However, differences can still be detected. First, the vertical distances between the incoming vortices and the foil in Fig. 6-25 are larger than those in Fig. 6-24, which prevents significant influences from incoming vortices on the foil including force generations and formations of LEVs and TEVs. As a

consequence, the force generations due to such vortex topologies have weaker resistance to the damper attached to the foil, resulting in less extracted energy than the case with $h_c = 0.25$. Moreover, since the effects of incoming vortices on the foil cannot be completely ignored in this case, the competitions among the damper, incoming vortices, and weakly-induced surface vortices do not give the system a very distinctly stable response; instead, it results in a semi-periodic response, as shown in Fig. 6-21 (c).

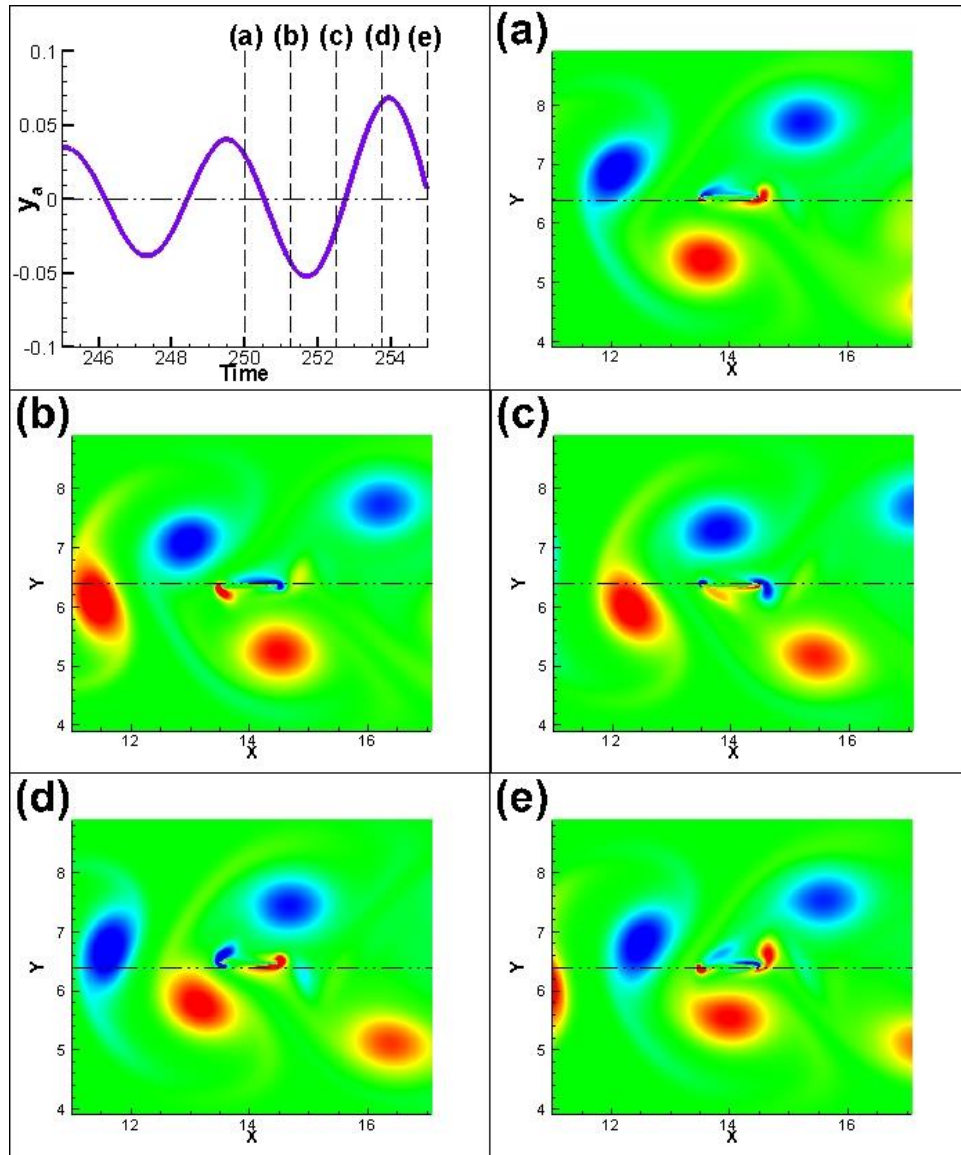


Figure 6-26 The history of approximate foil positions and vorticity contours over the oscillating

cycle of the foil for the case with $h_c = 0.1$

It is apparent that the vertical locations of the incoming vortices in Fig. 6-26 for the small amplitude case are very close to the mean position of the foil before their interactions. Under this circumstance, the foil substantially interacts with the incoming vortices and drastically influences the trajectories of the incoming vortices. Consequently, a two-way coupling is established between the incoming vortices and the energy harvester, and very non-linear phenomena may be induced. This could be the primary reason that, with $h_c = 0.1$, the dynamic response of the foil is quasi-periodic, which is not a good way to extract energy from the vortical wake.

6.2.3 Summary of Passive Energy Harvesters

It is found that energy harvesters, i.e. foils, function better with the presence of vortex generators, i.e. cylinders. However, well controlled properties of the generated wakes are necessary for good performance. A moderate width of a wake vortex street is preferable for the desired dynamic responses and optimal energy extraction performance of the harvesters.

In reality, it is not obligatory for good vortex generators to be very complicated; good examples could be a stationary cylinder, a passive mobile cylinder, or an actively oscillating cylinder. Simple objects like those have the potential to boost the performance of the harvester. Nevertheless, it may demand another systematic study to reveal the ideal size of the cylinders, their dynamic properties, and the relative positions corresponding to the harvester.

7 Conclusion

The conclusions for each section have been summarized previously. In this chapter, the overall achievements of this thesis are illustrated in Fig. 7-1.

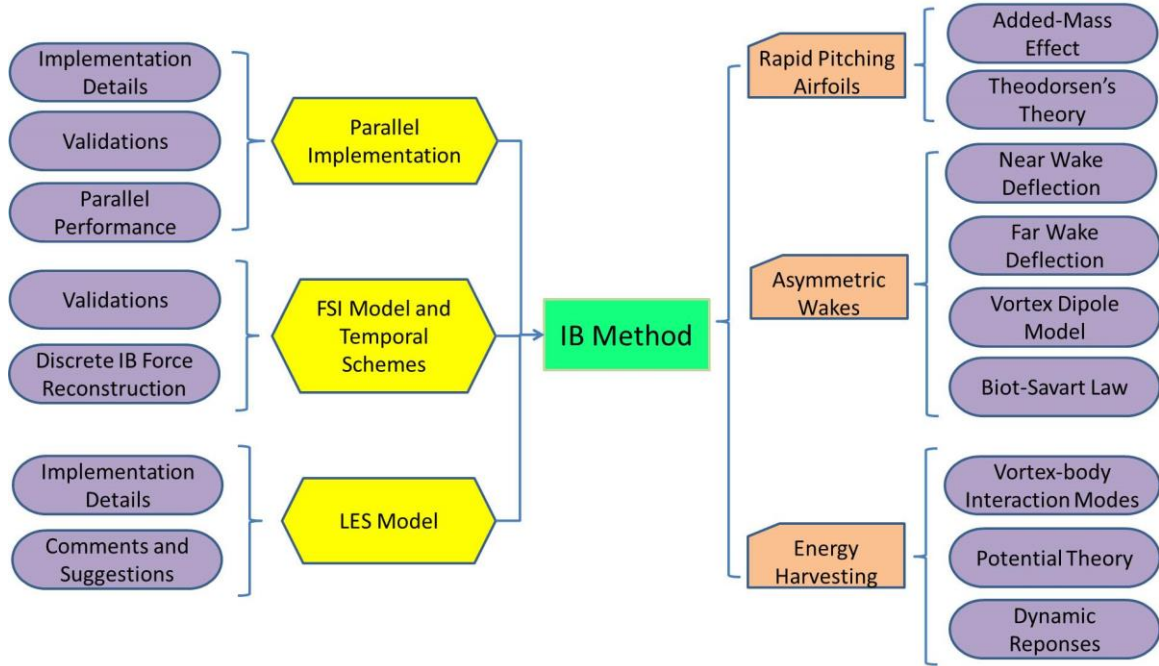


Figure 7-1 Summary of the dissertation.

The primary CFD algorithm employed in the current study is the IB method. The contributions of this dissertation regarding to the IB method can be summarized into the following three aspects.

1. The IB method is implemented in the parallel fashion with the assistance of the PETSc. It achieves good agreements in validations of the flow over solid bodies or through porous media. Implementation details are demonstrated; advanced MPI functions and good coding manner with parallel programs were found to be greatly helpful to enhance the parallel performance. The acceptable scalability is achieved; nonetheless potential improvements can still be made for future research. For example, the

calculations related to the IB points are not implemented in a completely parallelized approach, which may become a bottleneck to scale the current scheme to large-scale problems.

2. Different types of temporal schemes are discussed. The 1st-order temporal scheme with pressure shows its advantage in a three-dimensional simulation with coarse meshes. Without directly calculating the pressure field, the temporal schemes, i.e. the 1st-order temporal scheme without pressure and the RK3 scheme, require higher spatial resolutions compared with the one with the direct pressure solution, i.e. the 1st-order temporal scheme with pressure. The RK3 scheme provides much better numerical stability and higher order temporal accuracy, which is used in the IB method coupling with the FSI model and LES. The loosely-coupled FSI model is successfully coupled with IB method and the validation cases obtains good agreement in comparisons.

3. The IB method is tested to couple with LES, yet it has not been fully accomplished. Nevertheless, results and comments are summarized based on numerous testing cases for future research. The S-AMR is highly recommended since the near wall high spatial resolution is inherently desired for LES. Furthermore, the IB method with discrete forcing term in the current study suffers from the diffused interface issue; therefore, the sharp interface IB method is suggested to improve the local resolution of the IB method near the immersed boundaries.

With the IB method, three aerodynamic problems related to flapping foils have been studied. The contributions are achieved on the in-depth understanding of fluid dynamics.

1. The IB method is further validated with the case of rapid pitching airfoil. The results are well agreed with other simulations, experiments and canonical theories.

Theodorsen's theory divides the force generation of the airfoil to the circulatory part and the non-circulatory one, i.e. the added-mass effect. It explicitly demonstrated that the high-rate of sudden change of the motion results in substantial added-mass effect, which is unfavorable in terms of the loosely-coupled FSI model employed in the current work.

2. The current study deliberately investigated the asymmetric wakes downstream of a single heaving airfoil. It not only discussed the factors influencing the near wake deflection and theoretically interpolates the magnitude of the deflection angle but also explains the switch of vortex pattern in the far wake region. The potential theory is established to predict the development of the deflection angle from the near wake region to the far wake region. It provides a guideline to detect the trajectory of the irregular vortical wakes downstream of the airfoil.

3. The energy harvesting capacity of either passive or active flapping foil from vortical wakes is discussed. Two major vortex-body interaction modes are identified. The relation between the interaction modes and the energy extraction capacity of the active harvester is investigated. A potential theory is established to quantitatively demonstrate that the onset of those modes is primarily driven by the topology of the incoming vortices corresponding to the airfoil. Moreover, the passive energy harvester was found to perform better with the presence of the incoming vortical wakes instead of uniform free streams. However, moderate amplitudes of the wake are found to be preferable for desired stable response of the passive energy harvester to achieve an optimal energy harvesting capacity.

Reference

1. Betz, A. "Ein Beitrag zur Erklärung des Segelfluges," *Zeitschrift für Flugtechnik und Motorluftschiffahrt* Vol. 3, 1912, pp. 269-272.
2. Knoller, R. "Die Gesetze des Luftwiderstandes," *Flug und Mototechnik (Wien)* Vol. 3, No. 21, 1909, pp. 1-7.
3. Garrick, I. E. "Propulsion of a Flapping and Oscillating Airfoil," *NACA Rept. 567*, 1936.
4. Theodorsen, T. "General Theory of Aerodynamics Instability and the Mechanism of Flutter," *NACA Rept. 673*, 1935.
5. Koochesfahani, M. M. "Vortical Patterns in the Wake of an Oscillating Airfoil," *AIAA Journal* Vol. 27, No. 9, 1989, pp. 1200-1205.
6. Jones, K. D., Dohring, C. M., and Platzer, M. F. "Experimental and Computational Investigation of the Knoller-Betz Effect," *AIAA Journal* Vol. 36, No. 7, 1998, pp. 1240-1246.
7. Lua, K. B., Lim, T. T., Yeo, K. S., and Oo, G. Y. "Wake-structure formation of a heaving two-dimensional elliptic airfoil," *AIAA Journal* Vol. 45, No. 7, 2007, pp. 1571-1583.
8. Bratt, J. B. "Flow Patterns in the Wake of an Oscillating Airfoil," *Aeronautical Research Council, R&M2773*, 1950.
9. Sarkar, S., and Venkatraman, K. "Numerical simulation of incompressible viscous flow past a heaving airfoil," *International Journal for Numerical Methods in Fluids* Vol. 51, No. 1, 2006, pp. 1-29.
10. Lai, J. C. S., and Platzer, M. F. "Jet characteristics of a plunging airfoil," *AIAA Journal* Vol. 37, No. 12, 1999, pp. 1529-1537.
11. Heathcote, S., and Gursul, I. "Jet switching phenomenon for a periodically plunging airfoil," *Physics of Fluids* Vol. 19, No. 2, 2007, p. 027104.
12. Lewin, G. C., and Haj-Hariri, H. "Modelling thrust generation of a two-dimensional heaving airfoil in a viscous flow," *Journal of Fluid Mechanics* Vol. 492, 2003, pp. 339-362.
13. Blondeaux, P., Guglielmini, L., and Triantafyllou, M. S. "Chaotic flow generated by an oscillating foil," *AIAA Journal* Vol. 43, No. 4, 2005, pp. 918-921.
14. Zhang, X., Ni, S., Wang, S., and He, G. "Effects of geometric shape on the hydrodynamics of a self-propelled flapping foil," *Physics of Fluids* Vol. 21, No. 10, 2009, p. 103302.
15. von Ellenrieder, K. D., and Pothos, S. "PIV measurements of the asymmetric wake of a two dimensional heaving hydrofoil," *Experiments in Fluids* Vol. 44, No. 5, 2008, pp. 733-745.
16. Fuchiwaki, M., Kurinami, T., Tanaka, K., and Tabata, T. "Wake Structure of Heaving Elastic Airfoils and Their Dynamic Thrust," *Proceedings of the ASME 2009 Fluids Engineering Division Summer Meeting*. Vail, Colorado USA, 2009.

17. Godoy-Diana, R., Marais, C., Aider, J. L., and Wesfreid, J. E. "A model for the symmetry breaking of the reverse Benard-von Karman vortex street produced by a flapping foil," *Journal of Fluid Mechanics* Vol. 622, 2009, pp. 23-32.
18. Yu, M. L., Hu, H., and Wang, Z. J. "Experimental and Numerical Investigations on the Asymmetric Wake Vortex Structures around an Oscillating Airfoil," *50th AIAA Aerospace Sciences Meeting including the New Horizons Forum and Aerospace Exposition*. Nashville, Tennessee, 2012.
19. Liang, C. L., Ou, K., Premasuthan, S., Jameson, A., and Wang, Z. J. "High-order accurate simulations of unsteady flow past plunging and pitching airfoils," *Computers & Fluids* Vol. 40, No. 1, 2011, pp. 236-248.
20. Zheng, Z. C., and Wei, Z. "Study of mechanisms and factors that influence the formation of vortical wake of a heaving airfoil," *Physics of Fluids* Vol. 24, No. 10, 2012.
21. Triantafyllou, M. S., and Triantafyllou, G. S. "An efficient swimming machine," *Scientific American* Vol. 272, No. 3, 1995, pp. 64-70.
22. Taylor, G. K., Nudds, R. L., and Thomas, A. L. R. "Flying and swimming animals cruise at a Strouhal number tuned for high power efficiency," *Nature* Vol. 425, No. 6959, 2003, pp. 707-711.
23. Beal, D. N., Hover, F. S., Triantafyllou, M. S., Liao, J. C., and Lauder, G. V. "Passive propulsion in vortex wakes," *Journal of Fluid Mech.* Vol. 549, 2006, pp. 385-402.
24. Zhang, N., and Zheng, Z. C. "Flow/pressure characteristics for flow over two tandem swimming fish," *Computers & Fluids* Vol. 38, No. 5, 2009, pp. 1059-1064.
25. Moored, K. W., Dewey, P. A., Smits, A. J., and Haj-Hariri, H. "Hydrodynamic wake resonance as an underlying principle of efficient unsteady propulsion," *Journal of Fluid Mechanics* Vol. 708, 2012, pp. 329-348.
26. Jones, K. D., and Platzer, M. F. "Numerical computation of flapping-wing propulsion and power extraction," *35th Aerospace Sciences Meeting & Exhibit*. Reno, NV, 1997.
27. Anderson, J. M., Streitlien, K., Barrett, D. S., and Triantafyllou, M. S. "Oscillating foils of high propulsive efficiency," *Journal of Fluid Mechanics* Vol. 360, 1998, pp. 41-72.
28. Schouveiler, L., Hover, F. S., and Triantafyllou, M. S. "Performance of flapping foil propulsion," *Journal of Fluids and Structures* Vol. 20, No. 7, 2005, pp. 949-959.
29. Wang, Z. J. "Vortex shedding and frequency selection in flapping flight," *Journal of Fluid Mechanics* Vol. 410, 2000, pp. 323-341.
30. Peng, Z., and Zhu, Q. "Energy harvesting through flow-induced oscillations of a foil," *Physics of Fluids* Vol. 21, No. 123602, 2009, pp. 1-9.
31. Zhu, Q. "Optimal frequency for flow energy harvesting of a flapping foil," *Journal of Fluid Mechanics* Vol. 675, 2011, pp. 495-517.
32. Zhu, Q., and Peng, Z. "Mode coupling and flow energy harvesting by a flapping foil," *Physics of Fluids* Vol. 21, No. 033601, 2009, pp. 1-10.
33. Wu, T. Y. "Extraction of flow energy by a wing oscillating in waves," *Journal of Ship Research* Vol. 14, No. 1, 1972, pp. 66-78.

34. Liao, J. C., Beal, D. N., Lauder, G. V., and Triantafyllou, M. S. "Fish exploiting vortices decrease muscle activity," *Science* Vol. 302, No. 5650, 2003, pp. 1566-1569.
35. Gopalkrishnan, R., Triantafyllou, M. S., Triantafyllou, G. S., and Barrett, D. "Active vorticity control in a shear flow using a flapping foil," *Journal of Fluid Mechanics* Vol. 274, 1994, pp. 1-21.
36. Shao, X. M., and Pan, D. Y. "Hydrodynamics of a Flapping Foil in the Wake of a D-Section Cylinder," *Journal of Hydrodynamics* Vol. 23, No. 4, 2011, pp. 422-430.
37. Shao, X. M., Pan, D. Y., Deng, J. A., and Yu, Z. S. "Hydrodynamic performance of a fishlike undulating foil in the wake of a cylinder," *Physics of Fluids* Vol. 22, No. 11, 2010.
38. Streitlien, K., Triantafyllou, G. S., and Triantafyllou, M. S. "Efficient foil propulsion through vortex control," *AIAA Journal* Vol. 34, No. 11, 1996, pp. 2315-2319.
39. Xiao, Q., Sun, K., Liu, H., and Hu, J. X. "Computational study on near wake interaction between undulation body and a D-section cylinder," *Ocean Engineering* Vol. 38, No. 4, 2011, pp. 673-683.
40. Eldredge, J. D., and Pisani, D. "Passive locomotion of a simple articulated fish-like system in the wake of an obstacle," *Journal of Fluid Mechanics* Vol. 607, 2008, pp. 279-288.
41. Isogai, K., Fujishiro, S., Saitoh, T., Yamamoto, M., Yamasaki, M., and Matsubara, M. "Unsteady three-dimensional viscous flow simulation of a dragonfly hovering," *AIAA Journal* Vol. 42, No. 10, 2004, pp. 2053-2059.
42. Wang, Z. J., and Russell, D. "Effect of forewing and hindwing interactions on aerodynamic forces and power in hovering dragonfly flight," *Physical Review Letters* Vol. 99, No. 14, 2007.
43. Lan, S. L., and Sun, M. "Aerodynamic force and flow structures of two airfoils in flapping motions," *Acta Mechanica Sinica* Vol. 17, No. 4, 2001, pp. 310-331.
44. Maybury, W. J., and Lehmann, F. O. "The fluid dynamics of flight control by kinematic phase lag variation between two robotic insect wings," *Journal of Experimental Biology* Vol. 207, No. 26, 2004, pp. 4707-4726.
45. Broering, T. M., and Lian, Y. S. "The effect of phase angle and wing spacing on tandem flapping wings," *Acta Mechanica Sinica* Vol. 28, No. 6, 2012, pp. 1557-1571.
46. Broering, T. M., Lian, Y. S., and Henshaw, W. "Numerical Investigation of Energy Extraction in a Tandem Flapping Wing Configuration," *AIAA Journal* Vol. 50, No. 11, 2012, pp. 2295-2307.
47. Lim, K. B., and Tay, W. B. "Numerical analysis of the s1020 airfoils in tandem under different flapping configurations," *Acta Mechanica Sinica* Vol. 26, No. 2, 2010, pp. 191-207.
48. Rival, D., Hass, G., and Tropea, C. "Recovery of Energy from Leading- and Trailing-Edge Vortices in Tandem-Airfoil Configurations," *Journal of Aircraft* Vol. 48, No. 1, 2011, pp. 203-211.
49. Akhtar, I., Mittal, R., Lauder, G. V., and Drucker, E. "Hydrodynamics of a biologically inspired tandem flapping foil configuration," *Theoretical and Computational Fluid Dynamics* Vol. 21, No. 3, 2007, pp. 155-170.

50. Peskin, C. S. "Flow patterns around heart valves: a numerical method," *J. Comp. Phys.* Vol. 10, 1972, pp. 252-271.
51. Mittal, R., and Iaccarino, G. "Immersed boundary methods," *Annual Review of Fluid Mechanics* Vol. 37, 2005, pp. 239-261.
52. Peskin, C. S. "The Fluid-Dynamics of Heart-Valves - Experimental, Theoretical, and Computational Methods," *Annual Review of Fluid Mechanics* Vol. 14, 1982, pp. 235-259.
53. Fai, T. G., Griffith, B. E., Mori, Y., and Peskin, C. S. "Immersed Boundary Method for Variable Viscosity and Variable Density Problems Using Fast Constant-Coefficient Linear Solvers I: Numerical Method and Results," *Siam Journal on Scientific Computing* Vol. 35, No. 5, 2013, pp. B1132-B1161.
54. Kim, Y., Lai, M. C., and Peskin, C. S. "Numerical simulations of two-dimensional foam by the immersed boundary method," *Journal of Computational Physics* Vol. 229, No. 13, 2010, pp. 5194-5207.
55. Lushi, E., and Peskin, C. S. "Modeling and simulation of active suspensions containing large numbers of interacting micro-swimmers," *Computers & Structures* Vol. 122, 2013, pp. 239-248.
56. Miller, L. A., and Peskin, C. S. "Flexible clap and fling in tiny insect flight," *Journal of Experimental Biology* Vol. 212, No. 19, 2009, pp. 3076-3090.
57. Usabiaga, F. B., Bell, J. B., Delgado-Buscalioni, R., Donev, A., Fai, T. G., Griffith, B. E., and Peskin, C. S. "Staggered Schemes for Fluctuating Hydrodynamics," *Multiscale Modeling & Simulation* Vol. 10, No. 4, 2012, pp. 1369-1408.
58. Unverdi, S. O., and Tryggvason, G. "Computations of Multifluid Flows," *Physica D* Vol. 60, No. 1-4, 1992, pp. 70-83.
59. Unverdi, S. O., and Tryggvason, G. "A Front-Tracking Method for Viscous, Incompressible, Multi-Fluid Flows," *Journal of Computational Physics* Vol. 100, No. 1, 1992, pp. 25-37.
60. Goldstern, D., Handler, R., and Sirovich, L. "Modeling a no-slip flow boundary with an external force field," *J. Comp. Phys.* Vol. 105, 1993, pp. 354-366.
61. Mohd-Yusof, J. "Interaction of Massive Particles with Turbulence," *Dept. of Mechanical and Aerospace Engineering, Ph.D Thesis.* Cornell Univ. , 1996.
62. Uhlmann, M. "An immersed boundary method with direct forcing for the simulation of particulate flows," *Journal of Computational Physics* Vol. 209, No. 2, 2005, pp. 448-476.
63. Zhang, N., and Zheng, Z. C. "An improved direct-forcing immersed-boundary method for finite difference applications," *Journal of Computational Physics* Vol. 221, No. 1, 2007, pp. 250-268.
64. Fadlun, E. A., Verzicco, R., Orlandi, P., and Mohd-Yusof, J. "Combined immersed-boundary finite-difference methods for three-dimensional complex flow simulations," *Journal of Computational Physics* Vol. 161, No. 1, 2000, pp. 35-60.
65. Wang, S. Z., and Zhang, X. "An immersed boundary method based on discrete stream function formulation for two- and three-dimensional incompressible flows," *Journal of Computational Physics* Vol. 230, No. 9, 2011, pp. 3479-3499.

66. Balaras, E. "Modeling complex boundaries using an external force field on fixed Cartesian grids in large-eddy simulations," *Computers & Fluids* Vol. 33, No. 3, 2004, pp. 375-404.
67. Verzicco, R., Fatica, M., Iaccarino, G., and Moin, P. "Large eddy simulation of a road vehicle with drag-reduction devices," *Aiaa Journal* Vol. 40, No. 12, 2002, pp. 2447-2455.
68. Majumdar, S., Iaccarino, G., and Durbin, P. A. "RANS solver with adaptive structured boundary non-conforming grids," *Annual Research Brief, Center of Turbulence Research*, 2001, pp. 353-364.
69. Mittal, R., Seshadri, V., and Udaykumar, H. S. "Flutter, tumble and vortex induced autorotation," *Theoretical and Computational Fluid Dynamics* Vol. 17, No. 3, 2004, pp. 165-170.
70. Almgren, A. S., Bell, J. B., Colella, P., and Marthaler, T. "A Cartesian grid projection method for the incompressible Euler equations in complex geometries," *Siam Journal on Scientific Computing* Vol. 18, No. 5, 1997, pp. 1289-1309.
71. Kirkpatrick, M. P., Armfield, S. W., and Kent, J. H. "A representation of curved boundaries for the solution of the Navier-Stokes equations on a staggered three-dimensional Cartesian grid," *Journal of Computational Physics* Vol. 184, No. 1, 2003, pp. 1-36.
72. Udaykumar, H. S., Shyy, W., and Rao, M. M. "ELAFINT: A mixed Eulerian-Lagrangian method for fluid flows with complex and moving boundaries," *International Journal for Numerical Methods in Fluids* Vol. 22, No. 8, 1996, pp. 691-712.
73. Gazzola, M., Chatelain, P., van Rees, W. M., and Koumoutsakos, P. "Simulations of single and multiple swimmers with non-divergence free deforming geometries," *Journal of Computational Physics* Vol. 230, No. 19, 2011, pp. 7093-7114.
74. Kolomenskiy, D., and Schneider, K. "A Fourier spectral method for the Navier-Stokes equations with volume penalization for moving solid obstacles," *Journal of Computational Physics* Vol. 228, No. 16, 2009, pp. 5687-5709.
75. Laboratory, L. L. N. "Hypre Manual."
76. Logg, A., Mardal, K.-A., and Wells, G. *Automated Solution of Differential Equations by the Finite Element Method*: Springer, 2012.
77. Balay, S., Buschelman, K., Eijkhout, V., Gropp, W. D., Kaushik, D., Knepley, M. G., McInnes, L. C., Smith, B. F., and Zhang, H. "PETSc Users Manual," *Argonne National Laboratory, Tech. Rep. ANL-95/11 -Revision 2.1.5 2004*.
78. Saad, Y. *Iterative methods for sparse linear system*. Philadelphia: SIAM, 2004.
79. Bozkurtas, M., Dong, H., Seshadri, V., and Mittal, R. "Towards Numerical Simulation of Flapping Foils on Fixed Cartesian Grids," *43rd AIAA Aerospace Sciences Meeting and Exhibit*. 2005.
80. Hicken, J. E., and Zingg, D. W. "Parallel Newton-Krylov Solver for the Euler Equations Discretized Using Simultaneous-Approximation Terms," *AIAA Journal* Vol. 46, No. 11, 2008, pp. 2773-2786.

81. Gibou, F., and Min, C. H. "Efficient symmetric positive definite second-order accurate monolithic solver for fluid/solid interactions," *Journal of Computational Physics* Vol. 231, No. 8, 2012, pp. 3246-3263.
82. Robinson-Mosher, A., Shinar, T., Gretarsson, J., Su, J., and Fedkiw, R. "Two-way coupling of fluids to rigid and deformable solids and shells," *Acm Transactions on Graphics* Vol. 27, No. 3, 2008.
83. Borazjani, I., Ge, L., and Sotiropoulos, F. "Curvilinear immersed boundary method for simulating fluid structure interaction with complex 3D rigid bodies," *Journal of Computational Physics* Vol. 227, No. 16, 2008, pp. 7587-7620.
84. Yang, J., Preidikman, S., and Balaras, E. "A strongly coupled, embedded-boundary method for fluid-structure interactions of elastically mounted rigid bodies," *Journal of Fluids and Structures* Vol. 24, No. 2, 2008, pp. 167-182.
85. Yang, J. M., and Stern, F. "A simple and efficient direct forcing immersed boundary framework for fluid-structure interactions," *Journal of Computational Physics* Vol. 231, No. 15, 2012, pp. 5029-5061.
86. van Brummelen, E. H. "Added Mass Effects of Compressible and Incompressible Flows in Fluid-Structure Interaction," *Journal of Applied Mechanics-Transactions of the Asme* Vol. 76, No. 2, 2009.
87. Burman, E., and Fernandez, M. A. "Stabilization of explicit coupling in fluid-structure interaction involving fluid incompressibility," *Computer Methods in Applied Mechanics and Engineering* Vol. 198, No. 5-8, 2009, pp. 766-784.
88. Guidoboni, G., Glowinski, R., Cavallini, N., and Canic, S. "Stable loosely-coupled-type algorithm for fluid-structure interaction in blood flow," *Journal of Computational Physics* Vol. 228, No. 18, 2009, pp. 6916-6937.
89. Sagaut, P. *Large eddy simulation for incompressible flows : an introduction*. Berlin ; New York: Springer, 2006.
90. Abdilghanie, A. M., Collins, L. R., and Caughey, D. A. "Comparison of Turbulence Modeling Strategies for Indoor Flows," *Journal of Fluids Engineering-Transactions of the Asme* Vol. 131, No. 5, 2009, p. 051402.
91. Rohdin, P., and Moshfegh, B. "Numerical predictions of indoor climate in large industrial premises. A comparison between different k-epsilon models supported by field measurements," *Building and Environment* Vol. 42, No. 11, 2007, pp. 3872-3882.
92. Thai, Z. Q., Zhang, W., Zhang, Z., and Chen, Q. Y. "Evaluation of various turbulence models in predicting airflow and turbulence in enclosed environments by CFD: part 1 - Summary of prevalent turbulence models," *Hvac&R Research* Vol. 13, No. 6, 2007, pp. 853-870.
93. Tian, L., and Ahmadi, G. "Particle deposition in turbulent duct flows - comparisons of different model predictions," *Journal of Aerosol Science* Vol. 38, No. 4, 2007, pp. 377-397.
94. Zhang, Z., Zhai, Z. Q., Zhang, W., and Chen, Q. Y. "Evaluation of various turbulence models in predicting airflow and turbulence in enclosed environments by CFD: Part 2-comparison with experimental data from literature," *Hvac&R Research* Vol. 13, No. 6, 2007, pp. 871-886.

95. Di Sabatino, S., Buccolieri, R., Pulvirenti, B., and Britter, R. E. "Flow and pollutant dispersion in street canyons using FLUENT and ADMS-Urban," *Environmental Modeling & Assessment* Vol. 13, No. 3, 2008, pp. 369-381.
96. Hagen, L. J., Skidmore, E. L., Miller, P. L., and Kipp, J. E. "Simulation of Effect of Wind Barriers on Air-Flow," *Transactions of the Asae* Vol. 24, No. 4, 1981, pp. 1002-1008.
97. Lew, A. J., Buscaglia, G. C., and Carrica, P. M. "A note on the numerical treatment of the k-epsilon turbulence model," *International Journal of Computational Fluid Dynamics* Vol. 14, No. 3, 2001, pp. 201-209.
98. Liu, Q., Hoff, S. J., Maxwell, G. M., and Bundy, D. S. "Comparison of three k-epsilon turbulence models for predicting ventilation air jets," *Transactions of the Asae* Vol. 39, No. 2, 1996, pp. 689-698.
99. Poroseva, S., and Iaccarino, G. "Simulating Separated Flows using the k-e Model," *Center for Turbulence Research, Annual Research Briefs*, 2001, pp. 375-383.
100. Qian, W. Q., and Cai, J. S. "Parameter estimation of engineering turbulence model," *Acta Mechanica Sinica* Vol. 17, No. 4, 2001, pp. 302-309.
101. Richards, P. J., and Hoxey, R. P. "Appropriate Boundary-Conditions for Computational Wind Engineering Models Using the Kappa-Epsilon Turbulence Model," *Journal of Wind Engineering and Industrial Aerodynamics* Vol. 46-7, 1993, pp. 145-153.
102. Pope, S. B. *Turbulent flows*. Cambridge ; New York: Cambridge University Press, 2000.
103. Durbin, P. A., and Reif, B. A. P. *Statistical theory and modeling for turbulent flows*. Chichester ; New York: Wiley, 2001.
104. Smagorinsky, J. "General circulation experiments with the primitive equations: I. the basic equations," *Monthly Weather Review* Vol. 91, No. 3, 1963, pp. 99-164.
105. Lilly, D. K. "The representation of small-scale turbulence in numerical simulation experiments," *IBM Scientific Computing Symp. on Environmental Sciences*. IBM, Yorktown Heights, NY, 1967, p. 195210.
106. Hertel, C., Schumichen, M., Lobig, S., Frohlich, J., and Lang, J. "Adaptive large eddy simulation with moving grids," *Theoretical and Computational Fluid Dynamics* Vol. 27, No. 6, 2013, pp. 817-841.
107. Garmann, D. J., Visbal, M. R., and Orkwis, P. D. "Comparative study of implicit and subgrid-scale model large-eddy simulation techniques for low-Reynolds number airfoil applications," *International Journal for Numerical Methods in Fluids* Vol. 71, No. 12, 2013, pp. 1546-1565.
108. Germano, M., Piomelli, U., Moin, P., and Cabot, W. H. "A Dynamic Subgrid-Scale Eddy Viscosity Model," *Physics of Fluids a-Fluid Dynamics* Vol. 3, No. 7, 1991, pp. 1760-1765.
109. van Driest, E. R. "On Turbulent Flow near a Wall," *Journal of the Aeronautical Sciences* Vol. 23, No. 11, 1956, pp. 1007-1011.
110. Schlichting, H., and Gersten, K. *Boundary-layer theory*. Berlin ; New York: Springer, 2000.

111. Wu, H. W., and Perng, S. W. "LES analysis of turbulent flow and heat transfer in motored engines with various SGS models," *International Journal of Heat and Mass Transfer* Vol. 45, No. 11, 2002, pp. 2315-2328.
112. Xu, H. Y. "Direct numerical simulation of turbulence in a square annular duct," *Journal of Fluid Mechanics* Vol. 621, 2009, pp. 23-57.
113. Balaras, E., Benocci, C., and Piomelli, U. "Two-layer approximate boundary conditions for large-eddy simulations," *Aiaa Journal* Vol. 34, No. 6, 1996, pp. 1111-1119.
114. Wang, M., and Moin, P. "Dynamic wall modeling for large-eddy simulation of complex turbulent flows," *Physics of Fluids* Vol. 14, No. 7, 2002, pp. 2043-2051.
115. Tessicini, F., Iaccarino, G., Fatica, M., Wang, M., and Verzicco, R. "Wall modeling for large-eddy simulation using an immersed boundary method." Center of Turbulence Research, 2002, pp. 181-187.
116. Anderson, W. "An immersed boundary method wall model for high-Reynolds-number channel flow over complex topography," *International Journal for Numerical Methods in Fluids* Vol. 71, No. 12, 2013, pp. 1588-1608.
117. Roman, F., Armenio, V., and Frohlich, J. "A simple wall-layer model for large eddy simulation with immersed boundary method," *Physics of Fluids* Vol. 21, No. 10, 2009.
118. Ji, C., Munjiza, A., and Williams, J. J. R. "A novel iterative direct-forcing immersed boundary method and its finite volume applications," *Journal of Computational Physics* Vol. 231, No. 4, 2012, pp. 1797-1821.
119. Wilson, D. K., Collier, S. L., Ostashev, V. E., Aldridge, D. F., Symon, N. P., and Marlin, D. H. "Time-domain modeling of the acoustic impedance of porous surfaces," *Acta Acustica United with Acustica* Vol. 92, No. 6, 2006, pp. 965-975.
120. Xu, Y., Zheng, Z. C., and Wilson, D. K. "Simulation of Turbulent Wind Noise Reduction by Porous Windscreens Using High-Order Schemes," *Journal of Computational Acoustics* Vol. 18, No. 4, 2010, pp. 321-334.
121. Dong, H., Mittal, R., and Najjar, F. M. "Wake topology and hydrodynamic performance of low-aspect-ratio flapping foils," *Journal of Fluid Mechanics* Vol. 566, 2006, pp. 309-343.
122. Pozrikidis, C. *Introduction to theoretical and computational fluid dynamics*. New York: Oxford University Press, 1997.
123. Yang, J. M., and Balaras, E. "An embedded-boundary formulation for large-eddy simulation of turbulent flows interacting with moving boundaries," *Journal of Computational Physics* Vol. 215, No. 1, 2006, pp. 12-40.
124. Le, H., and Moin, P. "An Improvement of Fractional Step Methods for the Incompressible Navier-Stokes Equations," *Journal of Computational Physics* Vol. 92, No. 2, 1991, pp. 369-379.
125. Wei, Z., Zheng, Z. C., and Yang, X. "Computation of Flow through a Three-Dimensional Periodic Array of Porous Structures by a Parallel Immersed-Boundary Method," *ASME Journal of Fluids Engineering* Vol. 136, No. 4, 2014, p. 10.
126. Lee, J., Kim, J., Choi, H., and Yang, K. S. "Sources of spurious force oscillations from an immersed boundary method for moving-body problems," *Journal of Computational Physics* Vol. 230, No. 7, 2011, pp. 2677-2695.

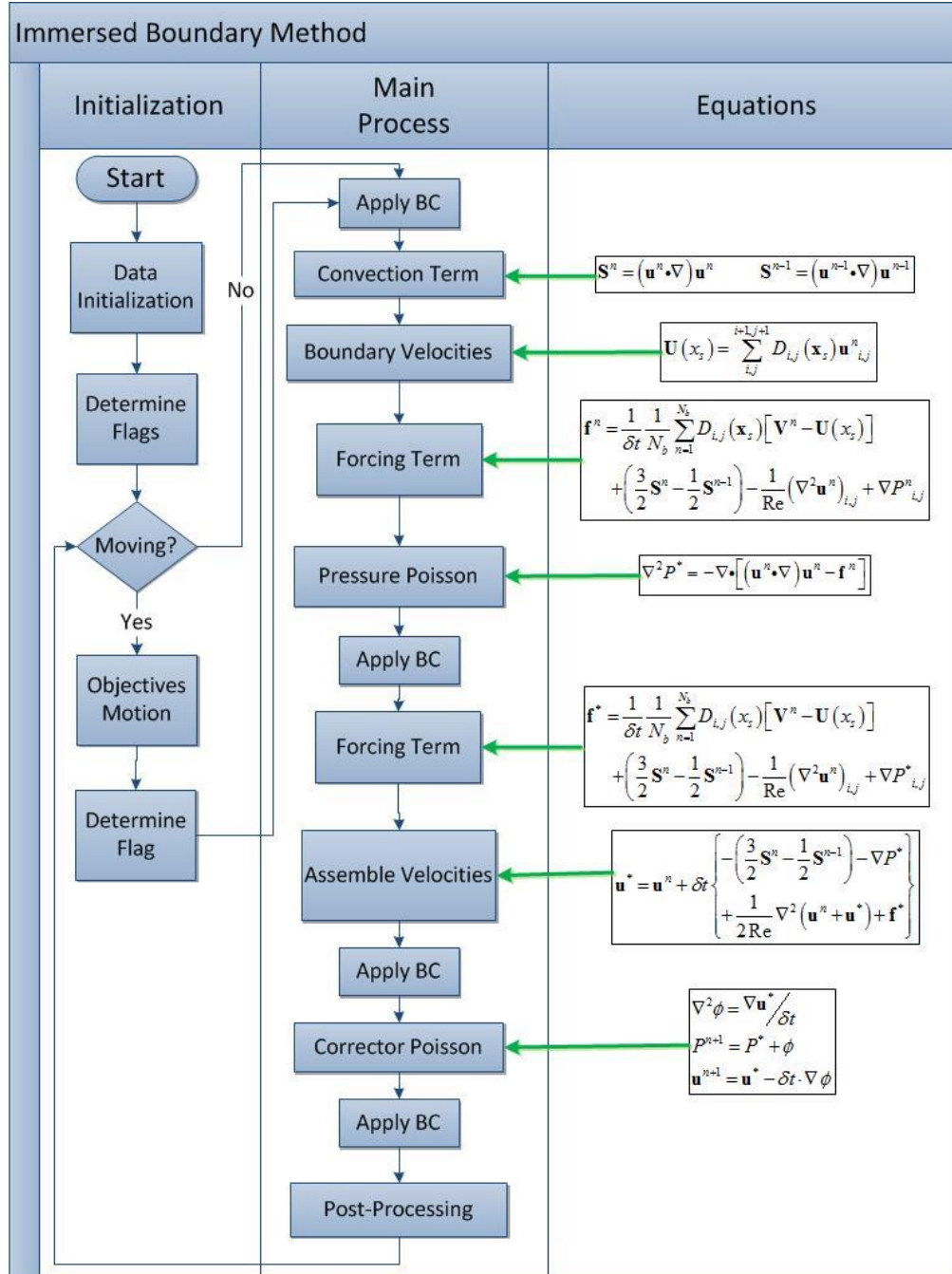
127. Breuer, M. "Large eddy simulation of the subcritical flow past a circular cylinder: Numerical and modeling aspects," *International Journal for Numerical Methods in Fluids* Vol. 28, No. 9, 1998, pp. 1281-1302.
128. Moin, P., and Kim, J. "Numerical Investigation of Turbulent Channel Flow," *Journal of Fluid Mechanics* Vol. 118, No. May, 1982, pp. 341-377.
129. McCormick, S. F. *Multigrid methods*. Philadelphia, Pa.: Society for Industrial and Applied Mathematics, 1987.
130. Baytas, A. C., Erdem, D., Acar, H., Cetiner, O., and Basci, H. "Analytical Determination of the Permeability for Slow Flow Past Periodic Arrays of Cylinders with Different Cross Sections," *Journal of Porous Media* Vol. 15, No. 11, 2012, pp. 1009-1018.
131. Kuwahara, F., Nakayama, A., and Koyama, H. "Numerical Modeling of Heat and Fluid Flow in a Porous Medium," *Proceedings of the Tenth International Heat Transfer Conference*. Vol. 5, Brighton, UK, 1994, pp. 309-314.
132. Montillet, A. "Flow through a finite packed bed of spheres: A note on the limit of applicability of the Forchheimer-type equation," *Journal of Fluids Engineering-Transactions of the Asme* Vol. 126, No. 1, 2004, pp. 139-143.
133. Vafai, K., and Hadim, H. A. *Handbook of porous media*. New York: Marcel Dekker, 2000.
134. Patankar, S. V. *Numerical heat transfer and fluid flow*. Washington, New York: Hemisphere Pub. Corp. ; McGraw-Hill, 1980.
135. Patankar, S. V., Liu, C. H., and Sparrow, E. M. "Fully Developed Flow and Heat-Transfer in Ducts Having Streamwise-Periodic Variations of Cross-Sectional Area," *Journal of Heat Transfer-Transactions of the Asme* Vol. 99, No. 2, 1977, pp. 180-186.
136. Yang, X., Zhang, X., Z, L., and G., H. "A smoothing technique for discrete delta functions with application to immersed boundary method in moving boundary simulations," *Journal of Computational Physics* Vol. 228, 2009, pp. 7821-7836.
137. Zheng, Z., and Zhang, N. "Frequency Effect on Lift and Drag of an Oscillating Cylinder in Flow," *Journal of Fluids and Structures* Vol. 24, 2008, pp. 382-399.
138. Kim, J., Kim, D., and Choi, H. "An immersed-boundary finite-volume method for simulations of flow in complex geometries," *Journal of Computational Physics* Vol. 171, No. 1, 2001, pp. 132-150.
139. Zhao, M. "Flow induced vibration of two rigidly coupled circular cylinders in tandem and side-by-side arrangements at a low Reynolds number of 150," *Physics of Fluids* Vol. 25, No. 12, 2013.
140. Ahn, H. T., and Kallinderis, Y. "Strongly coupled flow/structure interactions with a geometrically conservative ALE scheme on general hybrid meshes," *Journal of Computational Physics* Vol. 219, No. 2, 2006, pp. 671-696.
141. Johnson, T. A., and Patel, V. C. "Flow past a sphere up to a Reynolds number of 300," *Journal of Fluid Mechanics* Vol. 378, 1999, pp. 19-70.
142. Cristallo, A., and Verzicco, R. "Combined immersed Boundary/Large-Eddy-Simulations of incompressible three dimensional complex flows," *Flow Turbulence and Combustion* Vol. 77, No. 1-4, 2006, pp. 3-26.
143. Piomelli, U. "Wall-layer models for large-eddy simulations," *Progress in Aerospace Sciences* Vol. 44, No. 6, 2008, pp. 437-446.

144. Piomelli, U., and Balaras, E. "Wall-layer models for large-eddy simulations," *Annual Review of Fluid Mechanics* Vol. 34, 2002, pp. 349-374.
145. Rodriguez, I., Borell, R., Lehmkuhl, O., Segarra, C. D. P., and Oliva, A. "Direct numerical simulation of the flow over a sphere at $Re=3700$," *Journal of Fluid Mechanics* Vol. 679, 2011, pp. 263-287.
146. Vanella, M., Rabenold, P., and Balaras, E. "A direct-forcing embedded-boundary method with adaptive mesh refinement for fluid-structure interaction problems," *Journal of Computational Physics* Vol. 229, No. 18, 2010, pp. 6427-6449.
147. Laboratory, L. L. N. *SAMRAI Manual*.
148. Vanella, M., and Balaras, E. "A moving-least-squares reconstruction for embedded-boundary formulations," *Journal of Computational Physics* Vol. 228, No. 18, 2009, pp. 6617-6628.
149. Li, N., Balaras, E., and Piomelli, U. "Inflow conditions for large-eddy simulations of mixing layers," *Physics of Fluids* Vol. 12, No. 4, 2000, pp. 935-938.
150. Perret, L., Delville, J., Manceau, R., and Bonnet, J. P. "Turbulent inflow conditions for large-eddy simulation based on low-order empirical model," *Physics of Fluids* Vol. 20, No. 7, 2008.
151. Eldredge, J. D., and Wang, C. "A Computational Study of a Canonical Pitch-up, Pitch-down Wing Maneuver," *39th AIAA Fluid Dynamics Conference*. San Antonio, Texas, 2009.
152. Ol, M. "The high-frequency, high amplitude pitch problem: airfoils, plates and wings," *39th AIAA Fluid Dynamics Conference*. San Antonio, Texas, 2009.
153. Theodore, T. "General theory of aerodynamic instability and the mechanism of flutter," *NACA Rept. 496*, 1935.
154. McGowan, G. Z., Gopalarathnam, A., Ol, M., and Edwards, J. R. "Analytical, Computational, and Experimental Investigations of Equivalence Between Pitch and Plunge Motions for Airfoils at Low Reynolds Numbers," *47th AIAA Aerospace Sciences Meeting Including The New Horizons Forum and Aerospace Exposition*. Orlando, Florida, 2009.
155. Leishman, J. G. *Principles of helicopter aerodynamics*. Cambridge University Press, New York, 2000.
156. Platzer, M. F., Jones, K. D., Young, J., and Lai, J. C. S. "Flapping-wing aerodynamics_ Progress and challenges," *AIAA Journal* Vol. 46, No. 9, 2008, pp. 2136-2149.
157. Young, J., and Lai, J. C. S. "Oscillation frequency and amplitude effects on the wake of a plunging airfoil," *AIAA Journal* Vol. 42, No. 10, 2004, pp. 2042-2052.
158. Dohring, C. M. "Experimental analysis of the wake of an oscillating airfoil." Vol. Master, Naval Postgraduate School, Monterey, CA., 1996, p. 148.
159. Yang, X. F., and Zheng, Z. C. "Nonlinear spacing and frequency effects of an oscillating cylinder in the wake of a stationary cylinder," *Physics of Fluids* Vol. 22, No. 4, 2010.
160. Zheng, Z. C., Wei, Z., and Zhang, N. "Immersed-Boundary Simulation of a Fast Pitching Airfoil," *AIAA 40th Fluid Dynamics Conference and Exhibit*. Chicago, IL, 2010.

161. Zheng, Z., and Zhang, N. "Effects of Frequency on Lift and Drag of an Oscillating Cylinder in Flow," *Journal of Fluids and Structures* Vol. 24, 2008, pp. 382-399.
162. Liao, Q., Dong, G.-J., and Lu, X.-Y. "Vortex formation and force characteristics of a foil in the wake of a circular cylinder," *Journal of Fluids and Structures* Vol. 19, 2004, pp. 491-510.
163. Simpson, B. J., Hover, F. S., and Triantafyllou, M. S. "Experiments in direct energy extraction through flapping foils," *Proceedings of the Eighteenth (2008) International Offshore and Polar Engineering Conference*. Vancouver, BC, Canada, 2008, pp. 370-376.
164. Duncan, W. J., Thom, A. S., and Young, A. D. *Mechanics of Fluids*. New York: American Elsevier Publishing Company, Inc., 1970.
165. Marshall, J. S. *Invisi Incompressible Flow*. Canada: John Wiley & Sons, Inc., 2001.
166. Spurk, J. H. *Fluid mechanics : problems and solutions*. Berlin ; New York: Springer, 1997.
167. Chernyshenko, S. I., Galletti, B., Lo, A. I., and Zannetti, L. "Trapped vortices and a favourable pressure gradient," *Journal of Fluid Mechanics* Vol. 482, 2003, pp. 235-255.
168. Anderson, J. D. *Fundamentals of aerodynamics*. Boston: McGraw-Hill Higher Education, 2007.
169. Huang, M. K., and Chow, C. Y. "Trapping of a Free Vortex by Joukowski Airfoils," *AIAA Journal* Vol. 20, No. 3, 1982, pp. 292-298.
170. Dabiri, J. O. "Renewable fluid dynamic energy derived from aquatic animal locomotion," *Bioinspiration & Biomimetics* Vol. 2, No. 3, 2007, pp. L1-L3.
171. Huang, H., and Sun, M. "Dragonfly forewing-hindwing interaction at various flight speeds and wing phasing," *AIAA Journal* Vol. 45, No. 2, 2007, pp. 508-511.
172. Zhu, Q. "Energy harvesting by a purely passive flapping foil from shear flows," *Journal of Fluids and Structures* Vol. 34, 2012, pp. 157-169.
173. Wei, Z., and Zheng, Z. C. "Energy Harvesting of a Flapping Airfoil in a Vortical Wake," *AIAA Journal (In preparation)*, 2014.

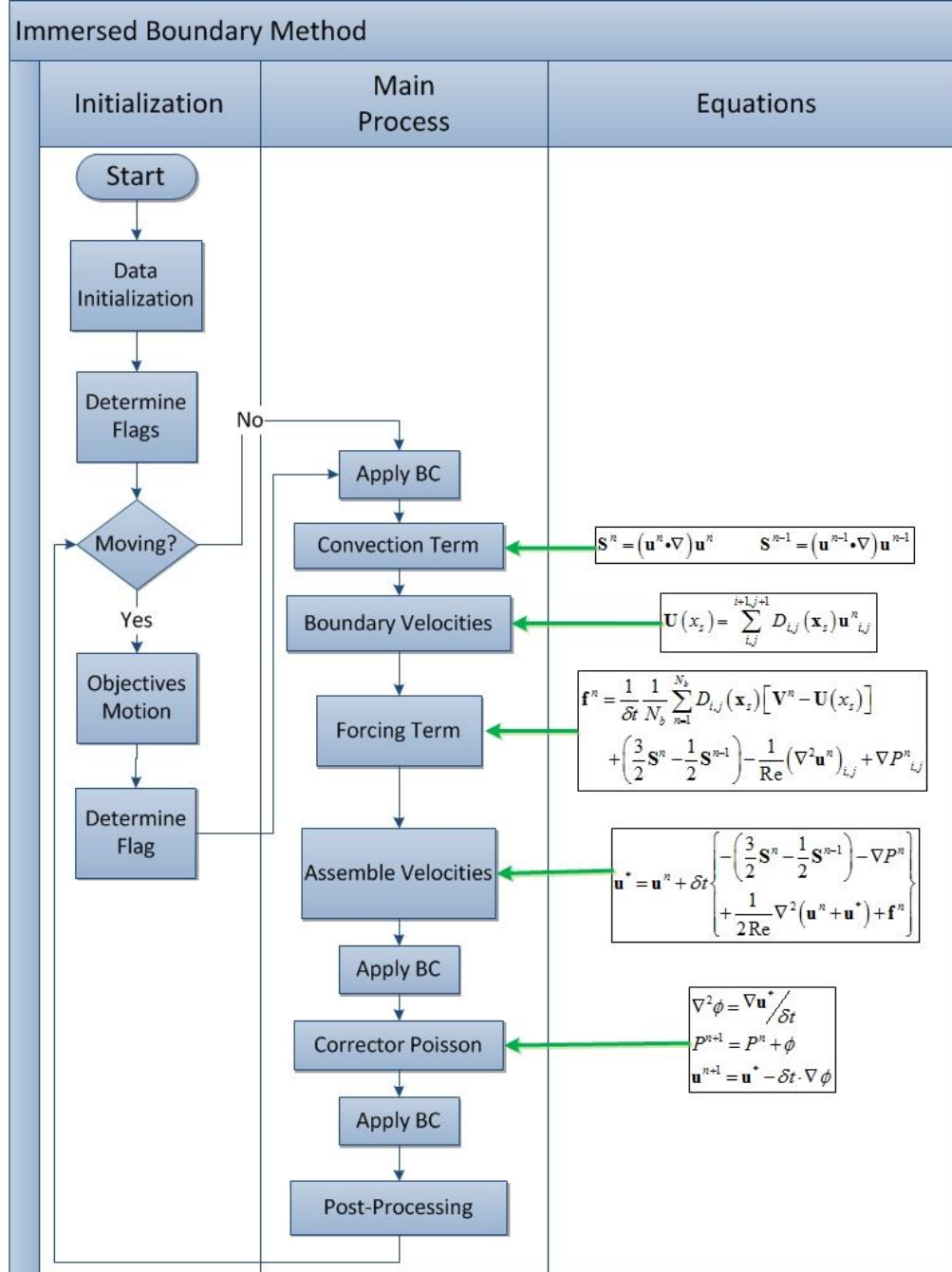
Appendix I

Flow Chart for the 1st-order Temporal Scheme with Pressure



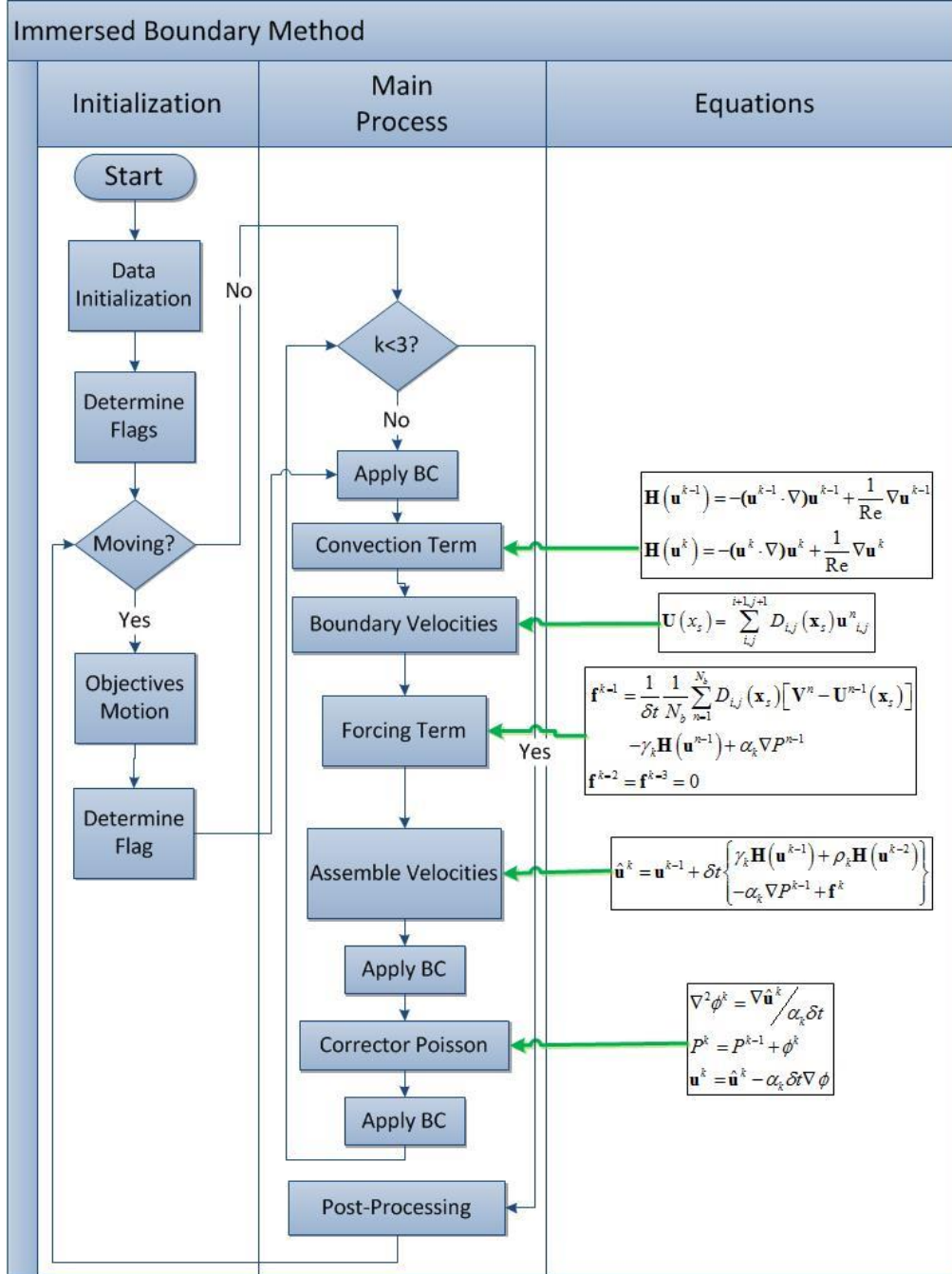
Appendix II

Flow Chart for the 1st-order Temporal Scheme without Pressure



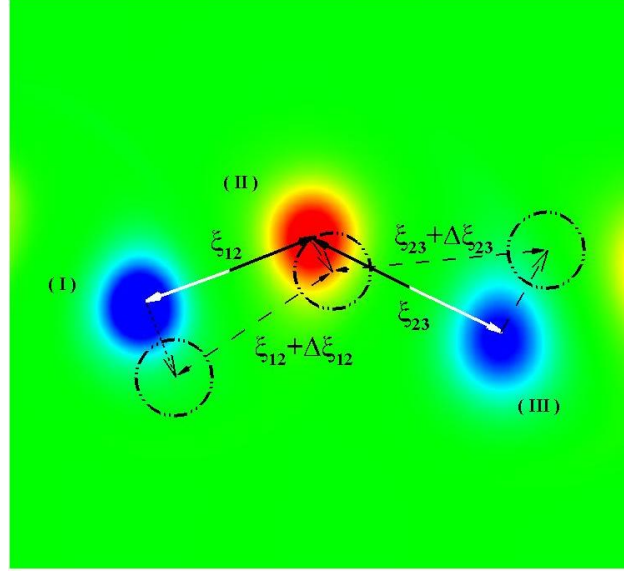
Appendix III

Flow Chart for the 3rd-order Runge-Kutta Scheme in the current work



Appendix IV

Theoretical Prediction of the Motion of Vortices



The example is made between the vortices II & III.

The distance for current moment

$$\xi_{current}^2 = (x_2 - x_3)^2 + (y_2 - y_3)^2$$

The distance for the next moment

$$\begin{aligned} \xi_{next}^2 &= [(x_2 + \Delta x_2) - (x_3 + \Delta x_3)]^2 + [(y_2 + \Delta y_2) - (y_3 + \Delta y_3)]^2 \\ &= [(x_2 - x_3) + (\Delta x_2 - \Delta x_3)]^2 + [(y_2 - y_3) + (\Delta y_2 - \Delta y_3)]^2 \\ &= (x_2 - x_3)^2 + 2(x_2 - x_3)(\Delta x_2 - \Delta x_3) + (\Delta x_2 - \Delta x_3)^2 \\ &\quad + (y_2 - y_3)^2 + 2(y_2 - y_3)(\Delta y_2 - \Delta y_3) + (\Delta y_2 - \Delta y_3)^2 \end{aligned}$$

The difference between the distances is

$$\begin{aligned}
\Delta L &= \xi_{next}^2 - \xi_{current}^2 \\
&= 2(x_2 - x_3)(\Delta x_2 - \Delta x_3) + (\Delta x_2 - \Delta x_3)^2 \\
&\quad 2(y_2 - y_3)(\Delta y_2 - \Delta y_3) + (\Delta y_2 - \Delta y_3)^2 \\
&= [2(x_2 - x_3) + (\Delta x_2 - \Delta x_3)](\Delta x_2 - \Delta x_3) \\
&\quad + [2(y_2 - y_3) + (\Delta y_2 - \Delta y_3)](\Delta y_2 - \Delta y_3)
\end{aligned}$$

Then

$$\Delta L = \boxed{[2(x_2 - x_3) + (\Delta x_2 - \Delta x_3)](\Delta x_2 - \Delta x_3) + [2(y_2 - y_3) + (\Delta y_2 - \Delta y_3)](\Delta y_2 - \Delta y_3)}$$

Therefore, if ΔL is proved to be negative, the distance between vortices II and III will decrease.

If the arrangement of these three vortices is I at the left, II at the middle and III at the right, then $(x_2 - x_3) < 0$

If the arrangement of these three vortices is I at the bottom, II at the top and III at the bottom, then $(y_2 - y_3) > 0$

Based on the vortex model, $\Delta x_2 \approx U_{dipole-12} \cos \alpha_{12} + U_{dipole-23} \cos \alpha_{23}$ and $\Delta x_3 \approx U_{dipole-23} \cos \alpha_{23}$. Therefore, $\Delta x_2 - \Delta x_3 \approx U_{dipole-12} \cos \alpha_{12} > 0$. The reason to use ‘approximate equal’ is that Δx_3 should depend on the induced velocity at vortex III from vortex II rather than dipole velocity of vortices II and III. But the induced velocity is very close to the dipole velocity in terms of magnitude.

Similarly, the vortex II is moving downwards and the vortex III is moving upwards. Therefore, $\Delta y_2 < 0$ and $\Delta y_3 > 0$. In conclusion $(\Delta y_2 - \Delta y_3) < 0$

The sign of each term of the previous equation reads

$$\Delta L = \left[\underbrace{2(x_2 - x_3)}_{(-)} + \underbrace{(\Delta x_2 - \Delta x_3)}_{(+)} \right] \underbrace{(\Delta x_2 - \Delta x_3)}_{(+)} \\ + \left[\underbrace{2(y_2 - y_3)}_{(+)} + \underbrace{(\Delta y_2 - \Delta y_3)}_{(-)} \right] \underbrace{(\Delta y_2 - \Delta y_3)}_{(-)}$$

If the magnitude of $(x_2 - x_3)$ is larger than that of $(\Delta x_2 - \Delta x_3)$ and magnitude of $(y_2 - y_3)$ is larger than $(\Delta y_2 - \Delta y_3)$, ΔL decrease. However, that is only for the usual cases.

For cases that

1. The magnitudes of $(x_2 - x_3)$ and $(\Delta x_2 - \Delta x_3)$ are in almost the same order, for example, $x_2 = x_3$.
2. The magnitude of $(y_2 - y_3)$ and $(\Delta y_2 - \Delta y_3)$ are in almost the same order, for example, $y_2 = y_3$.

Then, the changing trend of ΔL is unpredictable.